Quantitative Modeling of the Rise in Atmospheric Oxygen

Mark W. Claire

A dissertation
submitted in partial fulfillment of the
requirements for the degree of

Doctor of Philosophy

University of Washington

2008

Program Authorized to Offer Degree:
Astronomy

University of Washington
Graduate School

This is to certify that I have examined this copy of a doctoral dissertation by

Mark W. Claire

and have found that it is complete and satisfactory in all respects,
and that any and all revisions required by the final
examining committee have been made.

Chair of the Supervisory Committee:

David C. Catling

Reading Committee:

David C. Catling

Victoria S. Meadows

Suzanne L. Hawley

Date:_____

University of Washington

Abstract

Quantitative Modeling of the Rise in Atmospheric Oxygen

Mark W. Claire

Chair of the Supervisory Committee:
Professor David C. Catling
Department of Atmospheric Sciences and Astrobiology Program

The abrupt rise of molecular oxygen in Earth's atmosphere approximately 2.4 billion years ago was perhaps the most profound event in Earth's history after the evolution of life itself. Biogeochemical cycles in Earth's atmosphere, ocean, and crust were completely reorganized and it also likely marked the first moment when our planet could be deemed "inhabited" across interstellar space via identification of biogenically produced O_2 and O_3 in a spectrum of Earth's atmosphere. This dissertation explores the "Great Oxidation Event" via numerical modeling of evolving ancient atmospheres.

In creating a self-consistent description of evolving redox fluxes in the Earth system, we reach the following conclusions. After the evolution of oxygenic photosynthesis, the atmosphere has two primary stable states – one is methane-rich and produces mass-independent fractionation of sulfur isotopes (MIF-S), and one is oxygen-rich and does not produce MIF-S. These two stable states are separated by only a few percent in the fluxes of O_2 and CH_4 needed to sustain them. The atmosphere evolves rapidly from one state to the other when the net flux of reductants drops below the net flux of oxidants into the atmosphere. The transition between the two states - "the rise of

oxygen" - is only feasible once methane levels drop below ~50 ppm. We show numerically that hydrogen escape can drive irreversible oxidation of Earth's crust, leading to decreasing CH_4 concentrations over long timescales. We argue that the disappearance of the MIF-S signal is better described as recording a collapse of atmospheric CH_4, rather than the appearance of O_2. As CH_4 levels decrease, a positive feedback between oxidative weathering, oceanic sulfate concentrations, and the anaerobic oxidation of methane further drives atmospheric instability. Once a critical threshold in CH_4 concentration is overcome, the atmosphere transitions from an anoxic to oxic state on the timescale of 10^3 years. The post-transition levels of O_2 and CH_4 and the global climate are strongly driven by biological forcing. Considering the events of 2.4 Ga as a "Great Collapse of Methane" helps explain the initiation of Snowball Earth, the disappearance of MIF-S, and the rise of oxygen.

TABLE OF CONTENTS

LIST OF FIGURES

Figure Number Page

LIST OF TABLES

Table Number Page

ACKNOWLEDGEMENTS

There are so many things that have gone exactly right for me to be writing these words. At any one of multiple crossroads, my life could have lead in a completely in a different direction. That my path has lead to this dissertation has been the result of extreme luck and unimaginable privilege, and has been punctuated by interactions with multiple individuals, providing advice both direct and indirect. To list them all would take more time than reasonable. Scientifically, I thank Bob Grabhorn for forcing me to take Astronomy 101 seriously, Tom Grissom and John Marvin for helping me realize that graduate school was even a possibility, and by extension to all my teachers along the way. Personally, the love and support of Michelle Glatt and Amos Blanton have carried me through many tough times. And of course to my parents, who allowed me the freedom to find my own path.

I must also acknowledge my mentors and co-authors David Catling and Kevin Zahnle. The work described in Chapters 2 through 7 of this dissertation was a strongly collaborative effort, and their help and encouragement was instrumental. The ideas within the following chapters were developed in a series of papers with various perturbations in the authorship list, and so contains some words not written by me. These papers are included given that I was involved with all of the fundamental research and plots generated within, and that, together, they tell such a nice story. The contributions and authorship is directly acknowledged in the beginning of each chapter.

DEDICATION

To Michelle

Chapter 1 Introduction

1.1 Earth's oxygen rich atmosphere – How did it get here?

Earth's atmosphere is unique among the terrestrial planets, primarily due to abundant quantities of free oxygen (O_2). The reason is biology, as this is the only known source that can support 0.21 bar of O_2 in a planetary atmosphere. O_2 (and its photolytic product O_3) are readily apparent in the disk averaged spectrum of the Earth (Turnbull *et al.*, 2006), so that detection of this gas may be possible across interstellar distances (Des Marais *et al.*, 2002). We will be able to search for other planets with Earth-like biology in the solar neighborhood using next generation space telescopes such as the Terrestrial Planet Finder and Darwin, which are being developed by NASA and ESA, respectively[*]. Quantitative information derived from astronomical spectra are strongly dependent on models of the underlying processes affecting the atmosphere in question. This dissertation investigates quantitative models of oxygen in planetary atmospheres (Earth's in particular), with a focus on understanding atmospheric evolution on terrestrial planets. In particular, we attempt to conceptually understand and numerically model the strong evidence that oxygen levels in Earth's atmosphere have varied through time.

Earth's geologic record is subdivided based on age, in a manner that is roughly but not exactly correlated to oxygen levels in the atmosphere. The Phanerozoic is defined as the time period from 542 million years ago (Ma) to the present, and roughly corresponds to the time period when modern levels of atmospheric oxygen stimulated the Cambrian explosion of advanced animal life. The time period between 2.5 billion years ago (Ga) and 542 Ma is known as the Proterozoic, during most of which free O_2 existed at ~ 5 - 18% of present levels. The geologic era between 3.8 Ga and 2.5 Ga is known as the Archean. For all of the Archean and for the earliest portion of the Proterozoic, free

[*] The National Aeronautics and Space Agency (NASA) and European Space Agency (ESA) are the space agencies of the governments of the United States and the European Union member states.

oxygen existed at less than 0.001% of present levels. These changes in atmospheric oxygen have been discussed in the literature for half a century but nearly all theoretical analyses to date have been qualitative, as discussed in sections 2.6 and 3.2. The primary motivation of this dissertation is a quantitative examination of conditions leading to and affecting the "first rise in oxygen" or "Great Oxygenation Event" in which O_2 levels rose from trace quantities to ~10% of modern levels, which occurred between 2.45 and 2.32 Ga (Bekker *et al.*, 2004), during the earliest portion of the Proterozoic period known as the Paleoproterozic.

1.2 Redox Reactions Reduced*

Redox reactions and geochemistry are a vital portion of this dissertation, so we provide a brief review for the interested reader whose knowledge of general chemistry has been supplanted by other facts. There are two broad classes of chemical reactions – reactions that transfer protons between reactants (defined as "acid-base" reactions) and reactions that transfer electrons between reactants (defined as "redox" reactions). In a redox reaction, the reactant that gains an electron is "reduced", while the reactant that loses an electron has been "oxidized." Redox reactions are coupled by definition – the only way for a molecule to be oxidized in a reaction is for another molecule to be reduced at the same time. Another important definition is the "oxidation state" of an element. The oxidation states available to an element are determined by fundamental physics, but the oxidation state that the element actually exists in is set by the environment. For example, quantum mechanics dictates that iron (Fe) can exist as Fe^0, Fe^{2+}, or Fe^{3+}, meaning that iron is capable of donating 0, 2 or 3 of its electrons depending on what it meets in a chemical reaction. Rusting of iron ($4Fe(OH)_2 + O_2 \rightarrow 2Fe_2O_3 + 4H_2O$) is a redox reaction in which iron is oxidized from the Fe^{2+} oxidation state ("ferrous" iron) to the Fe^{3+} oxidation state ("ferric" iron). A major confusion is that the terms "oxidized/oxidizing/oxidant" need not have anything to do with the element oxygen: $FeCl_2+CeCl_4 \rightarrow FeCl_3 + CeCl_3$ is a redox reaction in which $FeCl_2$ (the "reducing

* The material in this section is adapted from a section I wrote for the *Astrobiology Primer – An outline of general knowledge* (Mix, L. J. *et al.*, 2006), an evolving "textbook" of basic ideas that astrobiology students should know, as conceived and written by a group of young astrobiologists.

agent" or "reductant") is oxidized by $CeCl_4$ (the "oxidizing agent" or "oxidant"). In exchange for oxidizing the iron from Fe^{2+} to Fe^{3+}, the cerium is reduced in oxidation state from Ce^{4+} to Ce^{3+}.

Redox reactions are exploited by biological metabolisms, and are also a very important for interpreting the paleo-envioronment. Examining the oxidation state of elements in the geological record helps us infer the paleo-conditions under which the rock formed. For example, if we observe lithified soils ("paleosols"), we notice that soils older than 2.4 Ga are generally free of iron, while younger paleosols are rich in iron, but only in the Fe^{3+} oxidation state (Rye & Holland, 1998). In the lab, we notice that Fe^{2+} is soluble in water but Fe^{3+} is not. The standard interpretation of these two facts is that ancient rainwater did not contain dissolved oxygen, and hence would have leached soils of soluble Fe^{2+}. Oxygenated rainwater (i.e. rainwater containing dissolved O_2) would oxidize iron to the insoluble Fe^{3+} oxidation state, retaining the iron in the soil. This geochemical interpretation is one of the arguments for a dramatic change in the overall oxidation state of the atmosphere at ~2.4 Ga, as discussed further in sections 1.3 and 2.5. Thus, the geochemistry of Fe and other (especially rare-earth) elements in well-preserved rocks can constrain the "redox state" of entire reservoirs such as the atmosphere and ocean. In this context, the terms "reducing" or "oxidizing" environments are commonly used. A reducing environment has an excess of available reductants (usually hydrogen), while an oxidizing environment has an excess of available oxidants (generally oxygen.)

1.3 The history of atmospheric oxygen

That Earth's oxygen level has changed through time has not always been accepted as fact. Interpretation of Earth's history by examination of the geologic record has been strongly influenced by the principle of "Uniformitarianism" – an unproven but foundational postulate that geological processes do not change and that the present is the key to the past. This worldview was strongly questioned in 1927, when Alexander Macgregor published "The problem of the Precambrian atmosphere" in the *South African Journal of Science*. As a geologist for the Rhodesian Geological Survey, he measured the ratio of

ferrous to ferric iron (Fe^{2+}/Fe^{3+}) in ancient rocks and found every "Precambrian"* rock to be enriched in Fe^{2+} compared to Fe^{3+}. Macgregor convincingly demonstrated that the iron redox state of Rhodesian rocks was very different from modern shales, quartzites, and igneous rocks, concluding:

> "It is not necessary to emphasize the bearing of these analyses upon the general question [the content of the ancient atmosphere]. Not one of the analyses gives indication of any oxidation having taken place during the formation of the rock. On the other hand, reduction is suggested in the case of some."

Macgregor (1927) further argues that atmospheric CO_2 levels were higher in the Precambrian, due to the high degree of fine-grained carbonation in the rocks. He argues that these two observations (high CO_2 and low O_2) can easily explain banded iron formations (BIFs). BIFs were the most well known Precambrian rocks at the time (and today), but their formation processes were a geologic mystery in 1927 (and to some extent still are (Klein, 2005)). We discuss BIFs in the modern context in section 2.5.1.2, noting here simply that they are indicative of reducing conditions in the deep ocean which allow for reduced iron concentrations to build up in the soluble Fe^{2+} redox state (see section 1.2). Macgregor's theory for why the atmosphere became oxidized was primarily the disproportionation of CO_2 -> C + O_2, an idea which hasn't held up given the realization that metamorphism of crustal materials would reverse this process. This can be forgiven given that basic geological principles such as continental drift and subduction of the continental crust were not fully developed in 1927 (see section 3.2.2.2.a).

Geologic work on "Precambrian" rocks continued through the 20th century, with geologist Preston Cloud as the strongest proponent of the ancient anoxic atmosphere (e.g. Cloud, 1972). The name most associated with the field in the second half of the 20th century is

* In 1927, this meant rocks without fossils, as modern methods of radioactive dating hadn't been established. The Rhodesian craton is now known to be of Archean age, with average age of 2.7 Ga (Wilson *et al.*, 1978)

Dick Holland, who painstakingly applied modern quantitative techniques to ancient rocks, compiled massive amounts of data, and attempted to assimilate them into models of ancient environments. His work, summarized in two major textbooks, 1978's "*The Chemistry of the Atmosphere and Oceans*" and 1984's *"The Chemical Evolution of the Atmosphere and Oceans*" provided the first well-defended quantitative predictions of ancient oxygen levels, which are summarized in Figure 1-1. Given his standing in the field, it was a quite an honor (and a bit scary) to have Dick Holland chosen as the primary peer reviewer for the material presented in Chapter 3 of this dissertation.

Not much quantitative work was done on the atmospheric side of the problem until Jim Kasting's Ph.D. dissertation which showed that Earth atmosphere prior to the evolution of life (or "prebiotic" atmosphere) would have ground level O_2 concentrations approximately 12 orders of magnitude below modern levels (Kasting, 1979). Without photosynthetic organisms producing O_2, the only free O_2 present in the prebiotic atmosphere would be produced by H_2O photolysis to H_2 and O, with subsequent escape of H to space (Kasting, 1998). Kasting (1979) showed that this process would produce a ground level O_2 mixing ratio (O_2 number density/total atmospheric density) of 10^{-13}.

After the publication of Holland's now classic books (Holland, 1978; Holland, 1984), a good portion of the Earth science community accepted the evidence for the rise of oxygen, but the consensus was not unanimous. Dick Holland's first graduate student Hiroshi Ohmoto has been a strong opponent of the theory championed by his mentor, and their conflict has driven much of the quantitative study of this field in the past few decades. An overview of the geologic data is provided in section 2.5, which also gives detailed references to the interested reader. Here, we introduce the data and the conflict by discussing Figure 1-1, a classic figure of Dick Holland's.

Holland compiled a huge compendium of data that, taken as a whole (Figure 1-1), is strongly suggestive of a lack of oxygen in the ancient atmosphere. No one piece or line of evidence, however, provides irrefutable proof. Many of Ohmoto's arguments focus on specific geochemical details of rocks at a single location and provide counterarguments

to the conclusion that the given rock requires low oxygen conditions. While at times this debate was acrimonious (e.g. Ohmoto, 1997; Holland, 1999), my view as an outsider privy only to the latest stages of it, is that it has been extremely good for the community interested in ancient rocks and their interpretations. As is necessary for any extraordinary scientific claim, a strong burden of proof for an oxygen-free ancient atmosphere was demanded by Ohmoto and his supporters.

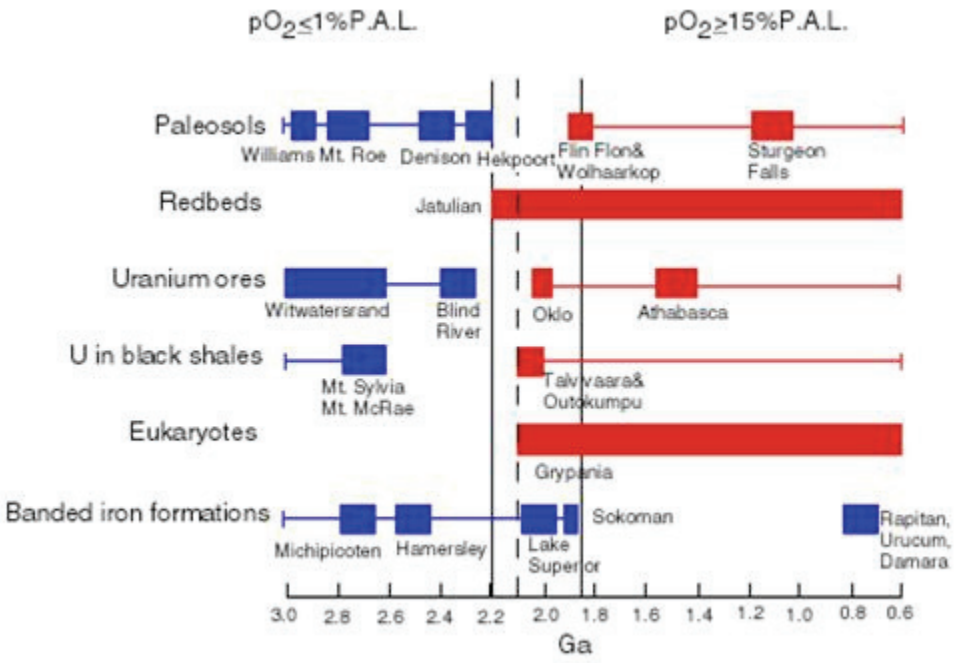

Figure 1-1 Diagram showing geologic indicators of atmospheric oxygen

The diagram represents a summary of detailed geologic evidence indicating either O_2 levels greater than 15% the present atmospheric level (PAL) in red or levels less than 1% PAL in blue. 6 different varieties of evidence are summarized, and are arranged according to the age of the geological sample from 3 Ga to 0.6 Ga on the horizontal axis. As discussed more fully later in this dissertation, paleosols are “petrified soil”, Redbeds are iron oxide containing sedimentary rocks, Uranium changes its redox state depending on O_2 availability, Eukaryotes (multi-cellular organism) use O_2 in their metabolism, and banded iron formations are indicative of reducing conditions in the deep ocean (Holland, 1994). The value of 15% PAL was based on a single paleosols which was analyzed using a different technique (Holland and Beukes, 1990). Most workers since then regard the level of oxygen in the Proterozoic as a few percent of present levels rather than >15% (e.g. Canfield and Teske, 1996).

While some members of the field feel that progress was slower than it could have been in the previous millennium, my view (as a newcomer) is that the field was strengthened

by constant scientific criticism from a small community of researchers led by a vocal, well-respected skeptic.

1.4 Isotope fractionation, sulfur photochemistry, and the resolution of the Ohmoto/Holland debate

In early 2000, James Farquhar from the University of Maryland published "Atmospheric influence of Earth's earliest sulfur cycle" in *Science*, which, with subsequent publications, effectively resolved the debate over free oxygen in early Earth's atmosphere. In 2002, Pavlov and Kasting provided a theoretical interpretation of Farquhar's data which constrains oxygen levels to be less than 10^{-5} present atmospheric levels (PAL), an interpretation we revise and extend in Chapter 5. Identification of the mass-independent fractionation in sulfur isotopes ("MIF-S" - described in detail below) has been described by Jim Kasting as the "smoking gun" piece of evidence for ancient anoxia. The few attempts to re-interpret the MIF-S signal by Ohmoto's research group (e.g., Ohmoto *et al.*, 2006) have been strongly addressed (Farquhar *et al.*, 2007), and it is a fair statement to say that low oxygen on early Earth represents the current scientific consensus.

1.4.1 Isotope fractionation explained

The MIF-S signal (and stable isotope fractionation in general) is so important to this dissertation that a few words about how these signals are generated is warranted. We will first describe the general principles. Isotope fractionation occurs because of changes in reaction rates when a rare (heavier) isotope substitutes for the primary isotope of an element. Sulfur has 4 stable isotopes, and using the example of sulfate, $^{32}SO_4$ (where ^{32}S is the dominant isotope of S) will always react more quickly in a chemical reaction than will $^{33}SO_4$, $^{34}SO_4$, or $^{36}SO_4$. These four molecules ($^{32}SO_4$, $^{33}SO_4$, $^{34}SO_4$, and $^{36}SO_4$) are collectively referred to as the "isotopologues" of sulfate.

Lighter isotopologues have higher vibrational frequencies. This can be understood using the classical analogy of a molecule as a harmonic oscillator, for which vibrational frequency varies as the inverse square root of mass. The zero point energy (ZPE) of a molecule in its ground state is given by ZPE = ½ hν, where h is Planck's constant and ν is the vibrational frequency of the atoms in the molecular bond. Therefore, lighter isotopologues have higher zero point energies than heavier isotopologues, which means that it takes less energy to break the bond of the lighter isotopologue than the heavier isotopologue. This general behavior applies to isotopologues participating in equilibrium processes, kinetic process, and processes involving diffusion across a membrane, which, together, encompasses nearly every reaction that occurs in nature (Criss, 1999).

For an example of "mass-dependent" isotope fractionation that we refer to later in the dissertation, we discuss the bacterial reduction of sulfate, which can be approximated with the following reaction:

$$SO_4^{2-} + 2\ CH_2O \rightarrow 2\ HCO_3 + H_2S \qquad (1.1)$$

$^{32}SO_4$ will proceed through reaction (1.1) more quickly than the heavier isotopologues of sulfate. If the reaction doesn't substantially alter the amount of sulfate or sulfide present in the system, the resulting sulfides (i.e the product in equation (1.1)) will contain a quantitatively higher percentage of ^{32}S than the remaining sulfates (i.e. the reactant in (1.1)). Isotope fractionations are defined by the fraction of the heavy isotopologue to the dominant isotope, relative to the isotopic makeup of universally accepted standard materials. Isotope fractionations are reported using the "del" notation in parts per thousand or *per mil* (‰), which for the case of ^{34}S and ^{32}S is defined as:

$$\delta^{34}S = \left[\frac{(^{34}S / {}^{32}S)_{sample}}{(^{34}S / {}^{32}S)_{standard}} - 1 \right] * 1000 \qquad (1.2)$$

Given abundant sulfate, the bacterial sulfate reaction described by equation (1.1) can impart $\delta^{34}S$ fractionations of approximately -40 ‰ (-4%) to the resulting sulfides.

Common isotopic geochemistry jargon describes the resulting sulfides as isotopically "light", while the remaining sulfates are isotopically "heavy." Isotope fractionations are only maintained in the geologic record if the fractionated product or reactant is removed from the system. In our example, sulfides are generally insoluble so the light sulfides produced by equation (1.1) tend to concentrate in marine sediments where they can be preserved, while the heavy sulfates remain dissolved in the ocean. Isotope fractionations can generally be measured to a precision of ~0.2 ‰ in the lab and, to the extent they can be tied to specific processes like equation (1.1) above, are a vital tool in understanding past and present environments in the Earth system

In elemental systems with more than 2 isotopologues, fractionations in nature are almost always "mass dependent", which means that the magnitude of the fractionation effect depends on the magnitude of the mass difference between the isotopes. Continuing to use the sulfur system as an example, ^{33}S is one atomic mass unit lighter than ^{34}S so $\delta^{33}S$ should be approximately 1/2 the magnitude of $\delta^{34}S$. The exact calculation (e.g. Criss, 1999) depends on the isotope masses such that

$$\delta^{33}S = 34/33 \times (33\text{-}32)/(34\text{-}32)\ \delta^{34}S \quad \text{or} \quad \delta^{33}S = 0.515\ \delta^{34}S \qquad (1.3)$$

Plots of $\delta^{33}S$ vs $\delta^{34}S$ for nearly every sulfur bearing compound in Earth's geologic record fall with 0.2 ‰ of equation (1.3), which is said to define the "terrestrial mass fractionation line". This is illustrated in the top panel of Figure 1-2. If any sample falls off of the terrestrial mass fractionation line, it is said to exhibit mass-independent fractionation (MIF). This is also referred to in the literature as non-mass dependent (NMD) fractionation or anomalous fractionation. MIF is quantified as the deviation from the terrestrial fractionation line in parts per thousand (‰), and is represented by a capital delta. MIF-S (for the ^{32}S, ^{33}S, ^{34}S system) is defined by equation (1.4) and illustrated in the lower panel of Figure 1-2.

$$\Delta^{33}S = \delta^{33}S - 0.515\ \delta^{34}S \qquad (1.4)$$

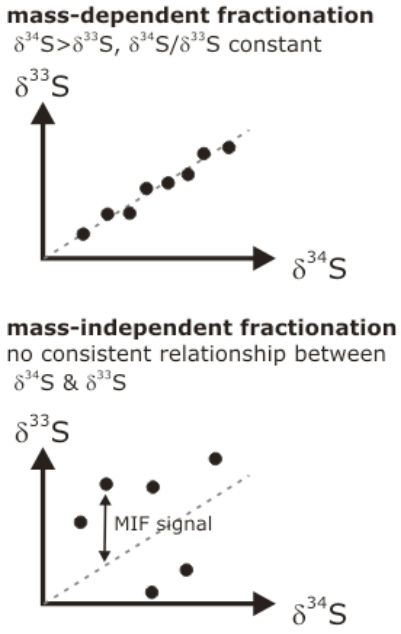

Figure 1-2 A cartoon explaining mass dependent and mass independent isotope fractionation in sulfur

The upper panel shows $\delta^{33}S$ versus $\delta^{34}S$ falling within 0.2 ‰ of the terrestrial mass fractionation line, which is shown as a dashed line with slope of 0.515 (equation (1.3)). MIF as defined by equation (1.4) is illustrated in the lower panel.

Before continuing with the discussion of MIF-S seen in Earth samples, it is worth a very brief digression to acknowledge how unusual MIF is in a geological context. Significant MIF has only been observed in two other elements – the seven isotope system of mercury and the triple isotope system of oxygen. MIF in mercury has only recently been discovered and is not well understood (Bergquist & Blum, 2007). MIF in oxygen is the most well understood, and has been observed in two different but very specific contexts. Oxygen isotopes in refractory calcium-aluminum inclusions in ancient meteorites show a MIF pattern when compared with most Earth and Moon materials (Clayton *et al.*, 1973; Thiemens, 2006; Franchi, 2008). This is most likely a result of self-shielding during the photolysis of CO in the early solar nebula (Young *et al.*, 2008). MIF is also generated in the production of ozone from oxygen during photolysis (Thiemens & Heidenreich, 1983; Gao & Marcus, 2001) which has been directly observed in the modern stratosphere (Mauersberger, 1987). Self-shielding and the photolysis of symmetric molecules are the

primary processes that generate MIF in nature, and both have been invoked for sulfur, but it remains unknown which process creates the signal seen in early Earth's sulfur isotopes.

1.4.2 Mass-Independent Fractionation of Sulfur isotopes

Very strong MIF-S signals (both $\Delta^{33}S$ and $\Delta^{36}S$) are seen prior to approximately 2.4 Ga, with an abrupt disappearance from the permanent geologic record in the Proterozoic or Phanerozoic eons. A summary of the data is shown in Figure 1-3 below. There have been some recent attempts to discuss variations in the magnitude of this signal during the Archean. In this section, I will focus on simply the on/off nature of the signal and why this provides such a strong constraint on atmospheric oxygen.

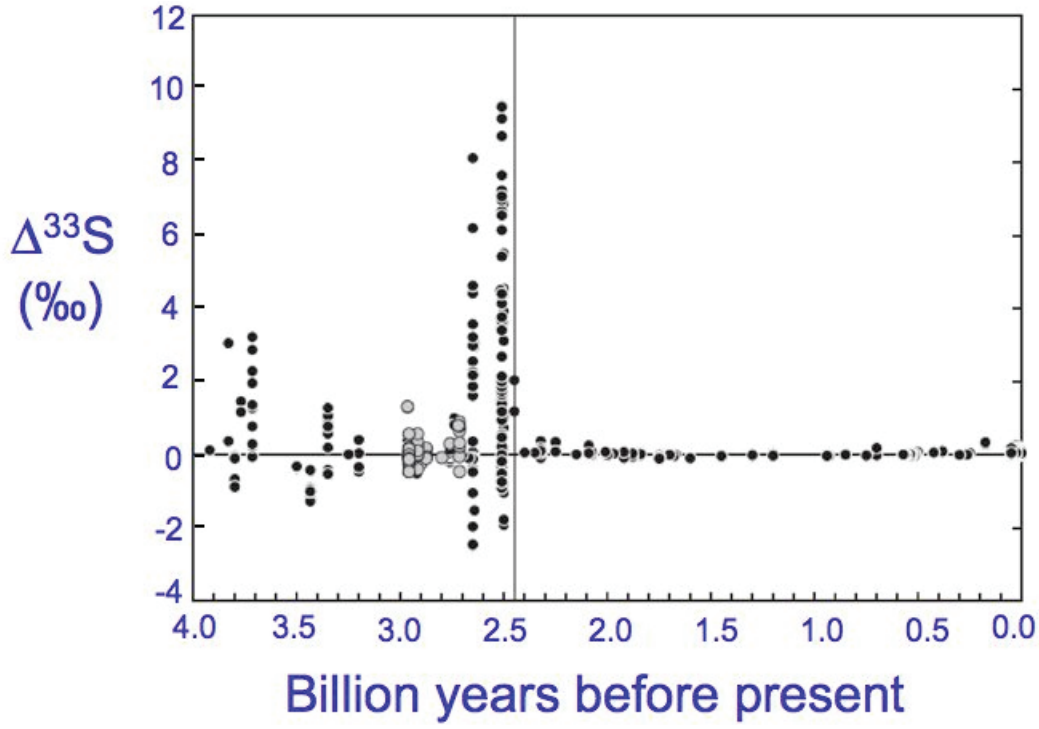

Figure 1-3 A compilation of MIF-S data versus time

A compilation of $\Delta^{33}S$ versus age for various rock samples adapted from Farquhar *et al.* (2007). The figure illustrates large $\Delta^{33}S$ before ~2.45 Gyr ago (indicated by vertical line), and small but measurable $\Delta^{33}S$ after 2.45 Gyr ago. Measurement errors are smaller than the plotted symbols.

Like many isotope fractionation processes, a full quantum mechanical description of how the MIF-S signal is generated is lacking. Isotope biogeochemistry is a field dominated by experimentalists, and MIF-S is no exception. The only known mechanism that produces substantial MIF-S is gas-phase photolysis of SO_2 between 190 and 220 nm, as identified experimentally by James Farquhar and colleagues (Farquhar *et al.*, 2000; Farquhar *et al.*, 2001). It is this experimental result that allowed Pavlov and Kasting (2002) to place the first of two constraints on ancient oxygen levels from this bizarre isotopic signature.

1.4.3 Constraints on oxygen levels from MIF-S production

Figure 1-4 is a plot of absorption cross sections, σ, of pertinent terrestrial gases, which are used in the photochemical models presented in Chapters 4, 6, and 7. Ozone is the only major atmospheric species that absorbs photons between 190 and 290 nm, with an absorption cross section as large as 10^{-17} cm^2 in most of this interval. The global average ozone column depth (the number of ozone molecules in a one square centimeter column of the atmosphere) in the modern atmosphere is ~ 1 x 10^{19} cm^{-2}, so a rough optical depth (τ) for photons in this waveband is 100. The presence of a stratospheric ozone layer thus completely shields the surface from radiation between 190 and 290 nm. This is important for surface dwelling organisms on Earth, as photons of this energy can cause significant damage to DNA (Cockell, 2000). More pertinent to this discussion is the fact that photons in the 190-220 nm window are absorbed by ozone high in the modern stratosphere (~40km), well above the region where SO_2 peaks in abundance (~20 km), and hence fully shields SO_2 photolysis at the 190-220 nm wavelengths known to create MIF-S.

Figure 1-5 shows the penetration of solar radiation as a function of O_2 levels. If atmospheric O_2 concentrations are less than 10^{-5} PAL (2ppmv), the surface is exposed to radiation longward of ~200 nm. By the time O_2 concentrations reach 10^{-3} PAL, the surface is shielded from radiation between 200 and 300 nm, due entirely to ozone absorption. In particular, the 190 – 220 nm photons which can photolyize SO_2 are

absorbed primarily above the troposphere (~11 km), so that MIF-S creation is not likely once O_2 concentrations are 10^{-3} PAL.

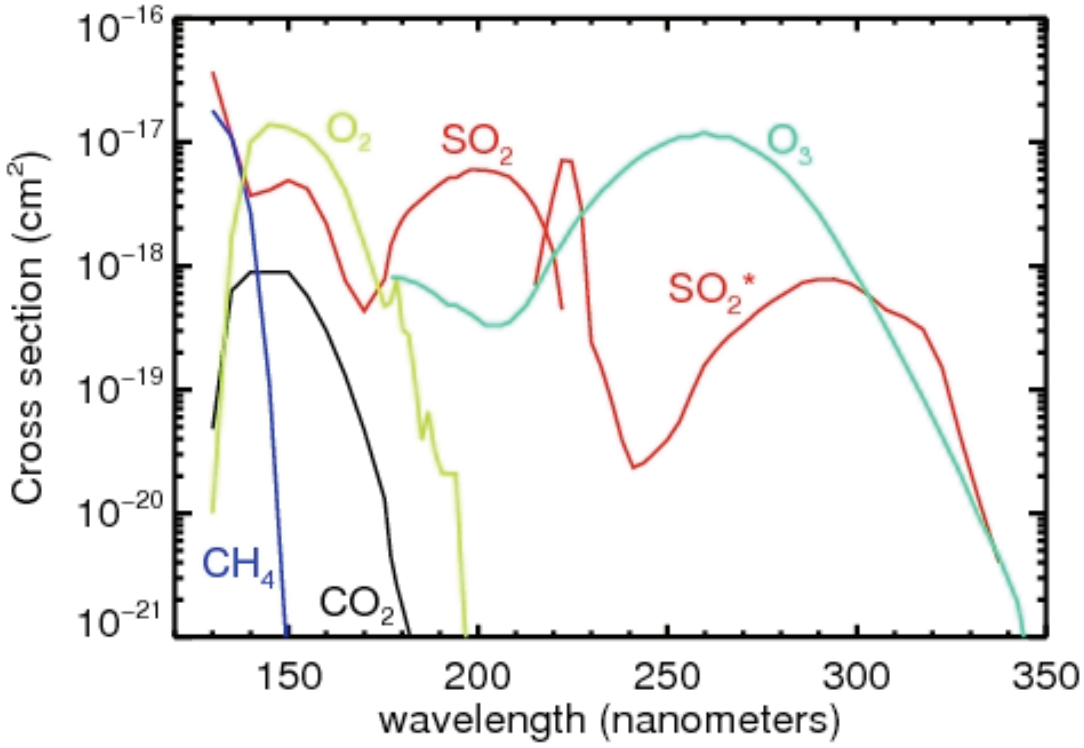

Figure 1-4 Some example atmospheric cross sections

A plot of atmospheric cross sections used in our photochemical modeling. Low resolution cross sections are shown for CH_4 photolysis, CO_2 photolysis (to O(^{1}D) and O), SO_2 photolysis (shortwave portion is photolysis to SO + O, longer wavelength portion to excited states (SO_2*) followed by decay to SO_2, O_2 photolysis (to O(^{1}D) and O), and O_3 photolysis (to O(^{1}D) and O)

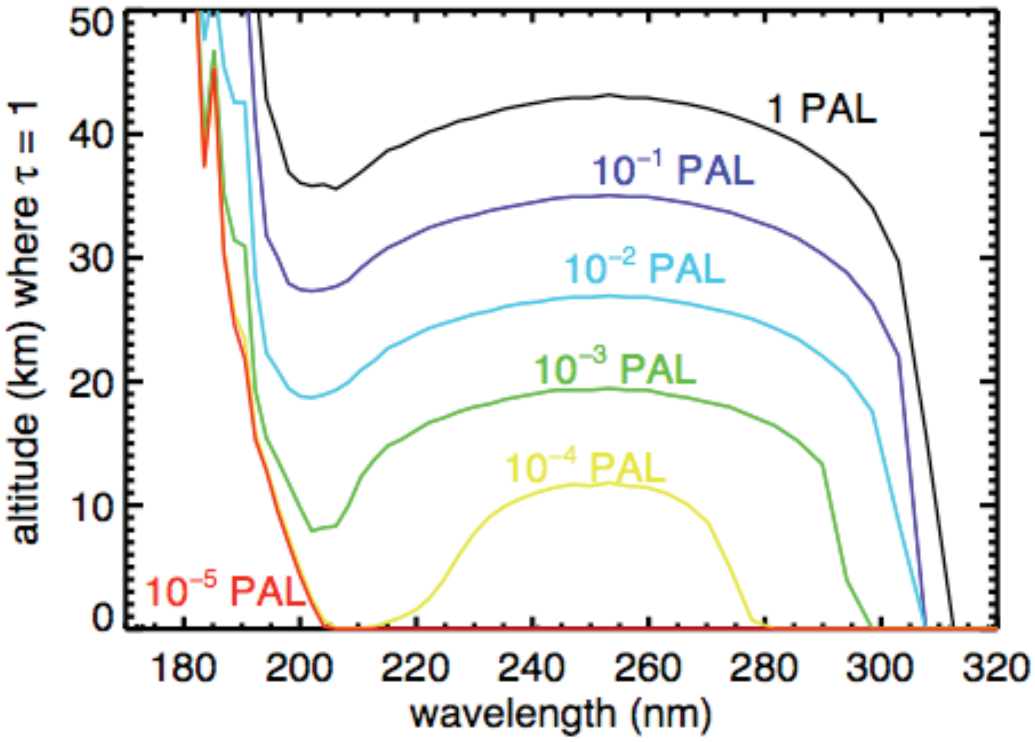

Figure 1-5 Absorption optical depth for 170 – 320 nm photons as a function of oxygen concentration

This plot of shows the atmospheric level for which $\tau = 1$ at wavelengths from 170 – 320 nm from 6 photochemical model runs, using the model described in Chapter 6. The 6 models were run at fixed methane mixing ratios of 2 ppmv, and fixed oxygen mixing ratios from present atmospheric levels (PAL) through 10^{-5} PAL. Even 0.1% of present atmospheric levels of oxygen, the surface is fully shielded from photons < 300 nm. By 10^{-5} PAL of O_2, nearly all stellar photons longward of ~200 nm reach the surface. The behavior on this plot is due primarily to the effects of ozone, which absorbs strongly in the 190 -300 nm region.

1.4.4 The photochemistry of sulfur in a reducing atmosphere, and constraints on oxygen levels from MIF-S preservation

The ozone shielding constraint on the production of MIF-S implies an upper limit of approximately 10^{-3} PAL of oxygen, which is an order of magnitude lower than the upper limits provided by the "classic" geologic indicators discussed in sections 1.3 and 2.5. But an even stronger constraint on atmospheric O_2 abundance can be derived from MIF-S when we consider not only the production, but also the factors necessary for its preservation in the permanent geologic record. Pavlov and Kasting (2002) argue that the atmosphere contained less than 10^{-5} PAL of O_2 when all MIF-S preservation factors are

accounted for. We explain this constraint by discussing the photolysis of sulfur in general and the production of the MIF-S signal as well as how sulfur exits the atmosphere. We conclude, with Pavlov and Kasting (2002), that the atmospheric deposition of polymerized elemental sulfur (S_8) is required for the geologic preservation of MIF-S, which provides the stronger upper limit on atmospheric oxygen levels.

The primary focus of this dissertation is numerical modeling of atmospheres that are very different from the modern atmosphere. We will introduce the photochemical modeling presented in Chapters 4, 6, and 7 via a discussion of the fate of volcanic sulfur in ancient atmospheres. The interaction of solar radiation with gases in the planetary atmosphere drives "photochemical" reactions that either dissociate molecules or excite molecules or atoms into higher energy states. The Sun drives non-equilibrium chemistry in the atmosphere that effectively disappears each night. Photolysis rates, *J*, as a function of height, z, in the atmosphere are calculated by

$$J(z) = \int \sigma(\lambda) \times \text{Flux}(z,\lambda) \times \text{quantum yield}(\lambda)\, d\lambda \qquad (1.5)$$

where σ is the absorption cross section (cm^2) (see Fig. 1-4), the solar flux (photons cm^{-2} s^{-1}) is attenuated by radiative transfer, and the quantum yield is unitless.

The photolysis cross section of SO_2 shown in Figure 1-4 shows that absorption of photons longward of 220 nm leads to excited states of SO_2 which decay quickly to the ground-state of SO_2 (or react with oxygen radicals to form SO_3). Photons shortward of 220 nm have enough energy to drive the dissociation reaction in which the MIF-S signal is thought to be generated

$$SO_2 + h\nu \rightarrow SO + O \qquad (1.6)$$

In the modern atmosphere, reverse reactions following (1.6) reform SO_2, via the subsequent reaction of SO with O_2, O_3, NO_2, OH, and O, listed in order of quantitative importance. By contrast, when the atmosphere is devoid of O_2, additional reaction pathways are available to SO created by equation (1.6), most importantly the photolysis of SO to S and O. In a reducing atmosphere, this can be followed by a sequence of linear chain polymerization reactions starting with $S + S \rightarrow S_2$, eventually leading to the formation of S_8, which forms a ring molecule and particulates (Kasting *et al.*, 1989). The pertinent atmospheric photochemistry of sulfur is summarized in Figure 1-6 below (a complete list of the 72 atmospheric sulfur reactions we use in our photochemical model is presented as Table 6-2).

The primary photochemical fate of SO_2 and H_2S in the modern atmosphere is gas phase oxidation with OH to sulfate (SO_4^{2-}) followed by dry or wet deposition, or aqueous phase oxidation to sulfuric acid (H_2SO_4) in cloud droplets, which rain out of the atmosphere on short timescales. Since all S exits the atmosphere as sulfate, the outgoing sulfate must have the same isotopic makeup as the S gases that are put into the atmosphere over long timescales, by the conservation of mass. A second atmospheric exit channel strongly improves prospects for preserving isotopic discrepancies, especially if the exit channel involves an insoluble species (such as S_8) that prevents homogenization of isotopes.

Pavlov and Kasting (2002) argue that S_8 deposition is necessary for the geologic preservation of the MIF-S signal. Using a photochemical model very similar to the one we use in Chapters 4 and 6, they show that no S_8 is produced in any of their models with ground-level O_2 greater that 10^{-5} PAL. This upper limit on O_2 levels compatible with MIF-S has become a remarkably well-enshrined result, given that it effectively resolves the debate on ancient oxygen levels. Unfortunately, it has led to an incomplete interpretation that the presence of MIF-S means the lack of oxygen. In Chapter 4, the

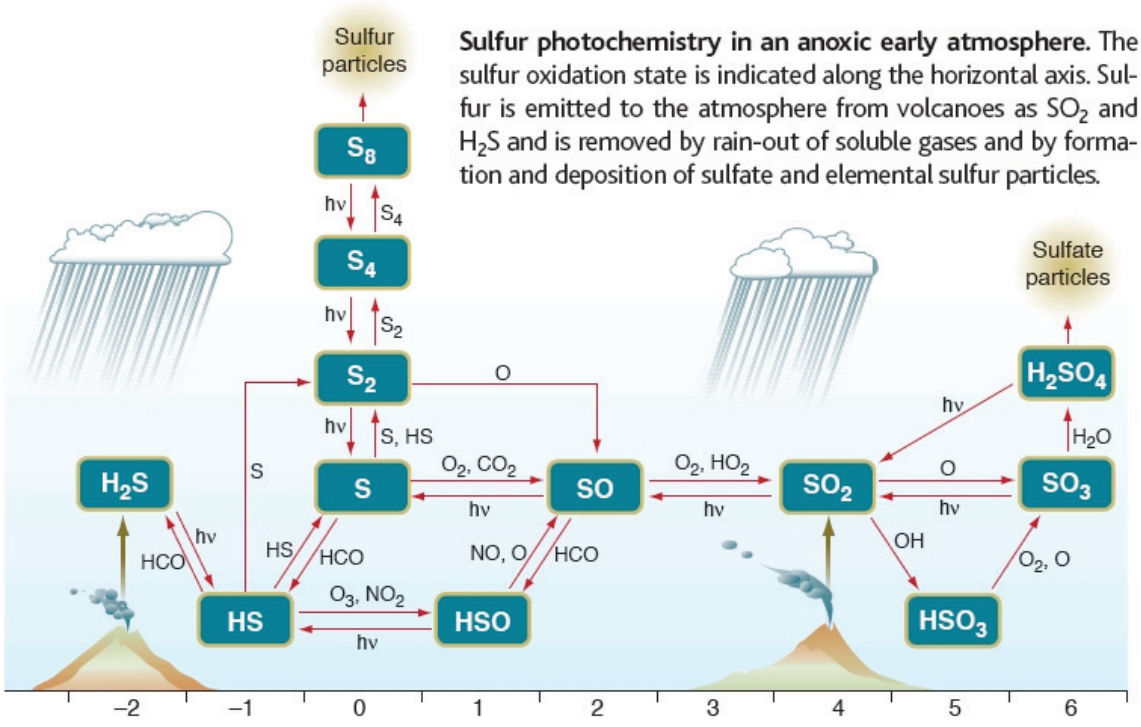

Figure 1-6 A cartoon of atmospheric sulfur photochemistry

The horizontal axis represents the redox state of sulfur gases from S^{-2} to S^{+6}. In the oxic atmosphere, all sulfur reactions are driven to the right side of the figure, and all S exits the atmosphere in the +6 redox state as sulfate. In a reducing atmosphere, reactions can occur in both directions, and sulfur exits as both sulfate and elemental sulfur particles (S^0 redox state). The figure appears in Kasting (2001) and is based on a figure originally drawn by Kevin Zahnle.

results of Pavlov and Kasting (2002) are extended by running a suite of over 2000 photochemical models and investigating the formation and deposition of S_8 as a function of both CH_4 and O_2 levels. It is shown that in addition to low O_2, there needs to be sufficient SO_2 flux and sufficient CH_4 levels to form S_8. The subtle but important distinction is that MIF-S is better seen as an indicator of the presence of CH_4 rather than the absence of O_2. As a corollary, the disappearance of the MIF-S signal at ~ 2.4 Ga is much better explained by a collapse in atmospheric methane concentrations than by a rise of oxygen. This discussion is extended in Chapter 6, where I argue that the entire "rise of oxygen" field might be better described as the "collapse of methane" and its consequences.

1.5 Planetary atmospheres, biosignatures, and observational astrobiology

Much of my motivation to study planetary atmospheres derives from the fact that astronomical technology will soon advance to the point where terrestrial planets around nearby stars may be directly detected and studied. The field of extrasolar planet discovery is moving so quickly that any quantification of the number of planets discovered is bound to be out of date once stated. As of the 19th of August, 2008, 307 extrasolar planets have been found, with the lower mass limits of 3-4 Earth masses. The field is technology (and to some extent, luck) limited – Assuming they exist, it is simply a matter of time before Earth mass planets are discovered. Next generation telescopes being considered by NASA and ESA (Terrestrial Planet Finder (TPF) and Darwin, respectively) should be capable of obtaining low resolution spectra of the atmospheres of terrestrial planets around nearby stars (Beichman *et al.*, 1999), which would revolutionize the field of terrestrial planetary atmospheres[*]. A very intriguing capability of these telescopes is the possible detection of gases that are produced by biological processes ("biosignatures"), and hence will be an avenue by which we can explore if life exists elsewhere in the universe (Des Marais, 2002).

This section introduces general concepts used in this dissertation regarding planetary atmospheres, the effect of biology on planetary atmospheres and their resultant astronomical detectability, and concludes with prospects for quantifying the presence of microbial life in the universe.

[*] A similar revolution is already underway in characterizing atmospheres of giant planets, where atmospheric spectroscopy has revealed the presence of gases such as CH_4 and H_2O (Swain *et al.*, 2008; Tinetti *et al.*, 2007), and provided constraints on the atmospheric circulation (Knutson, 2007).

1.5.1 Terrestrial planetary atmospheres are secondary atmospheres

Terrestrial planets can be roughly described as those incapable of retaining massive hydrogen atmospheres during planet formation (Chambers, 2004). If a protoplanetary core becomes large enough (thought to be around 10 Earth masses), the protoplanet is able to retain any gas (primarily H) it captures from the protoplanetary nebula. The result is a planet similar to Jupiter or Saturn, with a so-called "primary atmosphere" (Boss, 2002). Less massive planets are unable to retain their primary atmospheres against the hydrodynamic escape that follows giant impacts (Sleep & Zahnle, 1998), so any atmospheres that they have are defined as "secondary" – They are created by the planet itself, and do not reflect the composition of the gaseous component of the protoplanetary nebula.

To first order, secondary planetary atmospheres reflect volcanic outgassing, which occurs when physical conditions inside the plan*et al*low for temperatures large enough to melt rocks, approximately 1300 °C for the iron and silicate rocks that make up the terrestrial planets in our solar system. There are four heat sources for planetary volcanism: gravitational/potential energy of accretion, gravitiational/potential energy of core formation, radioactive heating, and tidal heating. In Chapters 2 and 3, I discuss how planetary volcanism can be modeled over the lifetime of planetary bodies from first principles, as constrained by geologic data. In addition to volcanic outgassing, we also discuss metamorphism, which occurs when rocks are heated and release gas (but do not melt). Other than the heating of rocks, the only other significant source of gases to a planetary atmosphere is biology.

The makeup of a planetary atmosphere is defined by the interplay of the gas sources (volcanoes and biology) with incoming stellar radiation, along with any processes which allow gases to be captured at the surface or escape the planetary atmosphere. These processes are summarized in Figure 1-7, which provides a schematic introduction to the numerical modeling presented in this dissertation. In Chapters 3 and 5, the complications of the center box are ignored, and the effects of varying boundary

conditions on the bulk amount of gases flowing into and out of the center box are investigated. In Chapters 4, 6, and 7, photochemical models which compute the complicated details represented in the center box are presented. These complicated details, however, are fairly well constrained by fundamental atmospheric chemistry and physics, so many of the results also arise from investigation of changing the boundary conditions represented by the outer boxes. In Chapter 8, I discuss the evolution of the solar flux, which describes the evolving radiation environment of Earth's atmosphere over the age of the solar system.

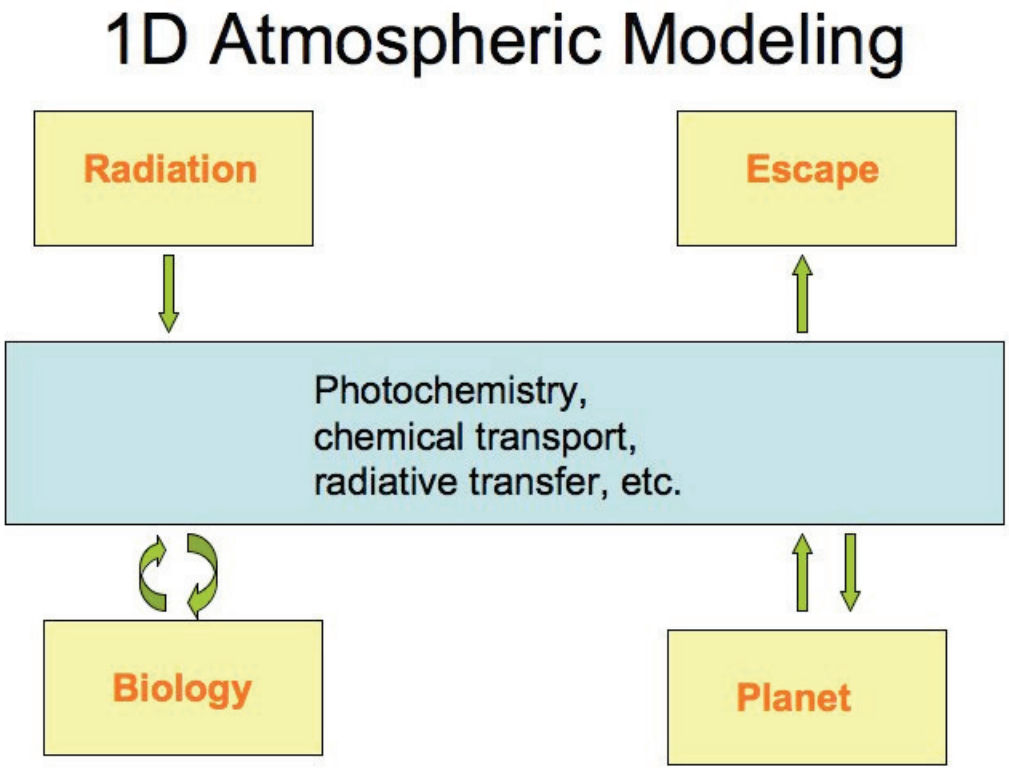

Figure 1-7 A cartoon describing 1 dimensional atmospheric modeling

The 1 dimension that is referred to is atmospheric height which is the implied vertical coordinate in this figure.

1.5.2 Earth's atmosphere is a biological construct

Gases in Earth's atmosphere rapidly exchange with surface reservoirs. The abundance of every major gas in Earth's atmosphere, with the exception of Argon, is controlled to some extent by biology. Table 1-1 lists atmospheric species and their lifetimes against geochemical loss. Even N_2, the most dominant component of our atmosphere, cycles through marine sediments on the order of hundreds of millions of years (Holland, 1978 p. 302 - 307). Amazingly, all atmospheric N_2 cycles through biology in a mere 30 years, given the size of the living biosphere of 6-13 $x10^{15}$ gm, and the flux from the atmosphere to the ocean/terrestrial biosphere of ~3 x 10^{14} gm yr^{-1} (*ibid.*).

Table 1-1 Lifetimes of some important atmospheric gases

Atmospheric lifetimes were taken from the 4th IPCC report (IPCC, 2007) or as constrained in this dissertation. In the case of O_2 and CH_4 which have changed abundances through time, we have put values representative of the Archean in parentheses. The lifetimes are computed in the simplest fashion as residence times: lifetime = amount of gas / geochemical loss rate.

Gas	Abundance	Lifetime
N_2	79%	10^7-10^9 years
O_2	(~0) 21%	(30 min) 2 x 10^6 years
Ar	~1%	long
CO_2	300 ppm	2 x 10^5 years
H_2O	3-6 ppm	6 years
CH_4	(1000) 1 ppm	(10^5 years) 12 years
N_2O	0.3 ppm	114 years

A similar argument applies to O_2 whose current loss to geochemical sediments is ~2 million years, but cycles through the biosphere in a few thousand years. In general, atmospheric lifetimes against geochemistry and biology are very short when considered on geologic timescales. The composition of Earth's atmosphere can change relatively rapidly in response to changes in fluxes from the biosphere, a concept explored

throughout this dissertation, but most fully with the time-dependent photochemical model in Chapter 7.

1.5.3 Atmospheric biosignatures

Earth's microbial activity is visible in its disk-averaged spectrum, which can be obtained via observation of Earthshine, Earth's reflected radiation scattered from the unlit portion of the Moon (Turnbull *et al.*, 2006). In Figure 1-8 below, absorption features due to O_3, O_2, H_2O and CH_4 are prominent. Methane by itself is not a biosignature, as it has abiotic sources, but in conjunction with large quantites of O_2/O_3 it provides a primary biosignature at Earth's abundances (Des Marais *et al.*, 2002). As discussed at various junctures in Chapters 2 through 7, O_2 and CH_4 rapidly react to form CO_2 and H_2O, and the presence of both of them at the quantities observed renders our atmosphere far out of thermodynamic equilibrium, implying a large surface source which overwhelms the tendency of the atmosphere towards thermodynamic equilibrium. This disequilibrium is at the heart of an atmospheric biosignature.

The first generation of telescopes designed to observe the spectral characteristics of extrasolar terrestrial planets will not be able to do so at the resolution of the earthshine spectra in Figure 1-8 above. Instruments like TPF and Darwin are under early stages of development, but current planning scenarios call for resolutions ($\lambda/\Delta\lambda$, where λ is wavelength) of 20-100. Only major absorption features are visible in low resolution spectra, which complicates the possibility of observing weaker biosignatures that might result from biogenic trace gases such N_2O, CH_3Cl, or biogenic sulfur gases in Earth's present atmosphere. Prospects for these biosignatures increase greatly if Earth was orbiting a K or M star, as the lower UV fluxes from the stars allow for longer atmospheric lifetime of trace species (Segura *et al*. 2003; Segura *et al*. 2005). Figure 1-9 shows that even at low resolution in the mid-IR, the dominant O_3 biosignature which typifies the present Earth is visible (depending on the signal to noise) in a spectrum modeled by the TPF team. In Chapter 7, we present disk-averaged spectra of Earth through time created from our photochemical models and provide additional support to the hypothesis of

Segura *et al*. (2003) that biology on Earth may have been more detectable during the Proterozoic. Much of the work on atmospheric biosignatures to date has focused on the present era of Earth's atmosphere. Earth's ancient atmosphere represents an habitable biosphere very different from our own. As such, further work on identifying how Earth's spectrum has evolved through time (Kaltenegger, 2007) and on anoxic biosignature is warranted.

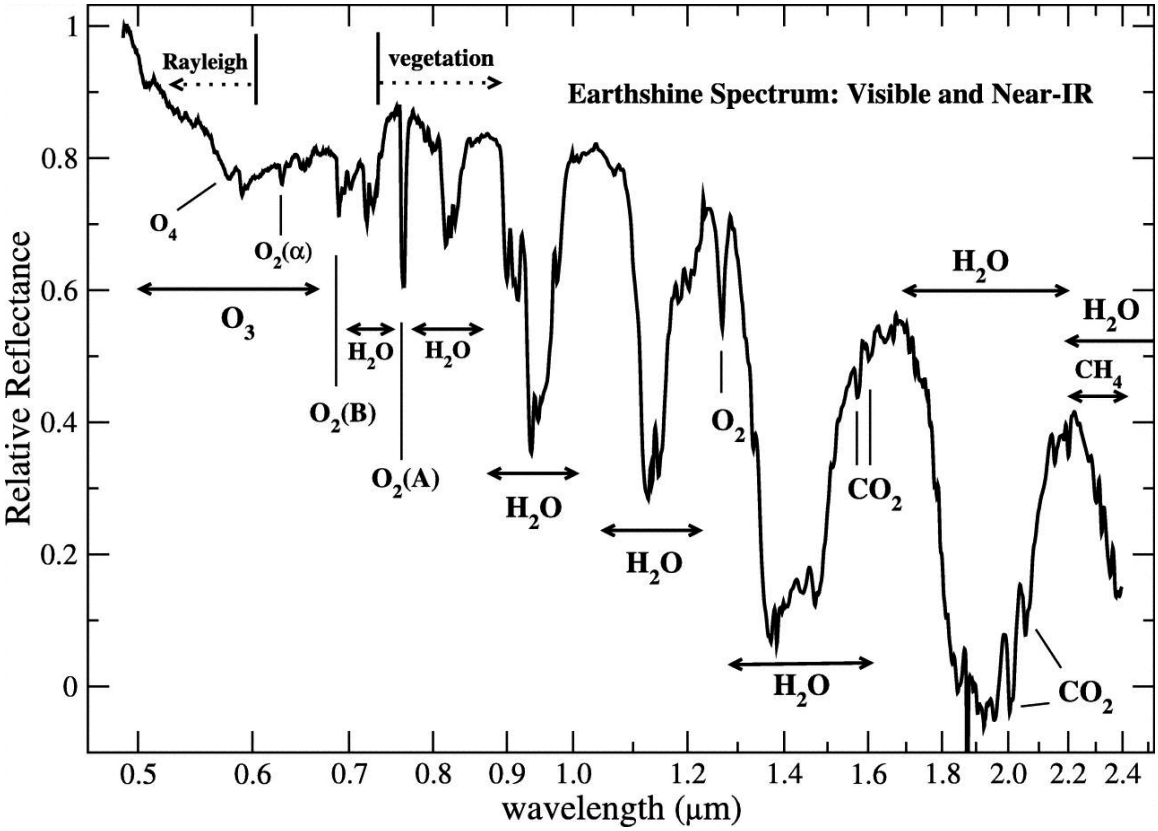

Figure 1-8 The visible and near-IR spectrum of the Earth from Earthshine data

This figure shows the reflection spectrum of the spatially-resolved Earth as recorded from Earthshine on the moon (Turnbull *et al.*, 2006). Important features and processes are annotated on the figure.

Assuming the detection of large numbers of earth mass planets within the habitable zone of their stars, missions like TPF/Darwin will be able to place quantitative limits on the presence of planets with substantial O_2/CH_4 biosignatures. Any positive results would strongly depend on models such as those generated in this dissertation, and all

possible “false positive” signals must be ruled out. Given the political will to build telescopes, a successful detection of microbial life in the Galaxy seems probable in the 21st century via the observation of disequilibrium in a planetary atmosphere. Sufficient null results will allow researchers to place statistically significant limits on the presence of earth-like life on terrestrial planets. The era of quantitative astrobiology is near.

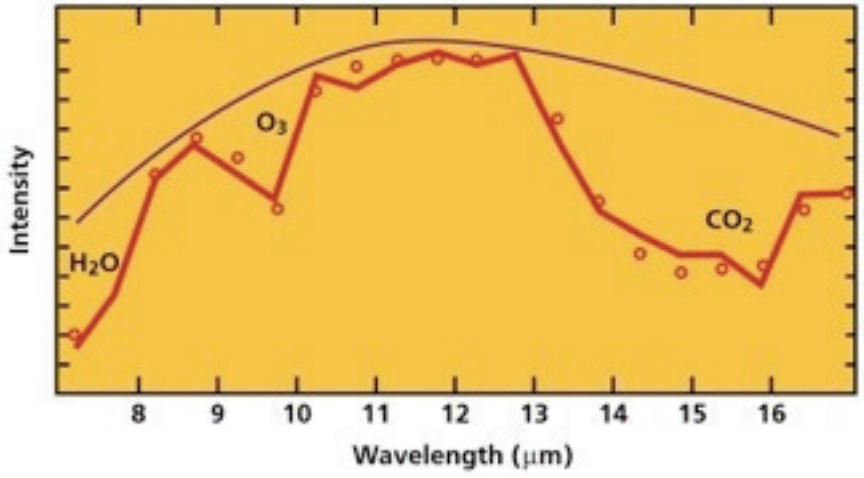

Figure 1-9 A modeled low-resolution spectrum of earth in the mid-IR

A modeled spectrum of the Earth in the mid-IR, showing that the 9.6 micron feature of O_3 would be detectable even at very low spectral resolution. O_3 concentration is non-linear with O_2 so atmospheres with even 1% the present level of O_2 should be detactable in the mid-IR.

1.6 Quantitative Modeling of Atmospheric Evolution

Here, I will provide additional background material and briefly motivate some basic arguments that are developed in detail in the following chapters. The purpose is to provide an overall narrative thread of the themes that tie the various investigations in this dissertation together. The chapters of this dissertation are presented in the chronological order that reflects how the work was done. Examinations with a biogeochemical model are presented in Chapters 3 and 5, while Chapters 4, 6, and 7 involve experiments with a photochemical model. They are presented in this order, rather than grouping the two biogeochemical model chapters together, because we were

motivated to update the biogeochemical model (Chapter 5) due to the photochemical results in Chapter 4. In addition, while performing the work described in Chapter 6, it was discovered that some of the earlier results needed updating. As the work presented in Chapters 2 through 5 has been published in peer-reviewed journals and given that the changes do not affect the primary conclusions, I left the original work intact, avoiding the temptation to present a revisionist history of ideas. Chapter 6 describes the changes made in the earlier results, and provides updated versions of Figures 3-3 and 3-7. Chapter 8 describes the evolution of the solar flux, an important "boundary condition" for understanding the evolution of planetary atmospheres.

1.6.1 The faint young sun and atmospheric evolution

The quantity and quality of the Sun's radiation has changed dramatically over the lifetime of the solar system. The Sun's output in the visible portion of the electromagnetic spectrum increases with time, due to the fundamental physics of nuclear fusion increasing the density of the stellar core, which increases the rate of energy generation in a positive feedback. This process has brightened the Sun's total luminosity (the solar flux integrated over all wavelengths) by 30% over the age of the solar system. The wavelength dependences of this process, along with a concurrent decreases in UV radiation is modeled in Chapter 8, which provides a first-order estimate of the solar flux at any time and place in the solar system. The increasing total luminosity of the Sun leads to the "faint young Sun problem" of atmospheric evolution (Sagan & Mullen, 1972; Kasting & Catling, 2003), which is the realization that if Earth's current atmosphere is subjected to less than ~85% of the current solar flux, the global average temperature would drop well below 0 °C, the freezing point of water. Massive glaciations are only seen a few times during Earth's history, while sedimentary rocks which imply deposition from liquid water are prevalent. Interestingly, the two most severe periods of glaciation in Earth's history are strongly correlated with changing oxygen levels, a theme we will discuss throughout the dissertation.

The faint young Sun "problem" is easily resolved if one allows for evolution of atmospheric gases, specifically greenhouse gases. Greenhouse gases, such as CO_2, H_2O, CH_4, N_2O, SO_2, O_2, and O_3 are small symmetric molecules whose strong vibrational and rotational modes cause them to absorb predominantly in the infrared, and less strongly in the visible. For a planet with an atmosphere, the global average surface temperature, T_s, is the sum of the planet's effective temperature and greenhouse warming, where the effective temperature (T_e) is (in its most simple form) defined by the balance of the incoming stellar flux minus the fraction of incoming photons which aren't absorbed (the planetary albedo, a), and the blackbody radiation of the planet:

$$\sigma T_e^{\,4} = \frac{S(1-a)}{4} \qquad (1.7)$$

where S is the stellar luminosity (W/m^2) and σ is the Stefan-Boltzmann constant ($W/m^{2/}K^4$). Greenhouse warming for a given atmospheric composition and insolation is determined using radiative convective climate models (e.g. Haqq-Misra, 2008). Figure 1-10 is a classic figure from Jim Kasting (Kasting *et al.*, 1993) illustrating how Earth's effective temperature changes with time as a result of increasing S, and how Earth's surface temperature would drop below freezing if atmospheric composition remained constant.

While atmospheric evolution seems the most likely resolution to the faint young Sun problem, there are other possibilities which require a brief mention. While the luminosity evolution of main sequence stars is a robust prediction from stellar astrophysics, we have implicitly assumed that the Sun's mass has remained constant. If the Sun's initial mass was 1.07 solar masses, there would have been enough extra photons 4.5 billion years ago to warm the Earth with the current atmospheric composition. If the Sun were to monotonically lose mass during its main sequence evolution, this could lead to the prediction of a relatively constant solar luminosity. The Sun's current mass loss rate of 2×10^{-14} solar masses/year is insufficient to remove any significant fraction of the Sun's mass over the age of the solar system. Studies of early G-type stars reveal mass loss

rates approaching 2 x 10^{-11} solar masses/year, but these high mass loss rates are only observed during the first ~100 million years of main sequence evolution (Wood *et al.*, 2002). Wood *et al*. (2002) conclude that a maximum of 3% of the total Solar mass could have been lost, which is significant enough to alter, but not completely change the faint young sun issue. For our purposes, the most important conclusion from the Wood *et al*. (2002) study is that any mass loss would have occurred during the first 500 million years of Earth's history. Thus, for the Archean era forward through time (i.e. from 3.8 Ga onwards - the time period considered in this dissertation) the Earth has been subject to the evolutionary effect of a constant mass star.

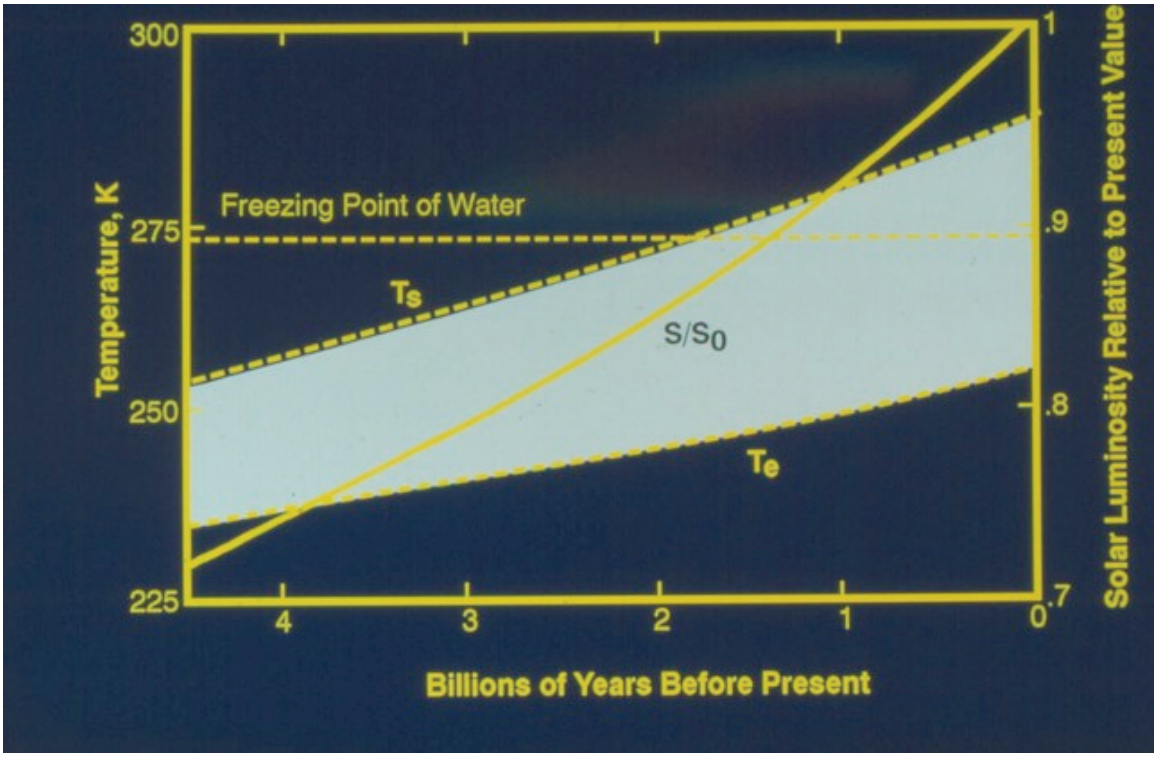

Figure 1-10 The faint young sun

The solid curve labeled S/S_0 maps to the right axis and shows the ~70% increase in solar luminosity over the age of the solar system. The dashed line labeled T_e is the effective temperature defined in Equation (1.7). The dashed line labeled T_s is the surface temperature computed by the climate model of Kasting (1993), assuming Earth's current atmosphere extrapolated back in time. The modern greenhouse effect of ~33 °C is seen on the rightmost axis as the difference between T_s and T_e. If the assumption of no atmospheric evolution were true, the Earth's globally-averaged surface temperature would have dropped below the freezing point of water prior to 1.8 Ga.

Another possible resolution to the faint young sun problem is that the albedo of the Earth was less during the Archean, allowing more stellar photons to be absorbed. While there is no general theory of cloud cover on a terrestrial planet, there is no reason to assume that global cloud cover would have changed on the early Earth(Kasting & Catling, 2003). I follow precedent and assume a constant albedo throughout Earth's history, but acknowledge that future understanding of planetary cloud cover could change this portion of the story.

In summary, atmospheric evolution of greenhouse gases is generally seen to be the most likely resolution to the faint young sun problem. As discussed in Chapters 2 and 3, volcanic outgassing was likely more vigorous in the past, which would have input more CO_2 into the atmosphere. In addition, there are strong theoretical reasons to suspect that methane (CH_4) played a much more prevalent role in the ancient atmosphere. We motivate this in the following two sections, and discuss the concept, reasoning, and evidence throughout the dissertation.

1.6.2 Methane and the temperature of the early earth

Methane is a very effective greenhouse gas, and is commonly invoked to provide the extra greenhouse warming on the Archean Earth (Kasting, 2005). Methane has also been invoked as a primary greenhouse gas during the Proterozoic (Pavlov *et al.*, 2003), an argument we advance in Chapter 5. Much of the recent work on the climatic effects of methane is influenced by the radiative-convective climate models of Pavlov *et al*. (2000), which provided estimates for the greenhouse forcing of various CH_4/CO_2 concentrations. A recent paper (Haqq-Misra *et al.*, 2008) has shown that methane's ability to act as a greenhouse warmer was significantly overestimated in the earlier study. We use the parameterization of Pavlov *et al*. (2000) in section 3.7 to extend the basic results from the biogeochemical model, which are independent of temperature. Given that the temperature-dependent application of the biogeochemical model is not used in subsequent chapters, we leave the original work intact, respecting our previously published work. The most important effect the new climate parameterization of Haqq-

Misra *et al.* (2008) are discussed in Chapter 6, where our predictions of atmospheres immediately prior to the rise of oxygen appear to be on the edge of greenhouse-mediated climate stability.

A main theme of this dissertation developed in Chapters 3 through 7 is that the late Archean/early Paleoproterozoic may be best described the period when a precipitous drop in atmospheric methane levels occurred. This drop in methane levels would halt the atmosphere's ability to polymerize sulfur and hence preserve the MIF-S signal, and also drastically cool the climate. This scenario is strongly supported by the evidence for massive glaciations that occurred at the same time as the rise of oxygen, as discussed more fully in Chapter 4.

1.6.3 Evidence for CH_4 in the early atmosphere

CH_4 is a relatively inert molecule in Earth's atmosphere. Its primary reactions are with oxidized radicals such as OH and excited singlet oxygen $O(^1D)$, which results from ozone photolysis. In the absence of biological free oxygen and the resulting O_3, CH_4 has only two major sinks, photolysis and photochemical destruction by any OH molecules created from H_2O photolysis. We use these facts in Chapters 2 and 3 to provide two independent estimates of the CH_4 concentrations in Earth's Archean atmosphere. Assuming the same biospheric fluxes as in the modern world, Archean CH_4 concentrations could have ranged from hundreds to thousands of ppm. CH_4 has a dramatically increased lifetime in an oxygen free atmosphere, and due to its recalcitrance to photochemical destruction becomes the dominant reducing gas. In Chapter 3, we discusses why quantitatively more methane fluxes might be expected in the late Archean atmosphere, and in Chapters 5 and 6, we discuss how the CH_4:O_2 flux ratio may have decreased with time.

CH_4 would not have left a similar trace on the Archean surface environment as O_2 (which is extremely reactive) has on the modern environment. As such, it will be difficult to ever

"prove" that the Archean atmosphere contained CH_4, without a novel discovery such as fluid inclusions found in an Earth meteorite on the Moon, which might contain pockets of the early earth atmosphere (Armstrong *et al.*, 2002). As discussed in detail in future chapters, the evidence for CH_4 in Earth's early atmosphere is the following collection of indirect evidence

- Methanogenesis is an ancient metabolism, as evidenced by whole genome analysis (House *et al.*, 2003)
- Carbon isotopes at 3.5 Ga, 2.9 Ga, and 2.7 Ga show extreme depletion in $\delta^{13}C$ indicative of isotope fractionation by methanotrophs (Hayes, 1994; Ueno *et al.*, 2006 ; Nisbet *et al.*, 2007).
- High methane concentrations occur as a natural result when photochemical models of the Earth's current biosphere are combined with enhanced volcanic activity (Chapter's 4, 6).
- The MIF-S signal seen prior to 2.4 Ga requires reducing conditions (Chapter 4). Although H_2 is also a plausible reductant, we argue in Chapter 2 (see Figure 2-6 for example) that it is thermodynamically favorable for biology to convert H_2 to CH_4.
- The lack of evidence for glaciations during most of the Archean and Proterozoic requires an additional greenhouse gas to counteract the faint young sun, and other candidates such as N_2O, NH_3 are rapidly photolyzed. Multiple bars of CO_2 are not supported by the geochemical record.

1.6.4 Evidence for the evolution of oxygenic photosynthesis

While oxygen is the most prevalent element on Earth, 99.9999% of it is tightly bound in rocks as silicates and iron oxides. Chemical reactions in the solid planet move oxygen between compounds, but free oxygen is not liberated by any known abiotic process, save the photodisassociation of water, which has been estimated to be a small flux for the Earth (Kasting & Donahue, 1980). Quantitatively speaking, the only important source of free oxygen is the complicated metabolism of oxygenic photosynthesis. Much

of the work in this dissertation invokes the assumption that oxygenic photosynthesis evolved significantly *before* the rise of oxygen. Some of the evidence for this claim is discussed in section 2.4.2 and Chapter 6, which includes:

- Ancient microfossils and stromatolites (Hofmann *et al.*, 1999; Rasmussen, 2000)
- Carbon isotope evidence (see Figure 2-8) showing $\delta^{13}C$ depletions consistent with oxygenic photosynthesis throughout the geologic record (Hayes, 1994).
- The presence of carbonate reefs at 2.9 Ga (Nisbet *et al.*, 2007)
- The presence of banded iron formations (which were deposited from solution and contain large amounts of O_2) (Holland, 1984)
- Evidence of oxidative weathering (i.e. caused by dissolved O_2 in water acting on continental rocks) at 2.6 and 2.5 Ga (Anbar *et al.*, 2007; Wille *et al.*, 2007).
- Direct evidence of the cellular decay products (2-alpha-methylhopanes) of cyanobacteria and eukaryotic organisms at 2.7 Ga (Brocks *et al.*, 1999; Summons *et al.*, 2006) and 2.5 Ga (Dutkiewitz *et al.*, 2006; George *et al.*, 2008).

This final piece of evidence had been regarded as the most convincing, but the interpretation has recently been complicated by detection of methylhopanoids in *Rhodopseudomonda palustris*, an anoxygenic phototroph (Rashby *et al.*, 2007). It should be noted however that this result is from a single, non-marine, strain of this organism, and that this strain also produces other biomarkers such as tetrahymanol whose decay products are not found in the ancient samples.

Although the data are all indirect, the overall consensus viewpoint appears to be that oxygenic photosynthesis evolved well prior to the oxic transition. A “simpler” argument discussed in section 3.2.2 is that oxygenic photosynthesis evolved exactly at ~ 2.4 Ga and that this evolutionary event is directly responsible for the rise in oxygen (Kopp *et al.*, 2005). This argument is partially predicated on the assumption that free oxygen would completely overwhelm an anoxic atmosphere, and that atmospheres with large oxygen fluxes do not have stable anoxic solutions. The numerical work in Chapters 3 through 7

shows this assumption to be false. In Chapter 3, we take the extreme view point when we assume that oxygenic photosynthesis has existed for the entire Archean, and show that the atmosphere remains anoxic until the net flux of reductants to the atmosphere falls below the net flux of oxidants. This returns us to the general concept described in section 1.5.2 that atmospheric composition reflects the gases put into it on very short timescales. There is no fundamental contradiction inherent in a stable anoxic atmosphere with large O_2 fluxes, provided the fluxes of reductants to the same atmosphere (as H_2, CH_4, H_2S, etc.) are quantitatively more significant.

Chapter 2 How Earth's atmosphere evolved to an oxic state

In this chapter*, we review evidence and theories for changing atmospheric oxygen levels. One of the primary conclusions is that a quantitative understanding of how and why O_2 became abundant on our reducing planet is still lacking, which motivates the work in future chapters of this dissertation. The story of oxygen is inherently interdisciplinary, and reference is made to virtually every realm of the Earth sciences - biology, geology, geochemistry, oceanography and atmospheric science – in putting together the pieces.

We review the classical geological data mentioned in section 1.3, but most of the effort is focused on data obtained within the last decade or so. This newer data has revealed that there were two significant increases in atmospheric O_2 levels at around 2.4-2.3 and 0.8-0.6 billion years ago, respectively. We describe how oceanic sulfate concentrations appear to have increased with increasing O_2, and introduce the idea that methane may have inversely mirrored O_2. We also discuss "Snowball Earth" – the hypothesis that Earth was completely ice covered at one time – as both oxic transitions occur during times when there is evidence for widespread glaciations.

This chapter also introduces the concept of biogeochemical cycles, which are fundamental to the modeling presented in Chapters 3 and 5, and hence demand a short introduction. "Biogeochemistry" is an imperfect label describing an interdisciplinary approach to understanding Earth Systems science. This approach focuses on a specific chemical element and follows one hypothetical atom as it travels through the various reservoirs of the Earth, ignoring the fact that each reservoir is the "scientific property" of a given discipline such as oceanography, atmospheric science, or volcanology. In the example of the carbon cycle, one attempts to understand how long a carbon atom input

* Material in this chapter was originally published as Catling, D. C. and M. W. Claire "How Earth's atmosphere evolved to an oxic state: A status report." *Earth and Planetary Science Letters* **237**(1-2): 1-20 (2005).

into the atmosphere as CO_2 stays in the atmosphere before it dissolves in the ocean, and whether it is more likely to get incorporated into a microorganism or carbonate rock, and how long it will be before the atom is transformed back into rock via sedimentation, and then transported by plate tectonics, metamorphosed, and released back into the atmosphere as CO_2. By quantifying the masses of the various reservoirs of carbon (i.e. biomass, rocks, dissolved inorganic carbon in ocean, atmospheric CO_2, etc.) and the fluxes between these reservoirs, one can understand the "lifetime" of a carbon atom in a given reservoir and in the entire cycle. To complete the example, the lifetime of a carbon atom in the global carbon cycle is approximately 1 million years, a fact which turns out to be of vital importance for the stabilization of climate over Earth's history. The biogeochemical "carbonate-silicate" cycle provides a strong negative feedback on atmospheric CO_2 levels which is modeled in sections 3.7.1 and 3.7.3, and more fully discussed in Kasting and Catling (2003).

Section 2.2 describes the basics of the biogeochemical cycle of oxygen, which is less well understood than the global carbon cycle outlined above. We describe Earth's reservoirs of oxygen, and what is known about the fluxes between them. Understanding the balance of fluxes in the modern system is fundamental when attempting to shed light on how ancient biogeochemical cycles may have functioned. The biogeochemical cycle of oxygen outlined in this chapter forms the basis of the numerical modeling presented in Chapters 3 and 5.

Also reviewed are theoretical concepts necessary for understanding the evolution of atmospheric oxygen, such as the composition of the prebiotic atmosphere and the effect that the evolution of life has on the early atmosphere. We describe how oxygenic photosynthesis may have evolved significantly prior to the oxygenation of the atmosphere, and provide the plausible explanation that excess reductants scavenged photosynthetic O_2 from the early atmosphere. As this chapter is a review, it concludes with a description of future research that could help shed light on unsolved problems.

2.1 Introduction

Abundant atmospheric O_2 distinguishes the Earth from all other planets in the solar system. Oxygen supports animals, fungi and multicellular plants, which makes Earth's surface stunningly different from that of Earth's apparently lifeless neighbors (Catling *et al.*, 2005). But when our planet formed, its surface must also have been devoid of life. Understanding how the complex world around us developed from lifeless beginnings presents a great interdisciplinary challenge. Part of this endeavor is to understand how atmospheric composition has changed in response to the activities of organisms and how the atmosphere, in turn, has affected biological evolution.

Changes in O_2 levels define the standard history of Earth's atmosphere. Over the past decade, new data has constrained this O_2 history, models have helped our understanding, and new questions have emerged. Geochemical data now suggest that there were two major increases in O_2. These occurred near the beginning and end of the Proterozoic eon (2.5-0.542 Ga), respectively. The first rise of O_2 occurred around 2.4-2.3 Ga, within the Paleoproterozoic era (2.5-1.6 Ga) (Bekker *et al.*, 2004). Then, about 1.0-0.6 Ga, within the Neoproterozoic era (1.0-0.542 Ga), O_2 plausibly rose a second time (Canfield & Teske, 1996; Canfield, 1998). Both O_2 increases appear in the same eras as substantial changes in the Earth's biota, geochemistry (Kaufman, 1997; Melezhik *et al.*, 1999; Lindsay & Brasier, 2002; Bekker *et al.*, 2004) and climate (Hoffman *et al.*, 1998).

O_2 is a result of oxygenic photosynthesis, whereby organisms split H_2O and release O_2. Oxygenic photosynthesis originated in the ancestors of cyanobacteria (Blankenship & Hartman, 1998), which, long before green plants evolved, generated O_2. Many cyanobacteria are phytoplankton—the microscopic, usually single-celled organisms floating in the surface waters of the ocean. Today, ~10^{27} cyanobacteria constitute the most numerous phytoplankton (Falkowski, 1997b) of which *Prochlorococcus* is the most numerous organism on Earth (Partensky *et al.*, 1999). Ancestral cyanobacteria were probably just as plentiful but their effect on the atmosphere was delayed. The evidence for the earliest oxygenic photosynthesis predates detectable atmospheric O_2 by several

hundred million years (section 2.4.2). Consequently, how Earth's atmosphere became oxic is not simply a question of the origin of cyanobacteria. Indeed, a quantitative understanding is still lacking for how free oxygen became abundant on a planet that is overall chemically reducing. Organic carbon or its reducing equivalent balances every oxygen molecule that is produced by photosynthesis and so Earth's initially reducing environment was not easily shifted. To determine why O_2 increased requires an integrated grasp of the redox behavior of the Earth system. In this review, we start by discussing the modern atmosphere because this enables us to lay some groundwork before turning to the ancient Earth.

2.2 How is oxygen regulated in modern biogeochemical cycling?

2.2.1 The "net" source of O_2

In oxygenic photosynthesis, the production of one mole of organic carbon (with average stoichiometry CH_2O) generates one mole of O_2 via

$$CO_2 + H_2O \rightarrow CH_2O + O_2 \qquad (2.1)$$

Respiration and decay reverse this reaction on a timescale of ~10^2 years, consuming >99% of the oxygen produced by photosynthesis. But a small fraction (0.1-0.2%) of organic carbon escapes oxidation through burial in sediments. From eq. (2.1), the burial of one mole of organic carbon liberates one mole of O_2. Such burial of organic carbon is referred to as the "net source" of O_2, but the fate of the O_2 depends on the kinetics of the various sinks for O_2. O_2 will not, in fact, accumulate in the atmosphere if the flux of kinetically rapid sinks exceeds the slow flux of organic burial (see section 2.2.3), which is important when considering the lack of O_2 in the Archean eon (before 2.5 Ga).

The oxygen cycle is complicated by the burial of other redox-sensitive elements besides carbon. The quantitatively important elements are sulfur and iron. During weathering, O_2 dissolved in water oxidizes sulfur within continental pyrite (FeS_2), making soluble sulfate (SO_4^{2-}), which is carried by rivers to the ocean. Then, in the ocean, bacteria reduce

sulfate and ferric iron (Fe^{3+}) to pyrite. The reducing power of photosynthesized organic carbon is essentially transferred to pyrite, so that pyrite buried in sediments is balanced by O_2 production (Berner, 2004):

$$\begin{gathered} 15CO_2 + 15H_2O = 15CH_2O + 15O_2 \\ \underline{15CH_2O + 2Fe_2O_3 + 16H^+ + 8SO_4^{2-} = 4FeS_2 + 23H_2O + 15CO_2} \\ 2Fe_2O_3 + 16H^+ + 8SO_4^{2-} = 4FeS_2 + 8H_2O + 15O_2 \end{gathered} \quad (2.2)$$

By examining the average composition of sedimentary rocks, Holland (Holland, 2002) estimates that organic carbon and pyrite burial contribute fluxes of 10.0±3.3 Tmol O_2 yr^{-1} and 7.8±4.0 Tmol O_2 yr^{-1}, respectively (where 1 Tmol = 10^{12} mol). The reduction of oxidized iron and the burial of ferrous iron ($2Fe_2O_3 = 4FeO + O_2$) also adds a minor flux of oxygen, whereas the burial of sulfate minerals in sediments removes O_2. Summing these fluxes, the total O_2 source is 18.4±7.8 Tmol O_2 yr^{-1} (Fig. 2-1).

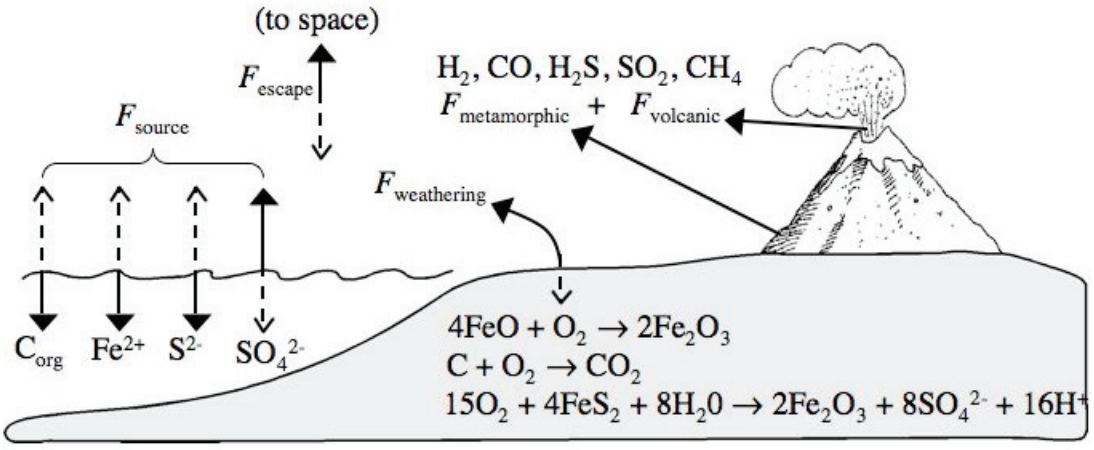

Figure 2-1 Schematic diagram showing the modern fluxes of O_2

The fluxes include metamorphic ($F_{metamorphic}$) and volcanic ($F_{volcanic}$) sources of reducing gases. F_{source} is the flux of burial of organic carbon, pyrite and ferrous iron that contribute equivalent oxygen into the atmosphere-ocean system. F_{escape} is the escape of hydrogen to interplanetary space and $F_{weathering}$ is the flux of reductants uplifted on continental surfaces that react with O_2 dissolved in rainwater. Solid arrows indicate flow of reductants, while dashed arrows indicate an equivalent flux of oxygen.

2.2.2 The balance of net O_2 production and loss

Because the amount of atmospheric O_2 is relatively stable, the net source of O_2 must be balanced by losses, otherwise O_2 levels would increase or decrease. Oxidative weathering consumes ~5/6 (~15 Tmol yr^{-1}) of the O_2 generated by burial of reductants, while ~1/6 (~3 Tmol yr^{-1}) is consumed by reaction with reducing gases emanating from the solid Earth, noting that these proportions are highly uncertain (Holland, 2002). Important reducing gases (i.e., gases that can consume O_2) include H_2, CO, CH_4, H_2S, and SO_2, produced in volcanism (when rocks melt) and metamorphism (when rocks are heated and/or pressurized but do not melt). Reducing gases are oxidized through photochemical reactions that sum to a net oxidation by O_2, effectively behaving like combustion. There are uncertainties in the O_2 source and sink. For the source flux, an underlying assumption is that buried organic matter is not chemically-resistant, fossil organic carbon eroded off the continents and simply reburied in a closed loop. Recent measurement of a fossil carbon flux of only ~0.06 Tmol C yr^{-1} confirms this assumption (Dickens *et al.*, 2004). An uncertainty in the O_2 sink concerns the contribution of volcanic versus metamorphic reducing gases. Volcanic gases are commonly studied, but metamorphic fluxes are spatially extensive with uncertain global magnitude. Mass balance suggests that metamorphic fluxes could be important. For example, 0.6%wt of C in average sediments compared to 0.45wt% of C in uplifted rock exposed to weathering (Holland, 2002) implies that that a 0.15% difference in reductant has been lost in reactions such as $C + 2H_2O = CO_2 + 2H_2$ (Mason, 1990). Given the organic burial flux of ~10 Tmol yr^{-1}, a crude upper limit on today's metamorphic reducing flux due to carbon alone is $(0.15/0.6) \times 10\,\text{Tmol} = 2.5$ Tmol O_2 consumption yr^{-1}, comparable to estimates of the total reducing gas flux.

2.2.3 A general theoretical framework for the history of atmospheric O_2

The history of O_2 can be described generally. The rate of change of the reservoir of O_2, R_{O2}, in the atmosphere (in Tmol) is

$$\frac{d(R_{O2})}{dt} = F_{source} - F_{sink} = F_{source} - (F_{volcanic} + F_{metamorphic} + F_{weathering}) \quad (2.3)$$

Here, F_{sink} is the removal flux of O_2 from the atmosphere (in Tmol yr^{-1}) due to numerous oxidation reactions. F_{source} is the source flux of oxygen (in Tmol yr^{-1}) due to burial of organic carbon and pyrite and the escape of hydrogen to space (Fig. 2-2). The sink fluxes are the reaction of O_2 with reduced volcanic gases ($F_{volcanic}$), reduced metamorphic gases ($F_{metamorphic}$), and reduced material on the continents ($F_{weathering}$). If R_{O2} is in "steady-state", F_{sink} will be close to F_{source} and $d(R_{O2})/dt \approx 0$. Oxygen levels have changed because the terms on the right-hand side of eq. (2.3) have altered over Earth history and been in imbalance in the past with $F_{source} > F_{sink}$ (see section 2.6).

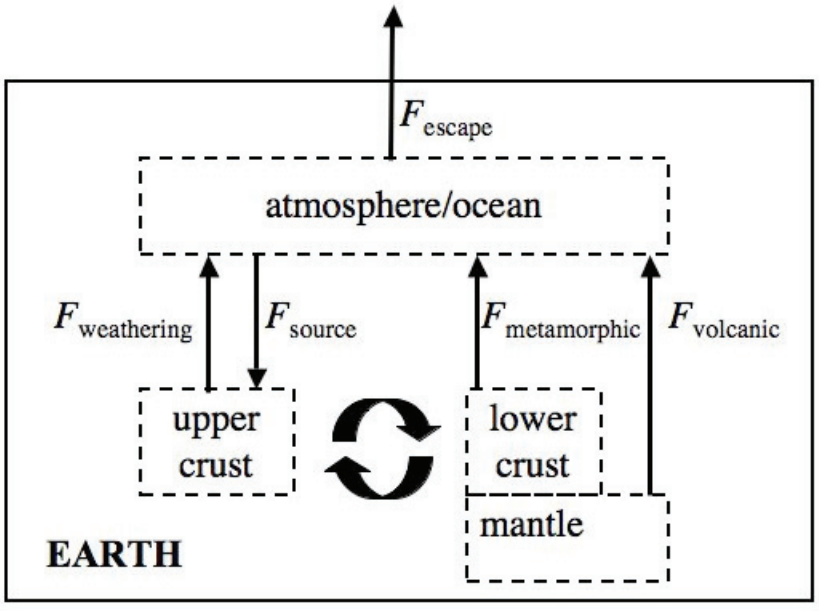

Figure 2-2 A schematic diagram showing reductant fluxes that govern the oxidation state of the atmosphere, ocean and lithosphere

Curved arrows between the upper and lower crust reservoirs indicate mixing due to tectonic activity. Summing fluxes into and out of the atmosphere-ocean box gives eq. (2.3).

2.2.4 The stability of atmospheric O_2 and negative feedbacks

Negative feedbacks exist that prevent O_2 levels from wildly fluctuating because evidence suggests that Phanerozoic O_2 levels have been stable at 0.2±0.1 bar. Animals, which require O_2 to grow and breathe, have been present throughout the Phanerozoic (Knoll & Carroll, 1999). Also, a charcoal record extends back ~350 m.y., which suggests that there has been sufficient O_2 (~15%) to burn trees (Chaloner, 1989; Wildman *et al.*, 2004). Yet the short residence time of O_2 in the atmosphere-ocean system means that Phanerozoic O_2 has been replaced more than 200 times. Dividing the atmosphere-ocean reservoir (3.8×10^7 Tmol O_2) by the source flux (18 Tmol O_2 yr^{-1}) gives ~2 million years for the average amount of time an O_2 molecule spends in the atmosphere-ocean system (Fig. 2-3).

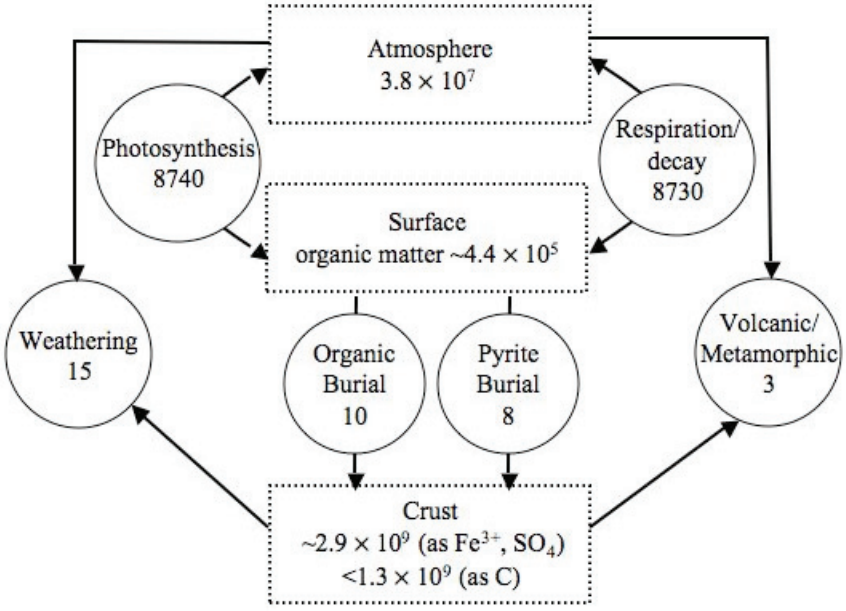

Figure 2-3 Oxygen reservoirs and fluxes in the modern O_2 cycle

Primary production is from (Field *et al.*, 1998). Fluxes of burial, weathering and reaction with volcanic and metamorphic gases are from (Holland, 2002).

So what sets the amount of O_2 in the air? It cannot be respiration and decay. The amount of organic carbon at the Earth's surface (~4.4×10^5 Tmol) is almost 10^2 times smaller than the atmospheric reservoir of O_2 (3.8×10^7 Tmol) so that respiration and

decay can modulate no more than 1% of the total amount of atmospheric O_2 (Walker, 1980). Instead, respiration and decay control the size of the small reservoir of surface organic carbon. O_2 must be regulated because an increase in O_2 hastens the consumption of O_2 and/or slows the rate of O_2 production, while a decrease of O_2 has the opposite effects. Because the oxidation of continental surfaces appears relatively complete, many researchers have favored a negative feedback on the O_2 source (organic burial) as a primary control. Evidence suggests that this feedback does not act directly, by oxidizing newly produced organic carbon and preventing its burial (Betts & Holland, 1991), but indirectly through the supply of nutrients. Most organic carbon is buried on oceanic continental shelves (Berner, 1982). Phosphorus acts as a limiting nutrient for marine photosynthesis because its only source is from continental weathering. In the ocean, the burial of phosphorus bound to iron hydroxides becomes less efficient under anoxic conditions (Van Cappellen & Ingall, 1996; Colman *et al.*, 2000). Thus a decrease of O_2 may increase phosphorus available for the production and burial of new organic matter. To counteract a rising O_2, some have hypothesized that the forest fires would become more frequent, triggering an ecological shift to grassland. In the long-term cycle, trees, whose roots break up bedrock, amplify the rate of rock weathering by about an order of magnitude relative to more shallowly rooted plants (Schwartzman, 1999). Rising O_2 would thus lower the supply of marine phosphorus and the rate of organic carbon burial, the O_2 source (Lenton & Watson, 2000). Alternatively, Falkowski (Falkowski, 1997a) argues that nitrogen can behave as the ultimate limiting nutrient and that higher O_2 leads to diminished nitrogen fixation and organic burial rates. To counter this, Tyrell (Tyrell, 1999) shows that N-fixing marine organisms (mainly cyanobacteria) can multiply to produce enough N. Let us now examine O_2 in the ancient atmosphere.

2.3 How reducing was the prebiotic atmosphere?

2.3.1 General considerations for the composition of the prebiotic atmosphere

Walker (Walker, 1977) argues that before life existed the atmosphere contained mainly N_2, with negligible O_2, probably more CO_2 than today, and only minor levels of reducing

gases such as H_2. N_2 was likely similar to modern levels, because it would have outgassed early and does not react easily with surface rocks (Fanale, 1971). Many early workers favored a highly reducing prebiotic atmosphere, with gases such as hydrogen or methane as major constituents. The Oparin-Haldane theory that life originated from compounds such as abiotically synthesized amino acids in highly reducing atmospheres helped motivate this view (Miller & Urey, 1959). However, such an atmosphere could only be sustained by outgassing that is far more reducing (richer in hydrogen) than modern volcanic emissions. Today's volcanic gases have a typical composition of 80-90% H_2O, 6-12% CO_2, ~3% S gases (H_2S and SO_2 in uncertain ratio (Aiuppa *et al.*, 2005)), 0.6-1.5% H_2 and <0.4% CO (Holland, 1978), which is weakly reducing because it contains no O_2 and only small amounts of H_2 relative to H_2O. The oxidation state of volcanic gases depends on upper mantle rocks, where the gases originate. The more reducing the mantle is, the more reducing the volcanic gases. The upper mantle would have needed to contain metallic iron in order to supply sufficiently reducing gases to a highly reducing prebiotic atmosphere. But metallic iron sank into the Earth's core within ~30 million years after the planet formed (Kleine *et al.*, 2002) (Fig. 2-4). Thus, the proportions of reducing versus oxidized gases from volcanism should not have changed hugely since then, although some shift is not excluded (see section 2.6.2).

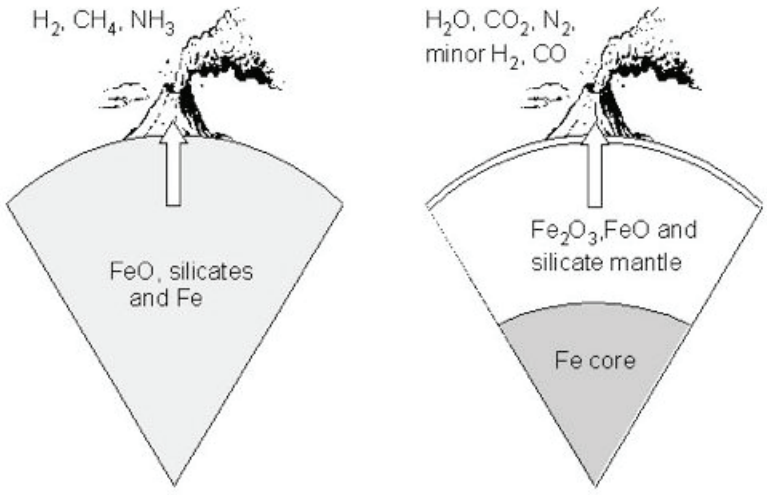

Figure 2-4 Schematic view of volcanic outgassing

(a) Reducing volcanic gases (with significant H_2, CH_4 and NH_3) were introduced into the atmosphere before core formation, when the mantle was rich in metallic iron. (b) A weakly reducing mixture of volcanic gases has fed the atmosphere for most of Earth history, after the Earth differentiated into core, mantle and crust.

A recent paper (Tian *et al.*, 2005) suggests that the early atmosphere was highly reducing because of a slower rate of hydrogen escape to space than previously thought. However, this slow escape rate stems from questionable assumptions. (Tian *et al.*, 2005) only consider temperature-dependent hydrogen escape and assume a pure H_2 upper atmosphere, which necessarily generates a cold exosphere because neither the absorption of extreme ultraviolet by other gases nor the higher temperature of atomic ions is considered. Also, non-thermal escape processes dominate today and cannot be dismissed for early Earth.

2.3.2 Hydrogen and oxygen in the prebiotic atmosphere

Theory implies that abiotic O_2 fluxes on the prebiological Earth would have been swamped by hydrogen. A balance between outgassing and loss to space would have determined H_2 levels (Fig. 2-5). Hydrogen atoms at the top of the atmosphere escape to space. Theory, which has been verified in today's atmosphere, shows that the rate of escape of hydrogen (ϕ_{escape}) is proportional to the sum of the mixing ratio, f, of all hydrogen-bearing gases above the troposphere weighted by the number of hydrogen atoms they contain ($f_{total} = f_{H2O}+f_{H2}+2f_{CH4}\ldots$). The proportionality constant is insensitive to plausible differences in structure and composition between a primitive and modern atmosphere, giving a simple equation (Walker, 1977):

$$\phi_{escape} = 2.5\times10^{13} f_{total} \ (\mathrm{H_2\ molecules\ cm^{-2}\ s^{-1}}) \qquad (2.4)$$

The modern H_2 outgassing rate is 4.8±3.6 Tmol H_2 yr^{-1} = 1.8±1.3 $\times10^{10}$ H_2 molecules cm^{-2} s^{-1} (Holland, 2002). The outgassing rate may have been a few times higher on early Earth because of increased heat flow and plumes from a more radioactive interior, but to within an order of magnitude, setting the escape rate on early Earth equal to the modern outgassing rate in eq. (2.4) yields an H_2 mixing ratio of ~7×10^{-4} ≈ 0.1%, assuming that f_{total} was dominated by H_2 (Fig. 2-5b).

Hydrogen exerts a control on oxygen through a net reaction

$$O_2 + 2H_2 \rightarrow 2H_2O \qquad (2.5)$$

Abiotic O_2 arises only from the photolysis of water vapor and associated escape of hydrogen to space. By itself, photolysis of H_2O or CO_2 does not provide a net source of O_2 because the photolysis products recombine. The rate of O_2 production from H_2O photolysis and hydrogen escape would have been ~ 0.01 Tmol O_2 yr^{-1} (Kasting & Brown, 1998). Thus, the volcanic flux of hydrogen would have overwhelmed the O_2 source by a factor of ~10^2. Under these circumstances, oxygen attains only ~10^{-13} bar partial pressure (Kasting, 1993).

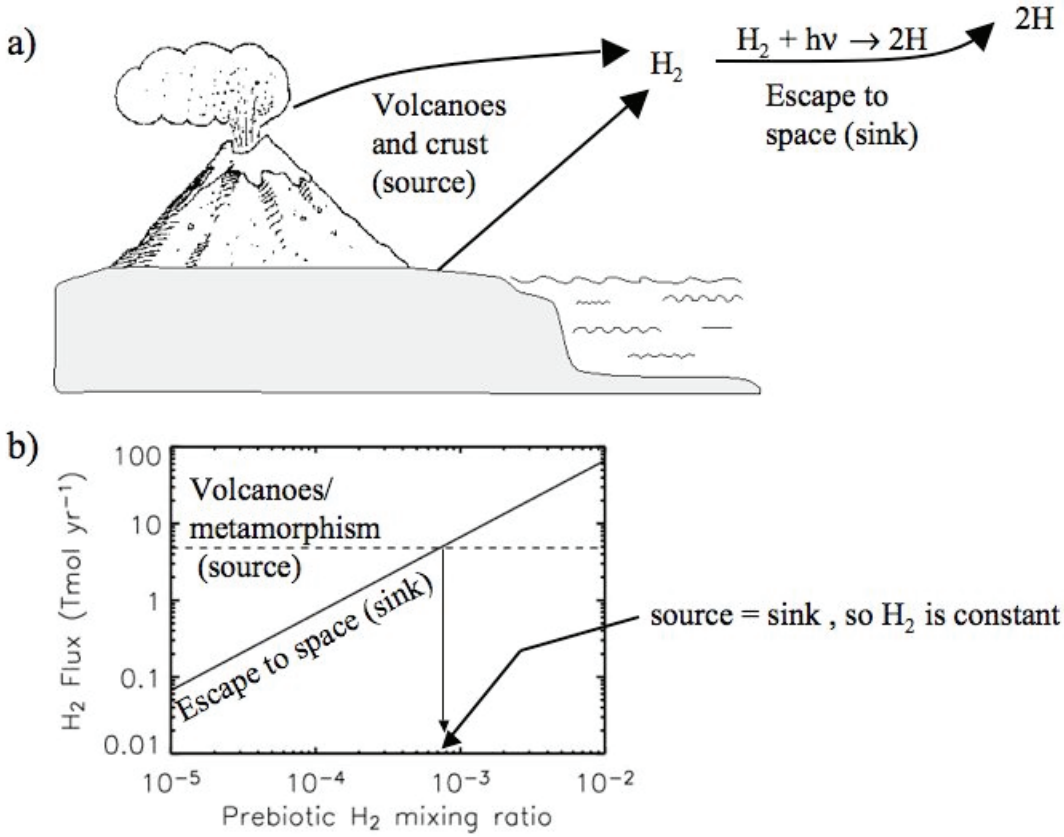

Figure 2-5 Hydrogen in the Earth's prebiotic atmosphere

(a) Schematic of outgassing source and escape sink (b) How dynamic equilibrium sets the prebiotic H_2 concentration.

2.4 How did the arrival of life affect the early atmosphere?

2.4.1 The effect of early life on atmospheric chemistry and climate

The coexistence of reducing and oxidized gases in the prebiotic atmosphere would have provided untapped chemical energy. At some point, life must have evolved to exploit this. Methanogens are modern microbes that exploit redox disequilibrium by combining H_2 and CO_2 to make methane:

$$4H_2 + CO_2 \rightarrow CH_4 + 2H_2O \quad (2.6)$$

In the laboratory, methanogens draw down H_2 to produce methane until they reach a thermodynamic limit at ~0.01% H_2 (Kral *et al.*, 1998). Methanogens are strictly anaerobic with a tendency toward thermophily, which suggests that they are evolutionarily ancient (Teske *et al.*, 2003); also remnant organic molecules and carbon isotopes suggest methanogens were present in the Archean (Hayes, 1994; Brocks *et al.*, 2003). Thus, methanogens likely would have converted atmospheric H_2 into methane, with H_2 dropping from 0.1% to 0.01% (Fig. 2-6a) (Kral *et al.*, 1998; Kasting *et al.*, 2001). CO_2 levels would have decreased as a consequence. CH_4 is a powerful greenhouse gas, and the warming associated with elevated CH_4 would have diminished CO_2 in temperature-dependent weathering, where CO_2 dissolved in rainwater reacts with continental silicates (Gaillardet *et al.*, 1999).

Anoxygenic photosynthesis would have also affected H_2 and CH_4 (Fig. 2-6b). This type of photosynthesis does not release O_2 but sulfur compounds or water (Fenchel, 1998), e.g.,

$$2H_2S + CO_2 + h\nu \rightarrow CH_2O + H_2O + 2S \quad (2.7)$$

$$2H_2 + CO_2 + h\nu \rightarrow CH_2O + H_2O \quad (2.8)$$

An organism using a metabolism such as (2.8) can flourish at lower H_2 concentrations than methanogens. Thus, the evolution of anoxygenic photosynthesis, perhaps before

3.5 Ga (Nisbet & Sleep, 2001), would have depressed atmospheric H_2 levels even more than the advent of methanogens. Also, photosynthesized organic matter would likely have been fermented to produce higher levels of CH_4 (Fig. 2-6b) via the overall metabolic pathway

$$2CH_2O \rightarrow CH_4 + CO_2 \qquad (2.9)$$

In the steady state, the influx of reductants would be balanced by an equal outflux. As a consequence, the supply of reductants, such as H_2 or H_2S, from geological sources would have restricted the productivity of early life.

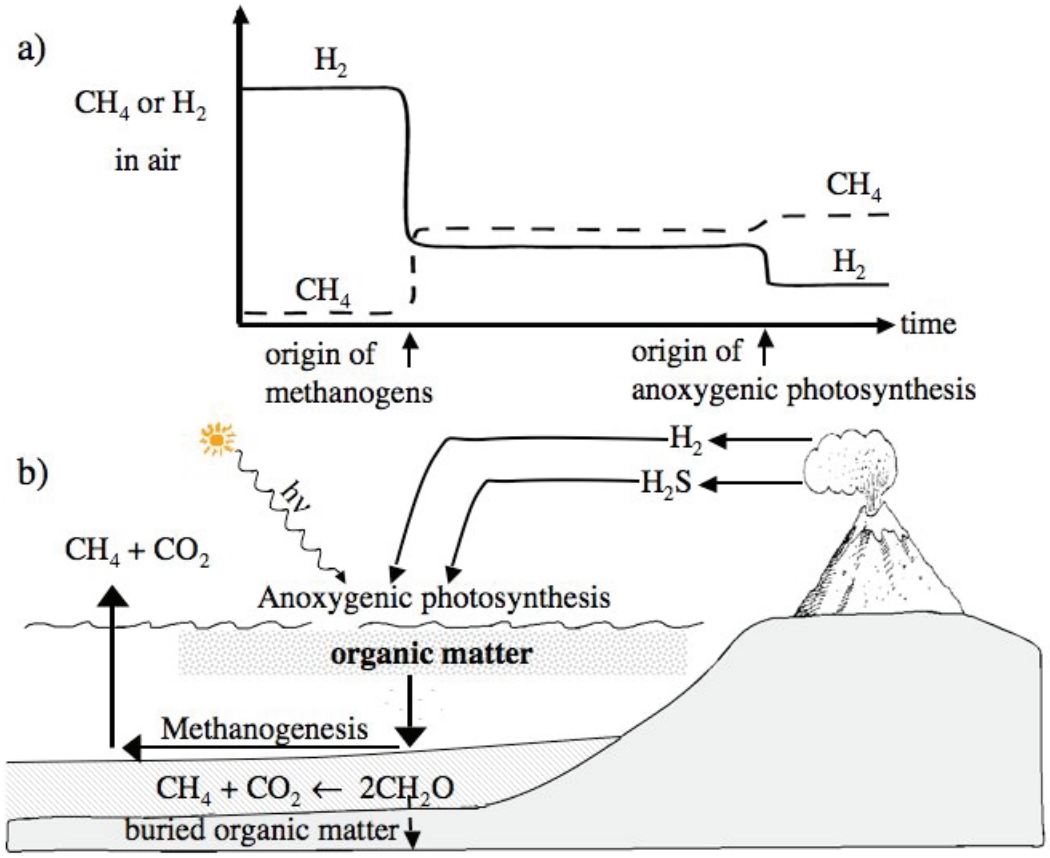

Figure 2-6 Schematic showing the effect of organisms on the early atmosphere before the origin of oxygenic photosynthesis

For the sake of argument, this graph assumes methanogens evolved before anoxygenic photosynthesis, but this is uncertain.

2.4.2 When did oxygenic photosynthesis appear?

Oxygenic photosynthesis extracts hydrogen from ubiquitous water and enabled life to overcome its dependency on geothermal sources of reducing gases (needed to reduce CO_2 to organic matter). Consequently, productivity was no longer limited by reductants but by nutrients, e.g., phosphorus (Tyrell, 1999; Des Marais, 2000).

Recent data shows that the atmospheric oxic transition occurred at ~2.4-2.3 Ga (Bekker *et al.*, 2004), while oxygenic photosynthesizers existed long before that (Brocks *et al.*, 2003). Microfossils (Knoll & Barghoorn, 1977; Rasmussen, 2000), stromatolites (fossilized remains of microbial communities) (Buick *et al.*, 1981; Hofmann *et al.*, 1999), and carbon and sulfur isotopes (Schidlowski, 1988; Rosing, 1999) all indicate global microbial life in the mid-Archean (Nisbet & Sleep, 2001). Specific evidence for oxygenic photosynthesizers comes from biomarkers, which are remnants of organic molecules diagnostic of particular organisms. At 2.7 Ga, 2-α-methylhopane biomarkers derived from oxygenic photosynthetic cyanobacteria and steranes derived from eukaryotic sterols are present (Brocks *et al.*, 1999; Summons *et al.*, 1999; Brocks *et al.*, 2003). Sterols require O_2 in their biosynthesis, so that eukaryotes presumably lived in proximity to O_2 producers. The only alternative is sterol biosynthesis without O_2 in a metabolic pathway that has since vanished, but no genetic evidence supports this. Sterols are also found in some planctomycetes, which are evolutionary ancient bacteria (Brochier & Philippe, 2002; Di Giulio, 2003), indirectly suggesting an early origin for O_2 producers. Stromatolites from a 2.7 Ga lake are consistent with the presence of oxygenic photosynthesis because the lake lacked sulfate and hydrothermal reductants needed for anoxygenic photosynthesis, while the stromatolites display a photosynthetic habit (Buick, 1992). Analysis of lead isotopes has also been interpreted to infer that oxygenic photosynthesis existed even as early as 3.7 Ga (Rosing & Frei, 2004). Isotopes of carbon in sedimentary organic carbon and carbonates back to 3.5 Ga are permissive of oxygenic photosynthetic fractionation, although anoxygenic photosynthesis is a possible alternative (Schidlowski, 1988). In summary, the data presents the puzzle that oxygenic photosynthesis existed at least 0.3 b.y., and perhaps >1 b.y., before the initial rise of O_2. Section 2.6 presents suggested solutions to this paradox.

2.5 What is the evidence for the Paleoproterozoic rise of O_2 and its effect?

2.5.1 Geochemical Evidence

2.5.1.1 Evidence from Continental Environments

Paleosols, detrital grains and red beds suggest very low levels of O_2 before ~2.4 Ga. Well-preserved paleosols (lithified soils) provide estimates of the oxygen partial pressure (pO_2) based on iron and rare-earth element geochemistry (reviewed by (Rye & Holland, 1998)) (Fig. 2-7). Iron was leached from soils before the ~2.4 Ga oxic transition but not afterwards because anoxic rainwater flushes soluble ferrous iron (Fe^{2+}) through a soil, whereas oxygenated rainwater produces insoluble and immobile ferric iron (Fe^{3+}). Cerium (Ce^{3+} and Ce^{4+}) can be used similarly (Murakami *et al.*, 2001). Other evidence comes from detrital grains, which are sedimentary minerals that never completely dissolve in weathering. Detrital grains in pre-2.4 Ga riverbeds commonly contain reduced minerals that would only survive at low pO_2 (Rasmussen & Buick, 1999). Grains of pyrite (FeS_2), uraninite (UO_2) and siderite ($FeCO_3$) place upper bounds on Archean pO_2 of ~0.1 bar, ~0.01 bar and ~0.001 bar, respectively. The roundness of such grains shows that they were transported long distances in aerated waters. A further constraint is the appearance of Proterozoic continental redbeds. Redbeds are sedimentary sandstones derived from windblown or river-transported particles coated with red-colored iron oxides, usually hematite (Fe_2O_3), which formed after atmospheric oxygenation (Eriksson & Cheney, 1992; Prasad & Roscoe, 1996).

2.5.1.2 Evidence from Marine Environments

Banded Iron Formations (BIFs) appear from the start of the geologic record but decline in abundance through the Paleoproterozoic and disappear after ~1.8 Ga, consistent with redox change. BIFs are laminated marine sedimentary deposits that contain iron-rich and iron-poor (usually silica-rich) layers. Trace and rare earth element patterns in BIFs

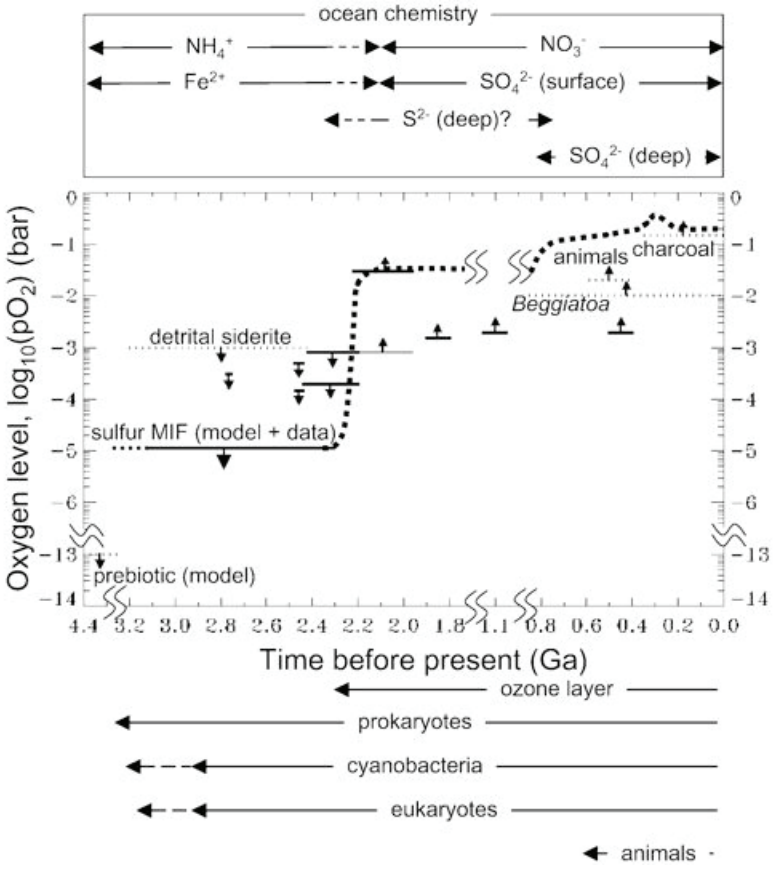

Figure 2-7 Constraints on the evolution of atmospheric oxygen

The history of O_2, where the thick dashed line shows a possible evolutionary path that satisfies biogeochemical data. Dotted horizontal lines show the duration of biogeochemical constraints, such as the occurrence of detrital siderite ($FeCO_3$) in ancient riverbeds. Downward-pointing arrows indicate upper bounds on the partial pressure of oxygen (pO_2), whereas upward-pointing arrows indicate lower bounds. Unlabelled solid horizontal lines indicate the occurrence of particular paleosols, with the length of each line showing the uncertainty in the age of each paleosol. Inferences of pO_2 from paleosols are taken from (Rye & Holland, 1998). An upper bound on the level of pO_2 in the prebiotic atmosphere at c. 4.4 Ga (shortly after the Earth had differentiated into a core, mantle and crust) is based on photochemical calculations. MIF is "mass-independent isotope fractionation", which in sulfur is caused by photochemistry in an O_2-poor atmosphere. The pO_2 level inferred from MIF observed in pre-2.4 Ga sulfur isotopes is based on the photochemical model results of (Pavlov & Kasting, 2002). Biological lower limits on pO_2 are based on the O_2 requirements of: (1) the marine sulfur-oxidizing bacterium, *Beggiatoa* (Canfield & Teske, 1996); (2) animals that appear after 0.59 Ma (Runnegar, 1991); (3) charcoal production in the geologic record. A "bump" in the oxygen curve around ~300 Ma, in the Carboniferous, is based on the interpretation of Phanerozoic carbon and sulfur isotope data by (Berner *et al.*, 2000).

indicate hydrothermal input of ferrous iron, which would have remained in solution if deep waters of the Archean ocean were anoxic (Holland, 1984; Bau *et al.*, 1997). Fe^{2+} is

hypothesized to have been transported to shallow continental shelves where oxidation precipitated ferric iron. BIFs' presence for ~0.5 b.y. after the rise of O_2 has been used to argue that the deep ocean was not oxygenated until 1.8 Ga (Habicht *et al.*, 2002). Recently, Canfield (Canfield, 1998) suggested that the deep ocean remained anoxic until the Neoproterozoic, with Fe^{2+} being removed by the precipitation of pyrite derived from sulfate reducing bacteria (section 2.7).

Isotopes of carbon, sulfur and iron in marine sediments also indicate major change in the Paleoproterozoic. Photosynthesis concentrates ^{12}C into organic matter, leaving inorganic carbonate relatively enriched in ^{13}C. Isotopic compositions are expressed as $\delta^{13}C$, a measure of $^{13}C/^{12}C$ in a sample relative to that in a limestone standard ($\delta^{13}C = [(^{13}C/^{12}C)_{sample}/(^{13}C/^{12}C)_{standard} - 1]\times 1000$, in parts per thousand (‰)). From ~3.5 Ga, sedimentary organic carbon is found to be ~30‰ (3%) lighter than marine carbonates with mean $\delta^{13}C \approx 0$‰. The difference reflects biological fractionation. Carbon entering the atmosphere-ocean system from volcanism, metamorphism and weathering has $\delta^{13}C_{in} \approx -6$‰. On timescales greater than ~10^5 years, the residence time of carbon in the ocean, the same mixture of isotopes entering the atmosphere-ocean system must exit, implying,

$$\delta^{13}C_{in} = f_{carb}\delta^{13}C_{carb} + f_{org}\delta^{13}C_{org} \qquad (2.10)$$

Here, f_{carb} is the fraction of carbon buried as carbonate with isotopic composition $\delta^{13}C_{carb}$, and f_{org} is the fraction buried as organic carbon with $\delta^{13}C_{org}$. Solving eq. (2.10) with the observed $\delta^{13}C$ values gives $f_{org} \approx 0.2$. Thus, over geologic time, ~20% of the carbon in CO_2 entering the ocean-atmosphere system has exited as buried organic carbon and ~80% as carbonate (Schidlowski, 1988). Very positive $\delta^{13}C_{carb}$ excursions (Fig. 2-8) occur in the Paleoproterozoic, the same era as the rise of O_2, and are possibly associated with enhanced organic burial (section 2.6.2.1). The sulfur isotope record indicates that while there was <0.2 mM sulfate in the Archean oceans, sulfate levels increased in the Proterozoic (Habicht *et al.*, 2002). For concentrations exceeding ~0.05-0.2 mM, sulfate reducing bacteria preferentially use ^{32}S rather than ^{34}S, producing

sulfides that are enriched in ^{32}S relative to co-existing seawater sulfate (Habicht *et al.*, 2002). Sulfides with significant ^{32}S enrichment only become widespread after 2.3 Ga, suggesting more available sulfate and hence oxygen (Huston & Logan, 2004). Changes in iron isotopes also provide evidence for an oxic transition (Rouxel *et al.*, 2005). When iron precipitates as iron oxide, ^{56}Fe is sequestered relative to more weakly bonding ^{54}Fe, which leaves $Fe^{2+}(aq)$ isotopically light. Negative $\delta^{56}Fe$ in pyrites before ~2.3 Ga suggests an anoxic deep ocean, rich in $Fe^{2+}(aq)$, with fractionating loss of iron to BIFs.

A small minority claims that the model of a Paleoproterozoic rise of O_2 is incorrect (Ohmoto, 1997). For the rest of the community, however, new mass-independently fractionated sulfur isotope data essentially prove a rise of O_2 at 2.4-2.3 Ga when considered in concert with all the above evidence (Farquhar *et al.*, 2000; Bekker *et al.*, 2004). Isotope fractionation is generally "mass dependent" and approximately proportional to the mass difference between isotopes. Photochemistry can produce "mass-independent fractionation" (MIF) where isotopes are still fractionated by mass, but relative abundances deviate from simple proportionality. In the modern atmosphere, volcanic sulfur volatiles are oxidized to sulfate, which dissolves in rainwater and produces isotopically uniform oceanic sulfate. An anoxic atmosphere has two differences. Firstly, the lack of a stratospheric ozone layer allows shortwave ultraviolet to penetrate the troposphere and produce MIF during photolysis (e.g., $SO_2 + h\nu = SO + O$ and $SO + h\nu = S + O$). Secondly, if $pO_2 < 10^{-5}$ bar, sulfur compounds exit the atmosphere in a range of oxidation states, allowing MIF to be preserved in sediments (Pavlov & Kasting, 2002; Farquhar & Wing, 2003; Ono *et al.*, 2003). Sulfur isotopes from a wide variety of depositional settings show MIF prior to ~2.4 Ga, but not afterwards.

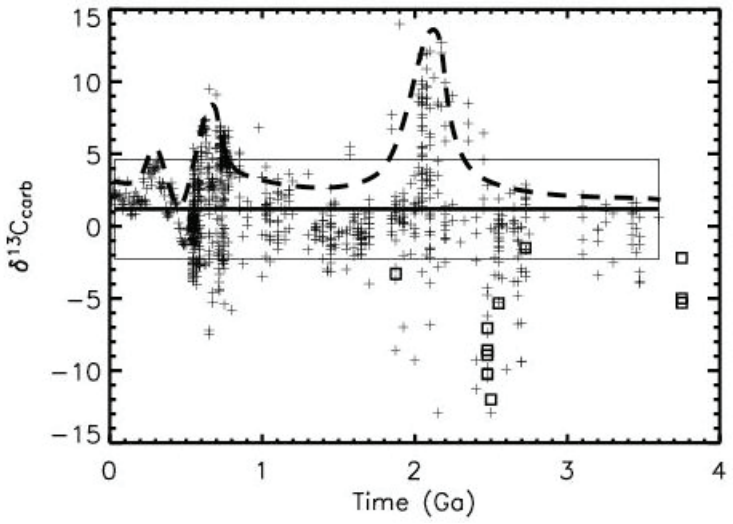

Figure 2-8 The carbon isotope record of $\delta^{13}C$ in marine carbonates

The horizontal line is the average of all values (neglecting those from banded iron formations (square symbols)) and the surrounding rectangular box extends to one standard deviation. The dashed line is a sketch indicating how the Paleoproterozoic and Neoproterozoic were times of unusually isotopically heavy carbonates. Isotopically light carbonates between 2.7-2.4 Ga are likely due to carbonates derived from respired organic matter, which is particularly true of banded iron formations (Kaufman *et al.*, 1990). The Precambrian carbon isotope data is from R. Buick (unpublished), modified from (Shields & Veizer, 2002) by additional literature and improved radiometric dating. Phanerozoic carbon isotope data is from (Hayes *et al.*, 1999).

2.5.2 What were the consequences of the rise of O_2 for atmospheric chemistry and climate?

Atmospheric O_2 and CH_4 annihilate each other. Consequently, for an anoxic Archean atmosphere, photochemical models simulate 10^2-10^3 ppmv CH_4 (Pavlov & Kasting, 2002), compared to ~1.75 ppmv today (Wuebbles & Hayhoe, 2002), if given a global methanogen methane source ranging 10-100% of today's flux. The early sun was 25-30% fainter than today and so the atmosphere must have had more greenhouse gas to prevent Earth from being globally frozen (Kasting & Catling, 2003). Abundant methane can provide such greenhouse warming (Pavlov *et al.*, 2000). A rise in O_2 would promote the rapid destruction of the methane, cooling the Earth by a few tens of °C, which could explain the ~2.4 Ga Paleoproterozoic "Snowball Earth" (Pavlov *et al.*, 2000). Oxygen also has another important repercussion. Ozone (O_3) derives from O_2. Once O_2 rose to

~1% of the current atmospheric level, an effective stratospheric ozone screen for ultraviolet radiation emerged (Fig. 2-7), shielding the surface biosphere.

2.6 Explaining the rise of O_2 and the oxidation of the surface of the Earth.

2.6.1 What defines an oxic versus anoxic atmosphere?

An oxidizing atmosphere is poor in hydrogen-bearing reducing gases whereas a reducing atmosphere is not. Even a small excess of hydrogen tips the balance. For example, an atmosphere with a steady-state abundance of ~0.1% H_2 (or equivalently, 0.05% CH_4) will be anoxic.

An atmosphere becomes anoxic if the flux of rapidly reactive reductants, principally reducing gases, exceeds the net flux of O_2. To be exact, an atmospheric oxygenation parameter, K_{oxy}, can be defined as follows,

$$K_{oxy} = \frac{F_{source}}{F_{Rsink}} = \frac{F_{source}}{F_{metamorphic} + F_{volcanic}} \tag{2.11}$$

where F_{source} (in Tmol O_2 yr^{-1}) is the net flux of O_2 due to burial of reductants and F_{Rsink} is the flux of metamorphic and volcanic reductants, expressed as Tmol O_2 yr^{-1} consumed (Figs. 2-1, 2-2). F_{Rsink} mostly consists of hydrogen-bearing gases and, conceptually, even hydrothermal reducing cations behave as effective H_2 through schematic reactions such as $2Fe^{2+} + 3H_2O = Fe_2O_3 + 4H^+ + H_2$. When $K_{oxy} < 1$, an atmosphere has very low O_2; when $K_{oxy} > 1$, an atmosphere is O_2-rich. Today, K_{oxy} ~6 because F_{Rsink} is ~1/6 of the O_2 source flux (section 2.2). As a consequence, F_{source} is mostly balanced by losses to oxidative weathering, which permits a high concentration of O_2. If in the past $K_{oxy} < 1$, the atmosphere would have been redox-dominated by hydrogen-rich species even if organic burial and associated O_2 production were exactly the same as today.

Another aspect of anoxic atmospheres is that the rate that hydrogen escapes to space (see eq. 2.4) can cause significant oxidation of the Earth over time. Terrestrial hydrogen

originates within water, hydrated silicates, or hydrocarbons. So when hydrogen escapes, matter left behind has been oxidized to balance the reduction of hydrogen from its original bound form to elemental hydrogen in space. It is immaterial whether the hydrogen is transported upwards through the upper atmosphere within CH_4, H_2, H_2O or some other H-bearing "vector". For example, when hydrogen emanates from volcanoes and subsequently escapes to space, the upper mantle is oxidized through schematic reactions such as $3FeO + H_2O = Fe_3O_4 + H_2 = Fe_3O_4 + 2H(\uparrow space)$. Similarly, when hydrogen derives from metamorphic gases, the crust is oxidized.

2.6.2 Theories for the rise of O_2

Understanding the history of O_2 involves explaining why there was a delay of 0.3-1 billion years between the earliest oxygenic photosynthesis and the rise of O_2 (section 2.4.2). For O_2 to rise, either the O_2 source (F_{source}) increased or the O_2 sink (F_{Rsink}) decreased.

2.6.2.1 Theories for an increasing flux of O_2

Some have argued that O_2 rose because the rate of organic carbon burial (O_2 production) increased, either as a pulse or long-term trend.

2.6.2.1.a Paleoproterozoic pulse of organic carbon burial

At 2.3-2.1 Ga, many marine carbonates are unusually depleted in ^{12}C (Melezhik *et al.*, 1999; Lindsay & Brasier, 2002). This can be explained if there was a large pulse of burial of organic carbon: a ^{12}C-enriched flux to sediments. The burial pulse could generate the equivalent of 12-22 times the present atmospheric O_2 inventory, which some have interpreted as causing the rise of O_2 (Karhu & Holland, 1996). However, the residence time of O_2 is only ~2 million years, even today (section 2.2). So a pulse of organic burial should merely cause a parallel O_2 pulse. O_2 would return to its previously low levels once burial and oxidation of previously buried carbon had re-equilibrated. Another problem is timing. The oxic transition occurred before 2.3 Ga (Bekker *et al.*, 2004), and

since the Paleoproterozoic organic burial pulse follows the rise of O_2, it cannot be its cause. Instead, perhaps the pulse is an effect of O_2. One speculation is that increased oxidative weathering produced copious sulfuric acid (the reverse of eq. 2.2), which dissolved rocks more efficiently during weathering (Chigira & Oyama, 1999), releasing phosphorus that stimulated photosynthesis and organic burial. Perhaps organic burial slowly returned to normal rates because available phosphorus was diminished by adsorption onto iron oxides in oxygenated waters (Holland, 2002).

2.6.2.1.b Secular increase of organic carbon burial

A long-term increase in organic carbon burial rates relative to O_2 sinks would lead to a rise of O_2. Godderis and Veizer (Godderis & Veizer, 2000) follow the suggestion that growth of continental shelves increased organic burial (Knoll, 1979), and present a model showing how an assumed continental growth curve is paralleled by a growth of O_2. In their model, O_2 levels are tied to phosphorus delivery, which, in turn, is set proportional to continental area, so that the correspondence of continental growth and O_2 curves is an assumed foregone conclusion. Of course, large continents with substantial internal drainage would not necessarily deliver more phosphorus to the oceans. Bjerrum and Canfield (Bjerrum & Canfield, 2002) suggest that early phosphate delivery was limited by adsorption onto iron oxides and that a secular increase in organic burial rates overcame this. Specifically, if ^{12}C-depleted carbonate were precipitated during enhanced ancient hydrothermal weathering then Archean organic burial rates could have been lower (Bjerrum & Canfield, 2004). However, this is perhaps difficult to reconcile with the average sedimentary organic carbon content of ~ 0.5 wt% throughout geologic time (Holland, 1984). Des Marais *et al.* (1992) suggest a secular increase in organic carbon burial rates based on boxcar averaging of carbon isotopic data from 2.6 Ga onwards. However, the selection of this particular start-date is biased by organic matter anomalously enriched in ^{12}C, perhaps caused by an era of abundant methanotrophs, which are organisms that oxidize methane and incorporate its ^{12}C-enriched carbon (Hayes, 1994; Hinrichs, 2002). More recent data are interpreted as general stasis in carbon isotopes and a series of complex fluctuations in the Paleoproterozoic (Melezhik *et al.*, 1999; Lindsay & Brasier, 2002) and Neoproterozoic

(Kaufman, 1997) (Fig. 2-8), which may be linked to “Snowball Earth” events (Martin *et al.*, 2000; Hoffman & Schrag, 2002).

2.6.2.2 Theories for a decreasing sink of O_2

A conservative interpretation of the carbon isotope record (Fig. 2-8) is that it indicates no secular trend in organic burial rates. Carbon isotopes show that the Mesoproterozoic is characterized by a burial fraction ~20% organic carbon and ~80% carbonate carbon (Buick *et al.*, 1995), basically the same as Phanerozoic (Hayes *et al.*, 1999) and Archean averages (Schidlowski, 1988; Bekker *et al.*, 2003). In this case, a decrease in the O_2 sink would have been the key factor for the Paleoproterozoic rise of O_2 (Kasting *et al.*, 1993; Catling *et al.*, 2001; Kump *et al.*, 2001; Holland, 2002). The simplest suggestion is that as Earth’s interior cooled (Schubert *et al.*, 2001), the flux of volcanic reducing gases dwindled, lessening the sink for O_2. However, increased past volcanic outgassing would have also injected proportionately more CO_2. Since ~20% of the CO_2 was buried as organic carbon, increased past outgassing, on its own, cannot explain the oxic transition because going back in time, O_2 production due to organic burial would have paralleled O_2 losses.

The problem with the previous idea can be overcome if the proportion of reducing gases in volcanic and metamorphic fluxes has decreased. A decrease in the H_2 to CO_2 ratio in outgassing would flip the atmosphere to an O_2-rich state (section 2.6.1). Recent papers have therefore proposed that volcanic gases became less reducing with time (Kasting *et al.*, 1993; Kump *et al.*, 2001; Holland, 2002). However, studies of redox-sensitive chromium and vanadium abundance in igneous rocks (Delano, 2001; Canil, 2002) show that the mantle’s oxidation state, which controls the redox state of volcanic gases, only permits an increase in H_2 relative to CO_2 by a factor ≤ 1.8. Catling *et al.* (2001) emphasized the potential importance of a decrease in the reducing sink from metamorphic gases, which is independent of mantle redox state. Holland (Holland, 2002) presents another argument concerning sulfur. Today, pyrite burial contributes ~40% of net O_2 production (via eq. 2.2). But sufficient H_2 were outgassed, all accompanying SO_2 would be reduced and pyrite burial would no longer generate O_2:

$$5H_2 + FeO + 2SO_2 = FeS_2 + 5H_2O \quad (2.12)$$

Currently, ~1/6 of the flux of O_2 associated with reductant burial is consumed by reducing gases (Fig. 2-3), which suggests a factor of ~6 increase in the H_2 proportion of outgassing fluxes is needed to get K_{oxy} = 1 in eq. (2.11). But by accounting for sulfur, the factor needed is possibly only ~2-3 (Holland, 2002). Given sulfate-poor Archean oceans, subduction zone outgassing may have been sulfur-poor compared to today, producing gases rich in H_2 relative to sulfur. With sufficient H_2 to accomplish reaction (2.12) and consume O_2 from organic burial fluxes, the atmosphere would be anoxic (Fig. 2-9).

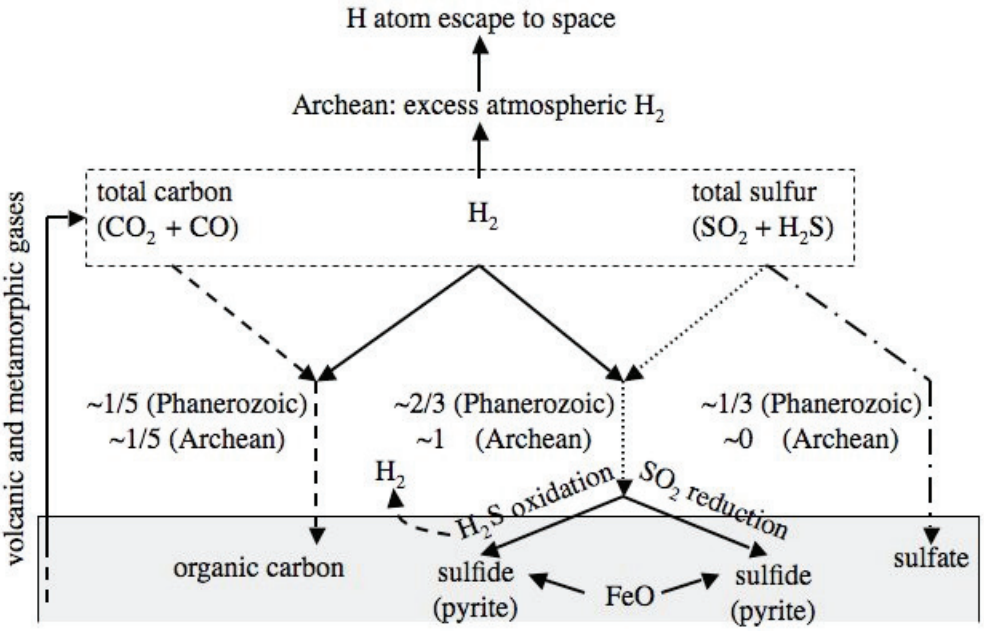

Figure 2-9 A schematic diagram showing the dependence of the atmospheric redox state on changes in the reduction of sulfur, following Holland, 2002

.. The dashed box indicates an average batch of volcanic and metamorphic gas. Hydrogen is ultimately used to reduce carbon gases to organic carbon and to reduce SO_2 to sedimentary sulfide. Geochemical data suggests that over the course of Earth history the fraction of carbon gas converted to organic matter has been about ~1/5 (dashed arrows). The fraction of sulfur gas reduced to pyrite has been ~2/3 in the Phanerozoic (dotted arrows). If enough H_2 had been present in Archean volatiles to convert all of the SO_2 to sulfide, excess H_2 would have accumulated in the Archean atmosphere making it anoxic. The consequence would be loss of hydrogen to space and oxidation of the lithosphere. As a result, volcanic and metamorphic H_2 fluxes would gradually dwindle. Eventually, not enough H_2 would be present to convert all the SO_2 to sulfide and instead SO_2 would be oxidized to create sulfate minerals (dash-dot arrows).

Abundant atmospheric H_2 is unlikely to persist because it is microbial "food" that gets transformed into methane — a lower energy molecule that is less easily microbially consumed in the sulfate-poor, anoxic Archean (section 2.4.1). Oxygenic photosynthesis would have also increased the amount of organic matter available for fermentation and methane production (eq. (2.9)). With ~10^2-10^3 ppmv CH_4 predicted for the Archean (Pavlov *et al.*, 2001), net methane production (i.e., the excess CH_4 flux that does not react with O_2) is balanced by ultraviolet decomposition in the upper atmosphere. Such methane photolysis promotes rapid escape of hydrogen to space, oxidizing the Earth. Indeed, without hydrogen escape, the number of moles of equivalent O_2 in the Earth's crust would be balanced by equimolar reduced carbon (eq. (2.1)), but instead there is excess oxygen (Fig. 2-10). The excess can be quantitatively reconciled with time-integrated hydrogen escape and oxidation expected from a methane-rich Archean atmosphere (Catling *et al.*, 2001).

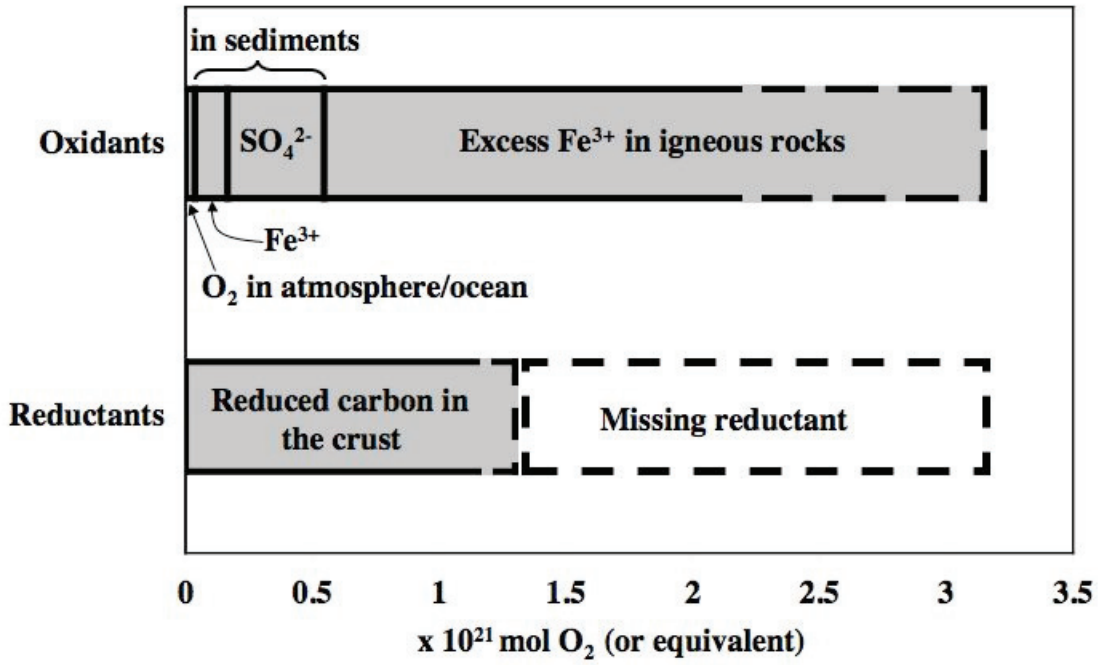

Figure 2-10 Oxygen inventory of Earth's crust

The inventory of oxygen in the Earth's crust shows that there is excess oxygen. Data is from a tabulated compilation in (Catling *et al.*, 2001).

In summary, a plausible explanation for why the late Archean atmosphere was anoxic is that excess reductants scavenged O_2, making K_{oxy} <1 (eq. 2.11). Hydrogen escape may have oxidized the Earth, lowering the sink flux for O_2 by Le Chatelier's principle, until an oxic transition occurred. Fig. 2-11 summarizes this self-consistent conceptual history of redox fluxes, atmospheric gases, and oceanic sulfate.

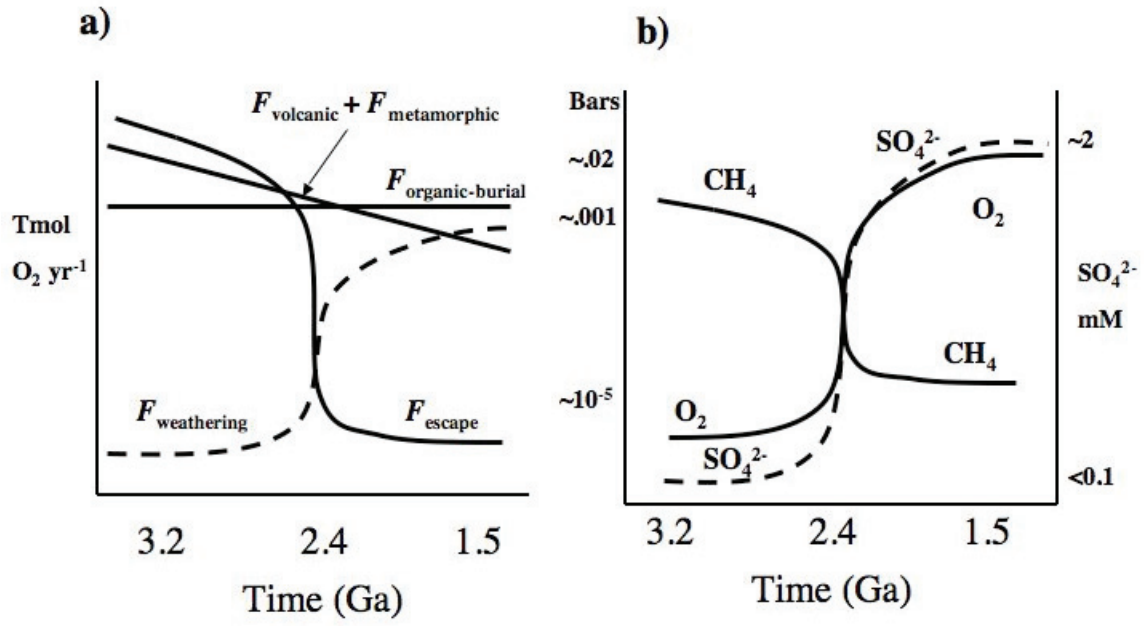

Figure 2-11 Schematic evolution of redox fluxes and atmospheric gases

(a) A schematic diagram showing a plausible evolution of redox fluxes due to oxidative weathering, hydrogen escape, volcanic and metamorphic gases, and the burial of organic carbon (a net source of O_2). (b) A schematic diagram showing the evolution of atmospheric gases (CH_4, O_2) and oceanic SO_4^{2-} from the late Archean to Proterozoic.

2.7 The Neoproterozoic second rise of oxygen

O_2 is inferred to have increased from about 1-3% to greater than 5-18% of present levels in the Neoproterozoic (Canfield & Teske, 1996; Canfield, 1998)(Hurtgen *et al.*, 2005) based on sedimentary sulfides with ^{32}S-enrichment exceeding the isotope discrimination of sulfate-reducing bacteria. The ^{32}S-enrichment can be explained if sulfide was re-oxidized at the sediment-water interface to SO_4^{2-} and cyclically reduced, increasing the isotope fractionation. Possibly, O_2 increased to the point where it penetrated marine sediments, ending a deeply sulfidic ocean (Canfield & Teske, 1996). A second increase

in O_2 is important for understanding the evolution of animals (Knoll & Carroll, 1999; Catling *et al.*, 2005). Recent molybdenum (Arnold *et al.*, 2004) and sulfur isotope studies (Shen *et al.*, 2003; Kah *et al.*, 2004), as well the geochemistry of the final stages of BIF deposition (Poulton *et al.*, 2004), provide some support for a deeply sulfidic Proterozoic ocean. In the Neoproterozoic, like the Paleoproterozoic, low-latitude glacial deposits occur along with extraordinary $\delta^{13}C$ excursions in carbonates perhaps associated with a second rise of O_2 (Hoffman & Schrag, 2002; Pavlov *et al.*, 2003; Rothman *et al.*, 2003). Possibly, Mesoproterozoic CH_4 persisted at $\sim 10^1$-10^2 ppmv until the Neoproterozoic if the global biogenic CH_4 flux were larger than today (Pavlov *et al.*, 2003). Today, a vast flux of seafloor CH_4 is consumed by microbial SO_4^{2-} reduction at the CH_4-SO_4^{2-} transition zone in sediments (D'Hondt *et al.*, 2002). But in a deeply sulfidic ocean, considerable methane perhaps fluxed to the atmosphere (Pavlov *et al.*, 2003). Thus, a possible explanation for the Neoproterozoic "Snowball Earth" is a second rise of O_2 and collapse in methane.

What could have caused a second rise of O_2? One hypothesis involves a larger biological ballast flux that dragged a greater amount of organic carbon into seafloor sediments. Logan *et al*. (1995) suggested that the evolution of fecal pellets played this role. However, fecal pellets are found near the Cambrian boundary (Walter, 1995), after the increase in oxidation indicated by sulfur isotopes (Canfield & Teske, 1996; Hurtgen *et al.*, 2005). Also, aerobic organisms large enough to produce significant ballast are likely to have evolved in response to higher O_2. Furthermore, greater organic carbon burial should shift carbon isotope compositions through time, but there is no obvious secular trend (Schidlowski, 1988). Perhaps the answer lies within the sulfur cycle. If the Proterozoic ocean were deeply sulfidic, seafloor sulfide would be subducted, given its refractory nature (Canfield, 2004). Such burial of sulfides is a net source of O_2 (eq. 2.2). The loss of isotopically light biogenic sulfur would make oceanic sulfate more ^{34}S-enriched over the Proterozoic (e.g., ~10‰ for 0.2 Tmol yr^{-1} S loss) but the paucity of sulfur isotope data for Mesoproterozoic marine sulfates does not permit a statistically meaningful analysis of trends. Finally, another possible cause of a second rise of O_2 is hydrogen escape to space. If atmospheric methane persisted from ~2.2 Ga to ~0.8 Ga at ~100 ppmv, as suggested by (Pavlov *et al.*, 2003), time-integrated hydrogen escape

over 1.4 b.y. would produce the equivalent of ~25 times of all the O_2 in the modern atmosphere and ocean, following the theory of (Catling *et al.*, 2001).

2.8 Conclusions and future directions

The atmosphere evolved from an anoxic to oxygenated state. Good theoretical reasons imply that the prebiotic atmosphere had negligible O_2 and was weakly reducing with ~0.1% H_2. The evolution of methanogens and anoxygenic photosynthesis would have increased atmospheric CH_4 at the expense of H_2. Geochemical evidence for a rise of O_2 at 2.4-2.3 Ga is strong. However, oxygenic photosynthesis appears to have existed at least 0.3 billion years beforehand. A self-consistent explanation for the delay between the origin of oxygenic photosynthesis and oxygenation of the atmosphere is that excess volatile reductants efficiently scavenged O_2 (sections 2.2.3; 2.6.1) Hydrogen escape through a CH_4 intermediary is a possible mechanism that oxidized the Earth, lowering the sink on O_2 until the oxic transition occurred. Following oxygenation, increased sulfate and associated pyrite burial would elevate the O_2 source. The ocean is hypothesized to have been deeply anoxic and sulfidic until the Neoproterozoic when a second rise of O_2 occurred and the ocean became fully oxygenated (Anbar & Knoll, 2002).

Considerable further research is needed to understand the history of O_2. Additional study of mass independent fractionation across the Paleoproterozoic is warranted, complemented by paleosol studies. Biogeochemical cycles of carbon, sulfur and nitrogen also need further constraint. Accurate dating and geological context is particularly important for correlating the large oscillations in carbon isotopes in the Paleoproterozoic and Neoproterozoic (Melezhik *et al.*, 1999). The Proterozoic sulfur cycle will be better understood with more isotopic determinations from sulfates, including substituent sulfates in carbonates (Hurtgen *et al.*, 2002). Whether there was a deeply-sulfidic Proterozoic ocean (Canfield, 1998) can be established by studying redox-sensitive metals (Wilde *et al.*, 2004), molybdenum isotopes (Arnold *et al.*, 2004), and the terminal phases of BIF deposition (Poulton *et al.*, 2004). Currently, our understanding of the ancient nitrogen cycle is extremely poor. Precambrian nitrogen isotope data is sparse (Falkowski, 1997a; Pinti & Hashizume, 2001; Pinti *et al.*, 2001) and a reliable

proxy for marine nitrogen isotopes is lacking. Biomarkers could also reveal the organisms in the Precambrian biosphere (Brocks *et al.*, 2003), including methanogens and methanotrophs (Hinrichs *et al.*, 2003; Wakeham *et al.*, 2004). Perhaps Archean biomarkers could settle whether anoxygenic photosynthesis predominated over oxygenic photosynthesis or vice-versa. Also, while biogeochemical models have illuminated the evolution of Phanerozoic O_2 and CO_2 (Berner, 2004), such models are largely lacking for the Precambrian. Finally, radiative-photochemical models, and time-dependent photochemical models coupled to biogeochemical box models are needed to decipher Precambrian atmospheric chemistry.

Chapter 3 Biogeochemical modeling of the rise in atmospheric oxygen

One of the primary conclusions reached in Chapter 2 is that a quantitative understanding of the evolution of atmospheric oxygen levels is lacking. Here* we begin our attempt to address this problem, by developing a quantitative biogeochemical model that simulates the Paleoproterozoic transition of the Earth's atmosphere from a weakly reducing state to an O_2-rich state. As is fitting for a complicated issue with limited constraints, we present a simple model from which only simple conclusions should be drawn. The primary purpose of this model is to gain an insight into factors that plausibly control the timing and rapidity of the oxic transition. We do this by first calculating a self-consistent description of oxygen in the Earth system, and then running perturbation analyses to determine the most important components of the model.

The biogeochemical model is described in sections 3.3 – 3.5, and contains simplified atmospheric chemistry (parameterized from complex photochemical models described in Chapter 4) and evolving redox fluxes in the Earth system. Time-dependent fluxes are considered, including organic carbon burial and associated oxygen production, reducing gases from metamorphic and volcanic sources, oxidative weathering, and the escape of hydrogen to space. We develop equations in section 3.3 which describe the evolution of atmospheric oxygen and methane as a competition between the sources and sinks of these gases. These equations are explored in section 3.4, and we derive analytic estimates in anoxic and oxic limits that guide our expectations of numerical results throughout this dissertation. Section 3.5 discusses the gritty details of a new parameterization for the evolution of metamorphic gases, a key component of the theoretical model of Catling *et al*. (2001) that the model was partially built to explore.

* Material in this chapter was originally published as Claire, M. W., Catling, D. C., and Zahnle, K. J. "Biogeochemical Modeling of the Rise in Atmospheric Oxygen." *Geobiology* **4**: 239-269 (2006).

In results described in section 3.6, we find that the oxic transition occurs in a geologically short time when the O_2-consuming flux of reducing gases falls below the flux of organic carbon burial that produces O_2. This short timescale for the oxic transition is enhanced by a positive feedback due to decreasing destruction of O_2 as stratospheric ozone forms, which is captured in the atmospheric chemistry parameterization. We show that one numerically self-consistent solution for the rise of O_2 involves a decline in the flux of reducing gases driven by irreversible secular oxidation of the crust caused by time-integrated hydrogen escape to space in the pre-oxic atmosphere, and that this is compatible with available constraints from the geologic record. In this model, the timing of the oxic transition is strongly affected by buffers of reduced materials, particularly iron, in the continental crust. An alternative version of the model, where greater fluxes of reduced hydrothermal cations from the Archean seafloor consumes O_2, produces a similar history of O_2 and CH_4.

The model presented in this chapter is very simple, as an effort was made to construct a model with the fewest number of parameterizations (and hence tuning parameters) to accurately represent the situation. The potentially most glaring omission in the model was the non-inclusion of temperature, so a few extra studies were run. When climate and biosphere feedbacks are included in section 3.7, multiple “Snowball Earth” events are simulated under certain circumstances, as methane collapses and rises repeatedly before reaching a new steady-state.

3.1 Introduction

Oxygen is the third most abundant element in the cosmos (Anders & Grevesse, 1989) and the most abundant (by number) element in the composition of the Earth (Kargel & Lewis, 1993). Most of these oxygen atoms are bound up in rocks (silicates and iron oxides) and water, with only a small portion (< 1 in 10^6) existing in molecular gaseous form (i.e., O_2 , “free” or “atmospheric” oxygen). Modern levels of atmospheric oxygen sustain virtually all multicellular life (Catling *et al.*, 2005), and recent geochemical work has confirmed the long-held hypothesis that oxygen levels have not remained constant

over geologic time. Recent summaries of the geologic evidence are provided by Canfield (2005) and Holland (2006) as well as in Chapter 2, and are summarized in Figure 3-1. Taken as a whole, the data separate two periods of earth history. Prior to approximately 2.4 Ga (billion years ago), atmospheric oxygen did not leave the characteristic signatures of oxidation that are prevalent in the geologic record from 2.4 Ga to the present. This chapter presents a quantitative examination of processes related to the timing and nature of this transition, named the "Great Oxygenation Event" (GOE) by Holland (2002).

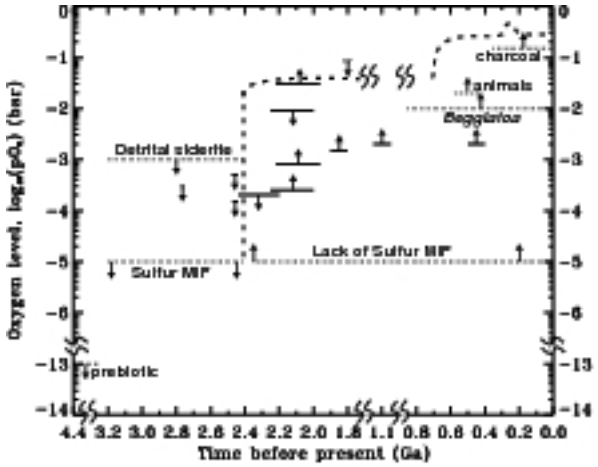

Figure 3-1 Evidence for the rise of oxygen

A compilation of upper and lower bounds on oxygen concentration from the literature, updated from the version in Chapter 2. A possible evolutionary path for atmospheric oxygen is sketched as a thick dashed line. Paleosols are shown as thick lines, with the width of the line corresponding to the age uncertainty (Rye & Holland, 1998). Updated constraints from the Hekpoort paleosol are shown (Yang & Holland, 2003) although others interpret a higher lower limit on pO_2 from this soil (Beukes *et al.*, 2002). Constraints shown as dotted lines pertain to the entire time span of their width. Dotted line constraints are taken from the presence and absence of mass-independent sulfur isotopes (Pavlov & Kasting, 2002), although see Chapter 4 for an additional viewpoint; presence of detrital siderite (Rasmussen & Buick, 1999) ; sulfidic deep waters at 1.84 Ga (Poulton *et al.*, 2004; Canfield, 2005) ; and the O_2 requirements of *Beggiatoa* (Canfield & Teske, 1996) ; animals (Runnegar, 1991); charcoal production (Chaloner, 1989). Phanerozoic oxygen curve is abstracted from models based on carbon and sulfur isotope data (Berner *et al.*, 2003)

3.2 Theories for the rise in oxygen

3.2.1 Sources versus sinks of O_2

In the modern atmosphere, free oxygen is relentlessly destroyed by reactions with reduced gases emanating from volcanoes and hot springs, and by the oxidation of the continents (i.e., kerogen oxidation and the "rusting" of exposed iron rich rocks). Holland (2002) estimates this modern rate of free oxygen destruction at 17.9 ± 8.5 Tmol yr^{-1}. Left unbalanced, destruction rates of this magnitude would deplete the atmospheric reservoir of free oxygen (3.4×10^7 Tmol O_2 (Petsch, 2004)) on the order of millions of years, implying there must be a continuous source to balance these geologic sinks.

The source is chiefly biological. Virtually all atmospheric oxygen derives from a single metabolism, oxygenic photosynthesis. The net redox reaction that this metabolism exploits can be loosely described by the following equation, where "CH_2O" approximates the average stoichiometry of organic matter:

$$CO_2 + H_2O \rightarrow CH_2O + O_2 \qquad (3.1)$$

To first order, respiration and decay (the reverse of equation (3.1)) rapidly consume all of the free oxygen liberated, so oxygenic photosynthesis by itself does not constitute a net source of free oxygen. It is only when the organic carbon produced by a photosynthesizer escapes re-oxidation by burial in sediments, that oxygen is effectively added to the system. The modern net free oxygen source of 10 Tmol yr^{-1} is supported by the burial of approximately 10 Tmol yr^{-1} of photosynthetically-derived organic carbon in sediments on the continental shelves (Holland, 1978, p. 215-219). By contrast, land-based photosynthesis provides a negligible net oxygen source despite its large gross flux, given the lesser area available for permanent burial of organic carbon (Field *et al.*, 1998). In addition, land-based plants did not evolve until the Phanerozoic (Kenrick & Crane, 1997), and so are not relevant to discussions regarding Archean and Proterozoic oxygen levels.

The other major source of oxidizing power to the Earth system is the escape of hydrogen atoms or molecules from the top of the atmosphere. This process ultimately oxidizes the reservoir from which the hydrogen originated. The reason for oxidation is that hydrogen was primarily delivered to Earth as H_2O, hydrated silicates, and hydrocarbons, given that any H_2 captured directly from the solar nebula would have been lost by subsequent impact erosion (Ahrens, 1993). Hydrogen that escapes ultimately originates by splitting hydrogen from one of these compounds, leaving behind an oxidized product to balance the redox reaction. Regardless of how the hydrogen atom is transported to the upper atmosphere (i.e., as CH_4, H_2O, H_2, or some other H bearing compound), escape of that hydrogen atom implies that the reservoir from which it originated has been oxidized to balance the reduction of hydrogen from its bound form (an oxidation number of +1) to the elemental form (an oxidation number of 0). In the modern day, hydrogen escape is limited by the abundance of H-bearing compounds in the lower stratosphere (Walker, 1977, p. 157-163) which contains approximately 1.7 ppmv of CH_4, 0.5 ppmv of H_2, and 3 ppmv of H_2O (Harries *et al.*, 1996). Unlike H_2O, CH_4 does not condense in the troposphere, and hence can act as a quantitatively significant carrier of hydrogen to the upper atmosphere. Given the antiquity of the methanogenic metabolism (Hayes, 1994; Brocks *et al.*, 1999; Brocks *et al.*, 2003) and arguments for enhanced levels of Archean CH_4 (Pavlov *et al.*, 2001), oxidation due to escape of H associated with CH_4 may have played an important role during the Archean (Catling *et al.*, 2001).

The only significant abiotic source of free oxygen is the photodissociation of H_2O with subsequent loss of hydrogen atoms to space (with a net reaction, $2H_2O + h\nu \rightarrow O_2 + 4H\uparrow$). Without the escape of hydrogen, the photodissociation products are free to recombine. Similarly, photodissociation of CO_2 is not a net source of free O_2, unless photochemically coupled to hydrogen escape, given that the photochemical products recombine quickly. A cold stratosphere forces water vapor to condense in the upper (tropical) troposphere, trapping water below the level where there are sufficient UV photons available for photolysis. This condensable nature of H_2O limits the supply of hydrogen to space and renders this source of abiotic O_2 insignificant. Although the modern tropopause temperature minimum is connected to the presence of the ozone

layer, condensation of clouds and a temperature minimum are common features of planetary atmospheres, so that we expect cold-trapping of water vapor to be limiting on early Earth. Well-defined tropopauses are found on Neptune, Saturn, Titan, Jupiter, and Uranus, largely because methane (or its photochemical products) plays a similar role in these atmospheres to terrestrial ozone (de Pater & Lissauer, 2001, p. 94-96). It is likely that methane played a similar role on the early Earth (Pavlov *et al.* (2001) and see later). If the early atmosphere were enriched in CO_2 (Kasting *et al.*, 1984), cold stratospheric temperatures would severely limit the abiotic production of oxygen (Kasting & Ackerman, 1986). H_2O photodissociation and H escape might have provided oxygen to the Hadean Earth, as water vapor can reach the upper atmosphere during magma ocean conditions (Kasting, 1988), subsequent to giant impacts. Focusing on the Archean forward, we ignore the photolysis of H_2O and CO_2 as an oxidizing source.

Oxygen readily reacts with reductants. Whether oxygen liberated by organic burial accumulates in the atmosphere or not depends entirely on the kinetics of its chemical loss to reductants in the atmosphere, ocean and on the land surface (Walker *et al.*, 1983). In its most general formulation, we describe the evolution of free oxygen on geologic timescales by the interplay between its sources (F_{SOURCE}) and sinks (F_{SINK}), i.e.

$$\frac{d}{dt}\left[\mathrm{O}_2\right] = F_{SOURCE} - F_{SINK} = (F_B + F_E) - (F_V + F_M + F_W) \qquad (3.2)$$

where $[O_2]$ is the total reservoir of atmospheric dioxygen, which we quantify in units of Teramoles (where 1 Tmol = 10^{12} mol), although we sometimes convert to bars for graphic display purposes. All source and sink fluxes are described in units of Tmol yr^{-1}. We split F_{SOURCE} into F_B, the flux of oxygen due to organic carbon burial, and F_E, the flux of oxygen to the Earth as a whole due to hydrogen escape. The oxygen sinks F_V and F_M represent reducing gases (i.e. H_2, H_2S, CO, CH_4) from volcanic/hydrothermal and metamorphic/geothermal processes, respectively, while F_W is the oxygen sink due to oxidative weathering of continental rocks. Equation (3.2) is illustrated by considering

fluxes in and out of the atmosphere/ocean/biosphere ("AOB") box in Figure 3-2, our first-order conceptualization of the Earth System.

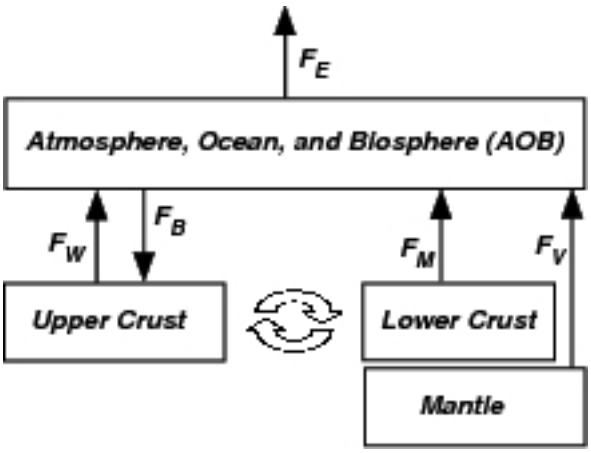

Figure 3-2 A schematic of our three-box model

The arrows represent fluxes of reducing material in units of "oxygen equivalents." Arrows leaving a box thus represent oxidizing processes, so equation (3.2) for the evolution of oxygen is obtained by subtracting the incoming reductant fluxes from the outgoing reductant fluxes. The unfilled arrows represent crustal mixing due to erosion, uplift, and tectonics.

The only way that oxygen levels could have changed with time is if the source or sink terms on the right hand side of equation (3.2) change with time. Clearly, for oxygen to rise, requires that $F_{SOURCE} > F_{SINK}$ at some time. A constant oxygen level in the atmosphere is achieved when the time derivative term is zero and $F_{SOURCE} = F_{SINK}$. Because equation (3.2) is general, these aspects of oxygen evolution are true irrespective of any particular model. If F_{SOURCE}, F_{SINK} or both terms are functions of the oxygen concentration in the atmosphere, in principle, we can solve equation (3.2) and determine Earth's oxygen history. This then, is the essence of the model that we construct in this chapter.

We now summarize various previous qualitative attempts at describing the evolution of atmospheric oxygen in terms of various changes in the long-term sources and sinks.

3.2.2 Increase in the O_2 source

One class of models discussed in the literature argues that increases in atmospheric O_2 are directly related to changes in the source flux.

3.2.2.1 Step changes

As nearly all free oxygen on Earth derives from oxygenic photosynthesis, it is reasonable to assume that the evolution of this metabolic pathway was the fundamental driver in the timing of the rise in planetary O_2 levels. Indeed, some have argued that oxygen appeared in the atmosphere as soon as oxygenic photosynthesis evolved (Ohmoto, 1996; Kopp *et al.*, 2005). However, multiple lines of evidence indicate that cyanobacteria evolved significantly prior to the rise of oxygen, which effectively rule out this hypothesis. The most direct evidence for the existence of ancient cyanobacteria occurs in the 2.7 Ga Pilbara Craton, in which 2-alpha-methylhopanes were found (Brocks *et al.*, 1999; Brocks *et al.*, 2003). The only known organisms that produce long chain (i.e. >C31) varieties of these particular molecules are certain cyanobacteria (Brocks *et al.*, 2003; Summons & Brocks, 2004). In addition, C28-C30 steranes were found in the same deposit as the 2-alpha-methylhopanes. Such steranes are the diagenetic derivatives of sterols. Sterols in the modern biosphere are found in eukaryotes and synthesized in a pathway that requires free molecular oxygen (Summons *et al.*, 2006). No bacteria are known to synthesize C28-C30 sterols and archea do not synthesize sterols at all. The simultaneous co-detection of long chain (>C31) 2-alpha-methylhopanes with eukaryotic sterols is a robust biosignature for organisms capable of oxygenic photosynthesis, and is strongly suggestive evidence for the existence of cyanobacteria at 2.7Ga.

Moreover, the detection of cyanobacterial biomarkers and steranes prior to the rise of oxygen is not one isolated result. Using a rigorous procedure, cyanobacterial biomarkers and diverse steranes have been detected in fluid inclusions in the 2.45 Ga Matinenda Formation at Elliot Lake, Canada (Dutkiewicz *et al.*, 2006), which is a uraniferous sandstone deposited in a reduced environment prior to both the rise of oxygen (Bekker *et al.*, 2004) and the Huronian glaciations (Young *et al.*, 2001). It seems

likely that as more biomarker analyses are conducted in the Archean, further evidence will accumulate for the origin of oxygenic photosynthesis prior to the oxygenation of the atmosphere. Additional evidence to support the early evolution of oxygenic photosynthesis (including non-sulfatic stromatolites, isotopic indicators of the presence of methanotrophs, and the isotopic records of C, S, U, and Pb) have been recently reviewed (Canfield, 2005; Holland, 2006 ; see also Chapter 2). Taken together, the data indicate an evolution of oxygenic photosynthesis at least 0.4 b.y. and perhaps as much as 1.3 b.y. prior to the GOE. Given the ubiquity of the substrate (CO_2, H_2O and photons), oxygenic photosynthesizers probably radiated quickly and became dominant players in the planetary ecosystem (Des Marais, 2000), as they are today, limited only by the availability of trace nutrients such as phosphorus and nitrogen (Tyrell, 1999). As a result, any theory for the rise in atmospheric oxygen levels must contain a mechanism by which reducing conditions can be maintained even in the presence of a substantial flux of organic carbon burial and associated net O_2 production prior to 2.4 Ga.

Before further discussion, we acknowledge that alternate views regarding whether or not the GOE took place do exist, albeit amongst a minority of researchers. Ohmoto and colleagues have argued that the geologic record preserves localized evidence of significant oxidation prior to 2.4 Ga (e.g. Ohmoto (1996)), but also propose a much earlier oxygenation of Earth's atmosphere. Analyses which show the presence of mass-independent fractionation (MIF) of sulfur isotopes in Archean rocks (Farquhar *et al.*, 2000; Farquhar & Wing, 2003; Ono *et al.*, 2003; Chapter 4) provide to many observers convincing evidence that the Archean atmosphere was globally weakly reducing. Local oxygen "oases" likely occurred in surface waters as the result of cyanobacterial activity and the limitation on the diffusion rate of oxygen from the surface ocean into the atmosphere (Kasting, 1992). In this chapter, we accept the consensus view that a major change in oxygen concentrations in the atmosphere occurred at approximately 2.4 Ga.

3.2.2.2 Cumulative burial of organic material

A small fraction (0.1% - 0.2%) of photosynthetically produced organic carbon escapes re-oxidation in the water column and the upper oxic layer of sediments (Betts & Holland, 1991; Field *et al.*, 1998), representing a net source of 10 ± 3 Tmol yr^{-1} of free oxygen to the hydrosphere via equation (3.1) (Holland, 2002). Given the direct correlation between organic carbon burial and the production of free oxygen, many models exist that tie oxygen levels to putative changes in the global burial flux of organic carbon.

3.2.2.2.a Disproportionation of CO_2

One historical line of argument arises from inspection of the bulk crustal rock record. Early compilations show an approximate correspondence between the total reservoirs of reduced sedimentary carbon and oxidized iron and sulfur (e.g., Ronov, 1983). Given this correspondence, one can imagine the "history" of the Earth system as the reduction of volcanically produced CO_2 to organic carbon with the excess oxygen consumed in the conversion of ferrous to ferric iron and sulfides to sulfates (Walker, 1990b). This hypothesis relied on estimates of bulk crustal composition that pre-dated the acceptance of plate tectonics and its influence on crustal production. Continents were assumed to be primary features of Earth, rather than formed from mantle-derived igneous rocks. Consequently, these early compilations ignored oxidized iron in the non-sedimentary components of Earth's crust. It is useful to think of the igneous and high-grade metamorphic rocks of Earth's crust as "hard rocks" and sediments as "soft rocks" (Sleep, 2005a). The inventory of excess oxygen in "soft" rocks (i.e. sulfates and iron oxides in sediments) plus the atmosphere and ocean, is vastly outweighed by excess oxygen in "hard" rocks. An excess inventory of 1000-2000 Examoles O_2 are observed in hard rocks and ~300 Examoles O_2 in soft rocks (Catling *et al.*, 2001; Sleep, 2005a; Hayes & Waldbauer, 2006), nullifying the assumptions of the CO_2 disproportionation hypothesis. This hypothesis also has additional difficulties in that there is no compelling reason that oxygen should rise (or even exist) in the atmosphere at all.

3.2.2.2.b Secular changes in the burial of organic carbon

Secular changes in the rate of organic carbon burial have been proposed to describe the history of atmospheric oxygen. Assuming the global carbon cycle is in steady state implies a mass balance for the ^{13}C and ^{12}C isotopes on timescales exceeding ~10^5 years, the residence time of oceanic carbon (Walker, 1990a). $\delta^{13}C$ is a measurement of the relative amount of ^{13}C to ^{12}C in a sample and is widely used as a paleoindicator given its comparative resistance to diagenetic resetting (Schidlowski, 2001). ($\delta^{13}C = [(^{13}C/^{12}C)_{sample} / (^{13}C/^{12}C)_{standard} - 1] \times 1000$, is measured in parts per thousand (‰) against the international standard of a fossil marine carbonate, Vienna Peedee Belemnite (VPDB) (Coplen, 1994)). Mass balance is commonly expressed as $\delta^{13}C_{in} = \delta^{13}C_{out}$, where $\delta^{13}C_{in}$ is the average isotopic composition of all carbon input into the rapidly exchangeable "AOB" reservoir, and $\delta^{13}C_{out}$ is the isotopic composition of all carbon removed from the AOB reservoir. ^{13}C and ^{12}C exit the global carbon cycle in either carbonates ($\delta^{13}C_{carb}$) or organic carbon ($\delta^{13}C_{org}$), so that

$$\delta^{13}C_{out} = \delta^{13}C_{carb} f_{carb} + \delta^{13}C_{org} f_{org} = \delta^{13}C_{carb} + f_{org}(\delta^{13}C_{org} - \delta^{13}C) \quad (3.3)$$

where f_{org} is the fraction of carbon buried as organic matter, f_{carb} is the fraction of carbon buried as carbonates, and $f_{carb} + f_{org} = 1$. Over rock-cycle timescales, the mass weighted average $\delta^{13}C$ of the recycled input into the global carbon cycle must equal the input from the mantle (Hayes & Waldbauer, 2006). Diamonds from peridotite xenoliths thoughout geologic time have $\delta^{13}C$ values similar to that of the modern mantle (Pearson *et al.*, 2004) so we follow the traditional approach and adopt the average mantle value of $\delta^{13}C_{in} = \delta^{13}C_{out}$ ~-6 ‰ (Holser *et al.*, 1988), as calculated from a subset of mantle diamonds and mantle-derived basalts. Measurements of average $\delta^{13}C_{carb}$ for all geologic eons are ~0 ‰ because the standard is itself a marine carbonate of typical isotopic composition (Schidlowski, 1988). Inserting these numbers into equation (3.3) along with the observed average difference between $\delta^{13}C_{org}$ and $\delta^{13}C_{carb}$ (~30 ‰ (Schidlowski, 1988)) provide the estimate that over most epochs of Earth history, approximately 1/5 of the carbon input is buried as organic matter. Currently, there is no complete explanation for why carbon should separate out in 4:1 proportions in carbonate and organic carbon

burial fluxes, despite the considerable changes in the structure of the biosphere over geologic history, although the geochemical cycle of phosphorus appears to be crucial (Junge *et al.*, 1975; Ruttenberg, 2004).

A secular increase in f_{org} from 2.6 Ga onwards is suggested based on boxcar averaging of ancient $\delta^{13}C$ measurements (Des Marais *et al.*, 1992), but these results are influenced by choosing starting dates at the period of Earth history with the most depleted $\delta^{13}C_{org}$ values. Methanotrophic recycling of organic carbon created by photosynthesizers has been implicated in the production of these anomalously low $\delta^{13}C_{org}$ values (Hayes, 1994; Hinrichs, 2002; Hayes & Waldbauer, 2006). Another recent model (Bjerrum & Canfield, 2004) also suggests that f_{org} increased from the mid-Archean forward by assuming significant loss of carbon to hydrothermal carbonates. While the process of hydrothermal carbonatization appears to be very important in quantitative treatments of the Archean carbon cycle, (Sleep & Zahnle, 2001; Hayes & Waldbauer, 2006), the Bjerrum and Canfield (2004) model assumes a biologically pumped gradient in $\delta^{13}C$ between the surface ocean and seafloor but measurements of 3.46 Ga seafloor show no such gradient (Nakamura & Kato, 2004). Hayes and Waldbauer (2006) provide additional arguments against the secular evolution of f_{org} via an expanded version of equation (3.3) incorporating hydrothermal carbonatization and subduction zone processes, arguing that f_{org} is approximately constant throughout most of the Archean and Proterozoic.

A different, albeit less direct, hypothesis in this category involves continental growth rates. Two important processes may be tied to the total volume of continental crust - organic carbon burial on the continental shelves and phosphorus weathering from continental rocks. Previous numeric models which incorporated continental growth have assumed pO_2 proportional to carbon burial and carbon burial proportional to continental area, and hence show the rise of O_2 as a direct product of continental growth (Godderis & Veizer, 2000), a result that is prescriptive rather than descriptive. Due to many measurement difficulties, the time evolution of the growth of the continents remains a

field of inquiry, although most models predict that at least 70% of current continental volume was in place by 2 Ga (Rogers & Santosh, 2004, p.48).

3.2.2.2.c A pulse in organic carbon burial

Karhu and Holland (1996) hypothesize that a pulse in organic carbon burial might have caused the rise in atmospheric oxygen. This was based on their interpretation of a prolonged 300 m.y. positive excursion in $\delta^{13}C_{carb}$, which, when coupled with a steady state interpretation of the global carbon cycle, implies that 11-22 times the present amount of atmospheric oxygen could have been generated (Karhu & Holland, 1996). The early Paleoproterozoic sedimentary record remains incomplete, but the required organic carbon associated with such a burial pulse appears to be missing (Melezhik *et al.*, 1999; Aharon, 2005). In addition, the peak of the isotope excursions occurred at 2.2 Ga, well after the initial rise in O_2 levels before 2.32 Ga, as evidenced by disappearance of MIF S (Bekker *et al.*, 2004), indicating that the carbon isotope excursion is more likely an effect rather than a cause (Holland, 2002; Hayes & Waldbauer, 2006). Finer resolution data reveal the "Lomagundi event" as several spikes of $\delta^{13}C$ in marine carbonates coupled with return to low values (Melezhik *et al.*, 1999; Lindsay & Brasier, 2002; Melezhik *et al.*, 2005), which argues for more complexity than a single pulse in the carbon burial. Hayes and Waldbauer (2006) argue that the $\delta^{13}C$ excursions may represent unusual times in Earth history when the diagenetic effects of methanogenesis were preserved.

3.2.3 A decreasing sink for O_2

Estimates of Archean global gross productivity are necessarily difficult to quantify but net production of O_2 via organic carbon burial is constrained by the record of carbon isotopes. Given the approximate stasis in global carbon isotopes (Schidlowski, 1988) and the approximately constant 0.5 wt% of organic carbon in sediments over geologic time (Holland, 1984, p. 352-364), many researchers conclude that once oxygenic photosynthesis evolved, net oxygen production since the late Archean has been

approximately constant relative to the total carbon flux in and out of the atmosphere-ocean system (Des Marais, 2000). This interpretation would leave a secular decrease in oxygen destruction as a plausible mechanism for explaining the rise in oxygen.

3.2.3.1 Decreasing Sink from Volcanic Outgassing

Simply decreasing the total flux of volcanic gases as the Earth cooled (Christensen, 1985) is not sufficient to decrease the O_2 sink. Increased volcanic outgassing would have injected proportionally more CO_2 into the atmosphere in addition to any enhancement in reducing gases. But since ~20% of CO_2 has been buried as organic matter over geologic time (see the previous section), oxygen production due to enhanced organic burial would counteract any enhancement in the reductant sink. To see this, consider a hypothetical volcano releasing 5 Tmol yr^{-1} of CO_2 and 1 Tmol yr^{-1} "O_2 equivalent reductants" (i.e. as H_2, CH_4, CO, etc.). This toy volcano does not change the steady state level of atmospheric O_2 if 1/5 of the CO_2 is buried as organic carbon, releasing 1 Tmol yr^{-1} of O_2. This conclusion is unchanged if the total volcanic outgassing rate increases – the only way to affect the net redox balance is via a change in the ratio of reducing gases to CO_2.

Realizing this, Kasting and colleagues developed a model invoking decreasing proportions of reducing to neutral gases (generally described as the H_2/CO_2 ratio) emanating from Earth's mantle as the mantle progressively oxidizes with time (Kasting *et al.*, 1993; Kump *et al.*, 2001). In this model, hydrogen escape is balanced by input of reductants from the mantle, so there is no net oxidation of the continents. This model can be formalized by a simplified version of equation (3.2) in which

$$\frac{d}{dt}[O_2] = F_B - F_{V,KK} - F_W \qquad (3.4)$$

where $F_{V,KK}$ indicates the volcanic parameterization in the manner of Kasting, Kump and colleagues (*ibid.*) which for our purposes are volcanic gases that can consume atmospheric O_2. Walker (1977) argues that at extremely low O_2 levels oxidative weathering will be negligible, at moderate O_2 the rate of oxidative weathering should be proportional to oxygen levels, and at high O_2 levels oxidative weathering should once again become independent of O_2 levels (Walker, 1977, p. 103-105). A function which fits this behavior is $F_W = k_W*[O_2]^{\beta}$, where k_W is a constant. We adopt a constant β=1/3 using an analog of CO_2 weathering behavior where β has been calibrated (Holland, 1978, p. 20), because this exponent probably captures the first-order behavior expected for O_2. Later we explore the sensitivity to changing the exact value of β in numerical computations. This general formulation of oxidative weathering is supported by the evolution in the ferric/ferrous ratio of shales, which show a dramatic increase between 2.3 and 2.1 Ga (Holland, 2006).

For a heuristic estimate below, we approximate the oxidative weathering flux in the "moderate O_2" regime by $F_W = C*[O_2]$, where C is a proportionality constant. In steady state, the time derivative of the oxygen reservoir in the atmosphere must be zero, i.e., $d[O_2]/dt = 0$. Substituting for F_W and assuming steady state in equation (3.4) yields:

$$[O_2] = (F_B - F_{V,KK}) / C \qquad (3.5)$$

In this fashion, the rise of O_2 can be explained by decreasing the magnitude of $F_{V,KK}$ relative to F_B (assumed constant). When $F_{V,KK}$ exceeds F_B, the oxygen concentration in equation (5) is negative and the equation no longer holds. In that case, the atmospheric redox state is dominated by reducing gases.

Measurements of the redox-sensitive trace elements Cr, V, and Sc in basalts (Canil, 1999; Delano, 2001; Li & Lee, 2004) have cast doubt on models which invoke redox evolution of the mantle. Because Sc and V partition similarly apart from their redox

sensitivity, Li and Lee (2004) have shown using V/Sc ratios that Archean mantle differed in oxygen fugacity from the modern mantle by no more that 0.3 $\log_{10}$ units, an amount insufficient to promote a reduced atmosphere (Holland, 2002). Rather than a smooth decline in volcanic reductants, some workers argue for a step change decrease in the reducing power from the mantle at ~2.4 Ga (Kump *et al.*, 2001; Barley *et al.*, 2005). This model speculates that the entire mantle overturns, bringing oxidized material from the core mantle-boundary to the upper mantle. The V/Sc data for Archean and modern basalts reveal nearly identical oxygen fugacity and spread, so any argument that invokes mantle redox evolution requires that the entire signal from changes in mantle fugacity are completely buried in the noise. Given these arguments, we concur with Li and Lee (2004) that the oxygen fugacity of the mantle is unlikely to be the major driver of atmospheric O_2 levels.

A further refinement of the declining volcanic flux model involves an enhanced Archean flux of both H_2 and hydrothermal cations (Fe^{2+}) venting from mid-ocean ridges (Kump & Seyfried, 2005). This process perhaps avoids the constraint on mantle redox evolution. Conceptually, reduced hydrothermal/geothermal cations behave as effective reductant contributions to F_V or F_M through schematic reactions such as $2Fe^{2+} + 3H_2O = Fe_2O_3 + 4H^+ + H_2$. Kump and Seyfried (2005) argue that lower oceanic sulfate levels and shallow mid-ocean ridges will increase the Fe^{2+}/H_2S ratio of vent fluids, allowing for an iron-rich deep ocean conducive to the deposition of banded iron formation and supportive of vigorous methanogenesis. This process could certainly be important on the Archean earth, but we are unable to evaluate it further as the authors do not present quantitative estimates of the magnitude of the enhanced fluxes.

3.2.3.2 Decreasing Sink of Metamorphic Gases

Catling *et al.* (2001) suggest evolution in the redox state of metamorphic gases derived from Earth's crust. The crustal reservoir evolves independently of redox state of the mantle, so the Cr, V, and Sc data do not bear on it. This model requires high rates of hydrogen escape early in Earth history relative to the present day, which drives a redox

change of the crust and mantle. The model allows for mantle redox change within the small limits constrained by observations but assumes that the mantle oxidation state is strongly buffered. The rise of oxygen is explained by the progressive oxidation of the continental crust by hydrogen escape, which in turn reduces the proportions of reductants from crustally-derived metamorphic gases, decreasing the sink for O_2. The primary drawback of this model is the lack of a general theory for the evolution of metamorphic gases, and the absence of geological proxies for paleo CH_4 levels.

Holland has a somewhat similar conceptual model, which emphasizes low temperature hydrothermal/geothermal sources of reductants from the seafloor and considers the effects of the sulfur cycle on the oxidation state of the atmosphere (Holland, 2002). He argues that the Archean sulfate-poor oceans (Canfield *et al.*, 2000) would have led to slower sulfur cycling, and hence volcanic and metamorphic gases with a lower $\Sigma S/H_2O$ ratio. Excess hydrogen could have reduced all SO_2 to pyrite without the corresponding O_2 source that occurs at higher $\Sigma S/H_2O$ levels from pyrite burial. Testing this hypothesis lies beyond the scope of this chapter, as it would require incorporation of the sulfur cycle into our biogeochemical model. However, the Catling *et al*. (2001) model is qualitatively similar to Holland (2002) in that hydrothermal/geothermal fluids can become more oxidizing, with CH_4 derived from excess H_2 via biological activity. Indeed, there are good reasons to believe that a significant concentration (>100 ppmv) of H_2 is unlikely to exist in the Archean atmosphere because it can serve as a substrate for anoxygenic photosynthesis and methanogenesis, which together recycle the hydrogen to organic matter and then methane. In laboratory experiments, methanogens draw down H_2 to produce methane until they reach a thermodynamic limit at ~0.01% H_2 (Kral *et al.*, 1998). Biomarkers and carbon isotopes suggest methanogens were present in the Archean (Hayes, 1994; Hinrichs, 2002; Brocks *et al.*, 2003). In addition, methanogens are strictly anaerobic with a tendency toward thermophily, which suggests that they are evolutionarily ancient (Teske *et al.*, 2003). Thus, methanogens likely would have converted any excess atmospheric H_2 into methane (Kasting *et al.*, 2001; Kharecha *et al.*, 2005).

The purpose of this chapter is to extend the above qualitative descriptions of the rise of oxygen to the quantitative realm, and to obtain a fully self-consistent mathematical framework for the redox evolution of Earth's atmosphere and lithosphere. Consequently, we continue the discussion by considering analytical and numerical viewpoints in the following sections.

3.3 Global Sources vs. Sinks of Reductants

We have introduced the concept of the evolution of atmospheric O_2 as interplay between its sources and sinks, an idea that we now extend by expanding the RHS of equation (3.2). For the purposes of this chapter, we must consider the effect of reductant fluxes on both the oxygen level and reduced components of the atmosphere. We represent the reduced gas component of the atmosphere as $[CH_4]$ which we take as a proxy for all reduced hydrogen-containing gases. In this way, for example, we treat H_2 as 1/2 of a $[CH_4]$ redox equivalent (i.e. via net atmospheric or metabolic reactions like $CO_2 + 2H_2 \rightarrow CH_4 + O_2$).

3.3.1 Biosphere

For clarity, our model is solely concerned with modeling the Earth after the advent of oxygenic photosynthesis, estimated by various workers as >2.5-3.7 Ga (see previous discussion). Given sufficient nutrient availability, oxygenic photosynthesis probably dominated global productivity once it evolved because cyanobacteria can extract H from ubiquitous water rather than relying on spatially scarce geological sources of reductant (Des Marais, 2000). Consequently, we consider photosynthesis as our key source of organic matter whose subsequent processing could potentially affect gas fluxes to the atmosphere. Other organic generation, e.g., by high temperature life, is unlikely to significantly affect gas fluxes once oxygenic photosynthesis has emerged. Considering changes in Earth's redox evolution over long time periods allows us to examine net redox fluxes and not gross cycles of all redox changes within all microbial communities, greatly simplifying our mathematical treatment of the biosphere. Heterotrophy (including

respiration), microbial Fe-oxidation/reduction, and other detailed microbial redox interactions result in zero-sum redox exchanges that do not contribute directly to redox change in the atmosphere. For example, respiration consumes ~99.9% of photosynthesized organic matter, so that we need only consider the long-term O_2 flux associated with the leak of organic matter into buried sediments rather than the gross photosynthesis-respiration cycle. Furthermore, the organic burial rate is constrained by the carbon isotope record so that it is not necessary to consider all ancient pathways of remineralization in order to deduce organic carbon burial and associated O_2 production. Similarly, we ignore the gross microbial iron oxidation-reduction cycle, including only the net effect on the oxygen cycle, which is evident in the evolution of the ferric/ferrous ratio in shales (Holland, 2006).

We do not have inferential geochemistry for biogenic CH_4 or H_2 fluxes to the ancient atmosphere. Our approach in these cases is to impose gas fluxes that are redox balanced with corresponding production of O_2 (which may, of course, create its surrogates (Fe^{3+}, SO_4, etc.)), assuming that the metabolic source for any organic matter derives from photosynthesis. Such gas fluxes can be varied to assess model sensitivity, bounded by what is known about modern fluxes subject to changing physical conditions such as nutrient limitation or substrate availability. In essence, such variations parametrically take into account possible scenarios with different degrees of heterotrophy, anaerobic CH_4 oxidation, etc., relative to methanogenesis (Kharecha *et al.*, 2005). We begin our expansion of equation (3.2) to include the quantitatively important biospheric redox terms by expanding on F_B, the organic carbon burial term.

Information on organic burial, F_B, comes from the carbon isotope record that suggests ~20% of the carbon coming into the system was buried as organic carbon during most of Earth's history (Schidlowski, 1988). Today, F_B ~ 10 Tmol O_2 yr^{-1} (Holland, 2002). If the amount of carbon entering the Archean atmosphere-ocean system was similar to today, C isotopes roughly constrain F_B to be similar to today. To first-order then, we assume oxygen production due to organic burial has remained constant (relative to the influx of carbon to the atmosphere-ocean system) since the evolution of oxygenic

photosynthesis. On the modern Earth, photosynthetically-produced organic carbon is used by microbes to reduce sulfate to pyrite, so that when such pyrite is buried, oxygen is effectively liberated to a degree that is quantitatively significant (Holland, 2002; Berner, 2004, p. 101-103). However, in the Archean oceans, the lack of significant sulfur isotope fractionation implies that sulfate levels were low (Canfield *et al.*, 2000; Habicht *et al.*, 2002). Consequently, to keep our early Earth model simple, we assume that the F_{SOURCE} term was dominated by the burial flux of organic carbon (F_B) for the Archean.

The net effect of oxygenic photosynthesis is the slow flux of oxygen via organic carbon burial discussed previously, but alternate fates exist for photosynthetically-produced organic carbon. The important fate to consider for our model is methanogenesis because this process releases a redox-sensitive gas to the atmosphere. Rather than respiration or burial, a microbial community of fermenters and methanogens can further processes organic carbon via the following net redox reaction:

$$2CH_2O \rightarrow CH_4 + CO_2 \qquad (3.6)$$

The net effect of methanogenic recycling of photosynthetically-produced organic carbon is found by summing 2 times equation (3.1) and equation (3.6), yielding:

$$CO_2 + 2H_2O \rightarrow CH_4 + 2O_2 \qquad (3.7)$$

Thus, the combination of oxygenic photosynthesis and methanogenesis produces O_2 and CH_4 in a 2:1 ratio. Methane oxidizing bacteria (methanotrophs) live off the reverse reaction of equation (3.7), although their habitat is limited to regions where both methane and oxygen can coexist, such as the anoxic/oxic boundary layers at the sediment/water interface. “Anaerobic” methane oxidation (AMO) occurs by a consortium of organisms, but all known pathways require either SO_4^{2-} (Valentine, 2002), or NO_3^- (Raghoebarsing *et al.*, 2006). The quantitatively significant source of oceanic SO_4^{2-} is O_2-dependant

oxidative weathering (Holland, 1978, p.46-49; Walker & Brimblecombe, 1985), and the lack of $\delta^{34}S$ fractionation in sediments argues for low sulfate levels in the Archean oceans (Canfield *et al.*, 2000; Habicht *et al.*, 2002). Nitrogen-fixation (N_2 -> NH_4^+) is thought to be genetically ancient, but O_2 is required to further oxidize the ammonia to nitrate, so NH_4^+ was likely the dominant nitrogen species in Archean oceans prior to the rise in oxygen (Beaumont & Robert, 1999; Berman-Frank *et al.*, 2003). For simplicity, we assume Archean AMO to be limited by sulfate and nitrate availability, allowing for a greater CH_4 flux, although both of these pathways may have been important in the transitional atmosphere.

The global occurrence of kerogens strongly depleted in ^{13}C at ~2.8-2.5 Ga is likely evidence for isotopically light CH_4, >20 ppmv, generated by methanogens and incorporated into methanotrophs (Hayes, 1994). Today, ~4% of organic carbon from total gross productivity (~10^4 Tmol yr^{-1}) is estimated to undergo anaerobic conversion into CH_4 (Watson *et al.*, 1978). However, upward diffusion of CH_4 from seafloor sediments is almost totally cancelled by SO_4^{2-} reduction (i.e. AMO) at the CH_4-SO_4^{2-} transition zone (D'Hondt *et al.*, 2002). This means that an enormous oceanic flux of CH_4 never reaches the modern atmosphere. Unlike today, there was very little sulfate in the Archean oceans (Habicht *et al.*, 2002), which were deeply anoxic as evidenced by the transport of ferrous iron (Holland, 1984, p. 379-388). Thus, it is probable that the Archean ocean was a much larger source of CH_4 than today. If all the CH_4 escaped today without oxidation, ~200 Tmol CH_4 yr^{-1} ($4\% \times 10^4$ /2) would be released to the air via equation (3.6), with the net effect of 400 Tmol yr^{-1} of O_2-consuming reducing equivalents. The Archean CH_4 flux could have been similar or greater due to the lower rates of aerobic remineralization in anoxic waters. In the Black Sea, the burial efficiency is ~10 times higher than in the modern oceans (Arthur *et al.*, 1994) and if there were negligible sulfate, the CH_4 flux from the Black Sea to the air would be ~70 times greater than present (Reeburgh *et al.*, 1991). To first order, we assume that Archean CH_4 was derived from photosynthetized organics so that O_2 and CH_4 were generated in stoichiometric 2:1 abundance via equation (3.7). Today's net CH_4 flux of ~30 Tmol CH_4 yr^{-1} (Watson *et al.*, 1990) and the numbers quoted above bound a reasonable range of probable CH_4 fluxes.

We note that laboratory experiments with microbial mats conducted in the modern oxic atmosphere but at low sulfate levels show only modest remineralization (~0.4%) by methanogenesis and a methane flux increase by only a factor of ~10 (Bebout *et al.*, 2002). As described above, anoxic seafloor sediments could produce a very significant Arcehan methane flux, and are not constrained by these mat experiments. Similarly, although large H_2 fluxes may also emanate from mats (Hoehler *et al.*, 2001), H_2 is unlikely to have built up in the atmosphere because of its tendency to be converted to less metabolically desirable methane (Kral *et al.*, 1998; Kasting *et al.*; Kharecha *et al.*, 2005), as discussed previously. In our model, for simplicity, biological H_2 fluxes are effectively carried in the CH_4 flux budget.

3.3.2 Effective reaction of CH_4 and O_2

We have chosen to use a single reservoir for the entire AOB for our box model (see section 3.2 and Figure 3-2), so we do not separate aqueous biological chemistry from atmospheric chemistry when considering the mutual annihilation of CH_4 and O_2, which is a simplification. It would be highly desirable to add methanotrophic destruction of CH_4 and O_2 (or SO_4^{2-}), but our initial goal is to study the simplest system with a minimum number of tunable parameters. In essence, we assume aqueous methanotrophy is relatively minor in the low sulfate Archean ocean and what does occur is a closed cycle that need not concern us. Thus, we parameterize the mutual annihilation of CH_4 by O_2 solely from atmospheric destruction, and apply the parameterization to the entire AOB reservoir. We define an effective rate constant k_{eff}, with units of $Tmol^{-1}\ yr^{-1}$, via:

$$F_{CH4} = k_{eff}\,[O_2][CH_4] \tag{3.8}$$

where F_{CH4} is the CH_4 flux into the atmosphere, $[O_2]$ and $[CH_4]$ are the global atmospheric inventories in Tmol, and k_{eff} is itself a function of the O_2 and CH_4 levels.

The atmospheric annihilation of O_2 by CH_4 is the net sum of many photochemical reactions that are initiated with a photochemical reaction involving an attack on a methane molecule by the OH radical ($OH + CH_4 \rightarrow CH_3 + H_2O$). In the modern

atmosphere, away from polluted areas, OH is produced in the troposphere by a series of steps beginning with the photochemical destruction of tropospheric O_3 (Finlayson-Pitts & Pitts, 2000, p. 179-180):

$$O_3 + h\upsilon \ (\lambda \leq 336nm) \rightarrow O(^1D) + O_2$$
$$O(^1D) + H_2O \rightarrow 2OH$$

where $O(^1D)$ is an electronically excited oxygen atom. The tropospheric ozone itself derives from the collision of an oxygen molecule with an oxygen atom and a third body, and so depends on the presence of an oxic atmosphere. Prior to the rise of O_2, photochemical models show limited OH abundances (Kasting, 1979). Although shortwave ultraviolet reaches the lower atmosphere in the absence of a stratospheric ozone layer and can photolyze water vapor directly, the photolysis products rapidly recombine given that O_2 molecules are not available to rapidly remove the H produced in photolysis. The net result is that the anoxic Archean atmosphere allows a steady-state CH_4 concentration that is much larger than today, given a plausible flux of methane (Pavlov *et al.*, 2001). These same photochemical models show that O_3 levels rise non-linearly with O_2 so that significant OH is produced even at intermediate oxygen levels (Kasting & Donahue, 1980). This positive feedback on CH_4 destruction with rising levels of O_2 leads to a prediction of a geologically quick transition between O_2 and CH_4 dominated atmospheres.

In any regard, $k_{eff} = k_{eff}(O_2,CH_4)$ is a complicated function. In the modern atmosphere, we can compute $k_{eff} = 3.02 \times 10^{-9}$ Tmol^{-1} yr^{-1} from a (net) CH_4 flux of 33 Tmol yr^{-1} (Houghton *et al.*, 1994) into an atmosphere with 21% O_2 and 1.7ppm CH_4. In an anoxic atmosphere, the multiple competing processes sketched above necessitate a numerical solution. We used the photochemical model described in Chapter 4 to compute k_{eff} in 1372 steady-state atmospheres with fixed O_2 surface mixing ratios ranging from 10^{-14}-10^{-1} bar and fixed CH_4 levels from 10^{-6} to 4×10^{-3} bar. CO_2 was fixed at 10^{-2} bar and the upper bound on CH_4 levels was chosen to keep the CH_4/CO_2 ratio < 0.5, thus avoiding the regime of particulate chemistry and photochemical smog (Pavlov *et al.*, 2001). Figure 3-3 shows some of our computed values of k_{eff} as function of CH_4 and O_2.

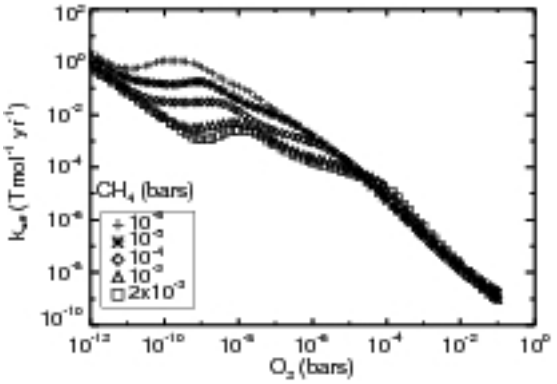

Figure 3-3 Effective photochemical rate constant

Plots of $k_{eff}(O_2,CH_4)$ versus O_2, as computed using the photochemical model in Chapter 4. In the biogeochemical model, k_{eff} values were computed from a logarithmic weighting of the four grid points that bracket the given $[CH_4,O_2]$ pair. CH_4 values outside the computed limits were taken to be the limiting value.

3.3.3 Hydrogen escape

The final item to discuss is the calculation of the rate that hydrogen escapes to space from an anoxic atmosphere so we can quantify its effect on the redox evolution of the Earth System. As previously discussed, the permanent removal of H to space acts to irreversibly oxidize the reservoir from which the H originated. H escapes the planet by a combination of thermal and non-thermal processes acting high in the atmosphere (Hunten & Donahue, 1976; Hunten, 1990). According to this model, verified for the modern atmosphere by satellite and in situ measurements (Hunten & Donahue, 1976), the escape of H atoms is limited by the rate at which H atoms can make their way to the upper atmosphere, with two significant bottlenecks. First, hydrogen contributed from the ultraviolet decomposition of water vapor is throttled by the condensation of water vapor in the upper troposphere (see section 3.2). Second, hydrogen that reaches the homopause then has to diffuse slowly to reach the exosphere. (Below the homopause (about 100 km altitude), the atmosphere is well mixed by turbulence; above the homopause atmospheric gases separate out according to their mass by diffusion and the atmospheric composition changes). The ultimate bottleneck lies in the upward transfer of hydrogen (in all its forms) from the region above the tropospheric cold-trap. Despite the complexities of atmospheric photochemistry and dynamics, the numerical representation of hydrogen escape simplifies to a form proportional to the mixing ratios

(*f*) of hydrogen-bearing compounds above the cold-trap in the upper troposphere (Walker, 1977, p. 157-163). For a hydrogen escape rate Φ, expressed in units of H_2 molecules cm^{-2} s^{-1}, we can write

$$\Phi = k_e f_{TOTAL} = k_e(0.5f_H + f_{H_2} + f_{H_2O} + 2f_{CH_4} + f_{H_2S} + ...) \quad (3.9)$$

where f_{TOTAL} is the total hydrogen mixing ratio, composed of the sum of the mixing ratios (*f*) of H_2, H_2O, CH_4, HCN, NH_3 and any other hydrogen bearing gases that exist above the cold trap in the tropopause, weighted by the amount of hydrogen that they contain. In equation (3.9) above, we have described the hydrogen in terms of H_2 equivalents, although, depending on thermospheric conditions, hydrogen can also escape in atomic form. The numerical constant in equation (3.9) is an average diffusion constant for H and H_2 divided by an atmospheric scale height and to a reasonable approximation is given by $k_e = 2.5 \times 10^{13}$ H_2 molecules cm^{-2} s^{-1} (Walker, 1977, p. 164).

In our model, fluxes are expressed in teramoles per year, which demands some numerical conversion. Given that the area of the Earth is 5.1×10^{18} cm^2, we have a hydrogen escape flux as follows:

$$\begin{aligned}\Phi &= \left[\frac{(2.5\times10^{13}\ \text{molecules cm}^{-2}\ \text{s}^{-1})(3.15\times10^{7}\ \text{s yr}^{-1})(5.1\times10^{18}\ \text{cm}^2)}{(6.02\ \times10^{23}\ \text{molecules mol}^{-1})(10^{12}\ \text{mol Tmol}^{-1})}\right] \times f_{TOTAL} \\ &= 6680\ f_{TOTAL} \quad (\text{Tmol } H_2\ \text{yr}^{-1}) \\ &= 3340\ f_{TOTAL} \quad (\text{Tmol } O_2\ \text{yr}^{-1})\end{aligned} \quad (3.10)$$

We express all reductant gas fluxes as O_2-consuming equivalents, so the stoichiometry of $H_2 + 0.5O_2 = H_2O$ dictates that the redox flux in the second equality above must be divided by 2. In addition, we work with global atmospheric reservoir concentrations of teramoles rather than mixing ratios, which demands further numerical conversion for the f_{TOTAL} term, as follows. Assuming a 1 bar N_2 atmosphere with ζ bars of CH_4, the conversion factor between a Tmol of methane and a bar of methane is given by:

$$\frac{(\text{column mass of air}) \times (\text{area of Earth})}{\text{mean molar mass of air}} = \frac{(10^5 \text{ Pa}/9.81 \text{ m s}^{-2}) \times (5.1 \times 10^{14} \text{ m}^2)}{(\frac{0.028 \times 1 + 0.016 \times \zeta}{1 + \zeta} \text{ kg mol}^{-1})(10^{12} \text{ mol Tmol}^{-1})} \quad (3.11)$$
$$= 1.8 \times 10^8 \text{ Tmol CH}_4 \text{ bar}^{-1}$$

which holds over the CH_4 range from $\zeta = 10^{-6}$ to 10^{-2}. The simplification of a 1 bar N_2 atmosphere is justified by the near-equivalent molecular weights of O_2 and N_2.

In our model, $[CH_4]$ includes all hydrogen bearing compounds, so we use a first-order simplification of $f_{TOTAL}=2[CH_4]$, where the factor of two arises because CH_4 contains the equivalent of two hydrogen molecules. Consequently, the diffusion-limited hydrogen escape parameterization in our model is expressed by substituting $f_{TOTAL}=2[CH_4]$ into equation (3.10) and using the conversion factor of equation (3.11) to obtain:

$$F_E = k_{esc}[CH_4] \quad (3.12)$$

where k_{esc}= 6680/ 1.8×10^8 = 3.7x10^{-5} (Tmol O_2 equivalents yr^{-1} (Tmol CH_4)$^{-1}$).

Numerically, as 4 H atoms escape, we subtract a "CH_4" from the methane reservoir of our model atmosphere. The dominant pathway for the remaining carbon atom (in both anoxic and oxic atmospheres) is to form CO_2 by a series of photochemical reactions, which acts as a sink for atmospheric O_2. Because of this, we must also subtract one O_2 redox equivalent from our atmospheric oxygen reservoir. However, since one mole of methane ordinarily consumes two moles of O_2 (the reverse of equation (3.7)), the net effect is that the Earth system has gained an O_2 equivalent somewhere by hydrogen escape. Schematically, the overall effect is represented by $2O_2 + CH_4 \rightarrow CO_2 + 4H\uparrow_{space} + O_2$ (Catling *et al.*, 2001). Thus, planetary oxidation via hydrogen escape is indirect. The H that escapes was ultimately derived from an oxidized form of hydrogen (H_2O, OH in silicates, or hydrocarbons). The oxidation occurs in the original reservoir when the reduced hydrogen-bearing gas was released by oxidizing the surroundings, and is made permanent and irreversible if the resulting hydrogen atom escapes to space.

Reducing gas emanating from the solid Earth does not necessarily give rise to hydrogen escape directly but enables biogenic methane to serve as the source for hydrogen escape in the following subtle way. In the Archean, the reductant flux supplied by metamorphism or volcanism consumes oxygen that is co-generated with methane in 2:1 ratio via equation (3.7), so that the methane flux is no longer redox-balanced by oxygen equivalents. Consequently, methane is able to exist at higher abundance in the atmosphere and promote enhanced hydrogen escape according to equation (3.12).

There has been a recent suggestion (Tian *et al.*, 2005) that hydrogen escape on the pre-biotic earth might have been slower than that predicted via diffusion-limited H escape. As our chapter deals with the consequences of a microbially inhabited Earth, the prebiotic atmosphere has no direct relevance to our argument. If, however, hydrogen escape was slow for a prolonged period on early Earth, the only way to quantitatively reconcile the observed surface oxidation is to preferentially subduct reduced materials to the mantle, a mechanism that runs counter to commonly expressed view of a gradual oxidation of the mantle and crust, and seems difficult in the face of large fluxes of ferric iron to the mantle (Lecuyer & Ricard, 1999). The conclusions of Tian *et al*. (2005) depend on an assumed cold thermospheric temperature and an assumed lack of importance for nonthermal escape. These assumptions have been called into question (Catling, 2006), and the results are inconsistent with other computations of a hot thermospheric temperature on early Earth (Kulikov *et al.*, 2006) and similar computations of hydrogen escape that allow atomic hydrogen to escape(Watson *et al.*, 1981). This complicated issue will certainly be the focus of continued research. Here, we retain the practice of most workers in the field using diffusion-limited parameterization to describe hydrogen escape from the Archean atmosphere.

3.3.4 Equations

The above arguments lead us to expand equation (3.2) into the following coupled time-dependent differential equations for the first-order redox evolution of the atmosphere:

$$\frac{d}{dt}\left[\mathrm{CH_4}\right] = \phi_{\mathrm{CH4}} - k_{\mathrm{eff}}\left[\mathrm{O_2}\right]\left[\mathrm{CH_4}\right] - k_{\mathrm{esc}}\left[\mathrm{CH_4}\right] \quad (3.13)$$

$$\frac{d}{dt}\left[\mathrm{O_2}\right] = 2\phi_{\mathrm{CH4}} - 2k_{\mathrm{eff}}\left[\mathrm{O_2}\right]\left[\mathrm{CH_4}\right] - k_{\mathrm{esc}}\left[\mathrm{CH_4}\right] + F_{\mathrm{B}} - (F_{\mathrm{V}} + F_{\mathrm{M}} + F_{\mathrm{W}}) \quad (3.14)$$

where ϕ_{CH4} is the flux from methanogenic microbial communities to the AOB, k_{eff} is the effective rate constant for the kinetic destruction of O_2 and CH_4 discussed in section 3.3.2, $F_E=k_{esc}$ $[CH_4]$ is subtracted from both equations as discussed in section 3.3.3, and F_B, F_V, F_M, F_W are the reductant fluxes due to burial of organic carbon, volcanism, metamorphism, and oxidative weathering defined previously. It is important to remember that our fluxes are reductant fluxes, not total fluxes of all species, so that, for example, F_V is the total amount of reducing gases (i.e. H_2, H_2S, CH_4, CO, etc.) from volcanoes, and does not include the much more prevalent (by mole) gases (H_2O, CO_2) that do not consume O_2.

3.4 Analytic solutions of equations in the ancient and modern limits

In steady state (i.e. $d[CH_4] = d[O_2] = 0$), we can eliminate ϕ_{CH4} between equations (3.13) and (3.14) to find that:

$$F_E + F_{\mathrm{B}} = F_{\mathrm{V}} + F_{\mathrm{M}} + F_{\mathrm{W}} \quad (3.15)$$

This balance allows an atmosphere to remain at a constant redox state, a condition which appears to mostly hold during the Phanerozoic as evidenced by the continuous presence of animals (Knoll & Carroll, 1999) and charcoal (Chaloner, 1989; Wildman *et al.*, 2004), although minor deviations have likely occurred (Berner *et al.*, 2003). The total hydrogen mixing ratio (as H_2 equivalents) above the modern tropopause is ~ 6 ppmv (Harries *et al.*, 1996), yielding a modern hydrogen escape flux of $F_{E,NOW}$ = 0.02 Tmol O_2 yr^{-1} via equation (3.10). Holland (2002) compiles estimates we use to constrain modern values of the remaining parameters in equation (3.15). The rate of O_2 production during organic carbon sedimentation is estimated 10.0 ± 3.3 Tmol yr^{-1} and the rate of O_2 use

during weathering is estimated as 7.5 ± 2.5 Tmol yr^{-1}, so we adopt the nominal values of $F_{B,NOW}$ = 10 Tmol yr^{-1} and $F_{W,NOW}$ = 7 Tmol yr^{-1} for the calculations below. Holland (2002) further estimates $F_{V,NOW}$ = 2.4 ± 1.8 Tmol yr^{-1}, although two recent papers have suggested that this estimate may be too large by an order of magnitude (Hayes & Waldbauer, 2006; Sleep & Bird, 2006). We estimate $F_{M,NOW}$ by combining the two largest quantified fluxes of non-volcanic lithospheric CH_4; global oceanic microseepage of 18 - 48 Tg CH_4 yr^{-1} (Hornafius *et al.*, 1999), and mud volcanoes 6 - 13 Tg CH_4 yr^{-1} (Milkov *et al.*, 2003; Milkov & Etiope, 2005), yielding an estimate of 2.8 - 7.6 Tmol O_2 equivalents yr^{-1}. In section 2.2.2 we independently estimated $F_{M,NOW}$ ~ 2.5 Tmol O_2 equivalents yr^{-1} from the bulk composition of sedimentary rocks. For the sake of rough estimation, we adopt $F_{V,NOW}$ = 1.5 Tmol yr^{-1} and $F_{M,NOW}$ = 1.5 Tmol yr^{-1}, although we note that our estimate of $F_{V,NOW}$ may be too large, $F_{M,NOW}$ too small, and that all these numbers have broad uncertainties.

We examine the steady-state behavior of the modern-day atmosphere by substituting hydrogen escape $F_{E,NOW}$ = 0, and oxidative weathering $F_W = k_W[O_2]^\beta$ into equation (3.15), to yield:

$$[O_2]\Big|_{modern} = \left(\frac{F_{B,NOW} - (F_{V,NOW} + F_{M,NOW})}{k_W} \right)^{\frac{1}{\beta}} \qquad [Tmol] \qquad (3.16)$$

where we define k_w = 0.021 $Tmol^{2/3}$ yr^{-1} from equation (3.16) using the modern values of the parameters. We see that modern oxygen levels are set numerically by the imbalance between F_B and (F_V+F_M), are modulated by oxidative weathering constants, and have no direct dependence on CH_4 levels.

Solving equation (3.13) for [CH_4] in the modern limit (i.e. $F_E \rightarrow 0$) yields:

$$[CH_4]\Big|_{Modern} = \frac{\phi_{CH4}}{k_{eff}\,[O_2]} \qquad [Tmol] \qquad (3.17)$$

Equation (3.17) is analogous to equation (3.8) defining k_{eff}, which predicts 1.7ppm CH_4 when the other modern parameters cited in section 3.3.2 are substituted. The direct applicability of equation (3.17) to the Phanerozoic is somewhat complicated given our choice of an atmospheric k_{eff} for the entire AOB reservoir, which effectively couples the redox state of the atmosphere to that of the ocean. Equation (3.17) exhibits constant behavior of ~18000 Tmol CH_4 (~10^{-4} bar) above oxygen concentrations of approximately 1.8×10^5 Tmol O_2 (10^{-3} bars) for ϕ_{CH4}=400 Tmol yr^{-1}, given the functional dependence of k_{eff} as described in section 3.3.2 and shown in Figure 3-3. These predicted levels of O_2 and CH_4 (10^{-3} and 10^{-4} bar respectively) are perhaps relevant to the Mesoproterozoic, given that this estimate effectively releases the total flux of seafloor methane directly into an oxic atmosphere, a physical condition more likely to have occurred in a stratified Mesoproterozoic ocean (Anbar & Knoll, 2002).

During the Archean we assume that oxygen concentrations were low and hence the oxidative weathering flux (F_W) was negligible, as witnessed by the redox state of detrital minerals and the absence of continental redbeds (Holland, 1984, p. 277-332). Substituting the definition of the escape flux F_E (equation (3.12)) and F_W = 0 into equation (3.15) we find that:

$$\left[CH_4\right]\Big|_{Archean} = \frac{(F_V + F_M) - F_B}{k_{esc}} \qquad \text{[Tmol]} \qquad (3.18)$$

From comparison with equation (3.16) we see that in the steady-state ancient and modern limits oxygen and methane have opposite approximately-constant behavior dictated by the numerical values of the fluxes of organic carbon burial, volcanism, and metamorphism, and are both independent of the level of the trace redox gas. We refine the estimate in equation (3.18) by rearranging algebraically, and substituting the numeric value of k_{esc} converted from Tmol to bars using equation (3.11):

$$\left[CH_4\right]\Big|_{Archean} = 1.5 \times 10^{-4}\left(F_{V,NOW}\frac{F_V}{F_{V,NOW}} + F_{M,NOW}\frac{F_M}{F_{M,NOW}} - F_{B,NOW}\frac{F_B}{F_{B,NOW}}\right) \qquad \text{[bars]} \quad (3.19)$$

If we make the first order assumption that F_B has remained constant over Earth history (i.e. F_B=$F_{B,NOW}$), we can derive a rough estimate for the CH_4 content of the Archean atmosphere. Making this assumption and substituting the given numeric values for $F_{V,NOW}$, $F_{B,NOW}$ and $F_{M,NOW}$, we find:

$$\left[CH_4\right]\Big|_{Archean} = 1.5\times10^{-3}\,\text{bar}\times\left(\frac{3}{20}\left(\frac{F_M}{F_{M,NOW}}+\frac{F_V}{F_{V,NOW}}\right)-1\right) \qquad (3.20)$$

an estimate applicable only if the combined Archean volcanic and metamorphic reductant fluxes are ~7 times higher than modern values, agreeing with our earlier theoretical conclusion that enhanced reductants fluxes are required in order to maintain an anoxic atmosphere. If, as we argue is theoretically possible in section 3.5.1, F_M may have reached 20 times its current value, equation (3.20) predicts steady state CH_4 partial pressures of 0.003 bar or 3000 ppmv, even in the absence of mantle redox evolution. This simple analytic estimate agrees surprisingly well with the results of sophisticated photochemical models of the Archean atmosphere (Zahnle, 1986; Kasting & Brown, 1998). In addition, equation (3.20) predicts that CH_4 concentrations will decrease with decreasing F_M + F_V which is compatible with the notion that the left hand side of equation (3.13) will be negative as long as F_E is large (i.e. throughout the Archean), so we expect CH_4 concentrations should consistently drop in quasi-steady state through the Archean.

An analytic estimate for Archean oxygen levels is obtained by solving equations (3.13) and (3.14) in steady state and eliminating $k_{esc}[CH_4]$ to obtain an alternate steady state solution:

$$0 = \phi_{CH4} - k_{eff}\,[O_2][CH_4] + F_B - (F_V + F_M + F_W) \qquad (3.21)$$

To obtain an estimate for Archean oxygen levels, we take F_W=0 and solve equation (3.21) for $[O_2]$ to find:

$$[O_2]\Big|_{Archean} = \frac{\phi_{CH4} + F_B - (F_V + F_M)}{k_{eff}\,[CH_4]} \qquad [\text{Tmol}] \qquad (3.22)$$

Assuming $\phi_{CH4} \gg F_B - (F_V + F_M)$, taking a representative low oxygen/high methane k_{eff} value of 10^{-3} from Figure 3-3, using ϕ_{CH4} = 400 Tmol yr^{-1}, and converting from Tmol to bar we estimate:

$$[O_2]\Big|_{Archean} \cong \frac{1.2 \times 10^{-11}}{CH_4(\text{bar})} \qquad [\text{bar}] \qquad (3.23)$$

Using the estimate of Archean CH_4 derived above (0.003 bar), equation (3.23) predicts a steady state Archean O_2 value of 4×10^{-9} bar. This simple analytical estimate, which neglects complications such as horizontal and vertical variations, is consistent with results from more detailed photochemical models (Pavlov *et al.*, 2001).

The analytic solutions of our proposed equations (3.13) and (3.14) in the limits of low and high O_2 values support the general theoretical expectations of how the redox state of the atmosphere should evolve, as discussed in section 3.2. In general, our analytic results show that either O_2 or CH_4 will control the redox state of the atmosphere. The amount of the dominant gas in both limits (equations (3.16) and (3.18)) is strongly influenced by the quantity $F_B - (F_V + F_M)$, while the trace redox gas (equations (3.17) and (3.22)) are strong reciprocal functions of the dominant gas. The non-linearity of k_{eff} and F_W preclude simple analytic solutions in the transitional regime, and necessitate a numerical solution.

3.4.1 A definition for the oxic transition: K_{oxy}, the oxygenation parameter

An anoxic atmosphere can be defined as an atmosphere with an excess of hydrogen-bearing gases, such as H_2 and CH_4. Our modern atmosphere is called oxic given that the source of these reducing gases (volcanism, metamorphism) has been overwhelmed by the flux of oxidizing gases from the biosphere. On the ancient earth, however, the

proportions of reductants emanating from the planet were likely larger, and would have overwhelmed the oxygen source, forcing the atmosphere to be anoxic.

To make the above statements quantitative, we follow the approach described in Chapter 2 and motivated by the analytical results above, defining an oxygenation parameter, K_{OXY}, based on the proportion of kinetically active gases in the ground-level atmosphere:

$$K_{OXY} = \frac{F_{SOURCE}}{F_{REDUCED\ SINKS}} \sim \frac{F_B}{F_V + F_M} \tag{3.24}$$

If $K_{OXY} > 1$, the source of free oxygen outweighs the sinks and the atmosphere is oxic. The modern atmosphere has K_{OXY} of 3 when one considers, as we do in this chapter, only the carbon cycle as contributing to F_B. If the sulfur cycle is included (which is necessary for a quantitatively significant exploration of the Proterozoic and Phanerozoic (Holland, 2002)), the modern value of K_{OXY} is ~ 6 (Chapter 2). In our numerical results, we define the "oxic transition" as the first timestep at which $K_{OXY}>1$.

3.5 Numerical Approach

We now define first-order parameterizations of various earth system fluxes. The parameterizations and constants used for our model are summarized in Table 3-1. Extensions to some of these parameterizations are described in section 3.7.1.

3.5.1 Discussion of parameterizations

Reservoirs and redox fluxes in the box model are shown as Figure 3-2. The atmosphere and dissolved gases in the upper ocean equilibrate on timescales of 10-10^3 years (Berner, 2004, p. 3-5). Therefore, we do not resolve changes to the atmosphere/ocean/biosphere AOB reservoir that occur on shorter timescales. Our choice of a coupled AOB reservoir also precludes us from testing hypothetical ideas

regarding the Proterozoic in which the surface and deep ocean existed in separate redox states (Canfield, 1998; Anbar & Knoll, 2002; Huston & Logan, 2004), so we limit ourselves to considering the Paleoproterozoic oxic transition only. The parameterizations that have been described previously are presented in the upper section of Table 3-1. Parameterizations for the evolution of the continental redox state and metamorphic degassing have not been previously been described in the literature. We develop first-order parameterization for these processes below and summarize them in the lower portion of Table 3-1.

Table 3-1 Parameterizations in the biogeochemical model

Below the doubled line are the "enhanced" parameterizations described in section 3.7. The following parameterizations are given in the text and not reproduced here: k_{eff} is shown as Figure 3-3 ; Crustal mixing is shown as equation (3.25), $\Delta fO_2(Fe^{2+}/Fe^{3+})$ is equation (3.27). Numerical values are in Tmol O_2 equivalents yr^{-1} unless otherwise quoted.

Symbol	Name	Parameterization	Discussion
Q	Heat Flow	$(4.5/(4.5 - t))^{\eta}$	A dimensionless analytic approximation to heat flow models calculated from radioactive decay, where η=0.7 (Sleep & Zahnle, 2001). Time t is in Ga from 4.5 to 0 at the present day.
F_B	Burial	$1/5\ k_B\ (F_{CO2,V} + F_{CO2,M})$	We assume that the global O_2 flux due to organic carbon burial has remained approximately 1/5 of the total CO_2 outgassing rate over Earth history since oxygenic photosynthesis appeared, given the approximate constancy of organic carbon and carbon isotope fractionation in sedimentary rocks. $F_{CO2,M}$ is defined in equation (3.29), and we take $F_{CO2,V}=F_{CO2,V,NOW}*Q$. We set k_B = 10/6 (unitless) by substituting $F_{B,NOW}$ = 10 Tmol yr^{-1} (Holland, 2002), $F_{CO2,V,NOW}$=10 Tmol yr^{-1}, and $F_{CO2,M,NOW}$=20 Tmol yr^{-1} (Morner & Etiope, 2002)

Table 3-1 continued

F_E	H escape	k_{esc} [CH_4]	Diffusion limited hydrogen escape is assumed to have acted over Earth history (Walker, 1977, p. 157-163) k_{esc} = 3.7x10^{-5} Tmol O_2 equivalents yr^{-1} (Tmol CH_4)$^{-1}$
F_W	Oxidative Weathering	k_w [O_2]$^{\beta}$	The functional form of oxidative weathering suggested by Walker (1977), p.103-5. Oxidative weathering should be negligible if oxygen concentrations are low, it should be roughly proportional to oxygen levels at intermediate values, and relatively insensitive at high oxygen levels. We use β=0.4 but acknowledge that this parameterization is uncertain e.g. (Holland, 2003), so we investigate multiple values of β in the perturbation analysis. k_w = 0.037 $Tmol^{0.7}$ yr^{-1}.
ϕ_{CH4}	Net biosphere	400 Tmol yr^{-1}	An estimate of the pre-industrial *gross* flux of CH_4 from the degradation of photosynthetic organic carbon by methanogens, assuming the absence of sulfate reducers (see section 3.3.1)

Table 3-1 continued

$\chi_{H_2,CSAT}$	H_2/CO_2 ratio: C^0-saturated metamorphic gases	$a)\ 0.058e^{-1.75\Delta fO_2}$ $b)\ 0.012e^{-2.44\Delta fO_2}$ $c)\ 0.072e^{-0.85\Delta fO_2}$	Analytic fits to average ratio in Figure 3-6a. Curve a) is used for the ΔfO_2 range of [-3.0,-2.2], curve b) for [-2.2,-1.2], curve c) for [-1.2, 2.0]. A linear combination of the respective fits was made to smoothly join the curves in the ranges ΔfO_2=[-2.3,-2.1] and ΔfO_2=[-1.3,-1.1]
$\chi_{CH_4,CSAT}$	CH_4/CO_2 ratio C^0-saturated metamorphic gases	$a)\ 14.08e^{-1.23\Delta fO_2}$ $b)\ 0.06e^{-5.02\Delta fO_2}$ $c)\ 0.194e^{-1.36\Delta fO_2}$	Analytic fits to hybrid curve in Figure 3-6b. Curve a) is used for the ΔfO_2 range of [-3.0,-1.4], curve b) for [-1.4,-0.2], curve c) for [-0.2, 2.0]. A linear combination of the respective fits was made to smoothly join the curves in the ranges ΔfO_2=[-1.5,-1.3] and ΔfO_2=[-0.4,0.0]
$\chi_{H_2,NONSAT}$	H_2/CO_2 ratio: low C^0 activity metamorphic gases	$a)\ 0.383e^{-1.59\Delta fO_2}$ $b)\ 0.025e^{-2.79\Delta fO_2}$ $c)\ 0.187e^{-0.87\Delta fO_2}$	Analytic fits to average ratio in Figure 3-6c. Curve a) is used for the ΔfO_2 range of [-3.0,-2.2], curve b) for [-2.2,-1.2], curve c) for [-1.2, 2.0]. A linear combination of the respective fits was made to smoothly join the curves in the ranges ΔfO_2=[-2.3,-2.1] and ΔfO_2=[-1.3,-1.1]

Table 3-1 continued

$\chi_{CH_4,NONSAT}$	CH_4/CO_2 ratio low C^0 activity metamorphic gases	a) $1.323e^{-2.06\Delta fO_2}$ b) $0.015e^{-4.19\Delta fO_2}$ c) $0.263e^{-0.76\Delta fO_2}$	Analytic fits to hybrid curve in Figure 3-6d. Curve a) is used for the ΔfO_2 range of [-3.0,-1.9], curve b) for [-1.9,-0.8], curve c) for [-0.8, 2.0]. A linear combination of the respective fits was made to smoothly join the curves in the ranges ΔfO_2=[-2.0,-1.8] and ΔfO_2=[-1.0,-0.7]
χ_{H_2}	H_2/CO_2 ratio metamorphic gases	$\frac{\chi_{H_2,CSAT} + \chi_{H_2,NONSAT}}{2}$	To first order, we assume equal contributions from metamorphism of graphite-saturated rocks and rocks with low graphite activity. Representative values include: χ_{H2}(QFM-1) = 0.308, χ_{H2}(QFM) = 0.1296, and χ_{H2}(QFM+1) = 0.054
χ_{CH_4}	CH_4/CO_2 ratio Metamorphic gases	$\frac{\chi_{CH_4,CSAT} + \chi_{CH_4,NONSAT}}{2}$	To first order, we assume equal contributions from metamorphism of graphite-saturated rocks and rocks with low graphite activity. Representative values include: χ_{CH4}(QFM) = 5.053, χ_{CH4}(QFM) = 0.2289, and χ_{CH4}(QFM+1) = 0.086

Table 3-1 continued

F_M	Metamorphic outgassing of Reductants	$k_m Q\left[\frac{F_{C,NV,NOW}}{1+\chi_{CH_4}}(\chi_{H_2}+\chi_{CH_4})\right]$	Assuming the modern crust can be approximated by QFM allows us to calculate k_m = 0.256 (unitless) by setting $F_{M,NOW}$ = 1.5 Tmol yr^{-1}, $\chi_{H2,NOW}$= 0.13, $\chi_{CH4,NOW}$=0.23, Q_{NOW}=1, and $F_{C,TOTAL}$ = 20 Tmol yr^{-1}. Assuming the crust is buffered at QFM+1 yields k_m=0.58. We varied k_m to tune the reference model to transition near 2.4Ga, and adopted a tuned value of k_m=0.34 for the reference model calculations.
F_V	Volcanic Flux of Reductants	$k_V F_{CO2,V}$	We define k_V = 0.15 by setting $\chi_{H2,V,NOW}$ =1 and assuming $F_{V,NOW}$=1.5 Tmol O_2-consuming equivalents yr^{-1} and $F_{CO2,V,NOW}$=10 Tmol yr^{-1}. We account for the maximum allowable mantle redox evolution by multiplying by $F_{CO2,V,NOW}$ by $Q^{1/2}$, a factor which drops by ~2 over the course of Earth history. The use of $F_{CO2,V} = F_{CO2,V,NOW} Q^{1/2}$ is solely a numerical convenience without physical basis in the heat flow, given that oxygen fugacity increases with temperature at a fixed pressure

Table 3-1 continued

$T_{EFF}(t)$	Effective Temperature of the Earth	$T_{EFF,NOW} \times (1/(1+0.0835 * t))^{0.25}$	t in Ga from 4.5 to the present at 0. $T_{EFF,NOW}$ = 255K using modern values of the solar constant with an albedo of 0.3.
a(T)	Ice-albedo effect	T < 273: a=.6 T < 276: a=-.083T + 23.3	Parameterization of linear albedo increase between 3°C and 0°C.
GAT	Global Average Temperature	GAT=$T_{eff}(t)$ + f([CH_4], [CO_2],a(T))	GAT was fixed at 288K in reference model. In the enhanced model, GAT was calculated from the temperature parameterizations of (Caldeira & Kasting, 1992a) and (Kasting *et al.*, 2001), with the ranges of applicability described in the text. The (Kasting *et al.*, 2001) model was specifically calculated for a solar constant of 2.8Ga, so we compute the greenhouse effect as f = $T_{KASTING}(CH_4,CO_2)$ - T_{EFF}(2.8Ga), where T_{EFF}(2.8Ga) ~ 242K.
cyano(T)	Temperature dependent		μ_{MAX}=0.75 (doublings per day), T_{OPT}=28°C, ΔT=28°C, T_{LOW}=0°C, T_{HIGH}=46°C, T_{REF}=1400. The functional form is taken from (Tang *et al.*,

Table 3-1 continued

	growth curve	$\left[\mu_{max} - \mu_{max}\left(\frac{(T_{opt} - T)}{\Delta T}\right)^2\right] \times \mathrm{EXP}\left(-\frac{\lvert T - T_{opt}\rvert^3}{T_{ref}}\right)$	1997). These parameters were chosen to match the composite data described in the caption for Figure 3-12b. cyano(T) formally has units of μ (doublings per day), although we use it in ϕ_{CH4_NEW} as a dimensionless quantity. The "Lovelock" parameterization is parabolic: μ_{MAX}=0.38, T_{OPT}=9°C, ΔT=18°C, without an exponential cutoff.
ϕ_{CH4_NEW}	Temperature dependent biosphere	$\psi \times$ cyano(GAT-273.)	The maximum value of cyano(T) is 0.75 at T=24°C, so ψ=611 Tmol yr^{-1} ensures that $\phi_{CH4} = \phi_{CH4\_NEW}$(18°C) = 400 Tmol yr^{-1} to be compatible with the reference model. Similarily, ψ=1273 Tmol yr^{-1} ensures that the "Lovelock" parameterization is compatible with the reference model.

3.5.1.1 The Crust

We define the boundary between our upper and lower crust by the hydrological horizon below which weathering becomes largely unimportant, as opposed to more traditional definition based on the seismic velocity discontinuity at ~15km. The pore depth (and hence the weathering depth) of the crust is ~ 5 km (Manning & Ingebritsen, 1999) while the average thickness is ~ 41 km (Rudnick *et al.*, 1998). By our definition, the upper crust comprises ~5/41 the mass of the total continental crust (2×10^{25} g), so we take our upper crust to be 2.44×10^{24} g and our lower crust as 1.75×10^{25}g, assuming, for simplicity, a constant mean density.

We are primarily concerned with modeling the "hard rocks" (igneous and high-grade metamorphic) of the continental crust which contain excess ferric iron when compared to mid-ocean ridge basalts (Sleep, 2005a). These rocks are generally older than 2 billion years in age (Patchett & Arndt, 1986; Sleep, 2005b). These hard rocks need to be considered separately from "soft" continental rocks, which are sedimentary rocks. Data regarding the redox evolution of shales and other soft rocks was conceptually incorporated into our parameterization of F_W, but indicators from sedimentary environments (red beds, paleosols, etc.) do not directly help us in quantifying the redox evolution of hard rocks. Our model primarily applies to the late Archean after the evolution of oxygenic photosynthesis, a time period at which most continent growth scenarios have reached the present-day area. For simplicity, we chose not to model continental growth, implicitly assuming a steady-state volume for the continental crust. This simplification is justifiable as the crustal fluid parameterization we develop depends on the redox state of the crust rather than the absolute amount of the crust. Carbon isotopes constrain the oxygen (organic burial) flux only relative to the input flux of CO_2, so the relative sizes of fluxes matter not their absolute amount.

The weight % of iron in the continental crust is ~7% (Taylor & McLennan, 1995), which is similar to the mantle value of 6.26 weight % (McDonough & Sun, 1995). Currently the

amount of iron is not equivalent in the upper and lower crust (less total iron in upper crust than in lower crust), but there is no a priori reason to believe the crust would have formed in this fashion. For simplicity, we assume that 7% of the mass in both initial reservoirs is iron. Ultimately, all components of the crust must have been formed from mantle-derived igneous rocks. Thus, the reference percentage of Fe^{3+} from which we define "excess" Fe^{3+} in the crust is best taken from fresh mantle-derived igneous rock, for which mid-ocean ridge basalt (MORB) is a good standard. As an estimate for the initial portioning between ferrous and ferric iron, we take Fe^{3+}/Fe^{2+} ratio of 0.111 from measurements of fresh MORB which cluster near a common value of 10% ferric and 90% ferrous (Bezos & Humler, 2005). For comparison, the ferric to ferrous ratio in the modern crust is approximately 0.25 as estimated from modern continental basalts (Fe^{3+}/Fe^{2+} = 0.223) (Holland, 1984, p. 52-53) and from Mesozoic granites as Fe^{3+}/Fe^{2+} = 0.25 (Silver & Chappell, 1988; Kemp & Hawkesworth, 2004).

Reductants in the crustal boxes are tracked as Fe^{2+} directly and Fe^{3+} indirectly, fixed by assuming $Fe_{total} = Fe^{2+} + Fe^{3+}$ remains constant in the absence of significant quantities of native Fe^0. Organic carbon (C^0) is also tracked. In this simplified model, once carbon enters the crust, it is converted to Fe^{2+} equivalents. A justification for this simplification is that ferric iron is easily reduced by graphite in metamorphism (e.g., $6Fe_2O_3 + C = 4Fe_3O_4 + CO_2$ in greenschist facies (Melnik, 1982, p. 182)). Two processes change the ferrous/ferric ratio in the crustal reservoirs: the reductant fluxes described in sections 3.2 and 3.3, and geological mixing of the crust via weathering and tectonics. The reductants are tracked as mass concentrations (mass Fe^{2+}/total Fe mass), in variables [U] in the upper crust and [L] in the lower crust. We use mixing times τ_U and τ_L for the upper and lower crust, respectively. Using the average chemical sedimentary load of ~4×10^{15} g yr^{-1} (Garrels & Mackenzie, 1971, p. 120) allows us to estimate τ_U ~ 200-500 m.y. (we adopt $\tau_U \approx$ 400 m.y.) as the time to weather the upper crust and τ_L ~ 4 b.y. for the lower crust. We implement crustal evolution using these time constants as follows:

$$\frac{d}{dt}[U] = \frac{1}{\tau_U}([L] - [U]) + 4 \times (F_B - F_W)$$
$$\frac{d}{dt}[L] = \frac{1}{\tau_L}([U] - [L]) - 4 \times F_M \quad (3.25)$$

Here, the factors of 4 arise because we track all our fluxes in equivalent moles of O_2 that are consumed or produced, i.e. 4 moles of Fe^{2+} are oxidized to Fe^{3+} by one mole of O_2 via:

$$4\,FeO + O_2 \rightarrow 2\,Fe_2O_3 \quad (3.26)$$

Thus, in equation (3.25), a mole of O_2 contributed by the flux of organic burial (F_B) would add a reduced carbon or equivalently 4 moles of ferrous iron to the upper crust. Similarly, reductants released from the lower crust in the metamorphic reduced flux (F_M) sufficient to consume a mole of O_2 in the AOB system would remove 4 moles of equivalent ferrous iron from the lower crust (in reactions such as $H_2O + 2FeO = Fe_2O_3 + H_2$).

3.5.1.2 Redox Evolution of the Crust and Metamorphic Gases

Metamorphism is often considered redox neutral given that typical reactions such as graphite + $2H_2O \rightarrow CO_2 + 2H_2$ provide zero net redox change. However, when some of the resulting hydrogen irreversibly escapes the Earth, the net crustal reaction becomes an effective oxidation of graphite to limestone/marble. Any future metamorphic processing of the resultant crust must release slightly less reducing fluids by redox balance because the crust is now slightly more oxidized. The global reservoir of combined CO_2 is large, so this process would be unlikely to dramatically shift the $\delta^{13}C$ of the crust. We specify the redox evolution of metamorphic gases in a two-step manner. At each timestep, we calculate the oxygen fugacity of the lower crust, and then use that oxygen fugacity to calculate the composition of gases emanating from a C-O-H equilibrium fluid at metamorphic temperatures and pressures.

3.5.1.2.a Specification of Oxygen Fugacity

The complex redox geochemistry of the crust and mantle are often approximated by their similarity to laboratory buffers in pure-phase minerals. The oxygen fugacity is defined as the thermodynamic activity of oxygen in equilibrium with the rock suite (Frost, 1991), and its value is a function of temperature and pressure. We estimate the oxygen fugacity of the crust from high temperature silicate melt experiments that were extrapolated to subsolidus temperatures (Sack *et al.*, 1980). This particular form of the parameterization, which we reproduce as equation (3.27), was recently re-validated for low temperatures and pressures via modern Mössbauer techniques (Partzsch *et al.*, 2004).

$$f_{O_2} = \mathrm{EXP}((\mathrm{Log}(\frac{Fe^{3+}}{Fe^{2+}}) - b / T - c - \Sigma) / a) \quad \text{where } \Sigma = \sum_i d_i X_i \tag{3.27}$$

We take *a*, *b*, *c* and d_i from the experimental data in Table 3 of Sack *et al.* (1980). The summation in equation (3.27) is taken over the main components of the crust (X_i = SiO_2, Al_2O_3, FeO, MgO, CaO, Na_2O, and K_2O), where the X_i are the bulk compositions in weight percent, which we take from values representative of the bulk continental crust (Rudnick & Gao, 2004). While the above parameterization is more directly applicable to the basaltic portions of the continental crust, we adopt it as a representative first-order parameterization for the entire crust, as it encompasses the general direction and magnitude of change recorded in known crustal oxybarometers (Donohue & Essene, 2000).

At a MORB-like Fe^{3+}/Fe^{2+} ratio of 0.1/0.9 = 0.111, Equation (3.27) predicts log(fO_2) of -15.8. At Fe^{3+}/Fe^{2+} of 0.25, Equation (3.27) predicts log(fO_2) of -14.2, implying that the bulk crust might evolve approximately 1.5 log units in fO_2 from its initial to present configuration.

3.5.1.2.b Redox State of Metamorphic Gases

At a given pressure P, temperature T, and oxygen fugacity fO_2, the equilibrium redox speciation of the most important gaseous fluids in the crust (i.e. H_2O, CO_2, CH_4, CO, H_2, O_2) is completely specified (Huizenga, 2001). We used the "species" program from Perple_X modeling package (Connolly, 1990; Connolly & Cesare, 1993) to calculate the C-O-H fluid speciation under a variety of P, T, and fO_2 conditions encountered during metamorphism. We use the hybrid Redlich-Kwong equation of state to calculate the C-O-H fluid speciation as a function of oxygen fugacity in a graphite saturated field, given that average sedimentary rocks show carbonate/reduced carbon ratios of ~4:1 and that uplifted metamorphic rocks contain 2-7% carbon by weight (Wedepohl, 1995). Not all metamorphosed rocks contain graphite, so we also computed a similar series of models with a graphite activity of 0.1.

Figure 3-4 illustrates typical Perple_X outputs, displaying the species fractionation of volatiles versus oxygen fugacity at a pressure of 2kbar and temperature of 500°C for both the graphite saturated and low graphite case. These conditions are typical of high thermal gradient metamorphism in the amphibolite field (Rogers & Santosh, 2004, p. 196). The oxygen fugacities are displayed relative to the Quartz-Fayalite-Magnetite (QFM) buffer calculated by the following equation:

$$\log(\mathrm{QFM}) = 9.0 + 0.09(P - 1)/T - 25738/T \qquad (3.28)$$

where P is the pressure in atmospheres and T is the temperature in Kelvin (Ohmoto & Kerrick, 1977). If the crustal region represented by Figure 3-4 drifted one log unit below QFM in fugacity space, the H_2/CO_2 ratio changes from ~0.001 to ~0.1, while the CH_4/CO_2 ratio changes from 0.13 to 14.3. This implies that while CO_2 is the dominant metamorphic gas today, metamorphosing a more reduced Archean crust may have produced very much more CH_4 and H_2 relative to CO_2.

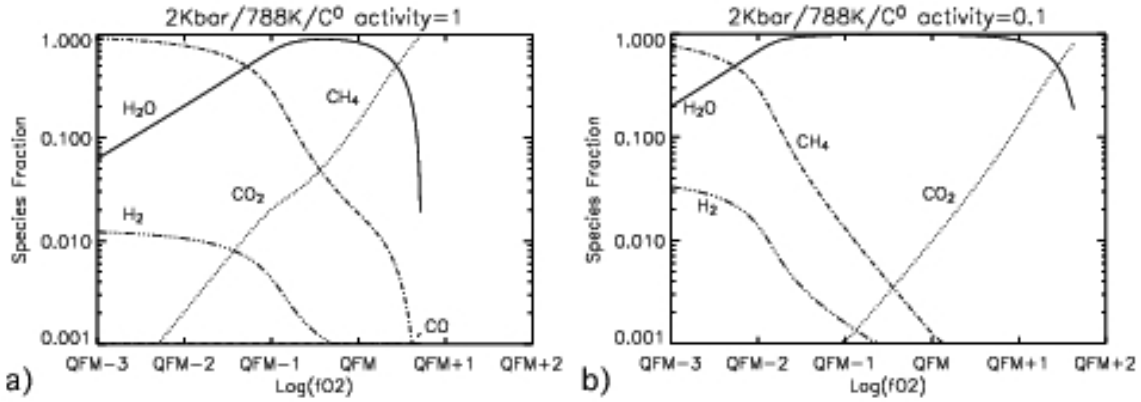

Figure 3-4 Species fraction versus oxygen fugacity for a rock suite at 2000bar and 500°C

a) Calculation was performed using the hybrid Redlich-Kwong equation of state (equation 8 of the Perple_X's *species* package) for a carbon-oxygen-hydrogen fluid equilibrated within a graphite saturated field. 3-4b) Calculation performed under same conditions but with graphite activity reduced to 0.1

To further explore this hypothesis, we constructed a grid of temperature and pressure ranging from 200°C to 800°C (in 100°C increments) and from 2kbar to 8kbar (in 2kbar increments, corresponding to depths of ~5-35 km.) Fluid speciation was calculated for each of these (P/T) grid points for a variety of oxygen fugacities, allowing specification of the H_2/CO_2 and $(CH_4+CO)/CO_2$ (hereafter referred to as CH_4/CO_2) ratios as function of P,T, and ΔfO_2, where ΔfO_2 is the oxygen fugacity relative to QFM for the given P/T conditions as specified by equation (3.28).

We calculate speciation ratios of $\chi_{H2} = H_2/CO_2$ and $\chi_{CH4} = CH_4/CO_2$ for low thermal gradients associated with subduction of oceanic lithosphere, medium thermal gradients associated with continental collisions, and high thermal gradients associated with regional and contact metamorphism (Rogers & Santosh, 2004, p. 196). Figure 3-5 plots χ_{H2} and χ_{CH4} versus ΔfO_2 for each of the 3 standard metamorphic thermal gradients through our P/T grid, with an average result computed via a logarithmic mean at each ΔfO_2 value taken to be representative for each thermal gradient.

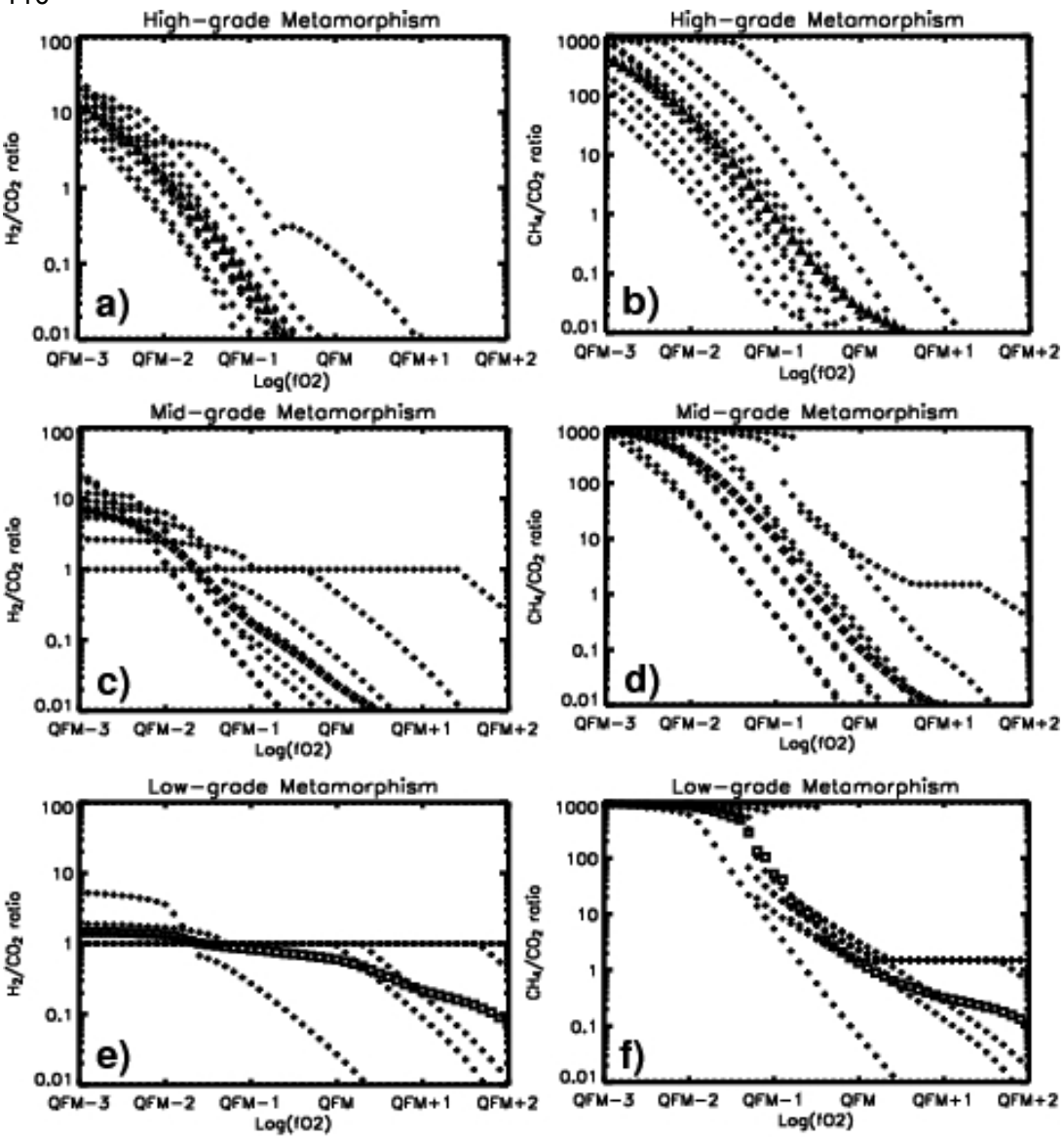

Figure 3-5 H_2/CO_2 and CH_4/CO_2 ratios under various metamorphic conditions

Compilations of the graphite saturated H_2/CO_2 and CH_4/CO_2 ratios under various metamorphic conditions as a function of oxygen fugacity. Similar compilations were made for the low graphite activity case, but are not displayed. 3-5a-b) H_2/CO_2 and CH_4/CO_2 ratios for the following [P,T] grid of conditions encountered in high-grade metamorphism, in units of kilobars and °C: ([2,400], [2,500], [2,600], [2,700], [2,800], [4,600], [4,700], [4, 800], [6,700]). 5c-d) H_2/CO_2 and CH_4/CO_2 ratios for the following [P,T] conditions encountered in medium-grade metamorphism ([4,300], [4,400], [4,500], [6,500], [6,600], [6,700], [8,600], [8,700]). 5e-f) H_2/CO_2 and CH_4/CO_2 ratios for the following [P,T] grid of conditions encountered in low-grade metamorphism ([4,200], [6,200], [6,300], [6,400], [8,300], [8,400], [8,500]). Inferred conditions were taken from Figure B.3 in Appendix B of (Rogers & Santosh, 2004, p. 196). In each [P,T] pair, the oxygen fugacity was normalized to QFM via Equation (3.28). The bold symbols on each plot (Medium-grade – diamonds, Low-grade – squares, High-grade – triangles) are a weighted logarithmic mean of all the points. These means are re-displayed on Figure 3-6.

A complete solution to the problem of metamorphic gas fluxes would entail quantification of the relative importance of each of these three forms of metamorphism throughout Earth History, along with a specification of the evolution in bulk composition of metamorphosed rocks. Here, we make the first order assumption that the proportions of metamorphic rock types in the available geologic record serve as proxy for the relative proportions of thermal gradients encountered. Wedepohl (1995) compiled average compositions of both Archean and modern continental crust, and estimated the vertically-averaged rock types of various metamorphic grades as 6.3km of low and medium grade metamorphic rocks (gneiss, schist, amphibolite, and marble) and 19.1 km of high grade metamorphic rocks (sum of felsic and mafic granulites). We therefore take 6.3/25.4 ~ 25% of metamorphism to occur under low and medium grade conditions (assumed equally distributed) and 75% of total metamorphism to occur under high grade conditions. In Figure 3-6, we compile the average results from each metamorphic gradient, and weight them by the above proportions. Analytic fits to these results are used in the numerical model are presented in Table 3-1.

We have shown in Figure 3-6 how the speciation ratios $\chi_{H2} = H_2/CO_2$ and $\chi_{CH4} = CH_4/CO_2$ of crustal metamorphic fluids vary as a function of oxygen fugacity. The final piece in our prescription of F_M is a description of the total flux of non-volcanic CO_2 through the crust ($F_{CO2,M}$) and how it may have evolved with time. Mörner & Etiope (2002) estimate a "conservative" lower limit for non-volcanic total carbon degassing of $F_{C,NV,NOW}$ ~ 17 Tmol yr^{-1}. We make the first-order assumption that the present measured levels of carbon degassing represent a steady-state flux of carbon bearing fluids throughout the crust and adopt $F_{C,NV,NOW}$ =20 Tmol yr^{-1}. Overall planetary thermal gradients were higher in the past, as indicated by the absence of Archean blueschists, which are metamorphic rocks that form under conditions of low temperature and high pressure, and the rarity of Phanerozoic komatiites (Sleep & Windley, 1982; Christensen, 1985). We account for this in our model by multiplying F_{C,NV_NOW} by the heat flow parameter Q described in Table 3-1.

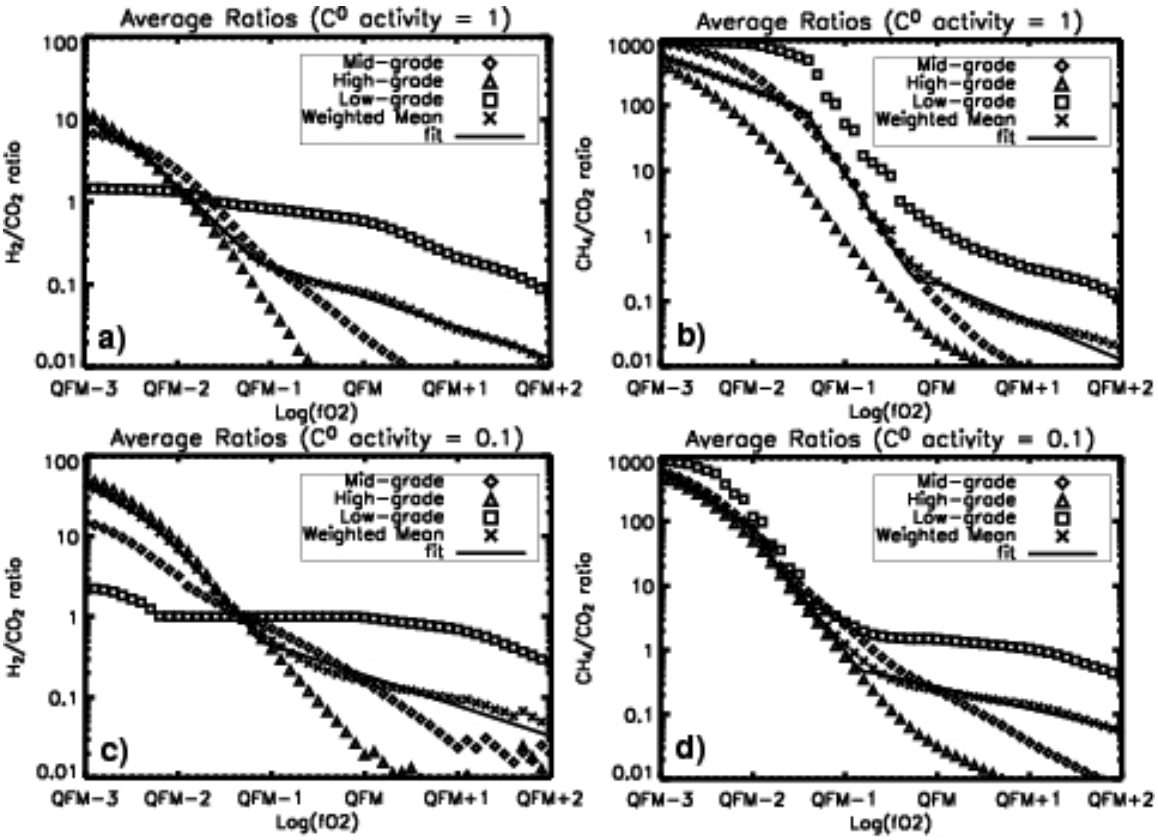

Figure 3-6 Compilation of average results displayed in Figure 3-5

A weighted linear mean (crosses) at each ΔfO_2 was calculated by assuming 75% high-grade metamorphism (triangles), 12.5% medium grade metamorphism (diamonds), and 12.5% low grade metamorphism (squares). Analytic fits to the data are shown as a solid line and are quantified in Table 3-1. Figures 3-6a and 3-6c show χ_{H2} (=H_2/CO_2) ratio for the graphite saturated and low graphite activity case respectively, while 3-6b and 3-6d show χ_{CH4} (=CH_4/CO_2) ratio for the graphite saturated and low graphite activity case.

Fixing $F_{C,NV,NOW}$ as the total flux of C-bearing fluids allows us to define:

$$F_{CO_2,M} = Q\left[\frac{F_{C,NV,NOW}}{1+\chi_{CH_4}}\right] \quad \text{and} \quad F_{CH_4,M} = Q\left[\frac{\chi_{CH_4}F_{C,NV,NOW}}{1+\chi_{CH_4}}\right] \tag{3.29}$$

which allows us to complete our description of F_M:

$$F_M = k_m(\chi_{H_2} F_{CO_2,M} + F_{CH_4,M}) = k_m Q\left[\frac{F_{C,NV,NOW}}{1+\chi_{CH_4}}(\chi_{H_2} + \chi_{CH_4})\right] \quad (3.30)$$

where k_m is a unitless constant which we use as a tuning parameter. End-member values for k_m of 0.25 and 0.6 are estimated in Table 3-1. We briefly note that radiolytic production of H_2 from H_2O might promote non-negligible crustal CH_4 fluxes from the Precambrian shield (Onstott *et al.*, 2006). This process would oxidize the crust while adding additional reductants to the F_M flux.

3.5.2 Numerical Code

The equations are solved via the reverse-Euler method with variable time-steps selected to ensure that the (discarded) non-linear terms would have contributed less than 1% of the computed solution (Walker, 1990a). At each step, time-dependent changes are made to the fluxes, allowing the solution to evolve as a succession of quasi-steady states. We compute solutions from 4.0 Ga to the present, but do not consider our parameterizations as representative prior to the end of the late heavy bombardment era at 3.8 Ga. The fluxes are driven to modern day values at time = 0, but the computed solutions after the oxic transition are not likely to be as accurate given that we do not incorporate the sulfur cycle. A similar model that considers the sulfur cycle will be necessary to model the evolution of redox state during the Proterozoic.

3.6 Model Results

First, we describe results using our parameterization of F_M described in section 3.5.1. We subsequently refer to these results as the reference model. A generic feature of any box model is tunable parameters. Choices of tunable parameters are generally restricted to quantities that are less constrained by available data, with the hope that exploring the available parameter space to arrive at a self-consistent result will help constrain the unknown quantity. Referring to the formulae in Table 3-1, we used the quantities η (the heat flow exponent), β (the oxidative weathering exponent), and k_m (the metamorphic proportionality factor), as our tunable parameters. We used η=0.6, β=0.4

and k_m=0.43 to tune the oxic transition in the reference model to occur near the observed time of 2.4 Ga.

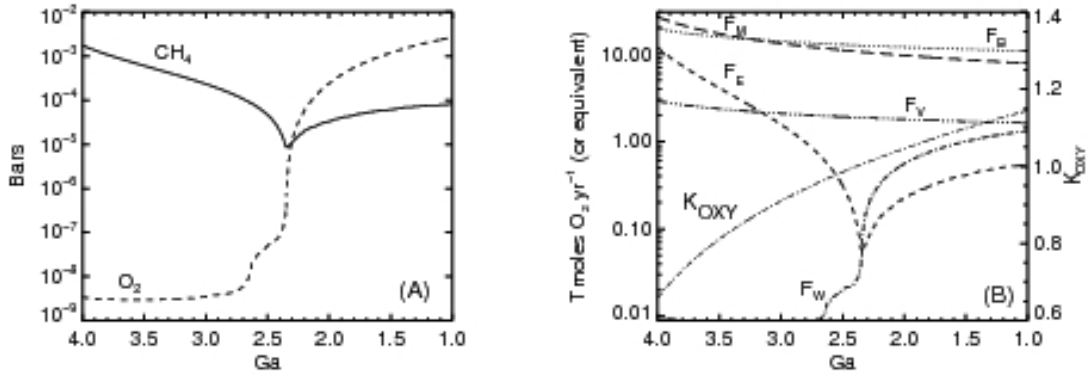

Figure 3-7 Biogeochemical Model Results

a) Evolution of atmospheric gases in the reference model. $[O_2]$ and $[CH_4]$ (in bars) are plotted versus time (in Ga). Interpretation of bars as partial pressures requires the further assumption that Earth's atmospheric pressure has remained constant, which may or may not be the case depending on the nature of the ancient nitrogen cycle. The behavior of the trace gas (i.e. O_2 prior to GOE and CH_4 after) is driven by the structure of $k_{eff}(O_2,CH_4)$ as shown in Figure 3-3. b) Evolution of Earth's major redox fluxes, shown on the logarithmic left side axis in Tmol yr^{-1} normalized as O_2 equivalents. The right side axis is a linear scale for the trace of K_{OXY}. In the reference model, K_{OXY} evolves from 0.7 at 3.8Ga to 1.15 at 1 Ga, first becoming greater than 1 at $T_{OXY,RM}$ = 2.425 Ga.

The main results of the reference model are illustrated in Figure 3-7. Figure 3-7a shows the evolution of atmospheric CH_4 and O_2, plotted in bars versus time in Ga. As expected from the theoretical arguments and analytical results in sections 3.3 and 3.4, the numerical model predicts an early atmosphere dominated by reducing gases with O_2 as a trace gas, followed by a geologically rapid transition to an atmosphere with significant O_2 and lower CH_4. Figure 3-7b shows the computed fluxes which drive the solutions of equations (3.13) and (3.14) shown in Figure 3-7a. Hydrogen escape (F_E) was a quantitatively important redox flux early in the reference model, with integration under the F_E curve in Figure 3-7b yielding ~4.8 billion Teramoles of oxygen equivalents added to the AOB prior to the oxic transition. In this same time period, 96.2 billion Tmol of oxygen equivalents are released from the crust by metamorphic degassing, while 93.1 billion Tmol are added via organic carbon burial, yielding a net gain in the crustal system of 1.7 billion Tmol oxygen equivalents. The self-consistent computation of 1.7 billion

Tmol of net oxidation in the crustal reservoir, although subject to large uncertainties, is consistent with the previously mentioned compilations of oxygen excess in “hard” igneous and high-grade metamorphic crustal rocks (Catling *et al.*, 2001; Sleep, 2005a). Crustal oxidation slowly reduces the flux of reduced species in metamorphic gases, which in turn reduces the magnitude of reductants (F_M) from the metamorphosed crust, eventually driving $K_{OXY} > 1$ and a transition to an oxic atmosphere. By the time of the transition, hydrogen escape (F_E) is a minimal redox flux, given the drop in CH_4 levels. At this point, the steady-state CH_4 mixing ratio is set by the approximate balance between the ground level flux and atmospheric destruction (see equation (3.13) with $F_E \rightarrow 0$) so that $\phi_{CH4} \approx k_{eff}[O_2][CH_4]$ at the time of transition. In addition, oxidative weathering of the crust (F_W) has not yet become a significant redox term, so the quantitatively important fluxes at the time of the transition are F_B, F_V, and F_M. These fluxes are numerically much smaller than the gross flux of methane ϕ_{CH4}, or its oxidation loss, but it is the difference between F_B and $F_V + F_M$ that appears to matter for the redox evolution of the atmosphere.

Restricting attention to the organic burial and outgassing reductant fluxes at the time of the oxic transition, condenses equation (3.14) for the evolution of atmospheric oxygen to:

$$\frac{d}{dt}[O_2]\Big|_{Trans} \sim F_B - (F_V + F_M) \tag{3.31}$$

so the slight imbalance between the production of oxygen via organic carbon burial and the reducing gases from the solid planet is of critical importance. The atmosphere will transition from anoxic to oxic (i.e from $K_{OXY}<1$ to $K_{OXY}>1$) when F_V+F_M becomes quantitatively smaller than F_B. Assuming a constant F_B, the timing of the oxic transition is thus set by geological processes and the preceding history of enhanced hydrogen escape, which together regulate the decrease in reducing gases from volcanoes and metamorphism. The reference model is a numerically self-consistent example of this

behavior including both crustal redox evolution and limited mantle redox evolution as constrained by available data.

To further examine the issues surrounding the timing of the oxic transition, we performed a series of perturbations to the reference model. Our first experiment, shown as Figure 3-8 consisted of numerically setting hydrogen escape (F_E) to 0. With this change, the reference model did not undergo an oxic transition, remaining in a Titan-like methane-rich atmosphere for over 4 billion years, despite levels of oxygen input from organic burial similar to modern levels. This result provides numerical support to the earlier statement that there is no conflict between the co-existence of modern levels of oxygen production and an anoxic atmosphere. In this experiment, Earth is unable to permanently lose the reductants that emanate from the solid planet, so the planet as a whole does not evolve in redox state. Hydrogen escape is a physical process which acts on terrestrial planets, so we do not present Figure 3-8 as being representative of a physically realistic Earth, but merely as a confirmation of the concept that hydrogen escape is vital to irreversibly oxidize a planet.

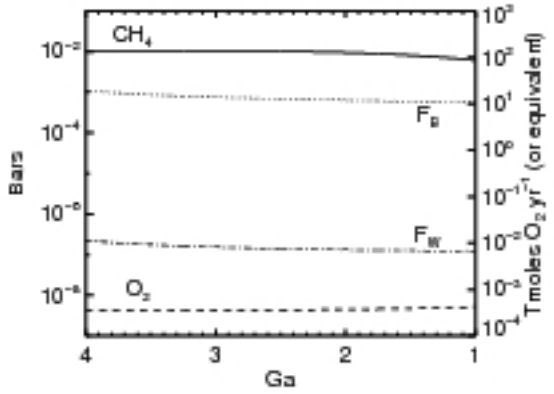

Figure 3-8 An experiment with the reference model in which hydrogen escape, $F_E(t)=0$

Atmospheric oxygen remains negligible despite a constant flux of organic carbon burial F_B = 10 Tmol yr^{-1}, over Earth history. O_2 and CH_4 gases map to the left axis, while the F_B and Fw fluxes map to the right axis.

We next examined the effect of decreasing the amount of reducing gases emanating from the crust. Our first experiment was to assume that metamorphic outgassing (F_M)

was a less important as a redox flux over Earth history. Figure 3-9 shows that reducing our numerical parameterization of F_M by decreasing k_m by 33% causes our reference model to transition within 10^8 years. This transition occurs when $F_B > F_E$ and the CH_4 concentration (and hence F_E) drops precipitously from its assumed initial condition without the influx of reductants from the solid planet. Figure 3-9 also shows an experiment in which F_M was decreased by 10% from the reference model values. In this experiment, we see that the amount of crustal degassing serves to significantly vary the timing of the oxic transition, and that quasi-steady state CH_4 levels increase with increasing F_M, as predicted by our analytical result in equation (3.20).

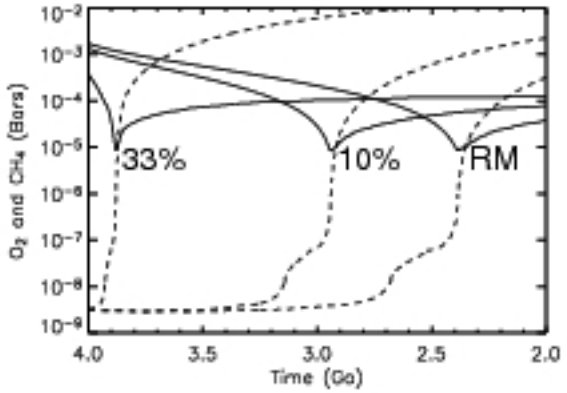

Figure 3-9 Effects of changing F_M

Modeled traces of atmospheric composition of [CH_4] (solid lines) and [O_2] (dashed lines) in bars versus time, as in Figure 3-7a. The right-most set of lines, marked by "RM", are the [CH_4] and [O_2] curves from the reference model. The middle set of lines, marked by "10%", are the gas curves resulting from decreasing the numerical parameterization of F_M in the reference model by 10%. The left-most set of curves represents the gas curves that result from decreasing F_M by 33%.

We next explored changes to k_{eff}, our parameterization of the effective destruction of CH_4 by O_2. Figure 3-10 shows that k_{eff} strongly affects the steady-state level of whichever gas is currently a trace gas (O_2 prior to the transition, CH_4 after), as well as the sharpness of the transition in time, but has no effect on the timing of the transition. The primary reason for this is that the appearance of atmospheric ozone is the driving factor in changing our atmospheric parameterization, and ozone does not begin to significantly appear in Earth's atmosphere until $O_2 >\sim 10^{-5}$ bar (Kasting, 1979). In the reference model, K_{oxy} first becomes larger than 1 at ~2.4 Ga, but the transition from O_2

to CH_4 dominated (by number) takes another 5 million years. The crossover point occurs at ~2.35 Ga at which point ~1 $x10^{-5}$ bar of each gas exist in our model atmosphere. It is only after this crossover point that the effects of ozone production on CH_4 levels will become important. However, the exact speed of the transition in our reference model should not be taken as realistic since the model is merely an idealized redox representation and does not include feedbacks on the climate, biosphere or ocean chemistry (e.g., the increase in sulfate levels and diminution of methane fluxes to the atmosphere due to methanotrophy). In general, we expect the transition to be even more rapid than modeled.

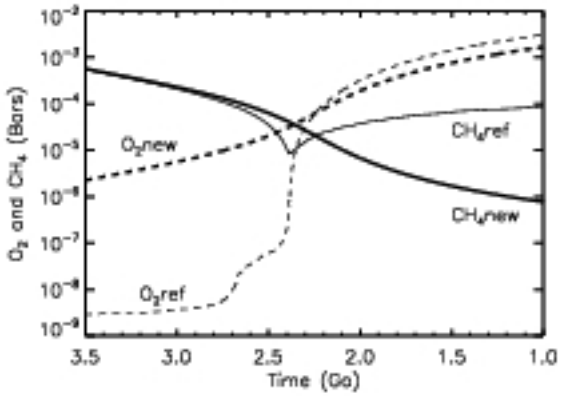

Figure 3-10 Effects of changing effective rate constant

The thick curves are atmospheric gas evolution curves (CH_4 = solid, O_2=dashed) obtained from setting $k_{eff}(t)=10^{-5}$ $Tmol^{-1}$ yr^{-1} in the reference model. For comparison, the reference model curves are plotted as thin curves. The effect on the timing of the transition and on the behavior of the dominant redox gas is negligible. The behavior of the trace redox gas is strongly affected by changes to k_{eff}.

After the oxic transition, the k_{eff} parameterization allows CH_4 levels to reascend to approximately 100 ppm, which is compatible with other predictions of the Mesoproteoroic greenhouse (Pavlov *et al.*, 2003; Kasting, 2005). In addition, oxygen levels approach 1-10% PAL consistent with other constraints on Proterozoic oxygen (Canfield *et al.*, 2000; Brocks *et al.*, 2005). That these results are obtained by attempting to drive the fluxes to modern day values raises the possibility that an additional buffer, likely sulfur, is needed to describe Proterozoic and Phanerozoic redox evolution. CH_4 rises in the Mesoproterozoic due to the complexities of atmospheric

chemistry at intermediate oxygen levels. Ozone begins to form at oxygen levels of 10^{-5} bar, and rises non-linearly with oxygen concentrations (Pavlov & Kasting, 2002). Ozone absorbs solar radiation between 200-320 nm, enhancing the CH_4 lifetime against photolytic destruction in the lower atmosphere, a process that competes with decreasing upper atmosphere CH_4 lifetimes due to the production of OH described in section 3.3.2. These, and the net results of other complicated competing behaviors relating the methane lifetime are captured within our parameterization of $k_{eff.}$ Equation (3.17) predicts that post-transition methane levels are proportional to $1/([O_2] \times k_{eff})$, and k_{eff} drops faster than O_2 rises in the pO_2 range between 10-1000ppmv (Figure 3-3), allowing for increasing CH_4 levels. Net methane fluxes may have decreased after the GOE due to greater respiration of organic matter using O_2 and sulfate, which would decrease the amount of methane predicted for the Proterozoic atmosphere.

Our results regarding the timing of the transition are limited to the statement that the timing of the transition depends on when $F_M + F_V$ drop below F_B in a permanent fashion. Curves similar to Figure 3-7 can be obtained by decreasing parameterizations of F_V or even by increasing F_B while keeping F_M and F_V constant. As an example, Figure 3-11 displays nearly identical results to Figure 3-7, except that F_M was held approximately constant and F_V was arbitrarily made proportional to the square of the heat flow term, Q. Curves similar to Figure 3-9 can be made by decreasing the total volcanic outgassing in a model similar to that of Figure 3-11. In section 3.2, we explained why the decreasing F_V scenario is difficult to reconcile with data on mantle oxygen fugacity or carbon isotopes, although models based on changing fluxes of hydrothermal cations (Holland, 2002; Kump & Seyfried, 2005) partially escape this criticism. The results shown in Figure 3-11 are not internally self-consistent in that the crust becomes significantly reduced by organic carbon burial, although the simplicity of our model rules out further analysis on this issue. While not the only possible solution, we believe that the reference model discussed above (and shown in Figure 3-7) forms the first numerically self-consistent model of Earth's redox fluxes that operates within all available constraints from the geologic record. The model invokes large-scale changes in the proportions of reducing gases from the crust, a hypothesis that requires geochemical tests. The model predicts redox evolution within the hard rocks of the bulk Archean crust. The predictions

of our reference model would be greatly bolstered when a stronger understanding of the both the modern and ancient geothermal, hydrothermal, and metamorphic degassing history of the planet is obtained.

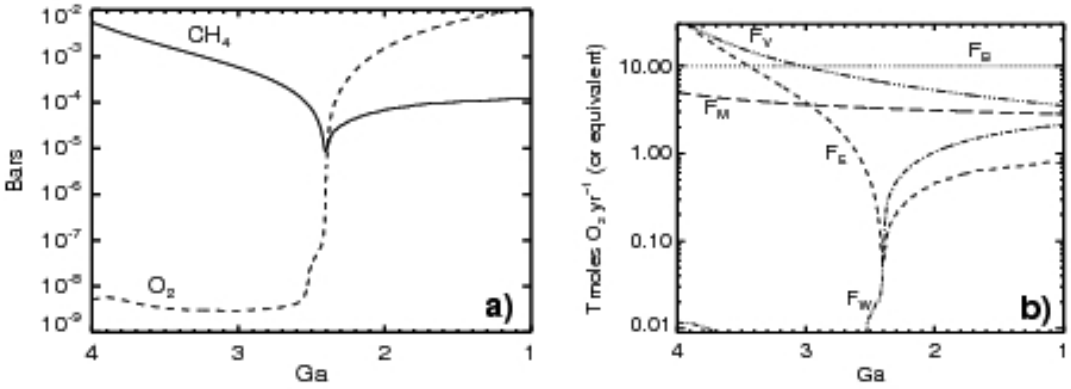

Figure 3-11 Effects of changing volcanic fluxes

a) Evolution of atmospheric gases simulating a oxic transition driven by declining volcanic fluxes. $[O_2]$ and $[CH_4]$ (in bars) are plotted versus time (in Ga). b) Evolution of Earth's major redox fluxes which result in the gas curves shown in 3-11a, shown on the logarithmic left side axis in Tmol yr^{-1} normalized as O_2 equivalents.

3.6.1 Sensitivity Analysis - the timing of the oxic transition

In order to test the sensitivity of our model to its various parameters, we subjected the parameters of reference model to single perturbations leaving all others unchanged. We compute the effect of the perturbation on the timing of the oxic transition by calculating the timestep in the perturbed model, $T_{OXY,PERT}$, at which K_{OXY} (defined by equation (3.24)) first exceeds 1. We compare $T_{OXY,PERT}$ with $T_{OXY,RM}$ = 2.425 Ga, which defines the time of the oxic transition in the reference model. Table 3-2 shows that the perturbations with the largest relative effects relate to the magnitude of metamorphic degassing, which is ultimately tied to the amount of iron in the continental crust. The largest relative perturbation we examined was that of reducing hydrogen escape (k_{esc}) in our reference model by two orders of magnitude, as recently suggested may have occurred (Tian *et al.*, 2005). This change prevents our model from transitioning until 0.06Ga, an effect similar to increasing the amount of iron in the lower crust by a factor of 7. This result supports the general idea that Earth needs to lose reductants in order to oxidize, and shows that any model invoking slow hydrogen escape will likely require preferential

subduction of reduced material to the mantle in order to conserve redox and explain an oxic transition at 2.4 Ga.

Table 3-2 Results from a perturbative analysis of the reference model

In each case, a single variable (first column) was modified by a given factor (second column) and the perturbed reference model was run with only this change. The time of the oxic transition in the perturbed model ($T_{OXY,PERT}$) was computed from the first time step when K_{OXY} = 1 in the perturbed model, and the normalized effect on the timing of the oxic transition is presented in the third column, with positive numbers reflecting an earlier oxic transition and negative numbers reflecting a later oxic transition.

Variable	Factor	$\frac{T_{oxy\_pert}}{T_{oxy\_ref}} - 1$
Initial $[CH_4]$	10x, 1/10x	.003 - .009
Initial $[O_2]$	10x, 1/10x	.0 .0
Initial Iron in Upper Crust	5x 2x 1/2x 1/5x	.025 .016 - .035 -.11
Initial Iron in Lower Crust	5x 2x 1/2x 1/5x	- .743 - .271 .204 .395
k_m	1/1.1 1/1.3 1/1.5 1.1 1.2 1.3	0.23 0.509 0.633 -0.313 -0.692 no trans
β (F_W O_2 exp.)	2x 1/2x	0 0
k_w	10x 1/10x	0 0
η (Heat flow exp.)	2x 1/2	-0.327 0.438
k_{eff}	Many	0
F_E	1/10 1/100	-0.148 -.975

3.7 Climate-Biosphere Feedbacks

We purposefully created a reference model without many tuning parameters. We now discuss some first-order additions to some of the parameterizations, and their influence.

3.7.1 Climate Feedbacks

Perhaps the most glaring omission in the reference model is a lack of surface temperature feedbacks. Methane is a strong greenhouse gas, and the collapse of this greenhouse gas upon the rise of O_2 would significantly affect temperature-dependent processes. Figure 1 of Pavlov *et al.* (2000) predicts that at a fixed CO_2 level in an anoxic atmosphere, a drop from 10^{-3} to 10^{-5} bar of CH_4 would decrease global average surface temperatures by 23K, a change that would likely affect the biosphere. The global temperature drop during the collapse of a methane greenhouse has been implicated in possible "Snowball Earth" events, (Pavlov *et al.*, 2000), which further impacts climate through the ice-albedo feedback.

We constructed a hybrid parameterization for the evolution of global average surface temperature based on atmospheric CH_4 and CO_2 levels from previously published radiative-convective modeling (Caldeira & Kasting, 1992a; Kasting *et al.*, 2001). The parameterizations of Kasting *et al.* (2001) are suitable for $10^{-5}<pCO_2<10^{-2}$ and $10^{-5}<pCH_4<10^{-2}$ in an anoxic atmosphere, while those of Caldeira and Kasting (1992a) are suitable for $10^{-8}<pCO_2<10^{-2}$ in an oxic atmosphere. We correct for solar luminosity evolution (Walter & Barry, 1991) keeping albedo fixed at 0.3 (although see below), and use the parameterization of Kasting *et al.* (2001) if $pCH_4>10^{-5}$, Caldeira and Kasting (1992a) if $pCH_4<10^{-6}$, with a logarithmic extrapolation at intermediate CH_4 levels. Our parameterization is suitable so long as we do not enter a regime in which $pCO_2<10^{-5}$ and $pCH_4>10^{-5}$. The temperature parameterization in the intermediate regime is presented as Figure 3-12a, for a solar luminosity at 2.4 Ga. The temperatures predicted by this parameterization at our computed CH_4 levels are supportive of a generally warm, but not

hot, Archean climate (Sleep & Hessler, 2006). While this is a reasonable first-order parameterization, a full computation using a time-dependent radiative-convective model would be needed to verify the details through the intermediate oxic states (represented here by falling CH_4).

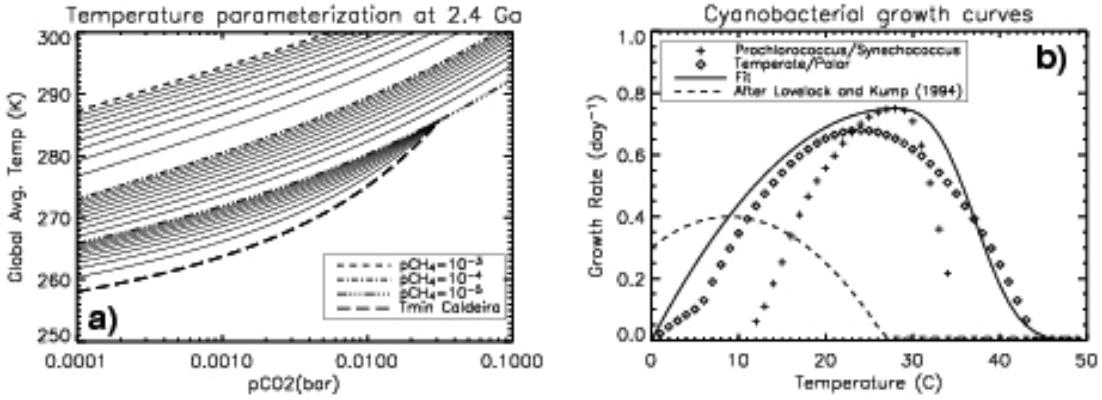

Figure 3-12 Major parametric changes to the reference model

a) A plot of our hybrid temperature parameterization. In the CH_4 range between concentrations of 10^{-6} and 10^{-5} we use a logarithmic weighted combination of the parameterizations of Kasting *et al.* (2001) and Caldeira and Kasting (1992a). Global average surface temperatures are shown for various concentrations of CH_4 and CO_2 computed for the solar constant at 2.4 Ga. The ice-albedo effect is not shown in this figure. b) The temperature dependence of cyanobacterial growth. Growth rates, in doublings per day (μ), are plotted versus temperature. Growth rate data for *Prochlorococcus marinus SS120* (μ_{MAX}=0.63, T_{OPT}=24°C, ΔT=11.5°C, T_{LOW}=12.5°C, and T_{HIGH}=28°C) and *Prochlorococcus marinus MED4* (μ_{MAX}=0.63, T_{OPT}=24°C, ΔT=12°C, T_{LOW}=12°C, and T_{HIGH}=28°C) from Moore *et al.* (1995) were averaged and combined those of *Synechococcus WH8103* (μ_{MAX}=0.75, T_{OPT}=28°C, ΔT=15.5°C, T_{LOW}=12.5°C, and T_{HIGH}=35°C). An average of the 33 temperate cyanobacterial species from (Tang *et al.*, 1997) were fit parabolically (i.e. using the form in Table 3-1 without the exponential cutoff) using μ_{MAX}=0.68, T_{OPT}=24°C, ΔT=20°C. An average of the 27 polar cyanobacterial species from Tang *et al.* (1997) were fit parabolically using μ_{MAX}=0.23, T_{OPT}=20°C, ΔT=20°C. A fit to the data is shown as a solid line, with coefficients given in Table 3-1. A composite cyanobacterial growth curve motivated by Lovelock and Kump (1994) is shown as a dashed line.

Our parameterization of the global average surface temperature drops below 0°C for certain concentrations of CH_4 and CO_2, depending on the solar luminosity. If global ice cover exceeds a certain fraction, a runaway negative feedback might occur in which the increased reflectivity of ice (versus land and ocean) accelerates the cooling of the planet. We modeled this “ice-albedo” feedback with a linear increase in planetary albedo from 0.3 to 0.6 between global average temperatures of 3º and 0º C, where we

take the upper-limit value of 0.6 as a representative "global average" albedo during a low-latitude glaciation event (Warren *et al.*, 2002).

Escape from a "Snowball Earth" at 2.4 Ga is a difficult proposition. The effective temperature of the Earth at 2.4 Ga is about -30ºC, so if the Earth was entirely frozen over due to a collapsing greenhouse, it follows that there needs to be a significant greenhouse in place upon thawing to keep the Earth system from re-freezing. One way of escaping a global glaciation is the volcanic buildup of CO_2 to levels approaching ~0.2 bar (Caldeira & Kasting, 1992b; Kirschvink, 1992), enhancing greenhouse warming to levels which melt the ice, with subsequent resumption of the carbonate-silicate cycle (Walker *et al.*, 1981) leading to massive carbonate deposits and stabilization of the temperature (Hoffman & Schrag, 2002). To parameterize this, we implemented a simple "carbon cycle" which attempts to maintain pCO2 at 0.01 bar by balancing a constant CO_2 source with a sink proportional to $RCO2^{0.5}$, where RCO2 is the ratio of CO_2 to the modern level (Berner & Kothavala, 2001). When global average temperatures fall below 0°C, the sink is turned off, allowing CO_2 levels to rise.

3.7.2 Biosphere-Temperature Feedbacks

We parameterize the temperature-dependent growth rates of cyanobacteria, the primary producers of our biosphere. Growth rates vary as a function of temperature for various genera of cyanobacteria that live at various latitudes. The maximum laboratory growth rates (generally reported in units of doublings per day with symbol μ) for many cyanobacteria occur around between 25°C and 35°C, with experimental data on temperature dependence usually fit by parabolas (Tang *et al.*, 1997) and/or competing exponentials (Moisan *et al.*, 2002). To create a general function for the temperature dependence of cyanobacterial activity, we combined growth rate data (Moore *et al.*, 1995) for the two dominant species of cyanobacteria: *Prochlorococcus* and *Synechococcus*, with the data weighted 1:6.1 by their seasonally averaged abundance (DuRand *et al.*, 2001). These species do not exhibit growth below 10-15°C, so we assume globally colder temperatures would shift the global species balance towards the

polar cyanobacteria, which are generally the dominant microbe in seasonal melt ponds on polar ice sheets (Tang *et al.*, 1997). We add in the averaged growth rates of 24 polar cyanobacteria, combining these with the *Synechococcus/Prochlorococcus* data. Fitting a exponentially damped parabola to the combined data yields the curve shown in Figure 3-12b and given parametrically as the unitless function cyano(T) in Table 3-1. Our cyanobacterial growth curve peaks at 24°C, 6°C warmer than the current global average surface temperature of 18°C that was assumed in the reference model. To account for this we modify our parameterization of ϕ_{CH4} to $\phi_{CH4\_NEW}(T)$= 611 Tmol $yr^{-1} \times$ cyano(T), given that cyano(T_{max})=0.75. This formula was selected so that $\phi_{CH4} = \phi_{CH4\_NEW}$ = 400 Tmol yr^{-1} at 18°C (as in the reference model), and has a new peak value of ϕ_{CH4_NEW} = 544 Tmol yr^{-1} occurring at T_{max}=24°C.

Lovelock and Kump (1994) point out that nutrient availability potentially has a stronger effect on growth rates than temperature. Indeed, satellite observations of chlorophyll shows significantly greater chlorophyll abundance in polar regions compared to the tropics, likely due to enhanced ocean circulation in cooler water bringing ample nutrients from deeper waters. To investigate the possibility that cyanobacterial productivity would be enhanced in a cooler climate, we use a parameterization similar to case 'A' of Lovelock and Kump (1994), shown as a dashed line on Figure 3-12b and described in Table 3-1.

3.7.3 Model results with feedbacks

The effects of incorporating the above parameterizations into our reference model are shown in Figures 3-13 and 3-14, which illustrate our enhanced reference model with both our cyanobacterial growth curve (Case 1) and that of Lovelock and Kump (1994) (Case 2). The effect on the timing of the oxic transition is minimal in both cases (Figures 3-13a and 3-14a), lending strength to the general conclusions presented in section 3.6. In both scenarios, global average temperatures reach their minimum value near the oxic transition (Figures 3-13d and 3-14b), and k_{eff} values (Figures 3-13c and 3-14c) are approximately 10^{-2} (Tmol $yr)^{-1}$ prior to oxic transition, and decrease to ~10^{-6} (Tmol $yr)^{-1}$

after. The primary difference is that Case 1 encounters “Snowball Earth” conditions while Case 2 does not. The reason for this is primarily the effect of the temperature dependence of our coupled biosphere. Figure 3-13f reveals a global minimum of ϕ_{CH4} at the time of transition, while Figure 3-14d shows a global maximum in ϕ_{CH4} at the time of transition. The solar luminosity is low enough at 2.4Ga that the methane produced by the biosphere is vital in maintaining clement conditions. Once the CH_4 greenhouse collapses, CO_2 is the only remaining mobile greenhouse gas (other than the assumed presence of H_2O vapor, which has been accounted for in the temperature parameterizations). The 0.01 bar CO_2 level assumed here cannot maintain temperate conditions at 2.4 Ga without a significant flux of CH_4. The ice-albedo effect is turned on once global average temperatures fall below 3 °C in Case 1 (Figure 3-13d), halting the sink on atmospheric CO_2. CO_2 rises to approximately 0.23 bar (Figure 3-13e) before the greenhouse effect becomes strong enough to melt the ice. Once the ice melts, our simple carbon cycle attempts to re-establish CO_2 levels at 0.01 bar. This drops temperatures below 3 °C, re-establishing a “Snowball Earth”, although a fully temperature-dependent carbonate-silicate feedback (Walker *et al.*, 1981; Berner & Kothavala) might prevent such a re-occurrence. This oscillation in global temperatures repeats a third time, with CH_4 levels (Figure 3-13b) dropping lower in each successive glaciation, until the biosphere regains control after the third event. The carbonate-silicate cycle and ice-albedo feedback represent complex systems that are difficult to model in a coupled AOB system without latitudinal extension, so we believe that the evolutionary details during our “Snowball Earth events” reflect the simplicity of the parameterizations rather than useful predictions of global biogeochemistry. We do note, however, that the temperature dependence of the biosphere can strongly affect the global average temperature, and that recovery from globally glaciated conditions is more likely with a thriving post-melting biosphere.

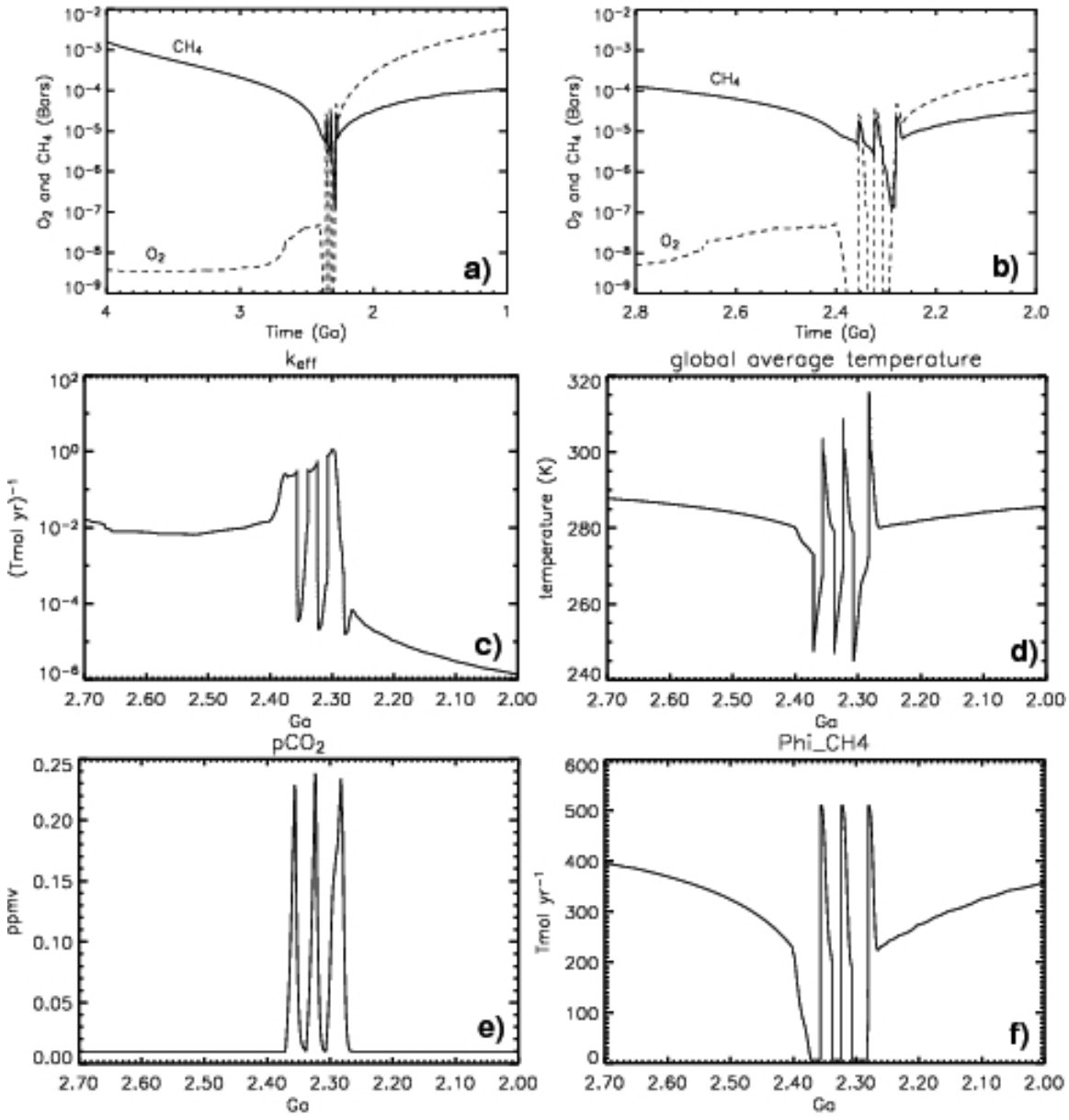

Figure 3-13 Effects of Case 1 temperature-dependent biosphere

Effect on the reference model from introducing the enhancements described in section 3.7: Case 1 Temperature-dependent biosphere. Note the change in time scales between Figures 3-13a and 3-13b-f. 3-13a) Atmospheric gases (bars) versus time: CH_4 – dashed line, O_2 –solid line 3-13b) Same as 3-13a, zoomed in on transitional time period. 3-13c) Atmospheric rate constant, k_{eff} versus time. 3-13d) Global average temperatures (K) versus time 3-13e) Partial pressure of CO_2 (bars) versus time. 3-13f) Gross CH_4 flux into AOB, $\phi_{CH4,NEW}$ versus time.

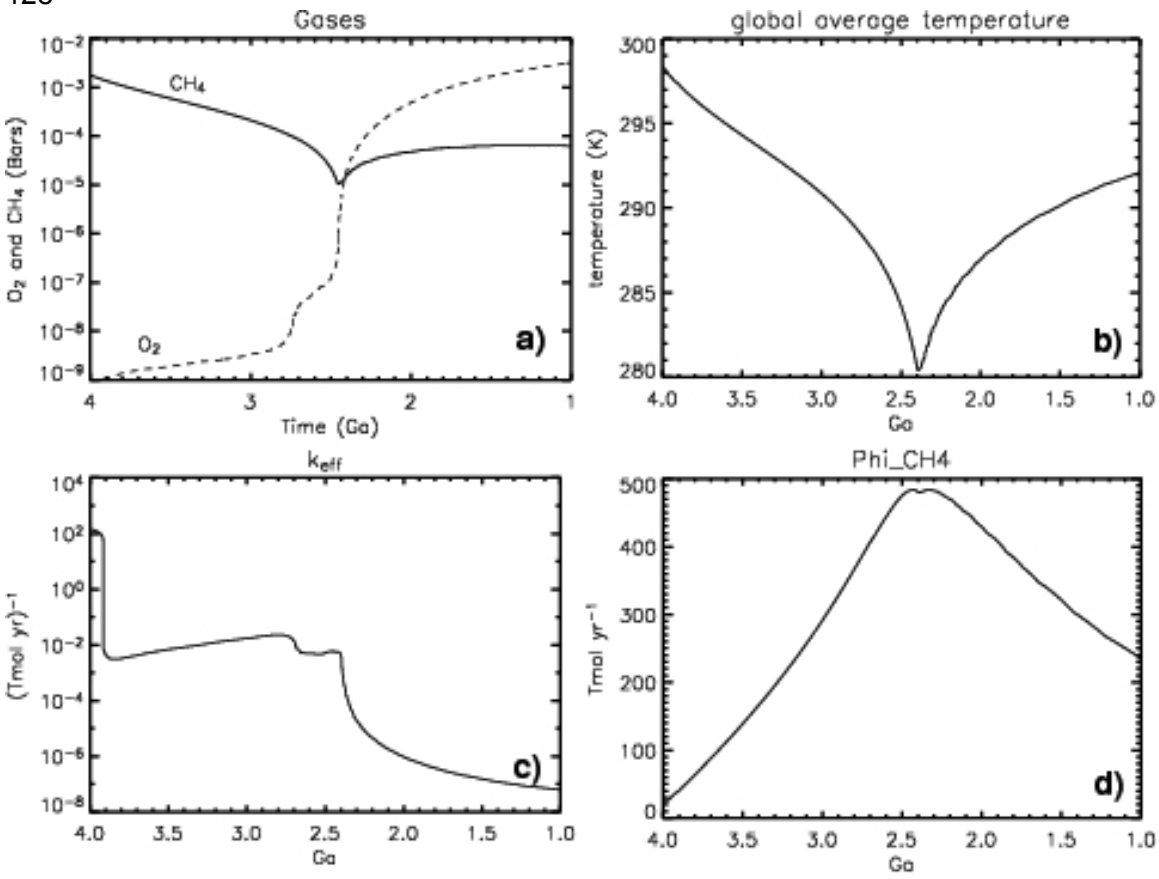

Figure 3-14 Effects of Case 2 "Lovelock" temperature-dependent biosphere

Effect on the reference model from introducing the enhancements described in section 3.7: Case 2 "Lovelock" temperature-dependent biosphere. 3-14a) Atmospheric gases (bars) versus time: CH_4 – dashed line, O_2 –solid line. 3-14b) Global average temperatures (K) versus time. 3-14c) Atmospheric rate constant, k_{eff} versus time. 3-14d) Gross CH_4 flux into AOB, $\phi_{CH4,NEW}$ versus time.

3.8 Discussion

We have presented a quantitative model for the rise of oxygen based on a simplified atmospheric chemistry and evolving redox fluxes in the Earth system. Our numerical fluxes are computed self-consistently from reservoirs that evolve in redox-state to approximately modern values. We find that a geologically rapid oxic transition occurs when the sum of reductant fluxes from metamorphism and volcanic sources ($F_M + F_V$) drops below the flux of organic carbon burial F_B. These results provide numerical support to the hypothesis (Walker *et al.*, 1983; Kasting *et al.*, 1993; Catling *et al.*, 2001;

Holland, 2002) that the geological fluxes of reducing volatiles and their rate of decrease set the timing of the oxic transition.

A perturbation analysis on the reference model shows that the amount of ferrous iron in the continental crust is the most sensitive parameter that affects the timing of the oxic transition. Increasing the modeled amount of iron in the continental crust increases the total mass of Fe^{2+} to be oxidized, which prolongs the amount of time that reducing gases emanate from the continental crust. In this way, the iron content of the crust can be thought of as a buffer that prevents the rise of oxygen even in the face of strong biological oxygen production from associated organic carbon burial. Once the buffer due to crustal iron content is overcome at the GOE, oxygen levels can rise to approximately 1% of present levels. After this point in time, other buffers likely become more important in regulating oxygen concentrations, with most attention focused on the biogeochemical cycles of sulfur and carbon (Canfield & Teske, 1996; Holland, 2002; Rothman *et al.*, 2003). Today, organic carbon burial is mostly balanced by oxidative weathering, where the oxidation of FeO is minor compared to oxidation of carbon and S^{2-}. Our model only contains a basic carbon cycle and does not include a sulfur cycle. Therefore, its predictive ability for the Proterozoic and Phanerozoic eons is limited. Future biogeochemical modeling that decouples the ocean from the atmosphere and considers carbon, sulfur, and iron cycling is needed to quantitatively explore the evolution of Earth's redox state during the second half of its history.

Another generic result of our model is that the oxic transition is inherently non-linear. At the low CH_4 concentrations predicted once oxygen levels begin to rise, the loss of CH_4 is quantitatively balanced by atmospheric oxidation so that the term $k_{eff}\,[O_2][\,CH_4] \approx$ constant. However, k_{eff} depends on the atmospheric reservoir of oxygen $[O_2]$, and decreases with a thicker ozone layer. This causes O_2 to rise relatively sharply because O_2 losses decrease as O_2 increases, producing a positive feedback. Consequently, the GOE should occur relatively quickly in geologic time. Recent geochemical evidence is consistent with this idea, as the South African craton reveals the disappearance of mass-independent sulfur isotope fractionation within ~100 Myr between 2.45 and 2.33

billion years ago (Bekker *et al.*, 2004). At the same time, tropospheric CH_4 levels are reestablished to ~100 ppmv in our model in the Mesoproterozoic because the ozone layer shields tropospheric CH_4 from destruction. Thus, hydrogen escape to space continues as a persistent flux in the Proterozoic and could conceivably be implicated in a second rise of O_2, assuming a further buffer in the Earth system is overcome, perhaps associated with sulfur.

Hydrogen loss to space is a fundamental characteristic of terrestrial planets (Kasting & Catling, 2003), so all Earth-mass planets should become more oxidized with time as a consequence of this physical effect. Indeed, hydrogen loss is the widely accepted explanation for the surface oxidation states of Venus and Mars (Hunten, 1993). The surface materials of an abiotic planet with only F_V, F_M, and F_E acting will certainly oxidize as a result of these physical processes. But the presence of oxygenic photosynthesis and methanogenesis on Earth combined to significantly decrease the time to the oxic transition by a) enhancing hydrogen escape via high levels of CH_4, and b) adding free oxygen into the Earth system. Indeed, for terrestrial planets in the habitable zone of their stars, substantial free O_2 buildup appears to require a biogenic source such as oxygenic photosynthesis (Kasting, 1997; Catling *et al.*, 2005). We have found that the fundamental timing of the transition from reducing to oxidizing conditions on a microbially-inhabited Earth depends on the reductant inventory in the solid planet.

A final, more speculative, interpretation of our results relates to the proposed NASA and ESA missions (currently named Terrestrial Planet Finder (TPF) and DARWIN, respectively), which seek to infer the presence of oxygen in the spectra of atmospheres of extrasolar planets (Des Marais *et al.*, 2002). The proposed architecture requires weeks of integration time to obtain spectra with sufficient signal to noise, effectively limiting mission planners to ~50 targets over the mission lifetime. Given that our model shows that a fully inhabited Earth would not have undergone its first oxygen transition until 0.6 Ga if it had been endowed with 5 times more iron, target selection should take into consideration those planets most likely to be oxygenated, which from this preliminary analysis would be those of Earth mass or smaller for a terrestrial-type

reductant inventory. A larger planet would, assuming a similar differentiation history, have a larger buffer of reduced materials to overwhelm in order to oxidize. Simulations show that the amount of iron delivered to "potentially habitable" terrestrial planets can vary by factors of 2 with Earth on the "high" end of possible iron contents (Raymond *et al.*, 2006b; Raymond *et al.*, 2006a), indicating that other microbially-inhabited Earth-like planets may contain less iron, and hence oxidize more quickly than the Earth did. The iron content of terrestrial planets has also been shown to vary as a function of both the density distribution of the protoplanetary disc (Raymond *et al.*, 2005b), and the radial position of any giant planets in the system (Raymond *et al.*, 2005a) so planetary context is also important. These simulations do not formally calculate core/mantle partitioning, which will be necessary to understand the final distribution of iron in a planetary mantle. It remains possible that the iron contents of terrestrial planet mantles will vary more strongly based on stochastic late-stage impacts which post-date core formation. Future simulations that combine the theories of accretionary planet formation and the geophysics of high temperature collisions and core formation are needed to understand the range of iron contents that might be present in the upper mantle and crust of terrestrial planets.

3.8.1 Future Work

Our model is a useful tool, but is highly simplified because important aspects of the Earth system are yet to be included. Such additions include additional climatic and physical feedbacks on the biosphere (i.e. limiting early CH_4 via organic haze), the details of how temperature structure bears on photochemistry, inclusion of the sulfur cycle, and crustal growth. Separating the atmosphere from the ocean would allow for a more accurate biosphere, although it would force us to take shorter timesteps. Further separating the ocean into upper and lower levels would allow for investigation of multiple stages of oxidation as predicted during the Proterozoic (Canfield, 2005) and Archean (Huston & Logan, 2004). Despite these suggestions for an enhanced model, our basic overall result – an oxic transition accompanied by a decrease of methane—remains a robust prediction, given the overall character of the equations and unidirectional hydrogen escape.

3.9 Conclusions

We have presented theoretical constraints on and a self-consistent numerical model for the rise of atmospheric oxygen at 2.4 Ga. Important results from analytical and numerical computations include:

- Decreasing geologic fluxes of reducing gases are a plausible cause of the oxic transition.
- Metamorphic degassing from a more reduced Archean crust could have released more reductants into the atmosphere than in the present day, particularly in the form of methane.
- The amount of reduced iron in the continental crust is likely a strong factor in the evolution of redox state of the crust and crustal fluids.
- Methanogenesis promotes enhanced methane levels that warm the early Earth and compensate for a lower solar luminosity. However, the methane inevitably means that there is a greater rate of hydrogen escape, which ultimately drives oxidation of the lithosphere, a lowering of oxygen sinks, the rise of O_2, and glacial cooling. The atmosphere should jump from a state in which oxygen is a trace gas (<1 ppmv) to 1% of present levels (~0.002 bar) in a geologically short time due to the decreasing photochemical destruction of O_2 as the ozone layer forms. The reaction of the biosphere as Earth cools due to decreasing methane levels strongly affects the transitional atmosphere.
- Other microbially-inhabited earth-like terrestrial planets could oxidize much earlier or later in their respective histories, so the consideration of planetary oxygen history is important in the search for astronomical biosignatures.

Chapter 4 The loss of mass-independent fractionation in sulfur due to a Paleoproterozoic collapse of atmospheric methane

The model described in Chapter 3 was conceptually simple, but very unconstrained. As a result, the conclusions drawn from Chapter 3 were general. In this chapter[*], we present a more physically constrained examination of atmospheric chemistry before the oxic transition. Specifically, we use a 1-D numerical model to study the atmospheric photochemistry of oxygen, methane, and sulfur after the advent of oxygenic photosynthesis. Photochemical models are useful because there are so many physical processes acting in the atmosphere that it is often difficult to describe from first principles what happens to a given species when the atmosphere is subject to a perturbation. A photochemical model simultaneously and self-consistently computes the net transformation of a given species interacting in multiple reactions with multiple species at multiple heights. The model results can then be used to determine the most important reactions operating under the specified conditions.

The model described in this chapter represents an advance over previous efforts in that it is internally self-consistent with respect to atmospheric redox. Informally, this means that what we put into the model is what we get out of the model, which hasn't always been true in previous efforts (see Appendix A). It turns out that this redox self-consistency is vital to solving both oxic and anoxic atmospheres with the same numerical model. Previous efforts have been marred by the necessity of using an anoxic model in its oxic limit, and using an oxic model in its anoxic limit. Our photochemical model performs very well in both redox extremes and in computing intermediate atmospheres. We also advance the methodology of photochemical model analysis, by computing a large grid of photochemical models differing by small amounts in their lower boundary conditions. We then constrain likely paths through portions of this

[*] Material in this chapter was originally published as Zahnle, K. J., Claire, M.W., and Catling, D.C. "The loss of mass-independent fractionation in sulfur due to a Paleoproterozoic collapse of atmospheric methane." *Geobiology* **4**: 271-283 (2006).

"photochemical phase space" using, in particular, the biogeochemical model described in Chapter 3.

In our modeling, we follow Pavlov and Kasting (2002) in assuming that the mass-independent fractionation of sulfur isotopes – characteristic of the Archean – was best preserved in sediments when insoluble elemental sulfur (S_8) was an important product of atmospheric photochemistry. We show that efficient S_8 production requires three things: (i) very low levels of tropospheric O_2 ; (ii) a source of sulfur gases to the atmosphere at least as large as the volcanic SO_2 source today; and (iii) a sufficiently high abundance of methane or other reduced gas. All three requirements must be met. The work in this chapter thus extends the previous result that linked MIF-S solely to a lack of O_2.

We suggest that the disappearance of a strong MIF-S signature at the beginning of the Proterozoic is better explained by the collapse of atmospheric methane, rather than by a failure of volcanism or the rise of oxygen. We show that the photochemical models are consistent in demanding that methane decline before O_2 can rise (although they are silent as to how quickly), and that the collapse of a methane greenhouse effect is consistent with the onset of major ice ages immediately following the disappearance of MIF-S. We attribute the decline of methane to the growth of the oceanic sulfate pool as indicated by the widening envelope of mass-dependent sulfur fractionation through the Archean.

Furthermore, we find that a given level of biological forcing can support either oxic or anoxic atmospheres, and that the transition between the anoxic state and the oxic state is inhibited by high levels of atmospheric methane. Transition from an oxygen-poor to an oxygen-rich atmosphere occurs most easily when methane levels are low, which suggests that the collapse of methane not only caused major ice ages and the end of MIF-S, but it may also have enabled the rise of O_2. In this scenario, the early Proterozoic ice ages were ended by the establishment of a stable oxic atmosphere, which protected a renewed methane greenhouse via an ozone shield.

We return to the concept of declining CH_4 in Chapter 6, when we argue that a "decline in methane" may better describe the conditions in late Archean/early Paleoproterozoic than does the "rise of oxygen." In Chapter 7, time-dependent photochemical model results are presented which address the timing of a decline in methane, and strongly support the hypotheses made here and in Chapter 6.

4.1 Introduction

Mass-independent fractionation (MIF, or nonzero $\Delta^{33}S$) of stable sulfur isotopes is widely recognized as a defining geological signature of the Archean Earth, even though the origin of the signal remains somewhat obscure. What is striking about the isotopic signature is that (i) it exists at all; (ii) the signal is strong through much of the Archean; and (iii) the strong signal seems to disappear abruptly ~ 2.45 Ga (Farquhar *et al*., 2000; Farquhar & Wing, 2003; Bekker *et al*., 2004; Papineau *et al*., 2005), just before a set of severe ice ages began, and somewhat before the classic indicators of an anoxic atmosphere disappeared and the classic indicators of an oxic atmosphere appeared (Cloud, 1968, 1988; Walker, 1977; Walker *et al*., 1983; Kasting, 1993; Holland, 1999, 2002; Canfield, 2005; Chapter 2). A much weaker MIF signal lingered on for some 400 Myr (Farquhar *et al*., 2003; who call the middle interval Stage 2), but clearly something changed abruptly and permanently.

Leading interpretations of the end of MIF stress the rise of O_2 as the cause (Farquhar *et al*., 2000; Pavlov & Kasting, 2002; Ono *et al*., 2003). These arguments are based on considerations of atmospheric photochemistry that will be discussed in detail below. The earlier consensus had placed the rise of O_2 at 2.2 or 2.3 Ga (cf. Holland, 1999, 2002), some 200 Myr after MIF S disappeared. The old chronology was strongly influenced by a pronounced and long-lasting excursion in carbonate $\delta^{13}C$ values between 2.05 and 2.25 Ga (Des Marais *et al*., 1992; Karhu & Holland, 1996). The isotope excursion has been widely interpreted as a major carbon burial event that in some sense caused the rise of

O_2 (Karhu & Holland, 1996). Whether there truly was a 200 Myr delay between the end of Stage 1 and the advent of an oxic atmosphere seems debatable, because the dates are uncertain and because the sedimentary record has been compromised by the ice ages (Farquhar & Wing, 2005). Nevertheless, the apparent mismatch between the two chronologies raises questions about why MIF S stopped when it did.

Known mechanisms for generating MIF signals require gas phase photochemistry stemming from the ultraviolet (UV) photolysis of SO_2 (Farquhar *et al*., 2001). Laboratory experiments show that SO_2 photolysis at 193 nm generates a strong MIF signal in the photolysis products and that 248 nm does not (Farquhar *et al*., 2000). Farquhar *et al*. (2001) hypothesized that the major source of the MIF signal is the photodissociation of SO_2 to SO and O, a channel that cuts off at 220 nm. More recent laboratory work suggests that MIF S can occur at wavelengths somewhat longer than 220 nm through excited states of SO_2 (Masterson *et al*., 2006).

In an oxic atmosphere, photons longer than 200 nm are chiefly absorbed by ozone. However, ozone is not extremely opaque to $200 < \lambda < 220$ nm; this is a spectral window between much stronger absorption at shorter wavelengths by water and CO_2 and at longer wavelengths by ozone. Consequently, it requires a considerable column of ozone, approaching modern levels, to fully suppress MIF-generating SO_2 photolysis. This in turn requires a considerable amount of O_2, on the order of 0.01 PAL (Kasting & Donahue, 1980; PAL means Present Atmospheric Level). We therefore would expect MIF S to persist in atmospheric gases until the atmosphere became mildly aerobic (Farquhar & Wing, 2005). Even today nonzero $\Delta^{33}S$ is found in some Antarctic ices, where it derives from stratospheric photochemical processing of volcanic gases and where competition from other sulfur sources is small (Savarino *et al*., 2003).

In the discovery paper, Farquhar *et al*. (2000) pointed out that the observed sedimentary signature of MIF S is best explained by separating the photochemically processed sulfur into water-soluble and water-insoluble fractions. Separate soluble and insoluble channels have the additional advantage of discouraging the sulfur from pooling in the

oceans, where the various S-containing species would mix back together and the MIF signature would be diluted or lost (Pavlov & Kasting, 2002). Pavlov & Kasting (2002) suggested that the key vector was elemental sulfur (S_8), which is insoluble and which photochemical modelling indicates a major product of sulfur photochemistry in oxygen-poor atmospheres (Kasting *et al*., 1989). Pavlov & Kasting (2002) computed that O_2 levels as low as 10^{-5} PAL (2 ppmv) would shut off S_8 production and thus prevent MIF S from reaching the sediments.

A potential problem with Pavlov & Kasting's (2002) result is that their model was not capable of treating atmospheres with intermediate levels of oxygen. Instead they used separate photochemical models for high and low oxygen levels. The two models do not meet in the middle. Unfortunately it is precisely in this unexplored space in the middle that S_8 production shuts off. We have therefore decided to revisit the S_8 production threshold using a model that does not have this problem.

In this study we accept the hypothesis that MIF S records the precipitation of S_8 from the atmosphere. However, we will show that S_8 production shuts off well before the atmosphere becomes oxic. In keeping with our focus on the rise of oxygen, we restrict our discussion to Earth after the origin of oxygenic photosynthesis.

4.2 The Photochemical Model

For our numerical experiments we used an updated version of the 1-D diffusive photochemical code originally developed by Kasting *et al*. (1989) to study sulfur photochemistry on early Earth. The version used here includes 46 chemical species that participate in 206 chemical reactions. As we will consider only atmospheres with more CO_2 than CH_4, hazes do not form (Zahnle, 1986), and so we truncate hydrocarbon chemistry at C_2H_6. Vertical transport occurs by eddy transport. H_2 and H also flow upward by molecular diffusion. The equations solved are

$$N\frac{\partial f_i}{\partial t} = P_i - L_i N f_i - \frac{\partial \phi_i}{\partial z} \quad (4.1)$$

and

$$\phi_i = b_{ia} f_i (H_a^{-1} - H_i^{-1}) - (b_{ia} + KN)\frac{\partial f_i}{\partial z} \quad (4.2)$$

where N is the atmospheric density; f_i is the mixing ratio of the (minor) species i ; P_i − $L_i N f_i$ are the chemical production and loss terms, respectively; ϕ_i is the upward flux of species i; b_{ia} is the binary diffusion coefficient between i and the background atmosphere a; H_a and H_i are the scale heights of the background atmosphere and of species i; and K is the eddy diffusion coefficient.

4.2.1 General model assumptions

Steady-state solutions are obtained for an average sun angle of 50°. The surface temperature is set to 284 K, the tropopause is at z_{tr} = 11 km, and the stratosphere is isothermal at 186 K. Tropospheric water vapor follows the Manabe-Wetherald (1967) relative humidity profile. The eddy diffusivity is set to 10^5 cm^2s^{-1} in the troposphere and to $10^3(p(z_{tr})/p(z))^{0.5} cm^2s^{-1}$ in the stratosphere. To take some account of the higher activity of the Sun ca. 2.5 Ga, UV at wavelengths longer than 175 nm is doubled over today and UV at wavelengths shorter than 175 nm is quadrupled (Ribas *et al.*, 2005). The surface pressure is set to 1 bar of N_2. The CO_2 mixing ratio is set at 1%. The top of the model is at 80 km. Results are not very sensitive to any of these assumptions.

4.2.2 Sulfur chemistry

Sulfur is injected into the atmosphere abiogenically as volcanic gases, chiefly SO_2 and H_2S, and it enters the atmosphere biogenically chiefly as CH_3SCH_3 (dimethyl sulphide, usually written 'DMS'), OCS, and CS_2 (Toon *et al.*, 1987). Our model does not yet include CS_2, DMS and their photochemical products. These gases are important when the biogenic sulfur source is strong, as seems likely for the late Archean and early

Proterozoic. DMS in particular is thought to be produced exclusively by eukaryotic phytoplankton (Charlson *et al*., 1987). A more complete accounting of the sulfur cycle that takes biogenic sources into account is clearly desirable but fell beyond the scope of this study.

In today's oxic atmosphere, S is either rained out as SO_2 or it is oxidized to SO_3, which after prompt reaction with H_2O precipitates as sulfuric acid (H_2SO_4). In a more reduced ancient atmosphere, sulfur can take any oxidation state from -2 to +6 (Kasting *et al*., 1989). As today, S can exit the atmosphere as SO_2 or H_2SO_4, but there are more reduced options as well. Most S-containing species are moderately soluble (SO_2, H_2S, OCS, CS_2) and can be washed out of the atmosphere in rain. If the atmosphere is sufficiently reducing and the sulfur source big enough, elemental sulfur particles can form and precipitate (Kasting *et al.*, 1989; Pavlov & Kasting, 2002; Ono *et al.*, 2003).

The model includes rainout of soluble species in proportion to their presence in raindrops. The model also includes sulfuric acid aerosols and elemental sulfur particles. H_2SO_4 condenses when its saturation vapor pressure is exceeded; the H_2O/ H_2SO_4 ratio of the particles is self-consistently predicted. Elemental sulfur particles can form when photochemically produced HS and S combine to form S_2. The S_2 can polymerize to form longer chains (the model uses only S_3 and S_4). Polymerization is assumed to stop at the stable ring molecule S_8, which is then assumed to immediately condense. Kasting *et al*. (1989), Kasting (1990), and Pavlov *et al.* (2001) describe in more detail how rainout, aerosol formation and deposition are implemented.

4.2.3 Redox

The model cannot explicitly conserve H or O because tropospheric water vapor is set by evaporation and precipitation of what is in effect an infinite ocean of water. However, the difference between H_2 and O – the redox – is conserved, and it is imperative that it be conserved in a model that purports to compute the redox state of the atmosphere. It is convenient to define H_2O, N_2, CO_2, and SO_2 as the redox neutral gases. These are the

most important volcanic gases for H, N, C, and S, respectively. The redox state of the atmosphere can be defined as the number of extra O atoms minus half the number of extra H atoms. For example, with this definition, H_2SO_4 has a redox state of +1 (H_2SO_4 = H_2O + SO_2 + O), and HCO has a redox state of -1.5 (HCO = CO_2 + 1/2 H_2O − 3/2 O). Minor volcanic gases, such as CO, H_2, and H_2S, are reducing. By assumption the major biogenic gases are CH_4 and O_2, the former strongly reducing and the latter strongly oxidizing. Other important terms in the atmosphere's redox budget include precipitation of S_8 and H_2SO_4 aerosols; rainout of soluble species, especially H_2CO and H_2O_2; and hydrogen escape to space.

Redox conservation is one of the best tests of how credibly the photochemical code performs and consequently it has been the focus of a great deal of development effort. The photochemical code used here always maintains redox conservation to better than 10 ppb, and usually to better than 10 ppt, when the O_2 source is significant. This is excellent performance. The code does not perform as well when the O_2 source is negligible, as would have been the case before the advent of oxygenic photosynthesis. In this study we use the code only in regimes in which it performs extremely well.

4.2.4 Hydrogen escape

We treat hydrogen escape using diffusion-limited flux. Diffusion-limited escape makes the single assumption that escape is easy for hydrogen once it has diffused through the lower, well-mixed atmosphere. This is a good approximation for Earth today. The upper boundary condition is implemented by setting an escape velocity at the top of the computational grid. In diffusion-limited flux the effusion velocity at the top of the grid is

$$v_e = \frac{b_{ia}}{N}(H_a^{-1} - H_i^{-1}). \qquad (4.3)$$

Equation (4.3) is readily derived from Equation (4.2) in the limit that $\partial f/\partial z \rightarrow 0$ (e.g. Walker, 1977). In diffusion-limited escape with modern volcanic degassing fluxes and no

biology, the H_2 mixing ratio would be on the order of 100–1000 ppmv, depending on the exuberance of the volcanic flux.

It has recently been suggested that the hydrogen escape rate might have been much lower than the diffusion-limited flux (Tian *et al.*, 2005). The Tian *et al.* (2005) model makes several assumptions that suppress H escape, the most important of which is to assume that the thermosphere was cold. The motivation for their model is that the thermospheres of Venus and Mars – both of which have CO_2 atmospheres – are cool. In our opinion Tian *et al.* (2005) have not made a convincing case against diffusion-limited flux for Earth (Catling, 2006).

4.2.5 Lower boundary conditions

Minor gases are treated assuming deposition velocities (in many cases set to zero, but these do not matter much because they are minor). The important lower boundary conditions are those for which the lower boundary is (or can be) an important source. In our model these species are O_2, CH_4, H_2, CO, SO_2, and H_2S. For most of the numerical experiments discussed in this study we have used constant mixing ratio boundary conditions for CH_4 and O_2, and constant flux boundary conditions for important volcanic gases H_2S, H_2, and CO. Kasting *et al.* (1989) argued that dissolution of SO_2 into the ocean was a major sink for SO_2. To allow for surface deposition of SO_2, we distributed the volcanic SO_2 source over the troposphere and lower stratosphere; this is also more in keeping with the nature of volcanic eruptions. Numerical experiments using flux boundary conditions on CH_4 and O_2 provide a different perspective on the relative likelihood of different atmospheres, but as a practical matter constant mixing ratio boundary conditions are computationally more robust and better suited to generating suites of output.

We also consider two alternative sets of lower boundary conditions on H_2 and CO. One set is simply to impose low mixing ratios at the surface (10 ppmv for H_2 and 1 ppmv for CO) that implicitly presume voracious biological consumption. A second set is to impose

deposition velocities at the surface that take into account the rate that gases can cross the air–water interface. Kharecha *et al.* (2005) suggest v_{dep} = 2.5 × 10^{-4} cm s^{-1} for H_2 and v_{dep} = 1.2 × 10^{-4} cm s^{-1} for CO. To include either of these alternatives as LBCs requires distributing the volcanic source. We distribute that source in the same way that we distribute volcanic SO_2. Numerical experiments indicate that model results are insensitive to the lower boundary conditions on H_2 and CO save where the biogenic O_2 and CH_4 sources are small.

4.2.6 Volcanic sources

We consider three sets of volcanic fluxes, which we call 'low modern', 'high modern', and 'high Archean'. We denote these cases V1, V2, and V3, respectively. These cases are summarized in Table 1. In practice the important role of volcanic gases in these simulations is that they are the source of S-containing gases to the atmosphere. The role of volcanic gases in governing the redox state of the atmosphere – crucial to dead planets – is questionable on a living world, and as a practical matter our numerical simulations are not very sensitive to CO and H_2 volcanic fluxes.

Table 4-1 Volcanic fluxes

All quantities given in units of molecules cm^{-2} s^{-1}

Model title	SO_2	H_2S	H_2	CO
V1 – 'modern low'	1 x 10^9	1 x 10^8	2 x 10^9	2 x 10^8
V2 – 'modern high'	3.5 x 10^9	3.5 x 10^8	1 x 10^{10}	1 x 10^9
V3 – 'Archean high'	1 x 10^{10}	1 x 10^9	3 x 10^{10}	3 x 10^9

For H_2 we use a low modern flux of 2 × 10^9 $cm^{-2}s^{-1}$ (= 5 × 10^{11} mol $year^{-1}$), as recommended by Sleep & Bird (2006). This estimate includes arc volcanoes and a serpentinization source of the same magnitude. The arc flux is based on the rate that hydrous minerals in ocean basalts are subducted and a volcanic QFM H_2/H_2O ratio of 0.02. Pavlov & Kasting (2002) used a much higher H_2 flux of 2.5 × 10^{10} cm^{-2} s^{-1} for the

Archean, which they attribute to Holland (1984). Holland's most recent estimate for $\phi(H_2)$ is 1.8×10^{10} cm^{-2} s^{-1} (Holland, 2002). Holland's estimate is bigger than Sleep and Bird's (2006) because Holland uses a bigger volcanic flux of H_2O, which he obtains from the CO_2 outgassing flux using a reported CO_2/H_2O ratio of 0.03. We have used 1×10^{10} cm^{-2} s^{-1} as the high modern flux for H_2.

For CO we scale directly from the reported modern volcanic CO_2 source of 3×10^{10} cm^{-2} s^{-1} (Sleep & Zahnle, 2001; Zahnle & Sleep, 2002) using a volcanic QFM CO/CO_2 ratio of 0.03. This results in a volcanic CO flux of 8×10^8 cm^{-2} s^{-1}. We use 2×10^8 cm^{-2} s^{-1} for a low modern case and 1×10^9 cm^{-2} s^{-1} for the high modern case.

Walker & Brimblecombe (1985) presented strong arguments that oceanic sulfate in the Archean had as its main source volcanic gases, chiefly SO_2 and H_2S. Estimates of the modern SO_2 range between 1×10^9 and 3×10^9 cm^{-2} s^{-1} (Andres & Kasgnoc, 1998; Marty & Tolstikhin, 1998; Arthur, 2000). We use 1×10^9 for the low modern value and 3.5×10^9 as the high modern value, as the latter is the SO_2 outgassing rate used by Pavlov & Kasting (2002). Ono *et al.* (2003) consider 3.5×10^8, 1×10^9, and 3.5×10^9 cm^{-2} s^{-1} for their low, medium and high volcanic fluxes, respectively.

The H_2S/SO_2 ratio is more uncertain. The volcanic QFM ratio of 0.02 is lower than field measurements seem to indicate. Recent measurements imply that the ratio can be much higher in certain volcanoes (Aiuppa *et al*., 2005). Global estimates for H_2S flux range from 2×10^8 and 7.7×10^9 cm^{-2} s^{-1}. Given the uncertainty, we have arbitrarily fixed the H_2S/SO_2 at 0.1 for all three cases.

We assume that Archean volcanic fluxes were roughly three times higher than modern volcanic fluxes. Hence for V3, we use 3×10^{10}, 3×10^9, 1×10^{10}, and 1×10^9 molecules cm^{-2} s^{-1} for H_2, CO, SO_2, and H_2S, respectively.

4.2.7 Oxygen and methane

There is compelling evidence preserved in molecular fossils that oxygenic photosynthesis originated no later than 2.75 Ga (Brocks *et al.*, 1999, 2003; Summons *et al.*, 2006) and therefore at least 300 Myr before the end of MIF S and 500 Myr before the rise of O_2. Early consequences of oxygenic photosynthesis are a jump in primary productivity and a jump in atmospheric methane (Walker, 1987; Catling *et al.*, 2001; Chapter 3). We expect the latter for two reasons. First, with more organic matter to ferment, more fermentation is to be expected; and second, because O_2 is a much more reactive molecule than CH_4, we expect that the geochemical sink for O_2 would have been bigger than the sink on CH_4 until the crust was oxidized. By contrast Kopp *et al.* (2005) reject a lengthy delay between the advent of oxygenic photosynthesis and the appearance of abundant free O_2. They suggest instead that oxygenic photosynthesis was invented during the early Proterozoic ice ages ca. 2.3 Ga and promptly annihilated a pre-existing methane greenhouse.

A fundamental assumption underlying most of our numerical experiments is that the net flux of photosynthetic O_2 into the atmosphere was approximately stochiometrically balanced by the net flux of biogenic reduced gases into the atmosphere, chiefly CH_4. The justification for this is that the atmosphere is a small reservoir that quickly equilibrates with the chemical forcing. The balance is inexact because we do not force it explicitly – our explicit assumption is that an atmosphere can exist with the ground level O_2 and CH_4 mixing ratios we prescribe. The photochemical model does the accounting and computes the fluxes consistent with a photochemical steady state. Any stochiometric imbalance between CH_4 and O_2 is accounted for in several generally smaller terms in the atmospheric redox budget, including H escape, rainout of reduced and oxidized species, volcanic gases, and fallout of sulfur.

By conserving the redox budget of the atmosphere, we have in effect put a bag around the atmosphere. The redox fluxes of gases entering and exiting the bag sum to zero. So

far as the atmosphere is concerned, this is correct: our possible atmospheres are self-consistent. We have not attempted to apply redox balance to the oceans, sediments, crust, and mantle that lie outside the bag. In our model there is in general a small net difference between the reducing power of volcanic gases added to the atmosphere and the reducing power lost to the atmosphere by hydrogen escape. This difference is proximally added to (or extracted from) the oceans. There are many terms in the ocean's redox budget that are comparable to or bigger than the atmospheric term. These include burial of reduced carbon in sediments, subduction of sediments and altered oceanic crust, volcanic gases vented directly into the oceans, and reduced or oxidized sediments and altered crust accreted by or weathered from continents. These terms involve big reservoirs with long time constants (e.g. 100 Myr for reduced carbon in continental sediments) that are not plausibly held to redox balance on time scales relevant to the atmosphere.

Captive cyanobacterial mats grown and monitored in the laboratory emit O_2 in the day and H_2 at night (Hoehler *et al*., 2001). The mats do not emit much CH_4 because methanogens lose the competition with sulfate reducers, and in the mats sulfate is generally present in excess. A net excess of photosynthetic O_2 is balanced not by burial of organic carbon but rather by the loss, or export of, soluble organic matter to the waters beyond the mat. The exported oceanic organic matter can be oxidized with sulfate and, if the sulfate runs out, it can be biologically reduced to CH_4.

Hydrogen has similar photochemical effects to CH_4 in an anoxic atmosphere with an underlying photosynthetic source of O_2. In particular, it is comparably effective as a reducing agent to precipitate S_8. If other factors are neglected, a big biogenic H_2 source provides as good an explanation for MIF S as a big biogenic source of CH_4. In other words MIF S does not distinguish between H_2 and CH_4 as the reduced partner to photosynthetic O_2.

Of course other factors do matter. One difference is that methane is not as biologically desirable as hydrogen. Methane can be eaten aerobically or anaerobically using sulfate

(Valentine, 2002). In the anoxic atmosphere aerobic oxidation would be restricted to localized oases. Sulfate would have been relatively unimportant while oceanic sulfate was scarce, as it was through much of the Archean (Canfield *et al*., 2000; Canfield, 2005). Anaerobic methane oxidation using sulfate provides another reason to expect that the methane source shrank as oceanic sulfate grew. On the other hand H_2 is very useful biologically for many purposes. We expect that the biological sink on atmospheric H_2 has always been significant. Some of the H_2 is converted to CH_4 by ordinary methanogenesis. A second difference is that CH_4 is an effective greenhouse gas; much of what makes methane attractive to theorists is that it is the only plausible supplement to CO_2 as a way of keeping the young Earth warm (Pavlov *et al*., 2000).

4.3 Results

Our numerical experiments are performed over a grid of constant O_2 and CH_4 ground-level mixing ratios. For CH_4 we consider mixing ratios between 10^{-6} and 10^{-3}. For O_2 we consider a wider range of mixing ratios, from extremely anoxic cases with less than 10^{-14} to quasi-modern atmospheres with 10^{-2}.

O_2 and CH_4 are photochemically consumed in the atmosphere to make CO_2 and H_2O. In the model, O_2 and CH_4 flow in through the lower boundary to maintain the assumed constant ground-level mixing ratios; this inflow we identify with the biogenic sources. When the model reaches steady state the computed O_2 and CH_4 lower boundary fluxes exactly balance the net photochemical destruction.

Long-lived CH_4 is generally well mixed, but O_2 is only well mixed when it is more abundant than methane. Examples of oxic and anoxic atmospheres are shown in Figs 4-1 and 4-2. To first approximation the less oxic atmospheres feature oxic stratospheres but extremely anoxic tropospheres. In these atmospheres, oxygen mixes up from the surface photosynthetic source and it mixes down from the stratosphere, to be consumed by the troposphere in the middle. This is a general property of reduced atmospheres.

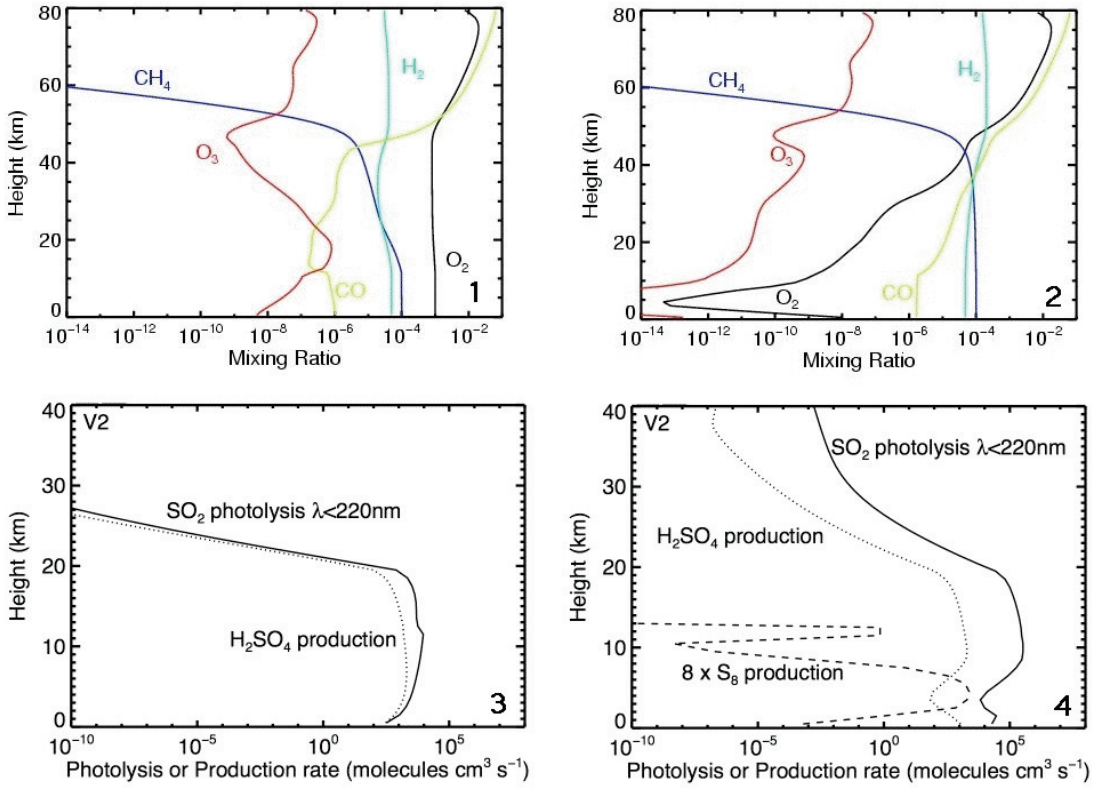

Figures 4-1 – 4-4 Mixing ratios, SO_2 photolysis rates, and H_2SO_4 production versus altitude in example oxic and anoxic atmospheres

4-1) This model assumes ground-level mixing ratios $f(O_2) = 10^{-3}$ and $f(CH_4) = 10^{-4}$. Volcanic fluxes Model V2. Note that O_2 and CH_4 are both reasonably well-mixed below 50 km.

4-2) This model assumes ground-level $f(O_2) = 10^{-8}$ and $f(CH_4) = 10^{-4}$. Volcanic fluxes Model V2. Note that O_2 is drastically ill-mixed, and that the troposphere is extremely anoxic despite the surface being a strong source of photosynthetic O_2.

4-3) Altitudes of sulfate and sulfur aerosol production compared to the altitudes where SO_2 absorbs UV shorter than 220 nm in an oxic atmosphere with $f(O_2) = 10^{-3}$ and $f(CH_4) = 10^{-4}$ and $\phi(SO_2) = 3.5 \times 10^9$ molecules cm^{-2} s^{-1} (V2). SO_2 rainout (not shown) is a major loss process but is confined to the troposphere (z < 11 km). The near coincidence of the SO_2 photolysis rate and the H_2SO_4 formation rate is accidental.

4-4) Altitudes of sulfate and sulfur aerosol production compared to the altitudes where SO_2 absorbs UV shorter than 220 nm in a moderately anoxic atmosphere with $f(O2) = 10^{-8}$ and $f(CH_4) = 10^{-4}$ and $\phi(SO_2) = 3.5 \times 10^9$ molecules cm^{-2} s^{-1} (V2). We expect the MIF S signal to be strongest when the production regions of S_8 and sulfate overlap with the region where SO_2 absorbs UV shorter than 220 nm. These conditions are met in this model. Elemental sulfur forms mostly in or near the strongly reduced troposphere, while sulfate forms everywhere. A more deeply anoxic atmosphere would suppress sulfuric acid formation in the troposphere.

Sulfate aerosols are produced at all heights, especially in the relatively oxidizing stratosphere. Elemental sulfur aerosols tend to form in the anoxic troposphere or near the tropopause, where descending products of SO_2 photolysis mix with ascending reduced gases from the troposphere. Figures 4-3 and 4-4 show where sulfur and sulfate aerosols form in the oxic and anoxic atmospheres of Figs 4-1 and 4-2. These are for the high modern volcanic S fluxes (V2). The S_8 and H_2SO_4 formation regions are compared to where SO_2 absorbs UV shorter than 220 nm. Rainout of SO_2, which is not shown, is confined to the troposphere. We expect that the MIF S signal is strongest when the production regions of S_8 and sulfate overlap with the region where SO_2 absorbs $\lambda < 220$ nm. These conditions are met in all the anoxic models.

In each model with significant S_8 deposition, we verified that the SO_2 photolysis rate by the MIF-producing photons ($190 < \lambda < 220$ nm, for $SO_2 + h\nu \rightarrow SO + O$) was higher than the S_8 production rate at every height at which S_8 was produced. In addition, each model shows numerically higher S production rates by the photolysis of $SO + h\nu \rightarrow S + O$, along with higher total S, S_2 and S_4 production rates at each model altitude with S_8 production. We use the above tests to identify our deposited S_8 as a likely carrier of the MIF signal, given that Pavlov & Kasting (2002) have shown that the MIF signature is distributed among sulfur species in an anoxic atmosphere.

Figure 4-5 is a summary figure over a grid of models differing only in the prescribed ground-level O_2 mixing ratio. The CH_4 mixing ratio is fixed at 100 ppmv, which is near the lower limit of what would be required for methane greenhouse warming to maintain temperate conditions at Earth's surface 2.8 Ga, given the upper limit on atmospheric CO_2 inferred by Rye *et al*. (1995). Figure 4-5 treats the O_2 mixing ratio as the independent variable. This gives an accurate description of how the photochemical model was implemented. The dependent variables are the O_2 and CH_4 fluxes required to sustain the assumed mixing ratios, and the various fluxes of chemical products leaving the atmosphere. The most important of the latter are rainout of formaldehyde (H_2CO) and hydrogen peroxide (H_2O_2).

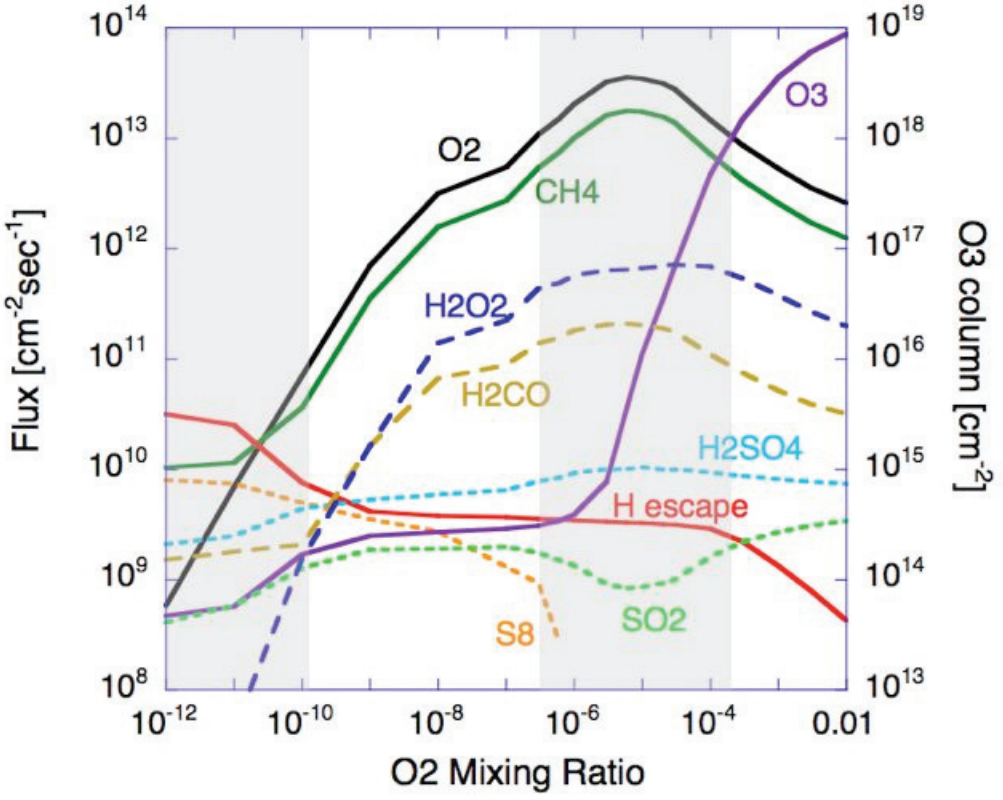

Figure 4-5 Major fluxes as a function of O_2 mixing ratio ($f(O_2)$) for a CH_4 mixing ratio fixed at 100 ppmv

The ozone column is shown against the right-hand axis. The CH_4 and O_2 fluxes are net biogenic sources. For the most part, O_2 and CH_4 in the atmosphere mutually annihilate. Hydrogen peroxide is the most important oxidized product, and formaldehyde is the most important reduced product; both rain out and their fluxes are shown. Hydrogen escape is most important at low $f(O_2)$ and becomes less important as $f(O_2)$ increases. Decreasing O_2 and CH_4 fluxes at high $f(O_2)$ is caused by the increasingly effective ozone shield. The shaded regions represent cases where the net biogenic O_2 fluxes are either implausibly low ($<10^{11}$) or implausibly high ($>10^{13}$ molecules cm^{-2} s^{-1}). At 100 ppmv methane, plausible atmospheres can be oxic or anoxic yet generated by effectively the same biological forcing. Either state is allowable, although the states in between are not. Only the anoxic solution generates S_8. Transition between the oxic and anoxic states is precluded by the impossibly high O_2 fluxes required; transition requires lowering CH_4 levels significantly below 100 ppmv. These are for the high Archean volcanic flux (V3).

Perhaps the first thing one sees in Fig. 4-5 is that the O_2 and CH_4 fluxes peak at an O_2 mixing ratio of 10 ppmv. The peak is caused by rising levels of ozone (also shown against the right hand axis). At low O_2 mixing ratios ozone is unimportant and the photochemical reactions between CH_4 (and its products) and O_2 (and its products)

increase as O_2 increases. But at higher O_2 levels the ozone becomes abundant enough that a significant fraction of the incident UV photons are wasted shuttling oxygen atoms between O_2 and O_3: $O_2 + O \rightarrow O_3$, $O_3 + hv \rightarrow O_2 + O$. In atmospheric photochemistry the ultimate speed limit is set by the number of photons.

As a philosophical point, one thinks of the O_2 and CH_4 fluxes as the true independent variables, and of the O_2 and CH_4 mixing ratios as the consequences of photochemical reactions acting upon the fluxes. This is correct to the extent that the effect of mixing ratios upon biological activity can be ignored – a significant caveat. When Fig. 4-5 is viewed from the perspective of flux as the independent variable, one sees that the solution is multiple valued. The same level of biological productivity can support either a highly anoxic or a rather oxic atmosphere. There is something to this, but recall that we have fixed CH_4 at 100 ppmv; as depicted here, the demonstration of multiple solutions is rigorously valid only if there is an external control over $f(CH_4)$, as for example might be provided by a Gaian thermostat.

Another perspective on Fig. 4-5 is to view the increase in $f(O_2)$ as an evolution through time. This is tempting; after all, O_2 did increase. Again there is something to this, but again, one must not ascribe too much import to $f(O_2)$ as an independent variable; it is not. Rather, explaining why $f(O_2)$ increases (i.e. the quest for the true independent variable) drives this whole field of research. An additional complication in viewing Fig. 4-5 as an evolutionary plot is that methane levels do not remain constant and are likely anticorrelated to oxygen levels in a nonlinear fashion, as discussed in Chapter 3.

Figure 4-5 also shows the three major losses for atmospheric sulfur. Fallout of sulfuric acid particles and rainout of SO_2 occur at all $f(O_2)$ but fallout of S_8 is restricted to anoxic atmospheres with $f(O_2) < 10^{-6}$. Separate exits through sulfate or through SO_2 allow for some preservation of photochemical MIF S in more oxic atmospheres, but as noted above the signal would be diluted or lost when the species dissolved together in liquid water. Today MIF S is restricted to extremely dry environments. In the early Proterozoic the MIF signal in SO_2 and sulfate should have been stronger, while the ozone layer was

thinner and lower; perhaps there is some explanation here for Stage II as defined by Farquhar *et al.* (2003).

The O_2 and CH_4 fluxes in Fig. 4-5 are large. The modern gross CH_4 flux is 1.5×10^{12} cm^{-2} s^{-1}. About 90% of this is consumed by methanotrophs before it reaches the atmosphere; we presume that a much higher fraction reached the anoxic atmosphere.

In the modern world oxygenic photosynthesis generates O_2 at a rate of $\sim 4 \times 10^{13}$ cm^{-2} s^{-1} (Walker, 1977). Obviously most of this O_2 is respired. Today, on geological time scales the net O_2 flux into the atmosphere is balanced by oxidation of rocks, minerals, and fossil carbon at a rate on the order of $\sim 4 \times 10^{10}$ cm^{-2} s^{-1} (Holland, 1984). On shorter time scales the imbalances are bigger. The annual imbalance between photosynthesis and respiration can be seen in the 6 ppmv annual variation of atmospheric CO_2, which implies that on seasonal timescales, O_2 production and consumption are out of balance by 4×10^{12} cm^{-2} s^{-1}, which is on the order of 10% of the total production.

Before O_2 became plentiful, respiration would have been local, confined to oxygen oases in the immediate vicinity of the photosynthetic source, and probably diurnal. Thus, there is no reason to expect that respiration should so nearly cancel O_2 emission as it does today, and we might reasonably expect the flux of O_2 into the atmosphere to have been as large as the annual imbalance today.

For specificity we have set an upper bound on the O_2 flux into the atmosphere at 1×10^{13} cm^{-2} s^{-1}. This is 25% of the modern total photosynthetic production, and 2.5 times bigger than today's net production/respiration imbalance on a seasonal timescale. We have set the lower bound at 1×10^{11} cm^{-2} s^{-1}. This is 2.5 times the modern net O_2 flux averaged over geological time scales. The lower bound is very conservative, given how rapidly O_2 would be consumed either in the environment by oxidative weathering or in the atmosphere by photochemistry (cf. Walker, 1987). For comparison Pavlov & Kasting (2002) set higher upper and lower bounds of $6 \times 10^{11} < \phi(O_2) < 3 \times 10^{13}$ cm^{-2} s^{-1}.

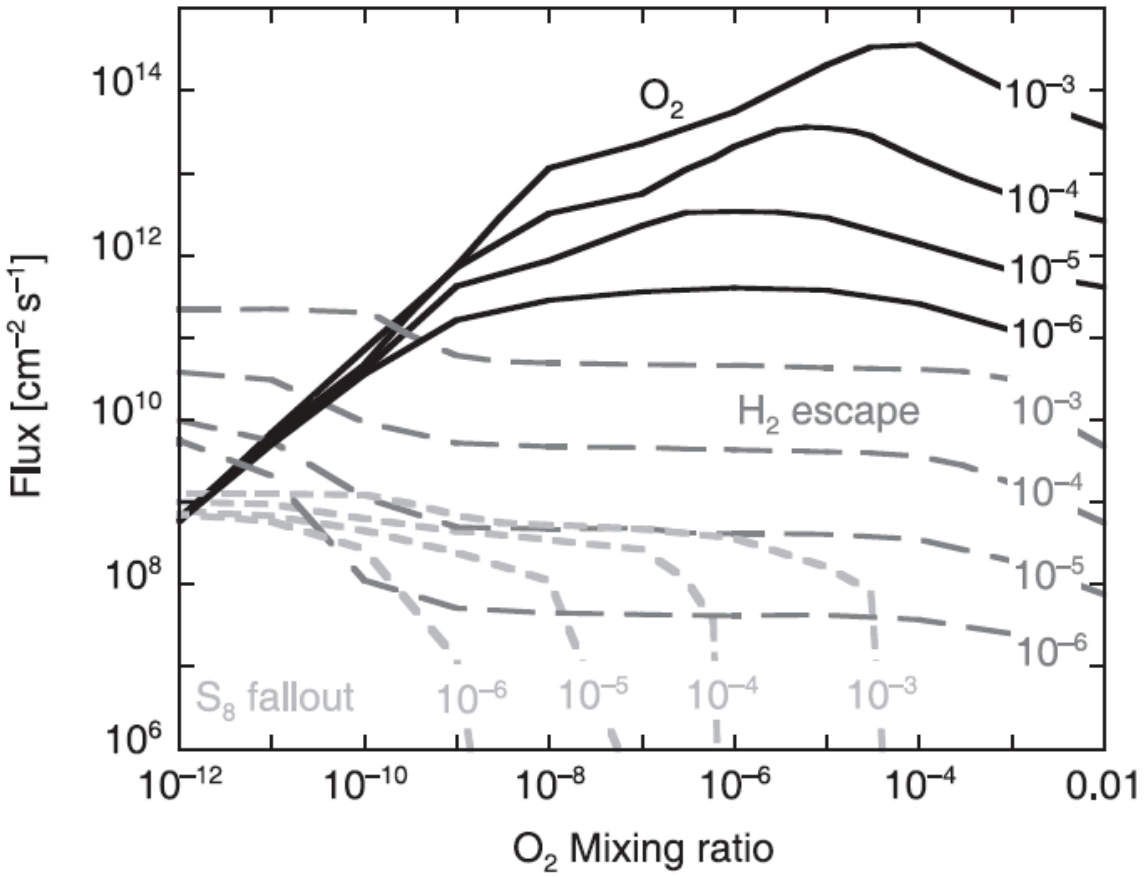

Figure 4-6 O_2 flux, H escape, and S_8 fallout as a function of $f(O_2)$ for $f(CH_4)$ between 10^{-6} and 10^{-3}

Curves are labeled by $f(CH_4)$. Hydrogen escape and the threshold for S_8 production increase directly with the amount of CH_4 in the atmosphere. Note that transition between low and high O_2 states is effectively impossible at 1000 ppmv CH_4, but is relatively easy for $f(CH_4)$ < 10 ppmv. These are high volcanic SO_2 flux models (V3).

Figure 4-6 is analogous to Fig. 4-5 for a range of methane mixing ratios. To limit clutter only the O_2 flux, the H escape, and the S_8 fallout are shown. Methane mixing ratios range from 1 to 1000 ppmv. Not surprisingly, the more methane-rich atmospheres are more reduced and permit proportionately higher levels of hydrogen escape. At $f(CH_4) < 10^{-3}$ only highly anoxic atmospheres (featuring $f(O_2) < 10^{-8}$) are accessible with $\phi(O_2) < 10^{13}$ cm^{-2} s^{-1}. The model predicts that such atmospheres generate S_8 abundantly. By contrast, we regard any $f(O_2)$ level as potentially accessible for CH_4 mixing ratios smaller than 30 ppmv.

Ono *et al.* (2003) showed that sulfur speciation depended on the methane mixing ratio, with the more strongly reduced atmospheres making more strongly reduced sulfur. One difference between our results and those reported by Ono *et al.* (2003) is that our reduced models are significantly less reduced than theirs. In their most reduced atmospheres, Ono *et al.* (2003) predicted that rainout or surface deposition of H_2S and the radical HS represent important atmospheric exit channels. We do not see this, and we have no explanation for the different model behaviours.

Figure 4-7 shows that S_8 production is a strong function of methane mixing ratio for the high modern volcanic SO_2 flux (Case V2) and for a ground-level oxygen mixing ratio $f(O_2) = 10^{-7}$. Higher $f(O_2)$ shifts the S8 cutoff to higher $f(CH_4)$, and lower $f(O_2)$ shifts the S_8 cutoff to lower $f(CH_4)$. A similar figure was presented by Ono *et al.* (2003; their Fig. 4) for extremely anoxic atmospheres with no biogenic O_2 source. In the absence of O_2 the dependence of S_8 production on $f(CH_4)$ is not as strong.

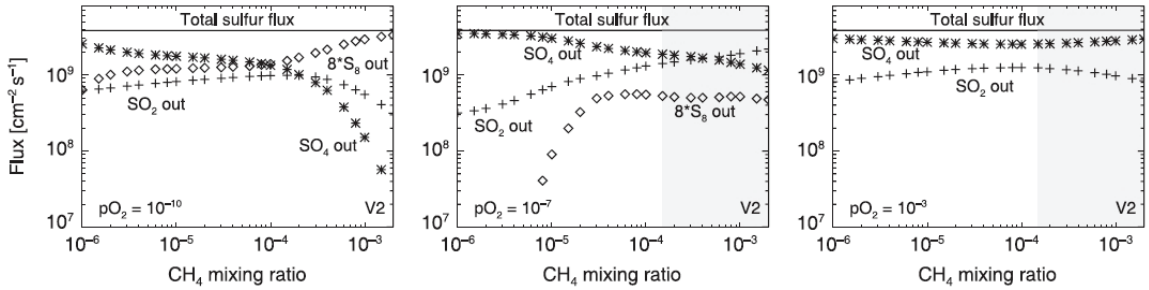

Figure 4-7 Sulfur fluxes as a function of CH_4 mixing ratio at a ground-level O_2 mixing ratio of 10^{-7}

In this particular example, with $f(O_2)$ fixed, S_8 production, and by presumption MIF S, shuts off for $f(CH_4) < 8$ ppmv. Volcanic fluxes are at the high modern levels (V2).

Ono *et al.* (2003) also showed that S_8 production is a strong function of the volcanic SO_2 source. They considered three SO_2 fluxes, two of which were equivalent to our V2 and V1 models, and a third with a smaller SO_2 flux of 3.5×10^8 cm^{-2} s^{-1}. They found that S_8 production is shut off at low SO_2 fluxes and low levels of CH_4. We see much the same.

Figures 4-8, 4-9, and 4-10 are contour plots that show the computed S_8 production as a function of $f(O_2)$ and $f(CH_4)$. These figures indicate the range of atmospheres that can give rise to substantial S_8 production. Production is given in units of Tmol of S per annum.

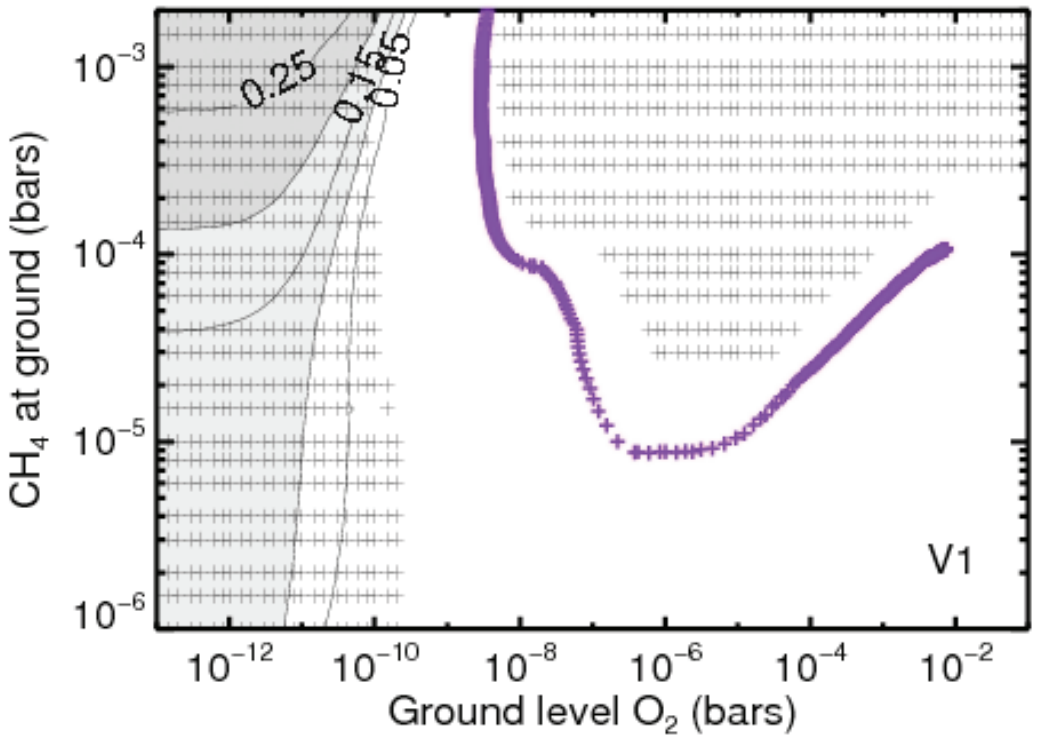

Figure 4-8 S_8 production in Tmol-S year^{-1} plotted on a grid of ground-level O_2 and CH_4 mixing ratios for our low modern volcanic flux case V1.

Atmospheres that require net O_2 fluxes greater than 1 x 10^{13} molecules cm^{-2} s^{-1} or fluxes less than 1 x 10^{11} molecules cm^{-2} s^{-1} are marked with '+' symbols. For reasons described in the text, we regard these as inaccessible. Significant S_8 production is limited to atmospheres with ground-level $f(O_2) < 2 \times 10^{-10}$. In these models ground-level $f(O_2) < f(CH_4)$ are effectively proxies for $\phi(O_2)$. We argue in the text that $\phi(O_2)$ is unlikely to be small enough to allow $f(O_2) < 10^{-10}$. We therefore do not expect MIF S for volcanic S fluxes as small as the fluxes in V1. Also shown on the plot is the trajectory of the reference model from Chapter 3. The reference model evolves in a counter-clockwise sense along this curve. For V1 fluxes, the reference model of Chapter 3 never generates MIF S.

Figure 4-8 addresses our low modern volcanic flux (V1) models with $\phi(SO_2) = 1 \times 10^9$ cm^{-2} s^{-1} and $\phi(H_2S) = 1 \times 10^8$ cm^{-2} s^{-1}. Atmospheres that require net O_2 fluxes greater than 1×10^{13} cm^{-2} s^{-1} are marked. For reasons discussed above, we regard O_2 fluxes greater than 1×10^{13} cm^{-2} s^{-1} as implausible. With this limitation, ground-level O_2 mixing ratios $2 \times 10^{-7} < f(O_2) < 2 \times 10^{-4}$ are inaccessible for $f(CH_4) \geq 5 \times 10^{-5}$. By net fluxes, we refer to the difference between production and respiration on timescale longer than the characteristic response time of the atmosphere. For an anoxic atmosphere with $f(O_2) < 10^{-7}$, the lifetime of atmospheric O_2 is measured in days to weeks. It seems obvious that such an atmosphere would be strongly driven by variable biogenic fluxes, so that specific steady state solutions such as those discussed here have limited value. For oxic solutions with $f(O_2) > 10^{-4}$, the O_2 lifetimes range from a decade up.

For the low SO_2 flux (Fig. 4-8), significant S_8 production is limited to atmospheres with ground-level $f(O_2) < 10^{-10}$. To first approximation very low $f(O_2)$ is better regarded as a proxy for $\phi(O_2)$ than as an actual O_2 mixing ratio. This occurs because the troposphere is both very reduced and very photochemically active. For all the models considered in this study, for very low $f(O_2) \sim 10^{-10}$ the relation between the flux and the mixing ratio is nearly linear and approximately given by $\phi(O_2) \approx 5 \times 10^{20} f(O_2)$ cm^{-2} s^{-1} (Fig. 4-6). If we take $\phi(O_2) > 10^{11}$ cm^{-2} s^{-1}, we would conclude that S_8 and therefore strong MIF S is unlikely for SO_2 fluxes smaller than 1×10^9 cm^{-2} s^{-1}.

Figure 4-9 addresses our high modern volcanic flux (V2) models with $\phi(SO_2) = 3.5 \times 10^9$ cm^{-2} s^{-1} and $\phi(H_2S) = 3.5 \times 10^8$ cm^{-2} s^{-1}. The inaccessible regions do not change appreciably for the different volcanic fluxes. Higher S fluxes increase the stability field of S_8. Dependence of S_8 production on $f(CH_4)$ is more pronounced than for smaller volcanic fluxes.

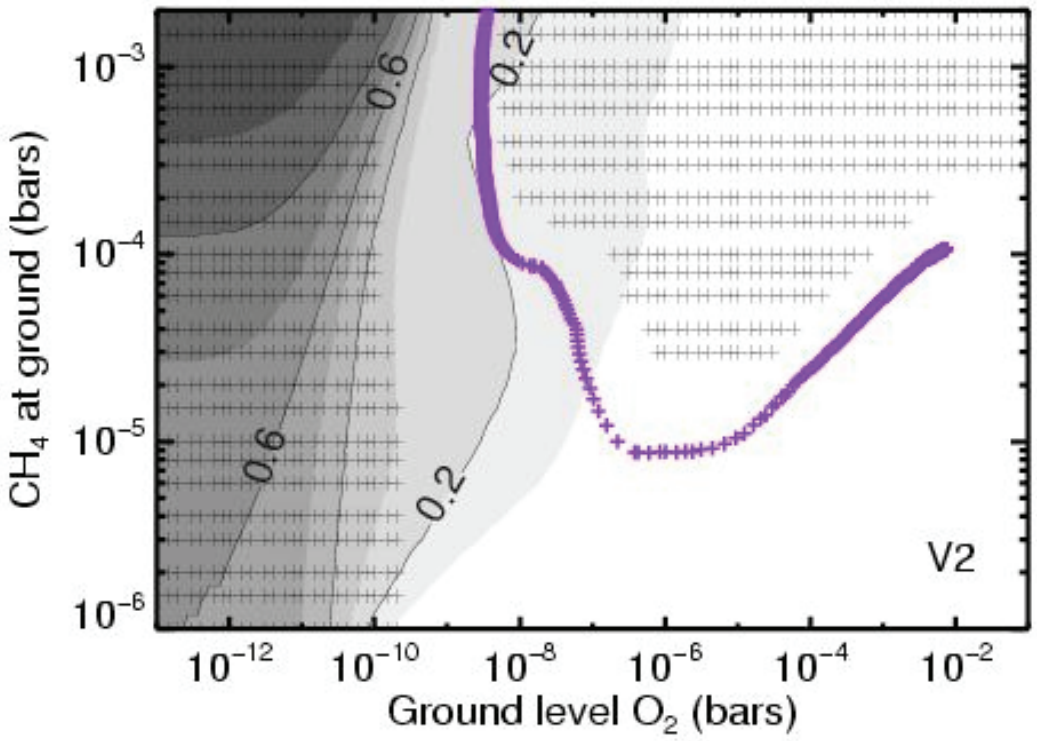

Figure 4-9 S_8 production in Tmol-S year^{-1} plotted on a grid of ground-level O_2 and CH_4 mixing ratios for our high modern volcanic flux case V2.

The reference model from Chapter 3 provides a credible history in this case. This history is replotted on Fig. 4-12 below.

Figure 4-10 addresses our high Archean volcanic flux (V3) models with $\phi(SO_2) = 1 \times 10^{10}$ cm^{-2} s^{-1} and $\phi(H_2S) = 1 \times 10^{9}$ cm^{-2} s^{-1}. At the higher S fluxes, S_8 production – especially the threshold for S_8 production, which may be the key quantity of interest – is as strong a function of $f(CH_4)$ as it is of $f(O_2)$.

As a general rule all of the atmospheres that generate significant S_8 are quite anoxic. In particular the tropospheres are very anoxic except near the ground. This point is made more clearly in Fig. 4-11, which shows S_8 production vs. the minimum $f(O_2)$ in the troposphere for the high modern volcanic fluxes (Case V2). These are the same models shown in Fig. 4-9. For the more reduced atmospheres the ground-level O_2 mixing ratio is

better understood as a proxy for the biogenic flux into the atmosphere. Instead of a small constant ground-level mixing ratio, one should imagine localized O_2-rich plumes emitted from photosynthetically active regions, mixing into and chemically reacting with the ambient tropospheric gases.

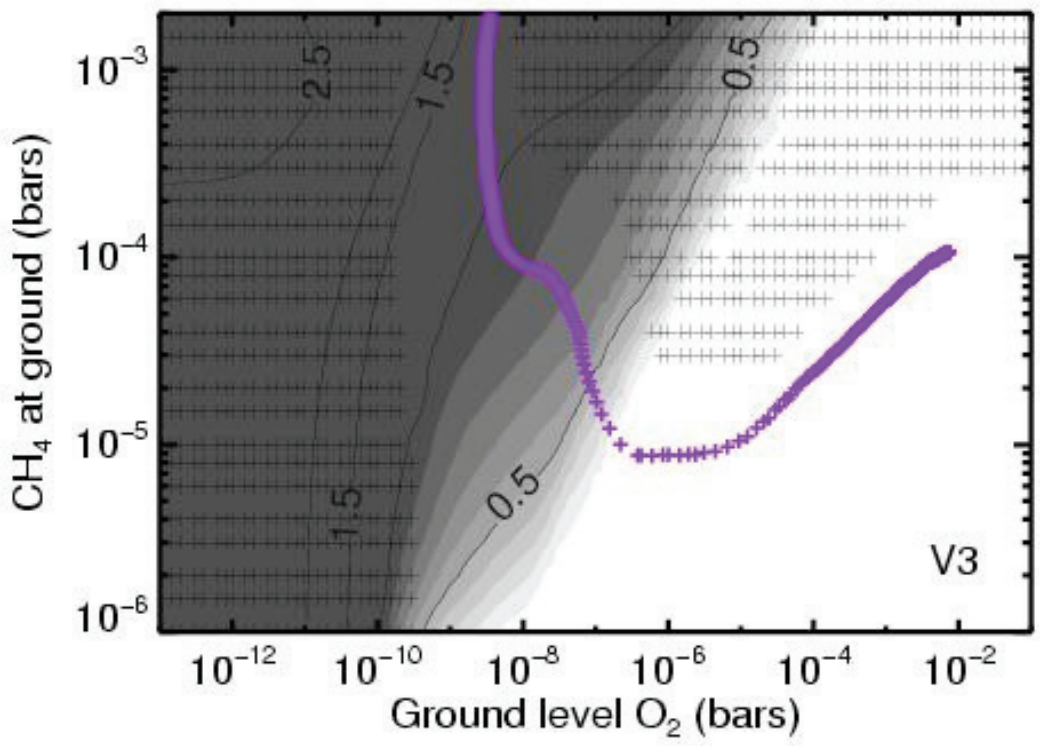

Figure 4-10 S_8 production in Tmol-S year^{-1} plotted on a grid of ground-level O_2 and CH_4 mixing ratios for our high Archean volcanic flux case V3.

It is noteworthy that the threshold for S_8 production is as strong a function of $f(CH_4)$ as it is of $f(O_2)$ at the higher S fluxes. The reference model from Chapter 3 also fares well in this case.

4.4 Discussion

The steadily widening envelope of mass-dependent sulfur fractionation (a.k.a. $\delta^{34}S$) seen through the Archean and early Proterozoic has been interpreted as a history of sulfate availability (Canfield, 2005). In the early Archean, mass dependent S fractionation is

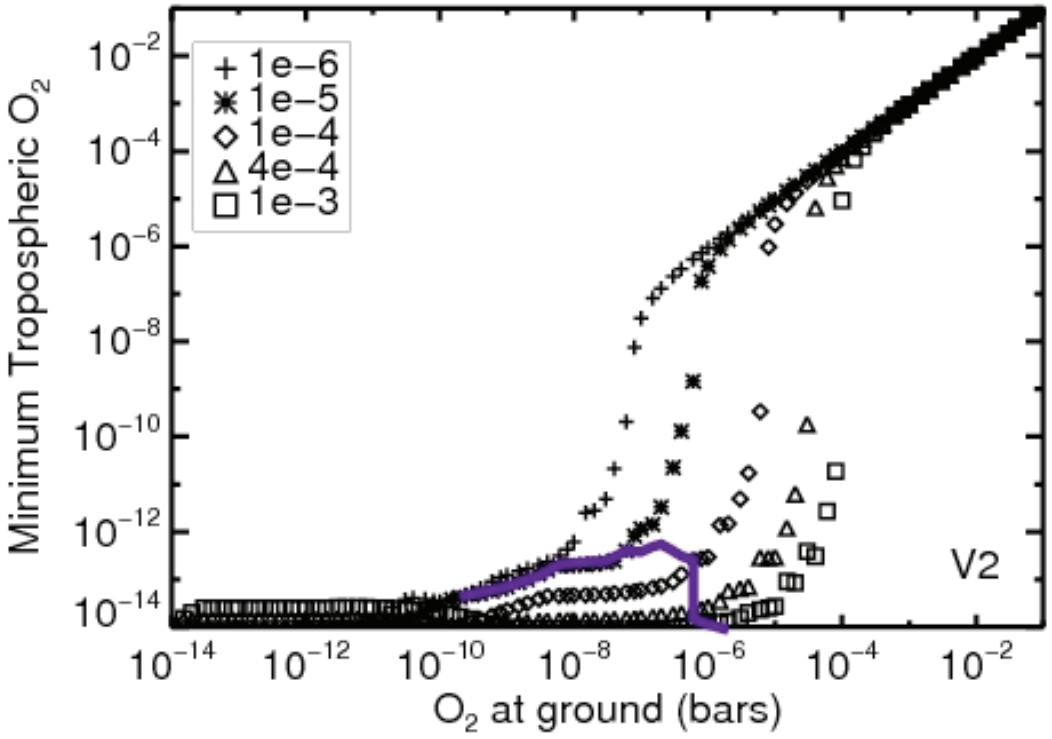

Figure 4-11 The minimum tropospheric oxygen levels ($f(O_2)$) as a function of the ground-level oxygen mixing ratio ($f_{gr}(O_2)$), labelled by the methane mixing ratio ($f(CH_4)$).

For low O_2 and high CH_4 the tropospheres are highly anoxic. At high O_2 ground-level mixing ratios the oxygen becomes well-mixed, as indicated by the diagonal line ($f_{tr}(O_2) \approx f_{gr}(O_2)$) rising to the right. The transition is abrupt, especially at the higher methane levels for which oxic atmospheres are in any event impossible. The snaking solid grey curve represents the threshold for S_8 production. S_8 production is always confined to atmospheres that feature extremely anoxic tropospheres. It is noteworthy that the atmosphere can be very anoxic and yet not generate S_8, even at, or especially at, high methane levels. The ground-level mixing ratio $f_{gr}(O2) \approx 10^{-6}$ for high $f(CH_4)$ is essentially the same result obtained by Pavlov & Kasting (2002) for the equivalent case. These computations use volcanic flux model V2.

modest. Evidently, S was in short supply and at most times in most places all of it was used up. Hence the natural inclination of biology to discriminate between the heavy and light isotopes of sulfur was not expressed: if every atom of sulfur is used, there is no fractionation. To first approximation we might regard the sulfate fractionation that did not occur as a measure of the organic matter left over after the sulfate was consumed. It is well known that sulfate reducers outcompete methanogens; when sulfate is abundant

methanogenesis is suppressed, but when the sulfate is gone away, the methanogens can play. The organic leftovers provided the substrate for the methanogens. The suppression of mass-dependent S fractionation through the Archean implies that methanogens ate well, and that methane fluxes into the atmosphere were big.

The envelope of $\delta^{34}S$ appears to increase steadily through the late Archean and through the early Proterozoic, reaching modern levels ~1.8-2.0 Ga. The increasing span of $\delta^{34}S$ -values implies that as time passed biology was being afforded more opportunities to discriminate between sulfur's isotopes. Evidently it was becoming more common to exhaust the pool of available organic matter before exhausting the pool of available sulfur. With less organic matter escaping sulfate reduction, there would be less organic matter reduced to methane and therefore a smaller source of methane. This also implies that the pool of available sulfur was growing. These seem to have been long-term trends that continued well into the Proterozoic. These trends imply a steady decline in the relative importance of methanogens.

As sulfate reducers gained prominence, it is likely that biogenic S-containing gases became more important. As noted above, biogenic sulfur gases include H_2S, DMS, OCS, and CS_2. It is possible that they achieved a level of importance in the anoxic late Archean or early Proterozoic atmosphere that they have not risen to since. The sulfur gases are much more photochemically reactive than methane; indeed, they are more reactive than O_2. At this point the role of biogenic sulfur gases is entirely speculative, but it is clear that to the extent they replaced CH_4 or H_2 as the reduced partner of photosynthetic O_2 they worked to favour the creation of an O_2 atmosphere.

The story told in this chapter begins with the invention of oxygenic photosynthesis. A likely consequence of this invention was a general increase in global productivity. Another likely consequence was an increase in atmospheric methane, because methane is a biological end-product and it is chemically more stable than O_2. Because methane is a potent greenhouse gas, it warmed the Earth. The warmer conditions promoted CO_2-

consuming weathering reactions, which suggests that atmospheric CO_2 levels were probably reduced by the increased methane.

A key consequence of abundant atmospheric methane was nontrivial H escape to space. Hydrogen escape irreversibly oxidizes the Earth, especially the near surface reservoirs, and the crust in particular (Catling *et al.*, 2001). It takes hundreds of millions of years to oxidize key crustal reservoirs of iron and sulfur. Both iron and sulfur record this history in their fractionated isotopes. With sulfur the record seems straightforward: available oceanic sulfate steadily increased through the Archean, as one expects of an inexorably oxidized crust.

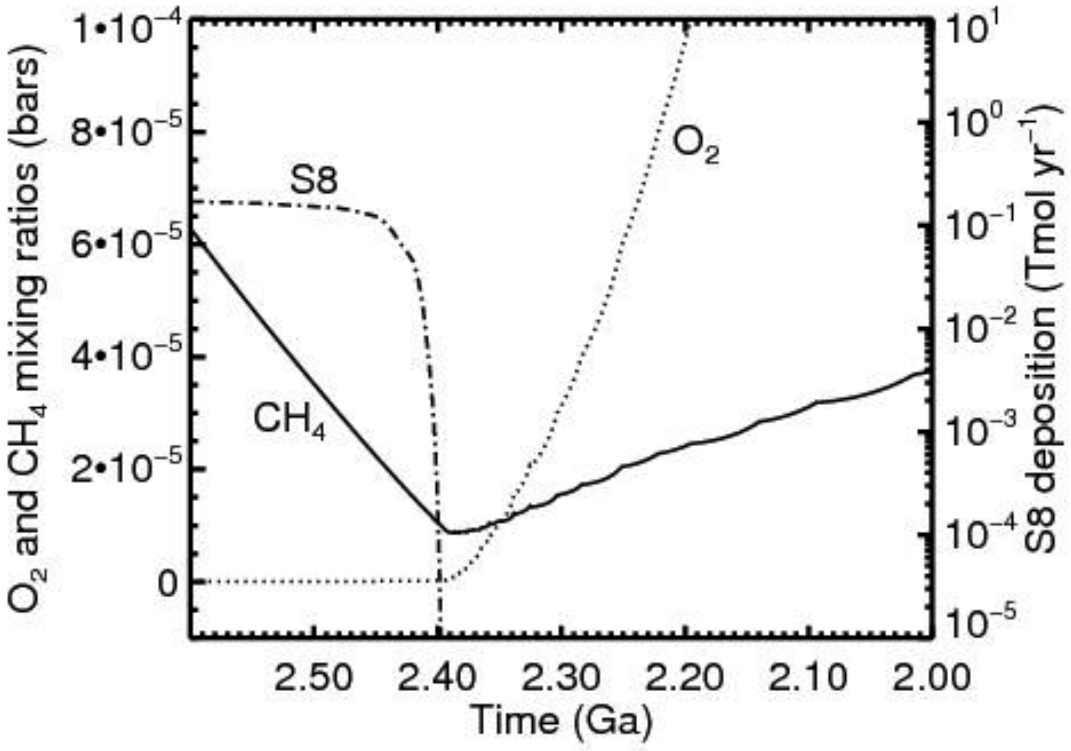

Figure 4-12 Histories of $f(CH_4)$, $f(O_2)$, and S_8 production as the atmosphere evolves along the reference model.

The order of events given here is general to any plausible narrative of the oxic transition. First MIF S disappears, then CH_4 reaches a minimum and temperatures reach a minimum because of this, then O_2 rises to mildly oxic levels, and finally CH_4 returns to provide greenhouse warming under the protection of an oxygen-ozone shield.

As the oceanic sulfate pool increased, greater competition with sulfate reducers left less room for methanogens. Net methane production must have decreased and atmospheric methane levels must have decreased accordingly (the O_2 flux to the atmosphere would also have decreased, although $\phi(O_2)$'s decrease may have been offset somewhat by increased emission of photochemically labile biogenic S-gases and of biogenic H_2). The decline of CH_4 caused sulfur MIF to stop and the climate to cool, the latter culminating in severe ice ages. This sequence of events is nicely illustrated in Fig. 4-12, which creates a history of MIF S by combining the Chapter 3 reference model for the histories of atmospheric O_2 and CH_4 with the S_8 production rates shown in Fig. 4-9. The order of events is general: (i) oceanic sulfate increases, (ii) atmospheric methane declines, (iii) sulfur MIF disappears and greenhouse warming collapses, (iv) oxygen rises and the methane greenhouse returns under the photochemical protection of abundant oxygen and ozone.

We speculate that it was the increasing sulfate pool and the concomitant reduction of atmospheric methane that made the transition to an oxic atmosphere possible. While CH_4 and O_2 fluxes remained large and methane abundant the atmosphere remained trapped in a stable anoxic state, as we showed most clearly in connection with Fig. 4-5. Although oxic atmospheres exist with essentially the same biogenic forcings as those driving the anoxic atmosphere, the oxic states are inaccessible when methane is abundant in the atmosphere. This is seen in Figs 4-5, 4-6, and 4-8–10. At lower levels of atmospheric CH_4 the barrier against transition to an O_2-rich atmosphere is small enough that realistic biogenic fluxes can overcome it. It is no accident that the rise of O_2 took place during ice ages at a time when atmospheric CH_4 levels were low.

4.5 Conclusions

- We assumed that the characteristic of the Archean sulfur MIF signal is a product of atmospheric photochemistry, and that the photochemical signature was preserved in the rock record when sulfur was able to leave the atmosphere in both soluble (e.g. SO_2, H_2SO_4) and insoluble (S_8) forms. We used a 1-D atmospheric photochemistry

model to characterize the conditions conducive to the condensation and precipitation of particles of elemental sulfur. We assumed a volcanic source of sulfur gases. Our models presume oxygenic photosynthesis and a rough stochiometric balance between the net fluxes of O_2 and CH_4 into the atmosphere.

- Precipitation of S_8 depends on the SO_2 source and the mixing ratios of CH_4 and O_2. In particular, we showed that S_8 deposition is a strong function of CH_4 for oxygen levels and SO_2 sources likely in the late Archean. The necessary conditions for forming S_8 are best understood as requiring a large sulfur source, an anoxic troposphere, and a sufficient amount of a reduced gas (either CH_4 or H_2 will do). All three requirements must be met to form S_8.
- Collapse of atmospheric methane in the late Archean to below 10 ppmv provides the best explanation of the disappearance of MIF in sulfur. This differs from previous work attributing the loss of MIF to the rise of O_2. We suggest that the methane collapse was driven by the increasing importance of sulfate and the increasing competitive advantage of sulfate reducers over methanogens. The collapse of CH_4 also explains widespread low-latitude glaciation in the early Proterozoic.
- We suggest that the growth of the oceanic sulfate pool reflects secular changes in the redox balance of the atmosphere-ocean-crust system, probably driven by hydrogen escape.
- The rise of O_2 to geologically detectable levels took place after the collapse of MIF, and was facilitated by generally low levels of atmospheric methane characteristic of the ice ages.
- The ice ages were ended by the rise of O_2. The Proterozoic was relatively rich in methane (at ~100 ppmv levels) because the ozone layer provided methane with protection against photochemical destruction.

Chapter 5 Anaerobic methanotrophy and the rise of atmospheric oxygen

This chapter* sees a return to the biogeochemical model described in Chapter 3, informed by the results presented in Chapter 4. In Chapter 4, we postulated that the decline in MIF-S might be better described by a decline in atmospheric methane concentrations, but provided only speculations as to why methane might have declined. Here, we explore the possibility that organisms in marine sediments can oxidize the CH_4 produced by methanogens once there is sufficient sulfate present in the oceans, effectively lowering the CH_4 flux to the atmosphere.

The anoxic decomposition of organic matter in modern marine sediments generates a significant flux of methane that is oxidized microbially with sulfate under the seafloor and never reaches the atmosphere. In contrast, prior to ~ 2.4 Ga, the ocean had little sulfate to support anaerobic oxidation of methane (AOM) and the ocean should have been an important methane source. As atmospheric O_2 and seawater sulfate levels rose on the early Earth, AOM would have increasingly throttled the release of methane.

We use the biogeochemical model described in Chapter 3 to simulate the response of early atmospheric O_2 and CH_4 to changes in marine AOM as sulfate levels increase. Semi-empirical relationships are used to parameterize global AOM rates and the evolution of sulfate levels. Despite broad uncertainties in these relationships, atmospheric O_2 concentrations generally rise more rapidly and to higher levels (~10^{-3} bar versus ~10^{-4} bar) as a result of including AOM in the model. Methane levels collapse prior to any significant rise in O_2, but counter-intuitively, methane increases to higher levels after O_2 rises when AOM is included. As O_2 concentrations increase, shielding of the troposphere by stratospheric ozone slows the effective reaction rate between oxygen

* Material in this chapter was originally published as Catling, D. C., Claire, M. W., and Zahnle, K. J. "Anaerobic methanotrophy and the rise of atmospheric oxygen." *Philosophical Transactions Of The Royal Society A-Mathematical Physical And Engineering Sciences* **365**(1856): 1867-1888 (2007).

and methane. This effect dominates over the decrease in the methane source associated with AOM. Thus, even with the inclusion of AOM, the simulated Paleoproterozoic atmosphere has a climatologically significant level of methane (~ 50 ppmv.)

5.1 Introduction

Oxygen concentrations in the Earth's atmosphere are inferred to be less than 1 ppmv prior to ~2.4 Ga (Pavlov & Kasting 2002; Bekker *et al*. 2004). In such an anoxic atmosphere, photochemical models show that methane has a lifetime of approximately 10^4 years and can reach levels of 10^2-10^3 ppmv, given a biogenic source of approximately 0.1–1 times present (Pavlov *et al*. 2001; Chapter 4). Methane at this abundance can provide sufficient greenhouse warming to counteract an early Sun that was 25–30% fainter (Pavlov *et al*. 2000; Kasting & Howard 2006). The ultraviolet decomposition of methane in the early upper atmosphere and the accompanying escape of hydrogen to space may have also been important for irreversibly oxidizing Earth's surface environment and enabling the rise of oxygen (Catling *et al*. 2001; Chapter 3).

Carbon and sulfur isotopes suggest that there was abundant methane in the Archean. A global distribution of ^{12}C-enriched kerogens of 2.5–2.8 Ga age can be attributed to isotopically light CH_4, greater than 20 ppmv abundance, generated by methanogens and incorporated into methanotrophs (Hayes 1994; Hinrichs 2002; Hayes & Waldbauer 2006). Strictly speaking, this evidence only indicates that methane had to be plentiful within worldwide sediments, but independent evidence for high methane in the atmosphere is provided by mass-independent fractionation (MIF) of Archean sedimentary sulfur isotopes (Farquhar *et al*. 2000). Abundant MIF is thought to occur only when sulfur exits the atmosphere in soluble and insoluble forms: in particular, soluble SO_4^{2-} and insoluble elemental polymerized sulfur (S_8) at different ends of the sulfur redox distribution (Pavlov & Kasting 2002). Models show that both low levels of oxygen and a sufficiently high abundance of methane are required for insoluble S_8 to be a significant photochemical product of the ancient anoxic atmosphere (Ono *et al*. 2003;

Chapter 4). Sufficient methane enables the photochemical reduction of sulfur-bearing gases to S_8. Thus, in Chapter 4 we showed that MIF is indirect evidence for high Archean methane.

Evidence from biomarkers suggests that oxygenic photosynthesis arose long before the rise of atmospheric O_2 around 2.4 Ga (Brocks *et al*. 2003; Summons *et al*. 2006), a puzzle that can be explained if the O_2 was efficiently scavenged by a glut of reductants in the early environment (e.g. Walker *et al*. 1983 and Holland 2002; see Chapter 2 for a review). Given little O_2 and abundant CH_4 in the Archean atmosphere, how did the atmosphere become oxygenated?

One way to understand the factors that influence the history of O_2 is through time-dependent biogeochemical box models that simulate changes in atmospheric O_2 levels as a result of redox fluxes in the Earth system. In such models, it is necessary to pay particular attention to atmospheric photochemistry in order to simulate realistic levels of O_2 or CH_4. In Catling *et al*. (2004), we presented preliminary results of a biogeochemical model where we parameterized an effective bimolecular reaction between CH_4 and O_2 with a rate constant that depended on the levels of CH_4 and O_2. We noted then that shielding of the troposphere by stratospheric ozone acts as a positive feedback on O_2 as O_2 rises (Catling *et al*. 2004). In Chapter 3 of this dissertation we subsequently enhanced this model and described its sensitivities and results in considerable detail (e.g. fig. 3-3 shows the effect of increasing stratospheric ozone on the effective reaction of O_2 and CH_4 from photochemical modeling). Goldblatt *et al*. (2006) present a similar model that also uses the idea of an effective bimolecular reaction between O_2 and CH_4; as in Catling *et al*. (2004), they found that ozone shielding acts as a positive feedback on the rise of O_2.

While the shielding effect of the ozone layer is important in understanding the steady-state differences between oxic and anoxic atmospheres, in Chapter 3 we demonstrated that this feedback alone does not cause an abrupt rise in oxygen. Instead, we hypothesized that the biosphere provided a strong positive feedback on atmospheric O_2

by diminishing the CH_4 flux to the atmosphere relative to the O_2 flux (Chapter 4). In particular, we hypothesized that the increase in oceanic sulfate (and nitrate) levels was accompanied by the increased activity of methanotrophs, which facilitated a rapid transition to an oxic atmosphere by lowering the ratio of CH_4:O_2 fluxes to the atmosphere.

In this chapter, we demonstrate the plausibility of this idea using our box model. Goldblatt *et al*. (2006) included aerobic methanotrophs in their model, i.e. microbes that directly use atmospheric O_2 to consume CH_4, but this has no effect on the CH_4:O_2 flux ratio and so is neutral with respect to atmospheric redox. In contrast, anaerobic methanotrophs are known to use sulfate or nitrate when O_2 is unavailable in the metabolic processes of 'anaerobic oxidation of methane' (AOM). In this chapter, we demonstrate how AOM was likely to have been important in determining the rapidity and magnitude of the ~2.4 Ga rise of O_2. We also show how AOM modulates the evolution of CH_4 levels, which has implications for Earth's climate.

5.2 Method: the box model and anaerobic oxidation of methane

In sections 5.2.1 - 5.2.3 we describe our biogeochemical model, how AOM should influence the rise of oxygen, and how we parameterize AOM in the model.

5.2.1 Model description

As our point of departure, we consider the atmosphere only after the advent of oxygenic photosynthesis. A full description of our biogeochemical model is given in Chapter 3. Here, we briefly reiterate the key equations so that modifications to take anaerobic methanotrophy into account can be appreciated.

In our model, the amount of O_2 in the atmosphere is determined by a kinetic competition between source (F_{SOURCE}) and sink (F_{SINK}) fluxes of O_2, i.e.

$$\frac{d}{dt}\left[\mathrm{O_2}\right] = F_{\mathrm{SOURCE}} - F_{\mathrm{SINK}} = (F_{\mathrm{B}} + F_{\mathrm{E}}) - (F_{\mathrm{V}} + F_{\mathrm{M}} + F_{\mathrm{W}}) \quad (5.4)$$

where $[O_2]$ is the total reservoir of atmospheric O_2, which we express in units of teramoles (10^{12} mol), sometimes converting to partial pressure units of bars for figures. We implement all source and sink fluxes in the model in units of Tmol O_2 yr^{-1} production or consumption. We divide F_{SOURCE} into F_{B}, the flux of oxygen due to organic carbon burial, and F_{E}, the flux of oxygen to the Earth as a whole due to hydrogen escape. The oxygen sinks F_{V} and F_{M} represent oxygen-consuming gases (i.e. H_2, H_2S, SO_2, CO, CH_4) from volcanic/hydrothermal and metamorphic/geothermal processes, respectively, while F_{W} is the oxygen sink due to oxidative weathering of continental rocks. Equation (5.1) is illustrated by summing fluxes in and out of the atmosphere–ocean–biosphere ('AOB') box in Figure 5-1.

We ignore the gross photosynthesis–respiration cycle because this rapid, closed cycle generates no net O_2 (e.g. see Garrels & Perry (1974) or Walker (1980)). However, in order to calculate the levels of methane in the Archean atmosphere, it is necessary to consider the fraction of photosynthesized carbon from gross primary productivity that gets converted to methane. The net effect of methanogenic recycling of organic carbon produced photosynthetically is found by summing the respective net reactions of oxygenic photosynthesis and methanogenesis, as follows:

$$\begin{aligned} &\mathrm{CO_2 + H_2O \rightarrow CH_2O + O_2 \ldots \times 2} \\ &+ \quad \underline{\mathrm{2CH_2O \rightarrow CH_4 + CO_2}} \\ &\mathrm{CO_2 + 2H_2O \rightarrow CH_4 + 2O_2} \end{aligned} \quad (5.5)$$

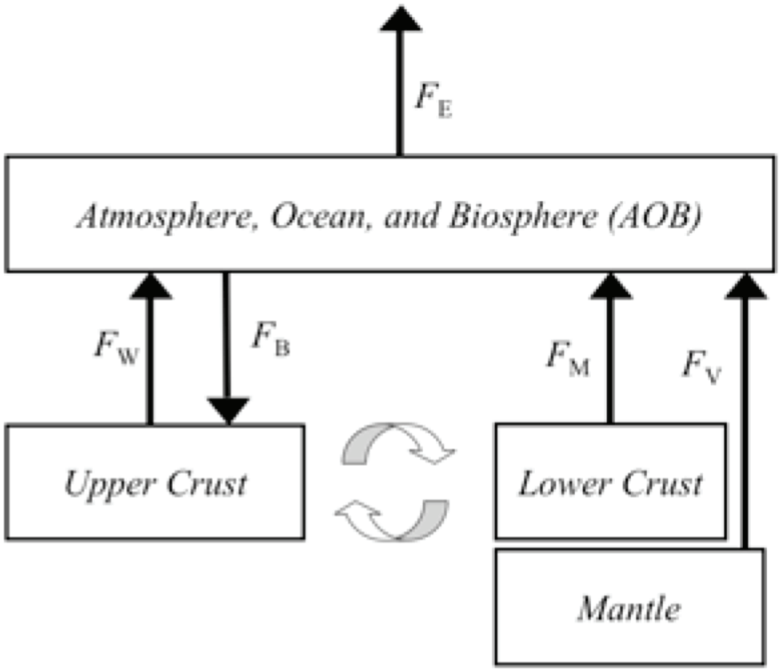

Figure 5-1 A schematic of the three-box model

Arrows represent fluxes of reducing material in Tmol O_2 equivalents yr^{-1}. Consequently, arrows leaving a box represent oxidizing processes. Equation (2.1) for the evolution of O_2 is obtained by subtracting incoming reductant fluxes from outgoing reductant fluxes. The unfilled arrows represent crustal mixing due to erosion, uplift and tectonics.

Thus, the combination of oxygenic photosynthesis and methanogenesis generates O_2 and CH_4 in the ratio of 2:1. Consequently, a flux of methane, ϕ_{CH4}, to the atmosphere is accompanied by a stoichiometrically balanced flux of O_2 of $2\phi_{CH4}$. This enables us to expand equation (5.1) to coupled time-dependent equations for the first-order evolution of atmospheric methane and oxygen:

$$\frac{d}{dt}\left[\mathrm{CH_4}\right] = \phi_{\mathrm{CH4}} - k_{\mathrm{eff}}\left[\mathrm{O_2}\right]\left[\mathrm{CH_4}\right] - k_{\mathrm{esc}}\left[\mathrm{CH_4}\right] \tag{5.6}$$

$$\frac{d}{dt}\left[\mathrm{O_2}\right] = 2\phi_{\mathrm{CH4}} - 2k_{\mathrm{eff}}\left[\mathrm{O_2}\right]\left[\mathrm{CH_4}\right] - k_{\mathrm{esc}}\left[\mathrm{CH_4}\right] + F_B - (F_V + F_M + F_W) \tag{5.7}$$

where k_{eff} ($Tmol^{-1}$ yr^{-1}) is the effective rate constant for a net bimolecular kinetic destruction of O_2 and CH_4. This reaction is 'effective' because it is not a real bimolecular reaction but the net result of many other reactions, starting with an attack on CH_4 by OH, the hydroxyl radical. We have numerically parameterized k_{eff} from over a thousand photochemical model runs as a function of CH_4 and O_2 levels, as described in Chapter 3. The constant k_{esc}= 3.7×10^{-5} Tmol O_2 equivalents yr^{-1} $(Tmol\ CH_4)^{-1}$ parameterizes the net photochemical destruction of methane associated with diffusion-limited hydrogen escape, $F_E = k_{esc}\,[CH_4]$. As four H atoms escape, a CH_4 molecule is subtracted from our tally of methane in equation (5.3) by the term "- $k_{esc}\,[CH_4]$". The remaining carbon atom (in both anoxic and oxic atmospheres) ultimately form CO_2 by a series of photochemical reactions, which acts as a net sink for atmospheric O_2. Owing to this, one O_2 redox equivalent is subtracted from our model atmosphere in equation (5.4) in the term "- k_{esc} $[CH_4]$". However, since one molecule of methane ordinarily consumes two molecules of O_2 (the reverse of equation (5.2)), the net effect of methane-induced hydrogen escape is that the Earth gains an O_2 equivalent (Catling *et al*. 2001). Parameterizations for the following (and their corresponding sensitivities in the model) are described in Chapter 3 and will not be repeated here: (i) evolution of the metamorphic reducing gas flux F_M as a function of crustal redox state and (ii) evolution of volcanic reducing gas flux F_V. The oxidative weathering loss is parameterized as $F_W = k_W\,[O_2]^{\beta}$, where β ~0.4 is a dimensionless constant (see Chapter 3 for justification) and the constant k_w = 0.0065 $Tmol^{0.6}$ yr^{-1} is based on the estimated modern flux, F_W ~ 7 Tmol O_2 yr^{-1} and the known modern concentration of oxygen, $[O_2]$ = 0.21 bar $\times$ (1.78×10^8 Tmol/bar) = 3.7×10^7 Tmol.

5.2.2 How methanotrophic feedback should influence the rise of O_2

Microbial methanotrophy results in the oxidation of methane with O_2, sulfate or nitrate. When sufficient methane and O_2 coexist, methane-oxidizing bacteria (methanotrophs) live off the reverse of equation (5.2). But in anoxic conditions, AOM is performed by a consortium of archaea and bacteria and requires either SO_4^{2-} (e.g. Barnes & Goldberg (1976) and Reeburgh (1976) for pioneering papers or Valentine (2002) for a recent review) or NO_3^- (Raghoebarsing *et al*. 2006). The main source of oceanic SO_4^{2-} today is

O_2-dependant oxidative weathering (Holland 1978; Walker & Brimblecombe 1985). The lack of $\delta^{34}S$ fractionation in Archean marine sediments indicates low oceanic sulfate levels, which is consistent with very small fluxes of oxidative weathering (Canfield *et al*. 2000; Habicht *et al*. 2002). In terms of our model, the F_W term in equation (5.4) was very small during the Archean. Fixation of N_2 to NH_4^+ is considered to be genetically ancient, but O_2 is required to further oxidize the ammonia to nitrate, so NH_4^+ was probably the dominant nitrogen species in Archean oceans (Beaumont & Robert 1999; Berman-Frank *et al*. 2003).

Owing to the lack of sulfate and nitrate in the Archean, we assumed Archean AOM to be fully limited in Chapter 3. Thus, all CH_4 that was likely to be made from organic carbon production was fluxed to the atmosphere. In this chapter, we explore the idea that any sulfate produced as the atmosphere transits to an oxic state would allow AOM to act as a significant throttle on methane fluxes through the following net reaction for AOM, which is performed by a consortium of CH_4-oxidizing archaea and sulfate-reducing bacteria (Boetius *et al*. 2000):

$$CH_4 + SO_4^{2-} \rightarrow HS^- + HCO_3^- + H_2O \qquad (5.8)$$

In the Archean ocean, which had abundant ferrous iron at depth, such sulfide generated by methanotrophy would be rapidly removed as iron sulfides (Walker & Brimblecombe 1985). We focus on sulfate rather than nitrate because methanotrophy with sulfate occurs at a lower redox state and the available evidence suggests that the nitrogen would predominantly be in the ammonium state prior to the oxic transition. Incorporation of nitrate methanotrophy and the nitrogen cycle is beyond the scope of this chapter.

The key point for the evolution of the environment is that with the presence of sulfate, the reducing partner that accompanies O_2 production in equation (5.2) is changed from volatile CH_4 to involatile sulfide. Clearly, O_2 and CH_4 would no longer flux to the atmosphere in the ratio of 2:1 under these circumstances. We would expect this flux imbalance to help O_2 win control of the redox state of the early atmosphere. The flux

imbalance should also amplify in positive feedback at the oxic transition as more sulfate is produced.

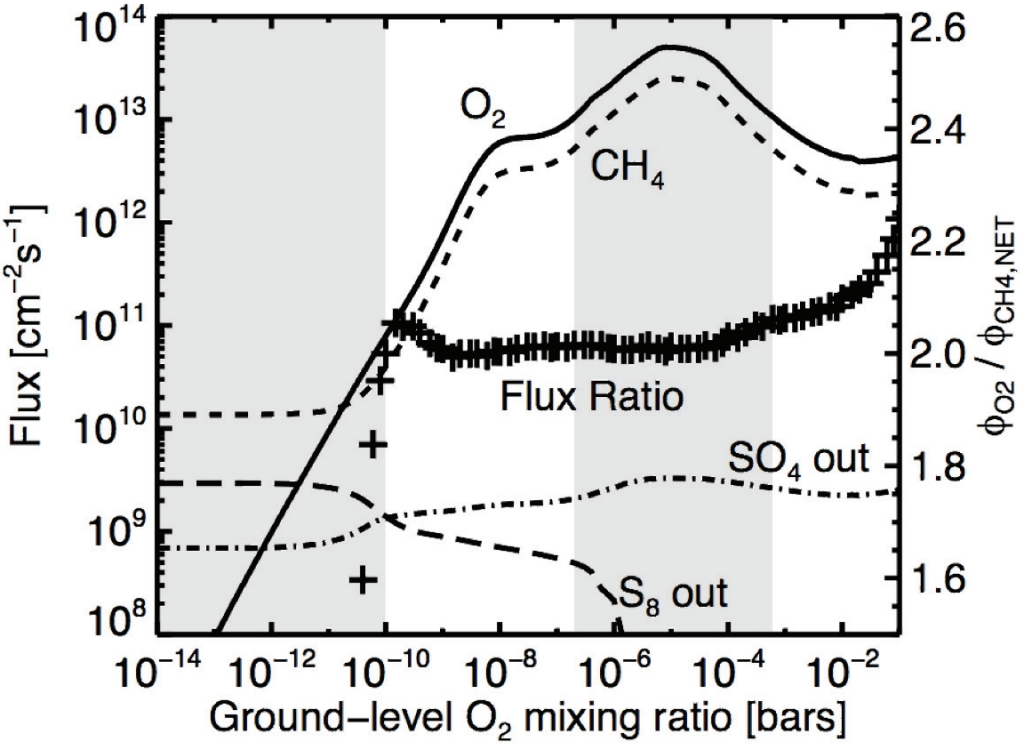

Figure 5-2 Major atmospheric fluxes for a fixed CH_4 mixing ratio of 100 ppmv

Fluxes of chemical species are given in molecules cm^{-2} s^{-1} as a function of the ground-level O_2 mixing ratio and fixed volcanic outgassing fluxes of sulfur gases and reducing gases (see text). Plus symbols (+) map to the right-hand ordinate axis and indicate the net ratio of the biogenic O_2 flux (ϕO_2)to CH_4 flux (ϕCH_4) as a function of the ground-level O_2 mixing ratio (equivalent to a partial pressure in bars to a 1 bar atmosphere). The shaded regions represent cases when the biogenic O_2 fluxes are either implausibly high or low.

With a given outgassing flux of reduced gases, the difference between an oxic and anoxic atmosphere can result from just a few per cent increase in the ratio of O_2:CH_4 fluxes, according to the calculations with the one-dimensional photochemical model that we have described in Chapter 4. In this model, the O_2:CH_4 flux required to support a given atmospheric composition is slightly different from 2:1 because atmospheric redox balance is not just between O_2 and CH_4, but modulated by rainout of photochemical oxidants and reductants, as well as the escape of hydrogen to space. Figure 5-2 shows

results from the photochemical model for assumed sulfur outgassing fluxes of approximately 1 Tmol S yr^{-1} (a modern, high-end estimate of outgassing with SO_2:H_2S fluxes in the ratio of 10 : 1, discussed in Chapter 4), a fixed methane mixing ratio of 100 ppmv, and fixed outgassing flux of H_2 (2.7 Tmol yr^{-1}) and CO (0.3 Tmol/yr). The plot shows the O_2, CH_4, SO_4^{2-} and S_8 fluxes which the photochemistry requires for a steady-state solution when the O_2 mixing ratio is set to that shown on the x -axis. The plus symbols ("+") are the ratio of the O_2 and CH_4 flux curves, which map to the right-hand ordinate axis. Shaded regions in figure 5-2 are considered 'forbidden' because they require biogenic fluxes that are unreasonable according to arguments presented in Chapter 4. Denoting O_2 and CH_4 fluxes by the symbols ϕ_{O2} and ϕ_{CH4}, respectively, the oxic solutions in figure 5-2 have slightly higher ϕ_{O2}/ϕ_{CH4} ratios than the anoxic solutions. The mean value of ϕ_{O2}/ϕ_{CH4} in the stable anoxic regime (O_2 with a mixing ratio of 1×10^{-10} to 2×10^{-7}) is 2.014, while the mean ratio in the stable oxic regime (O_2 with a mixing ratio 6×10^{-4} to 0.1) is 2.11, which is an average increase of 4.8%. The flux ratio change between the most oxic anoxic atmosphere and the least oxic oxygenated atmosphere (i.e. from both sides of the forbidden, shaded of $2\times10^{-7} < O_2 < 6\times10^{-4}$) is approximately 3%.

It is important to realize that for the results of our biogeochemical model, we are considering a non-steady-state, time-dependent Earth system. Consequently, one should avoid falling into a 'steady-state trap' of thinking that consumption of O_2 associated with continental sulfide weathering (which is included as a proportion of flux F_W in equation (5.4) in our model) must exactly balance any reduction of sulfate. Sulfate built up in the ocean going from the Archean to the Proterozoic, so that the summed flux of sulfate-producing weathering plus input from photochemical sulfate rainout must have outpaced sulfide deposition in the ocean. Indeed, during the Archean, the primary input of sulfate to the oceans would have been photochemical production in the atmosphere, as originally suggested by Walker & Brimblecombe (1985) and verified by our photochemical calculations (e.g. the sulfate rainout flux in figure 5-2 in the anoxic regime is approx. 0.25 Tmol S yr^{-1}). Thus, a curious subtlety is that marine microbial sulfate reduction should have exceeded the flux of sulfate from weathering in the Archean

because the sulfate at this time primarily derived from photochemical oxidation of volcanic gases. Hydrogen escape to space supported a sulfate rainout flux.

Finally, another potential subtlety is that with the wider availability of sulfate during the oxic transition, the gaseous reduced partner of O_2 may have changed from CH_4 to biogenic sulfur gases. These sulfur gases, unlike methane, are kinetically much more unstable than O_2. The photochemistry of such an atmosphere would clearly favour higher concentrations of O_2. Biogenic sulfur gases include CH_3SCH_3, OCS and CS_2. According to the review by Warneck (2000, p. 611), today's biogenic S flux of dimethyl sulfide is approximately 1.1 Tmol S yr^{-1}, which exceeds estimated volcanic sulfur fluxes ranging approximately 0.3–1 Tmol S yr^{-1}. However, the potential feedback of biogenic sulfur gases falls beyond the scope of the present chapter because they are not yet implemented in either our photochemical or biogeochemical models.

5.2.3 The magnitude of AOM and its parameterization

AOM with sulfate takes place in a narrow vertical zone in sediments called the sulfate–methane transition zone (SMTZ). Generally, in modern sediments, the sulfate–methane boundary lies at some distance (typically 0.1–4 m) below the seawater–seafloor interface. In this zone, virtually all the methane generated within marine anaerobic sediments is consumed by AOM before it can escape (Reeburgh 1996). Today, significant methane fluxes into the oceanic water column from sediments are produced only at rare places where very high methane fluxes, such as those from mud volcanoes, push the sulfate–methane boundary to within a few centimeters or less of the seafloor (Luff & Wallmann 2003). Consequently, today's oceans are estimated to be a relatively minor source of methane whereas land-based freshwater wetlands are relatively significant owing to their lack of sulfate.

In the Archean and during the oxic transition, the vertical redox profile of marine sediments is likely to have been markedly different from today. Figure 5-3a shows a schematic of the modern profile of sulfate and methane in marine sediments. Modern seawater contains around 29 mM of sulfate, which is often well mixed by fauna into a

bioturbation zone at the top of sediments. Below this bioturbation zone, the sulfate concentration starts to decline due to microbial sulfate reduction. Typically, methane concentrations are found to increase below the depth where sulfate concentrations fall below approximately 0.5–5 mM (Iversen & Jorgensen 1985; Whiticar 2002). The crossover depth, where sulfate and methane concentrations are small and roughly similar, is generally close to where the peak rate of AOM occurs (figure 5-3b; Devol 1983; Haese *et al*. 2003). In Archean sediments, there would be no bioturbation zone. Moreover, Archean oceanic sulfate concentrations were less than 0.2 mM (Habicht *et al*. 2002), so methane would be abundant in sediments all the way to the seafloor, where methane would flux out. During the rise of oxygen, the SMTZ would be a narrow interface just below the seafloor (figure 5-3c).

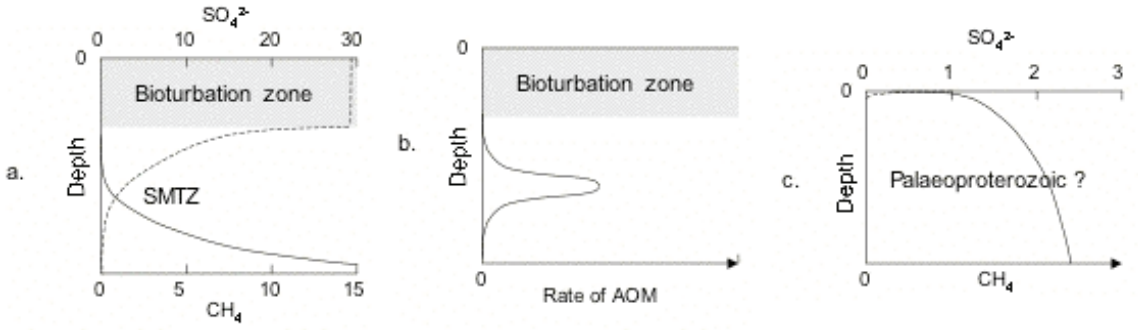

Figure 5-3 AOM Schematics

(a) A schematic showing typical profiles of methane and sulfate in modern marine sediments, where SMTZ is the sulfate–methane transition zone. Solid line, methane concentration in pore waters (mM); dashed line, sulfate concentration in pore waters (mM). Depth is relative. (b) A schematic showing the profile of AOM rate that corresponds to (a). (c) A schematic of relative methane concentration (solid line) and sulfate concentration (dashed line in millimolar) for the Paleoproterozoic.

The flux of methane consumed in modern marine sediments per unit area, f_{AOM}, can be estimated from empirical data as

$$f_{AOM} \sim Hr_{AOM} \tag{5.9}$$

Generally, there is a bell-shaped curve with depth of the AOM rate (figure 5-3b), and in equation (5.6), H is its characteristic half-width. The rate of AOM, r_{AOM}, is given by

$$r_{AOM} = K_{AOM} C_{SO4} C_{CH4} \tag{5.10}$$

where K_{AOM} is an empirical kinetic rate constant, and C_{SO4} and C_{CH4} are the concentrations within the SMTZ (Luff & Wallmann 2003; Wallmann *et al*. 2006). AOM depends on the abundance and activity of the AOM microbial community (Wallmann *et al*. 2006) but a reasonable average value is K_{AOM} ~8 mM^{-1} yr^{-1} = 8 mol^{-1} m^3 yr^{-1} (Van Cappellen & Wang 1996). Typical concentrations at the sulfate–methane transition are C_{SO4} ~ 3mM = 3 mol m^{-3}, C_{CH4} ~ 1 mM = 1 mol m^{-3} and H = 0.04 m (Devol 1983; Iversen & Jorgensen 1985; Haese *et al*. 2003), giving an estimate f_{AOM} = (0.04 m)(8 mol^{-1} m^3 yr^{-1})(3 mol m^{-3})(1 mol m^{-3}) ~ 1 mol CH_4 m^{-2} yr^{-1}. This value is consistent with the observation that a typical shelf sediment has a total C mineralization of about 10 mol C m^{-2} yr^{-1}, of which about 10% is due to methanogenesis, giving approximately 1 mol CH_4 m^{-2} yr^{-1} (Canfield 1991; Middelburg *et al*. 1997). Most organic matter accumulates in coastal sediments or ocean margin sediments that represent approximately 7 and 9% of the ocean area, respectively (Middelburg *et al*. 1997), with the former probably more important for methane generation. Given that the total ocean area is 1.8×10^{14} m^2, if roughly 10% of it generated an estimated 1 mol CH_4 m^{-2} yr^{-1}, the global amount of methane consumed today by marine AOM would be (0.1)(1.8×10^{14} m^2)(1 mol m^{-2} yr^{-1}) ~ 18 Tmol CH_4 yr^{-1}. This value is broadly consistent with an independent estimate of the global AOM rate from Hinrichs & Boetius (2002). They estimate mean AOM rates of 0.37, 0.22, 0.22 and 0.073 mol m^{-2} yr^{-1}, for inner shelf, outer shelf, inner margin and outer margin regions, respectively, and derive a global flux of approximately 24 Tmol CH_4 yr^{-1} when high flux seepage areas are also added. Thus, a potentially large flux of methane of a few tens of Tmol CH_4 yr^{-1} magnitude apparently never escapes from the marine sediments; this flux can be compared with the estimated total global flux of methane from all sources that actually reaches the modern atmosphere, which ranges from 31 to 38 Tmol CH_4 yr^{-1} (Prather *et al*. 2001).

The estimate of a few tens of Tmol CH_4 yr^{-1} from modern AOM rates may underestimate the amount of methane that was generated in the largely anoxic Archean after the advent of oxygenic photosynthesis. Methane is produced from organic carbon that would otherwise be buried or used for reduction of local oxygen carriers such as sulfate; in anaerobic sediments, organic carbon reduces sulfate directly, i.e. SO_4^{2-} + $2CH_2O$ = H_2S + $2HCO_3^-$. The average ratio of the AOM rate to the rate of sulfate reduction by organic

matter in modern continental margins is estimated to be approximately 30% (Hinrichs & Boetius 2002). Taking the modern rate of methanogenesis as approximately 24 Tmol CH_4 yr^{-1}, in the absence of sulfate, the potential rate of methanogenesis could have been approximately 100 Tmol CH_4 yr^{-1}. We adopt this value as a baseline estimate for the global flux of methane from all sediments, ϕ_{CH4}, in our biogeochemical model for the Archean and Early Proterozoic, as expressed in equations (5.3) and (5.4). In section 5.3.2, we describe the sensitivity of the model to this parameter. When methane fluxes are high and sulfate levels low, data from modern environments suggest that almost all sulfate couples to the AOM (Aharon & Fu 2000; Boetius *et al*. 2000). Thus, in the Archean and the Early Proterozoic, as a first-order approximation, we assume that AOM was the major process coupled with sulfate reduction, as argued by Hinrichs (2002) and Hinrichs & Boetius (2002).

In Chapter 3, we suggested that the Archean ocean could have provided a large flux of methane approximately 10^2 Tmol CH_4 yr^{-1} to the atmosphere owing to the lack of global reservoirs of sulfate and oxygen. How would the methane flux vary in time when sulfate levels increased? During the rise of oxygen, methane would be consumed at the seafloor in proportion to small amounts of increasing sulfate, according to equation (5.6). But once sulfate concentrations exceeded approximately 5 mM, the SMTZ would be pushed far below the seafloor into sediments, as it generally is today. At this point, virtually all the methane would be consumed by AOM and further increases in sulfate would not be expected to make any significant difference to the methane flux that escapes from sediments. Thus, the characteristic shape of the response of total AOM to sulfate may look like that schematically shown in figure 5-4. Proterozoic levels of sulfate after the rise of O_2 are constrained from sulfur isotopes to have been between 1.5 and 4.5 mM for ~1 Ga (Shen *et al*. 2003; Kah *et al*. 2004). Our proposed shape of the high sulfate end of the curve in figure 5-4 is probably relevant only to the Late Proterozoic 'second rise of O_2' at ~0.6 Ga (Fike *et al*. 2006; Canfield *et al*. 2007), because once sulfate levels exceeded approximately 5 mM, there is potential for rapid growth in oceanic sulfate and atmospheric O_2 levels. In this chapter, we leave the second rise of O_2 to future work and restrict ourselves to examining the ~ 2.4 Ga Paleoproterozoic oxic transition.

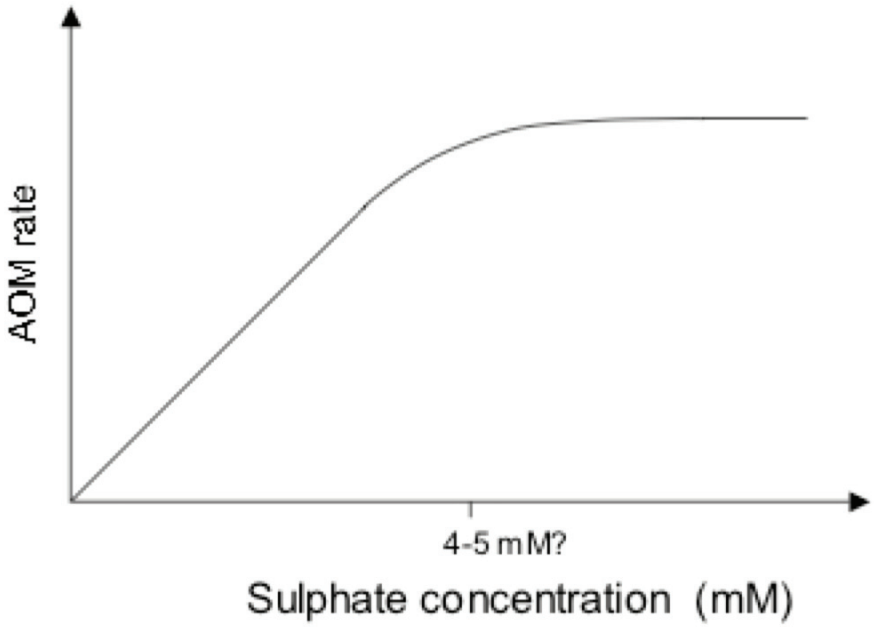

Figure 5-4 AOM rate vs. sulfate concentration

A schematic of the global rate of consumption of methane from AOM as the oceanic sulfate concentration increases.

To a first approximation, the global flux of CH_4 to the atmosphere is modulated by subtracting the flux of CH_4 consumed by anaerobic methanotrophy. Thus, we modify equation (5.3) as follows:

$$\frac{d}{dt}\left[\mathrm{CH_4}\right] = \left(\phi_{\mathrm{CH4}} - F_{\mathrm{AOM}}\right) - k_{\mathrm{eff}}\left[\mathrm{O_2}\right]\left[\mathrm{CH_4}\right] - k_{\mathrm{esc}}\left[\mathrm{CH_4}\right] \qquad (5.11)$$

where F_{AOM} is the global AOM in Tmol O_2 equivalents yr^{-1}, which is related to sulfate availability and hence the amount of O_2 in the atmosphere. To relate average oceanic sulfate concentrations to atmospheric O_2 levels, we use a semi-empirical approximation. Kah *et al*. (2004) derive a curve for the evolution of Precambrian oceanic sulfate levels based on sulfur isotope data and carbonate-associated sulfate from ancient sediments. For the period of interest, the Late Archean to Paleoproterozoic, marine sulfate concentrations range from less than 0.2 mM before 2.2 Ga, to approximately 0.7 mM at

1.7 Ga and 1.9–2.0 mM at 1.5 Ga. A power-law parameterization that crudely captures this behavior for the Archean and Paleoproterozoic is

$$C_{SO4} = k_{SO4}[O_2]^{0.4} \tag{5.12}$$

where k_{SO4} ~ 0.003 mM Tmol$^{-0.4}$, [O_2] is in Tmol, and C_{SO4} is in mM. Here, [O_2] is consistent with estimates and models for the Archean and Late Paleoproterozoic (Chapter 2; Canfield 2005), but we note that there is considerable uncertainty in this regard.

To relate ocean sulfate concentrations to the global rate of AOM, we consider a simple AOM model. AOM can be modeled given methane and sulfate profiles, along with sediment porosity (Martens & Berner 1977). A common method of estimating AOM rates is to assume that all AOM takes place in an infinitely thin layer at the depth where sulfate concentrations vanish (Haese *et al*. 2003; Jorgensen *et al*. 2004). In the simplest possible model, we ignore advection through fractures and faults, since most marine sediments are dominated by diffusion. Thus, the rate of methane consumption must be balanced by the downward diffusion of sulfate (J, e.g. in mol m^{-2} yr^{-1}) into the seafloor by Fick's first law (Berner 1980)

$$J_{SO4} = -\phi D_s \left.\frac{\partial C}{\partial x}\right|_{AOM} \tag{5.13}$$

where ϕ is the sediment porosity; C is the sulfate concentration in mole m^{-3} (numerically equivalent to millimolar); x is the depth in the sediment; and D_s is the diffusion coefficient in marine sediments. Porosity ϕ varies from 1.0 at the seafloor-water interface to smaller values with depth due to sediment compaction; for our model, where we are concerned with shallow penetration depths of low sulfate oceans, we assume a value of ϕ ~ 0.8. The sediment diffusion coefficient for sulfate depends on temperature and porosity. Taking a typical sediment temperature of ~4 °C, we use $D_s \sim 3 \times 10^{-10}$ m^2 s^{-1} (Iversen & Jorgensen 1993). The concentration gradient of sulfate is $\partial C/\partial x$, which goes from the seafloor to the depth x_{AOM}, of the maximum rate of AOM where $C \rightarrow 0$. Sulfate reduction

and oxidation of methane at the sulfate–methane transition is arguably the most important factor for the depth of the sulfate profile and its often quasi-linear shape when AOM dominates sulfate reduction (Jorgensen *et al*. 2004). Owing to this, we adopt a simple linear approximation to equation (5.10)

$$J_{\mathrm{AOM}} = -J_{\mathrm{SO_4}} = \phi D_{\mathrm{s}} \left.\frac{\partial C}{\partial x}\right|_{AOM} = \phi D_{\mathrm{s}} \frac{C_{\mathrm{SO4}}}{x_{\mathrm{AOM}}} \qquad (5.14)$$

This area flux is multiplied by area A, which we take as 10% of the ocean area, to give an estimated global flux F_{AOM}, of AOM. We note that coastal and shelf sediment area A should depend on the amount of continental landmass. The time evolution of the growth of the continents remains a controversial, open field of inquiry but most models predict that at least 70% of the current continental volume was in place by 2 Ga (Patchett & Arndt 1986; Rogers & Santosh 2004, p. 48), which is close to the time of interest for this chapter.

The AOM flux in equation (5.11) depends on sulfate concentrations and the depth of the sulfate–methane transition, i.e. x_{AOM}. In modern sediments, there is commonly a bioturbation zone that mixes sulfate downwards uniformly (figure 5-3a), and in this case, x_{AOM} is the depth beneath the base of the bioturbation zone rather than below the sediment–water interface. Defined in this way, x_{AOM} varies from a few centimeters depth in shallow coastal sediments to meters depth on the continental slope (Borowski *et al*. 1999; Kruger *et al*. 2005). In the modern ocean, x_{AOM} appears to be a function of organic content of sediments and methane supply (Borowski *et al*. 1996). Hence, x_{AOM} is a few centimeters depth around Black Sea mud volcanoes (Wallmann *et al*. 2006) when compared with many meters depth in oceanic sediments in regions of low methane flux. Since we are concerned with an anoxic, low sulfate ocean in the Archean that progresses to an ocean with a few millimolar sulfate in the Proterozoic, we note that for some globally averaged methane flux from sediments, at low sulfate levels, x_{AOM} must primarily depend on sulfate concentrations in the overlying water to a first approximation. For example, in lakes with anoxic bottom waters and sulfate approximately 2–5 mM, x_{AOM} depths are very close to the water–sediment interface (Ingvorsen & Brock 1982),

while freshwater stratified lakes with less than 0.01 mM sulfate essentially have negligible AOM (Reeburgh & Heggie 1977). Consequently, we parameterize the globally averaged depth of maximum AOM, as follows:

$$x_{\mathrm{AOM}} = k_{SMTZ} C_{\mathrm{SO4}}{}^{\alpha} \tag{5.15}$$

where k_{SMTZ} and α are constants. The connection of the average depth of AOM to sulfate concentrations in marine sediments has received little detailed investigation because modern seawater sulfate concentrations are uniform at 29 mM. Thus, the choice of k_{SMTZ} and α is arbitrary; consequently, we investigate the sensitivity of the model to these parameters when considering the results. We choose baseline values of $k_{\mathrm{SMTZ}} = 0.1$ and $\alpha = 0.4$, for which x_{AOM} varies from approximately 1–15 cm over sulfate concentrations of approximately 0.005–3 mM. Taking equation (5.12) and inserting into equation (5.11) gives the parameterization for the global AOM flux for the Archean to the Proterozoic, as follows:

$$F_{\mathrm{AOM}} = A\phi D_{\mathrm{s}} \frac{C_{\mathrm{SO4}}{}^{(1-\alpha)}}{k_{SMTZ}} \tag{5.16}$$

A full general treatment of the effect of AOM on the rise of O_2 would involve isolating the ocean from the atmosphere in our box model and examining all sulfur fluxes in and out of the ocean constrained by the isotopic record, i.e. integrating a complete sulfur cycle to our biogeochemical model. However, even adding one process such as AOM introduces two new free parameters, therefore a full model would obviously introduce many more. For present purposes, our rough approximations are sufficient to demonstrate the potential of AOM feedback to affect the history of O_2 and CH_4.

5.3 Results and discussion

We present the results of two numerical experiments that both perform a modulation of the methane flux according to equation (5.8). The first uses a simplistic approximation

without the AOM model developed above. The second makes use of the AOM model captured in equation (5.13).

5.3.1 Method 1: simple modulation of the CH_4 flux

For the first numerical experiment, we modulate the methane flux according to equation (5.8) with a factor that depends directly on oxidative weathering. Let us take the estimate that 45% of the oxidative weathering flux is used to mobilize sulfate (Holland 2002) and assume that the sulfate washed to the ocean by rivers is immediately available for methanotrophy. Thus, we take $F_{AOM} = 0.45F_W$ where F_W is the oxidative weathering flux, which is parameterized as a function of atmospheric O_2 levels as described in section 5.2. The advantage of this crude experiment is that it allows us to investigate the potential effects of any positive feedback and understand them algebraically.

Figure 5-5a shows the results of including this AOM feedback when compared with the reference model of Chapter 3 with ϕ_{CH4}=100 Tmol yr^{-1} CH_4, as discussed in section 5.2.3. Figure 5-5b shows the corresponding AOM fluxes and seawater sulfate concentrations. O_2 rises more rapidly when AOM is included and to a level about an order of magnitude higher than that without AOM. Surprisingly, methane 're-rises' faster after the oxic transition and to a higher value in this new scheme, despite the consumption of methane by AOM. Algebraic analysis helps explain this apparently counter-intuitive behaviour of methane. We can solve equation (5.3) in the steady state ($d[CH_4]/dt = 0$) by assuming that the hydrogen escape term is a minor term after the rise of O_2 (i.e. $F_E = k_{esc}\,[CH_4] \rightarrow 0$):

$$[CH_4]\big|_{Oxic} = \frac{\phi_{CH4} - F_{AOM}}{k_{eff}\,[O_2]} \tag{5.17}$$

The effective rate constant, k_{eff}, has a nonlinear dependence on CH_4 and O_2 levels, particularly below an O_2 level of 10^{-6} bar and for CH_4 levels more than 10^{-4} bar (see fig. 3-3). However, in the region $O_2 > 10^{-6}$ bar and $CH_4 < 10^{-4}$ bar, the dependence of k_{eff} on

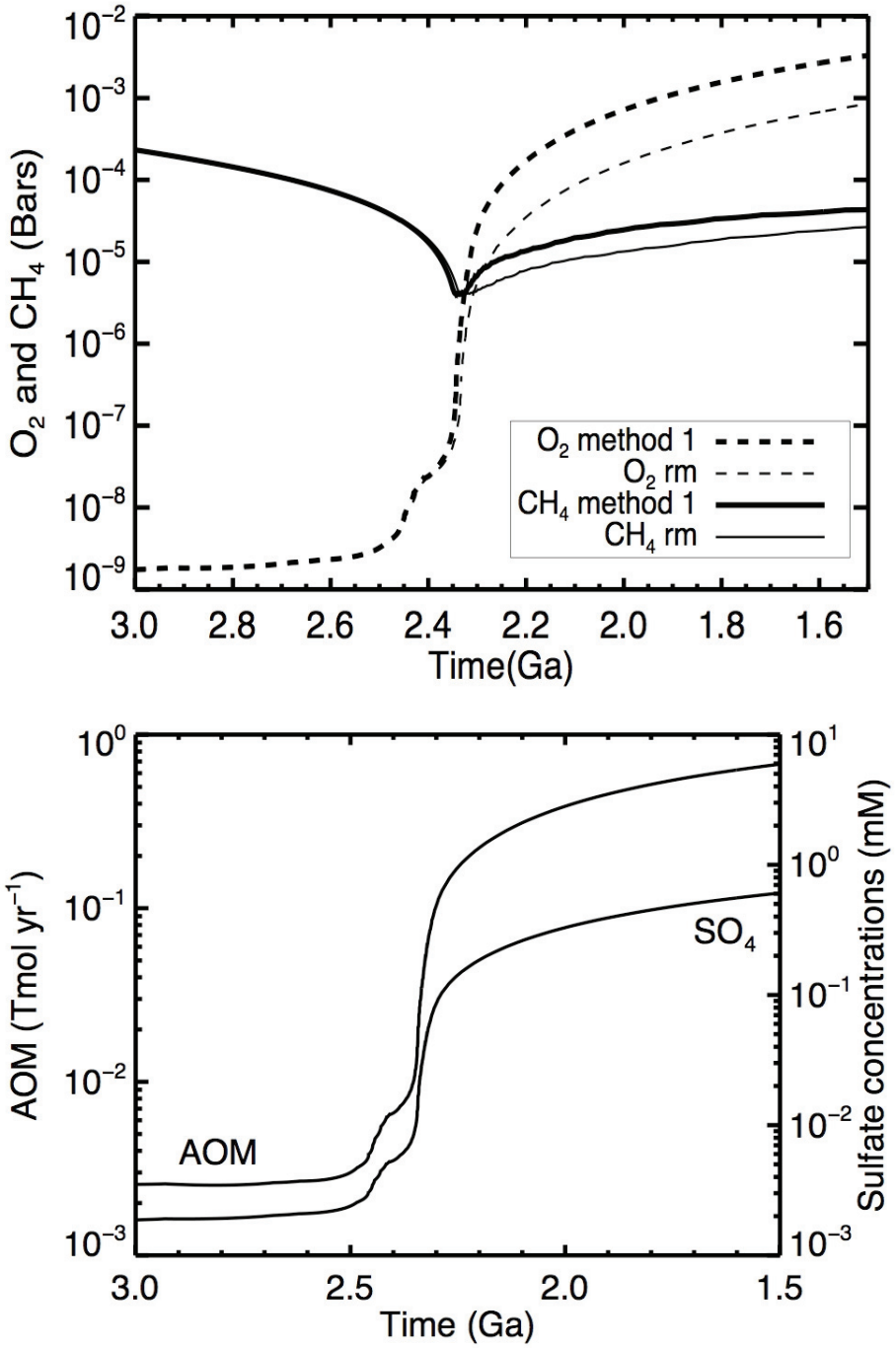

Figure 5-5 Effect of AOM on reference model – 'method 1'

(a) A comparison of the evolution of O_2 and CH_4 from the biogeochemical model with and without the inclusion of AOM using method 1 (see text). The model with AOM is labeled 'method 1' and the model without AOM is the reference model of Chapter 3, labeled 'rm'. (b) Corresponding plot of simulated seawater sulfate concentrations AOM rates versus time for method 1.

$[O_2]$ is approximately linear on a log–log plot so that a least-squares fit provides a power-law relationship, as follows (with correlation coefficient $R^2 = 0.994$):

$$k_{\text{eff}}(O_2) = 1.8368\ [O_2]^{-1.2448} \tag{5.18}$$

where $[O_2]$ is the global amount of atmospheric O_2 in Tmol. Equation (5.15) is applicable for $[O_2]$ amounts in the atmosphere greater than approximately 100 Tmol, where this amount of oxygen is equivalent to a partial pressure of approximately 10^{-6} bar in a 1 bar atmosphere. Substituting equation (5.15) into equation (5.14) gives

$$[CH_4]\big|_{\text{Oxic}} = \frac{\phi_{\text{CH4}} - F_{\text{AOM}}}{k_{\text{eff}}\ [O_2]} = 0.544\left(\phi_{\text{CH4}} - F_{\text{AOM}}\right)\ [O_2]^{0.2448} \tag{5.19}$$

In the absence of anaerobic methanotrophs, $F_{\text{AOM}} = 0$, hence post-transition CH_4 levels in the reference model are a monotonically increasing function of O_2. In other words, for a given methane flux, the effective rate constant for the oxidation of methane by oxygen in the atmosphere decreases with increasing $[O_2]$ according to equation (5.15), an effect that can be traced to the influence of a thickening stratospheric ozone layer (Catling *et al*. 2004; Chapter 3; Goldblatt *et al*. 2006). If we substitute $F_{\text{AOM}} = 0.45F_{\text{W}} = 0.45k_{\text{W}}[O_2]^{\beta}$ with $\beta = 0.4$ and $k_{\text{W}} = 0.006$ into equation (5.16), we obtain

$$\begin{aligned}[CH_4]\big|_{\text{Oxic}} &= \phi_{\text{CH4}}\,0.544\left(\ [O_2]^{0.2448} - \frac{0.45k_w}{\phi_{\text{CH4}}}\ [O_2]^{0.6448}\right) \\ &= 108.8\left(\ [O_2]^{0.2448} - 1.35\times10^{-5}\ [O_2]^{0.6448}\right)\end{aligned} \tag{5.20}$$

In evaluating the numerical constant, we take the gross production flux of methane ϕ_{CH4}, as a 200 Tmol O_2 yr^{-1} sink, equivalent to a worldwide production of 100 Tmol CH4 yr^{-1} in all Archean–Proterozoic anaerobic sediments, as discussed earlier. Comparing the two terms on the right-hand side reveals that the first term is a factor of 10^2–10^3 higher over the range of O_2 values considered for the Proterozoic after the oxic transition. Thus, in the methanotroph-modified world, CH_4 levels increase at higher O_2 levels in the Paleoproterozoic despite the lower CH_4 flux; this is primarily a result of atmospheric

chemistry as captured by k_{eff}. Overall, the results of our numerical experiment are consistent with the idea that CH_4 continued to be a significant greenhouse gas in the Proterozoic, albeit at a lower concentration than in the Archean (Pavlov *et al*. 2003; Chapters 3 and 4).

5.3.2 Method 2: modulation of CH_4 fluxes by parameterized AOM

In our second numerical experiment, we modulate the methane flux to the atmosphere in equation (5.8) based on relationships given in section 5.2.3 where sulfate diffusion into sediments balances the flux of methane consumed by AOM.

Figure 5-6a shows the results of using the parameterizations described by equations (5.11) and (5.12) ('method 2'), compared to the results presented in section 5.3.1. The O_2 and CH_4 curves are qualitatively similar in shape and slope, although the curves generated from computing F_{AOM} using method 2 hasten the time of oxic transition by ~0.1 Gyr. Figure 5-6b shows the two curves referenced to the oxic transition; with method 2, O_2 rises from less than $<10^{-6}$ to 10^{-4} bar in ~0.05 Ga, about twice as rapidly as 'method 1'.

The effect on the timing of the transition can be understood with algebra. In Chapter 3, we discussed the timing of the oxic transition in terms of the fluxes of organic burial (F_B) versus the flux of O_2-consuming species from volcanism/hydrothermal (F_V) plus metamorphism/geothermal reductants (F_M), following an argument originally advanced by Walker *et al*. (1983). Essentially, the oxic transition occurs at the point when the O_2 produced by the organic burial flux, F_B, exceeds the sum of the reductant fluxes, $F_V + F_M$. Consequently, we defined an oxygenation parameter K_{OXY}, based on kinetically active reduced gases in the ground-level atmosphere and reduced cations in the ocean

$$K_{OXY} = \frac{F_{SOURCE}}{F_{REDUCED\ SINKS}} \sim \frac{F_B}{F_V + F_M} \qquad (5.21)$$

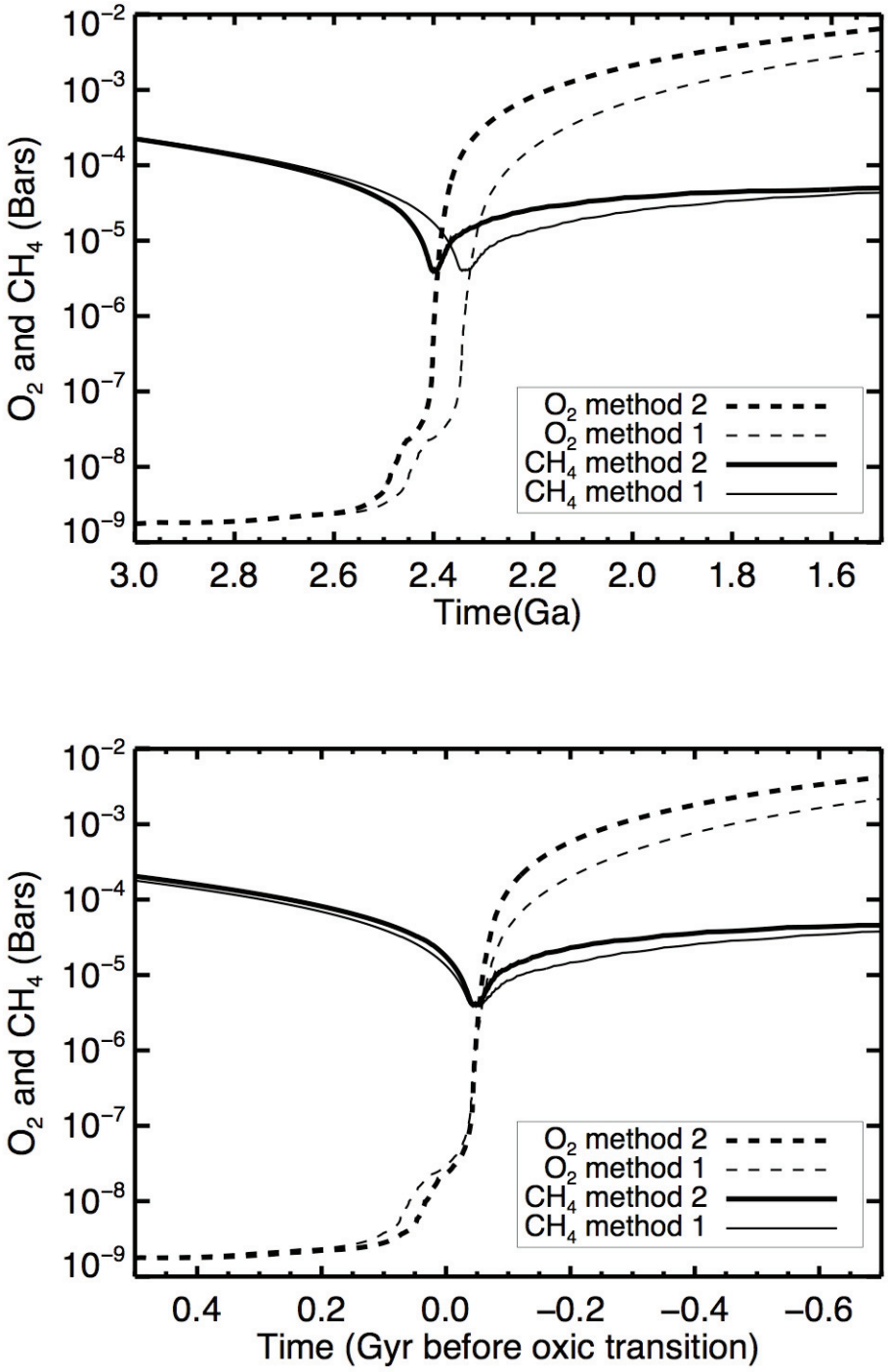

Figure 5-6 Effect of AOM on reference model – 'method 1' vs. 'method 2'

(a) A comparison of the evolution of O_2 and CH_4 in the model using method 1 and method 2 (see text). (b) The plots for each model run where the time axis has been referenced to the time (equal to 0) of the oxic transition.

We define the atmosphere as oxygenated when $K_{OXY} > 1$. If we include methanotrophy, it can impact K_{OXY} and hence the timing of the oxic transition in the following manner. An approximate steady-state solution for the evolution of CH_4 at the time of the oxic transition can be found by setting the hydrogen escape term, $F_E = k_{esc}[CH_4]$, to zero in equation (5.3) to obtain

$$\phi_{CH4}\Big|_{trans} \simeq F_{AOM} + k_{eff}\left[O_2\right]\left[CH_4\right] \tag{5.22}$$

Taking $F_E = 0$ and substituting twice equation (5.19) into equation (5.4) yields an equation for the evolution of O_2 at the time of the oxic transition:

$$\frac{d}{dt}\left[O_2\right]\Big|_{trans} = 2F_{AOM} + F_B - (F_V + F_M + F_W) \tag{5.23}$$

The balance on the right-hand side of equation (5.20) provides an expanded version of the oxygenation parameter (K_{OXY}*) that includes the AOM flux, F:

$$K_{OXY}{}^* \sim \frac{F_B + 2F_{AOM}}{F_V + F_M + F_W} \tag{5.24}$$

Method 1 used $F_{AOM} = 0.45F_W$ so that $2F_{AOM} \sim F_W$ and K_{OXY}* is approximately equal to K_{OXY} in the reference model. Thus, by coincidence, the timing of the oxic transition was essentially the same. In method 2, the numerical values of F_{AOM} were approximately equal in magnitude to F_W at the time of the oxic transition so that K_{OXY}* reached unity somewhat before K_{OXY}* of method 1.

Equation (5.12), which forms part of the parameterization of AOM, has two free parameters (k_{SMTZ} and α) and we can examine how the model responds to their choice. For the comparison between different parameter choices, we ignore the effect on the timing of the oxic transition because this actually lacks real significance: the timing of this transition in the model is primarily determined by the choice of the parameterization of F_V and F_M, as described in the Chapter 3, and so it is necessarily a tuned parameter. Instead, we reference the time to the oxic transition when K_{OXY}* = 1. In this manner,

figure 5-7 shows the model sensitivities to changing k_{SMTZ} and α from our reference values of 0.1 and 0.4. Figure 5-7a shows that decreasing k_{SMTZ} sharpens the rate of the oxic transition and increases the post-oxic atmospheric O_2 and CH_4 concentrations. Effectively, when k_{SMTZ} is decreased, AOM rates increase. In contrast, figure 5-7b shows that the model is relatively insensitive to the choice of α.

Finally, the qualitative results of the model are insensitive to the exact value chosen for the global methane flux generated in all sediments, ϕ_{CH4}, which we have nominally taken as 100 Tmol CH_4 yr^{-1} (see section 5.2.3). The main effect of changing ϕ_{CH4} is to alter the level of the minor gas (O_2 or CH_4) in the anoxic or oxic worlds. In the case of lower ϕ_{CH4}, O_2 is lower in the Archean, while CH_4 is proportionately lower in the Proterozoic, as predicted by equation (5.14).

5.4 Conclusions

Empirical data show that a significant flux of CH_4 is consumed by AOM in modern marine sediments before the methane even reaches the seafloor. This flux is estimated as roughly 20 Tmol CH_4 yr^{-1} (section 5.2.3). Consequently, a large amount of biogenic methane never reaches the modern atmosphere. However, in the Archean ocean with less than 0.2 mM sulfate, AOM and other forms of sulfate reduction would have been limited by the lack of oxidized substrate so that methanogenesis would arguably have dominated recycling of organic carbon. In this case, a very large flux of methane approximately 100 Tmol CH_4 yr^{-1} produced in anaerobic marine sediments could have fluxed out to the atmosphere. For some perspective, this flux is only 1% of modern net primary productivity approximately 10^4 Tmol C yr^{-1}.

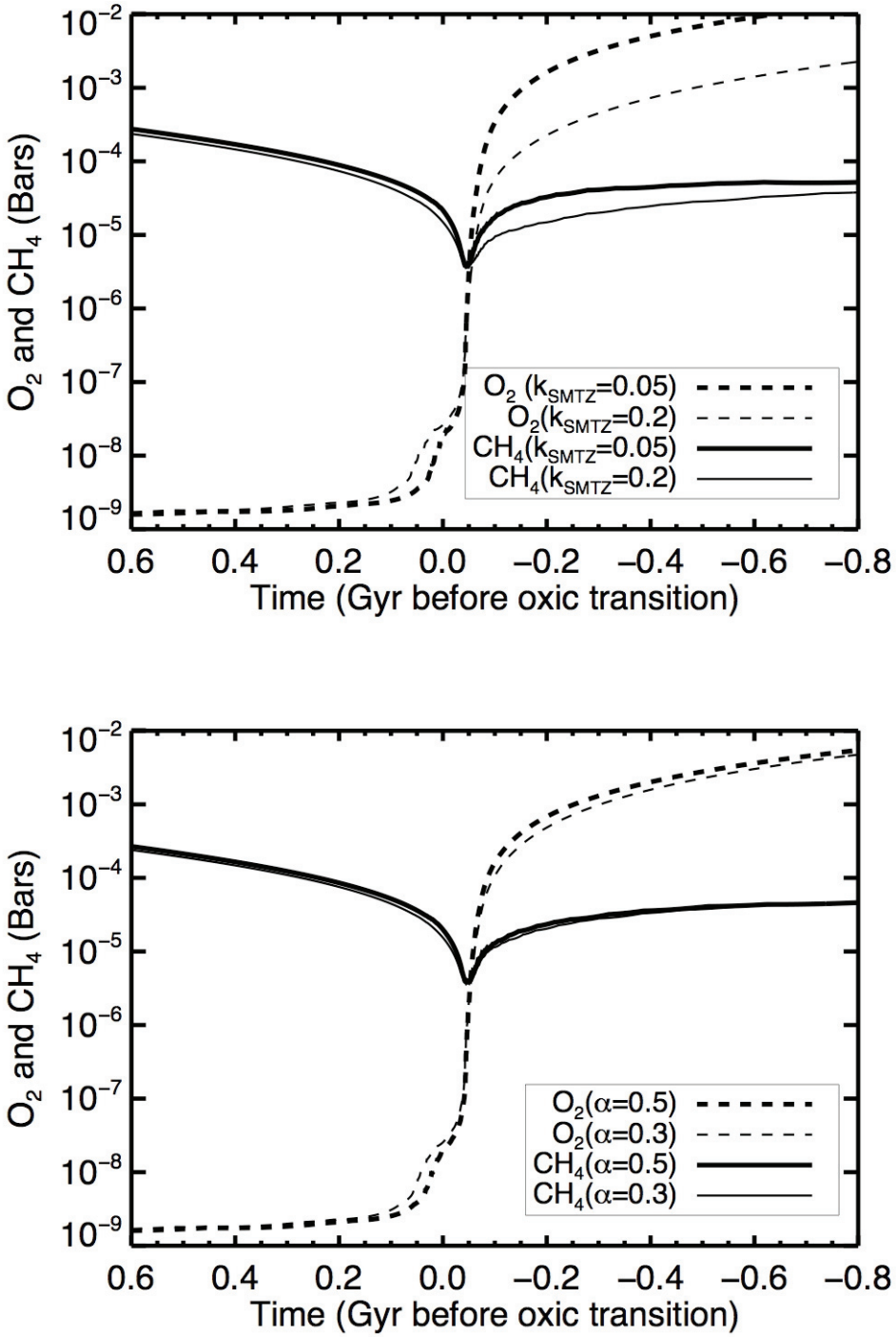

Figure 5-7 Model sensitivity to new tuning parameters

(a) Sensitivity of the model to changes in parameter k_{SMTZ}. (b) Sensitivity of the model to changes in parameter α.

Approaching, during and after the oxic transition, the $\delta^{34}S$ record in marine sediments suggests that the flux of sulfate to the oceans from continental oxidative weathering increased, consistent with the physical expectation that dissolved oxygen in rainwater and rivers would oxidize continental pyrite to sulfate (Habicht *et al*. 2002). We have shown how methanotrophy can act to diminish methane fluxes to the Late Archean atmosphere in the presence of increasing oceanic sulfate. This feedback means that gas fluxes to the atmosphere of O_2 and CH_4 increase slightly from the 2:1 ratio predicted from equation (5.2) because the reducing power of methane is converted to involatile sulfide.

When we include a simple AOM feedback in our model, O_2 rises more rapidly and to a higher value than in the model without the AOM feedback. The time-scale for the oxic transition is shortened, while O_2 rises to a level of a few $x10^{-3}$ bar (a few per cent of present levels) by 2.1 Ga instead of approximately 10^{-4} bar in the reference model. Methane also re-rises faster and to a value of approximately 50 ppmv by the end of the Paleoproterozoic, which is higher than that in the model without AOM feedback. At first sight, obtaining a higher level of Proterozoic methane when AOM is included in the model seems counter-intuitive because AOM diminishes the CH_4 flux to the atmosphere. However, the dominant effect of AOM is to enable O_2 to rise more rapidly to a higher level; consequently, methane levels also rise more rapidly to a higher level because they are enhanced more strongly by the effect of increased shielding effect of the stratospheric ozone layer than decreased by the lowering of the methane flux by AOM. We note that the effect of the nonlinear dependence of AOM at higher O_2 levels (figure 5-4) is not included in the model and may have been important for the Late Proterozoic second rise of O_2 ~ 0.6 Ga.

We showed in Chapter 4 that CH_4 levels should have collapsed in the Early Proterozoic before there was sufficient atmospheric O_2 to be detectable through conventional geologic indicators such as red beds and paleosols. The counter-intuitive twist that methanotrophy allows CH_4 to re-rise after the oxic transition to higher levels in the Proterozoic is relevant to the Proterozoic climate. Stable, relatively high levels of

methane in the Proterozoic may help account for a prolonged period exceeding 1 Gyr where there is no reliable evidence for glaciation (Eyles 1993). Moderately abundant methane could have provided a greenhouse effect that compensated for a fainter Proterozoic Sun (Pavlov *et al*. 2003). The total oxidation of the Earth from the slow leak of hydrogen via methane-induced hydrogen escape may also be important when integrated over more than 1 Gyr of the Proterozoic, as mentioned in Chapter 2.

Finally, our computational experiments provide motivation for laboratory experiments and fieldwork. Clearly, more field data would constrain controls on AOM in sediments and the globally averaged magnitude of AOM, while, in principle, an O_2-free chamber in the laboratory could simulate the response of AOM in marine sediments to increasing levels of seawater sulfate.

Chapter 6 Resolving the paradox of oxidative weathering before the rise of oxygen

This chapter* represents a culmination of the work described in Chapter 3 through 5, but was only enabled by a surprising data set obtained by the NASA Astrobiology Institute Archean Drilling Project (Anbar *et al.*, 2007; Kaufman *et al.*, 2007). The drill core was taken through the upper portion of the Mt McRae shale in the Hamersley basin of Western Australia. The rare-earth elements Molybdenum (Mo) and Rhenium (Re) participate in a time-dependent pulse at 2.501 Ga (Anbar, 2007). These elements are stable and insoluble in their reduced oxidation state, and exist in continental sulfides, primarily as replacement minerals for iron in pyrite (FeS_2). In their oxidized forms, Mo and Re are soluble. The only known source of Mo and Re to the ocean is the oxidative weathering of sulfides, which occurs when oxygen interacts with continental materials. Thus, their data provide evidence of limited oxidative weathering of sulfides prior to the rise of oxygen in the atmosphere, and this may have occurred in a time-dependent fashion, a hypothesis which was whimsically titled “whiff of oxygen” by Anbar *et al.* (2007).

The evidence for oxidative weathering coexists with a very strong MIF-S signal (Kaufman, 2007), which we showed in Chapter 4 can only be produced and preserved in a reducing atmosphere. Taken together, these data present a paradox that we investigate with an updated version of the 1D photochemical model presented in Chapter 4. We show that a strongly anoxic troposphere is still consistent with small amounts of O_2 at the ground sufficient for limited oxidative weathering. MIF-S arises from photochemical processes at altitude, so we suggest that a non-uniform vertical distribution of O_2 resolves the paradox and reaffirms the consensus view that the atmosphere prior to 2.4 Ga was anoxic overall. The ground level concentration of O_2 is not a meaningful metric prior to the rise of oxygen. In our model, increased concentrations of ground level O_2 only become possible after a substantial decrease in

* The formatting in this chapter reflects its submission to *Nature*, which declined to publish the article in the days immediately prior to completion of this dissertation. The material in this chapter will be expanded into a longer and more readable format for submission to an alternate journal.

atmospheric methane concentrations. Therefore, we suggest that the widespread description of Earth's "rise in oxygen" might be better seen as primarily a "collapse of methane" and its consequences.

6.1 Introduction

Multiple lines of evidence show that before 2.4 Ga, Earth's atmosphere was essentially devoid of oxygen (Bekker *et al*., 2004; Canfield, 2005; Chapter 2; Holland, 2006). The strongest constraint is an upper limit of 2 ppm on Archean O_2 (Farquhar *et al*., 2000; Pavlov and Kasting, 2002), which arises from theoretical considerations regarding the production and preservation of MIF-S. Significant Archean O_2 is precluded, because the resulting stratospheric ozone layer would have hindered production of MIF-S (Farquhar *et al*., 2001; Pavlov and Kasting, 2002; Farquhar and Wing, 2003; Chapter 4). In addition, the simultaneous atmospheric deposition of insoluble polymerized sulfur (S_8) and sulfate greatly enhances prospects for geologic MIF-S preservation (Pavlov and Kasting, 2002). The preservation hypothesis provides a stronger constraint on the Archean atmosphere because S_8 aerosol formation requires reducing atmospheric conditions (Pavlov and Kasting, 2002; Chapter 4). As such, MIF-S in ancient rocks (Farquhar *et al*., 2000; Ono *et al*., 2003; Bekker *et al*., 2004; Ono *et al*., 2006; Farquhar *et al*., 2007) provides circumstantial evidence (Chapters 4 and 7) for a CH_4 enriched Archean atmosphere (Kasting, 2005).

In contrast to evidence for anoxia, new data from the 2.50 Ga Mt. McRae shale (Anbar *et al*., 2007; Kaufman *et al*., 2007) in the Hamersley Basin, Western Australia, indicates oxidative processes in the surface ocean. Mo and Re enrichments in multiple locations (Anbar *et al*., 2007; Wille *et al*., 2007) suggest the onset of oxidative weathering of readily soluble continental pyrites that are the primary hosts of these elements, albeit at a much lower rate than today. But the Mt. McRae shale also contains strong MIF-S (Ono *et al*., 2003; Kaufman *et al*., 2007), and hence contains geochemical signatures indicative of both a reducing atmosphere and oxidative weathering, an apparently

contradictory combination of conditions that we describe as a “whiff of oxygen”, following Anbar *et al*. (2007).

This study was motivated by our biogeochemical box model predictions for the coupled evolution of atmospheric methane and oxygen in Chapters 3 and 5. Figure 6-S1 shows updated model results consistent with whiff conditions for approximately 100 million years prior to the oxic transition (see Supplementary Discussion in section 6.6). The whiff solutions occur during a monotonic decrease in the net CH_4:O_2 flux ratio to the atmosphere and arise from incorporation of realistic photochemistry parameterized from a 1D photochemical model. Here, we examine the reasons for a whiff atmosphere using the 1D photochemical model developed in Chapter 4 to simulate the transition from oxygen poor to oxygen rich atmospheres.

6.2 The Photochemistry of Methane and Oxygen

A photochemical model must account for large biogenic fluxes of oxidizing and reducing gases. After the advent of oxygenic photosynthesis and an accompanying jump in primary productivity (Kharecha *et al*., 2005), significant atmospheric CH_4 fluxes would be generated due to enhanced fermentation of organic matter (Walker, 1987; Catling *et al*., 2001). Over long timescales, organic decomposition in anoxic sediments by methanogenesis results in a CH_4 flux to the atmosphere in a 1:2 stoichiometric ratio with respect to the O_2 generated during production of the organic matter (Catling *et al*., 2001; Kasting *et al*., 2001; Chapter 3). The early atmosphere is subject to additional reducing fluxes of H_2 and CH_4 from the solid Earth, where excess H_2 is likely to be microbially converted to CH_4 (Kasting *et al*., 2001; Chapter 2). Consequently, the initial net CH_4:O_2 flux to the atmosphere is greater than 1:2. Once oxidants such as seawater sulfate build up and are able to diffuse into sediments (Chapter 5), or geological reductants decline (Chapter 3; Holland, 2006; Kump and Barley, 2007), the methane flux reaching the atmosphere would be lowered with respect to oxygen fluxes, so that the net CH_4:O_2 flux ratio would drop below 1:2.

Given the input of CH_4 and O_2 fluxes, let us consider the question of which gas dominates the atmospheric redox state. Methane's primary atmospheric destruction pathways are initiated by reactions (R1) - (R5):

$$\begin{aligned}
&\text{(R1)} \quad CH_4 + h\nu \rightarrow {}^1CH_2 + H_2\\
&\text{(R2)} \quad CH_4 + OH \rightarrow CH_3 + H_2O\\
&\text{(R3)} \quad CH_4 + O(^1D) \rightarrow CH_3 + OH\\
&\text{(R4)} \quad CH_4 + O(^1D) \rightarrow H_2CO + H_2\\
&\text{(R5)} \quad CH_4 + O \rightarrow CH_3 + OH
\end{aligned}$$

Prior to significant fluxes of biospheric O_2, (R2) is the strongest tropospheric CH_4 loss process, via OH radicals created by H_2O photolysis in the absence of a stratospheric ozone shield. Once oxygenic photosynthesis evolved (Nisbet *et al*., 2007), biogenic O_2 would be lost subject to the following quantitatively significant tropospheric reactions:

$$\begin{aligned}
&\text{(R6)} \quad O_2 + CH_3 \rightarrow H_2CO + OH\\
&\text{(R7)} \quad O_2 + HCO \rightarrow HO_2 + CO\\
&\text{(R8)} \quad O_2 + H \rightarrow HO_2\\
&\text{(R9)} \quad O_2 + O \rightarrow O_3\\
&\text{(R10)} \quad O_2 + h\nu \rightarrow O + O
\end{aligned}$$

(R9) is not an O_2 sink given the near immediate reverse photolysis reaction to O_2 + $O(^1D)$, but the resulting $O(^1D)$ can attack CH_4 via (R3) and (R4), or react with H_2O to make OH which attacks CH_4 via (R2). (R8) is only a net O_2 sink under reducing conditions which favor H + HO_2 -> OH + OH. Under oxidizing conditions, reactions following (R8) tend to re-make O_2 via O + HO_2 -> OH + O_2 or OH + HO_2 -> H_2O + O_2. Regardless of whether the overall process is O_2 destruction, the photolytic by-products of the O_2 reactions attack CH_4. Although there are complex intermediaries, the net result is a catalytic destruction of CH_4 by O_2. The atmosphere reverses the disequilibrium created by the biosphere (Kasting *et al*., 2001; Kharecha *et al*., 2005), remaking the neutral species CO_2 and H_2O from CH_4 and O_2, with net reaction:

$$CO_2 + 2H_2O \underset{\text{atmospheric chemistry}}{\overset{\text{biology}}{\rightleftharpoons}} CH_4 + 2O_2 \qquad (6.1)$$

The atmospheric redox state is determined by the molecules remaining after the bulk of the destruction in reversing eq. (6.1). CH_4 is relatively inert, while O_2 (and H_2O_2 made from O_2) can react quickly with rocks and reducing species other than CH_4. Thus it is inevitable that the initial atmospheres after the advent of oxygenic photosynthesis are anoxic and CH_4-rich, and concurrently help initiate the oxidation of easily accessible reduced minerals of the Earth.

6.3 Results

In our photochemical models with CH_4:O_2 fluxes > 0.5, O_2 is rapidly consumed and declines in abundance by ~ 6 orders of magnitude in the first few kilometers of altitude (Fig. 6-1).

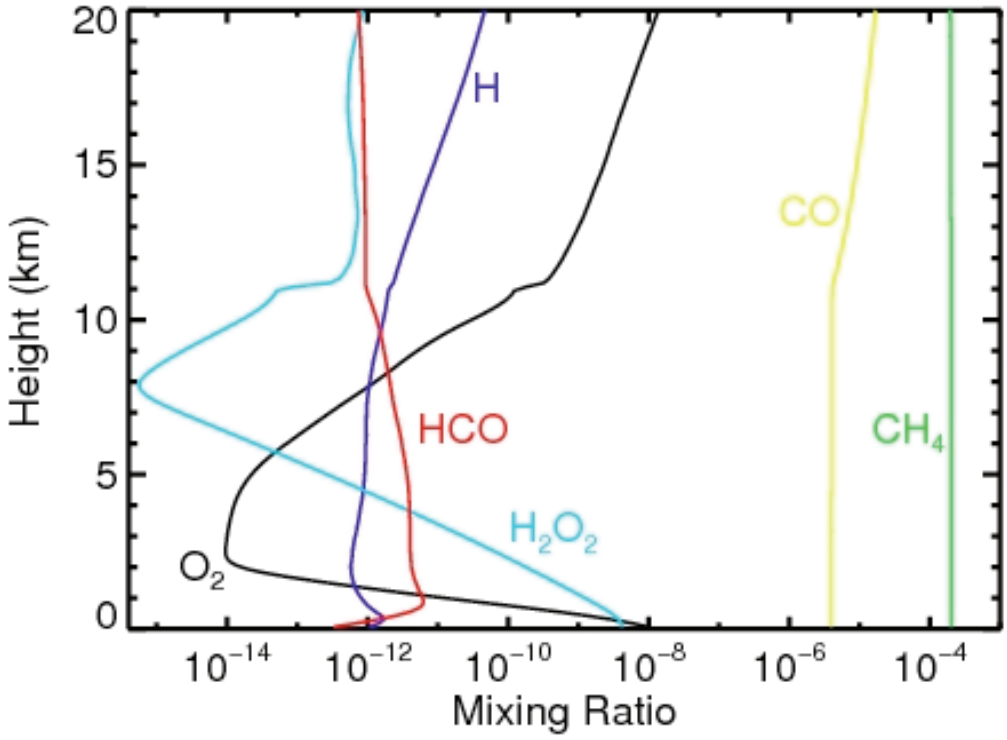

Figure 6-1 The Archean Reference Model

The tropospheric and lower stratospheric vertical profiles for various species in the Archean reference atmosphere, specified by an O_2 mixing ratio of 10 ppb and a CH_4 mixing ratio of 200 ppm (Table 6-1). CH_4 is well mixed throughout the troposphere, while O_2 drops sharply from a maximum of 10 ppb at the ground to 10^{-14} bar in the mid-troposphere. O_2 returns to ppb (and higher) levels in the lower stratosphere, but this is primarily due to CO_2 photolysis.

Table 6-1 Photochemical model results

Results from 7 photochemical models defined by the CH_4 and O_2 mixing ratios in the first row. The O_2 lifetimes are computed by dividing the O_2 number density in the troposphere (summed from 0-11 km) by the vertical sum of all tropospheric O_2 loss processes. The "Archean" O_2 lifetime, O_3 column, and S_8 deposition fractions (S_8 deposition flux / total volcanic S flux) are consistent with previous haze-free Archean photochemical models after the evolution of oxygenic photosynthesis (Pavlov *et al*., 2001; Pavlov and Kasting, 2002). Hydrogen peroxide is the dominant oxidized species raining out of the atmosphere after the evolution of oxygenic photosynthesis, and perhaps plays an important role in early oxidative weathering. The "Proterozoic" atmosphere is defined by O_2 and CH_4 mixing ratios commonly invoked for Proterozoic atmospheres after the rise in oxygen (Pavlov *et al*., 2003; Chapter 4). The CH_4 and O_2 fluxes computed by the photochemical model are consistent with previous estimates in which anaerobic ecosystems (Canfield *et al*., 2006; Sleep and Bird, 2007) produce CH_4 at approximately modern rates (Kharecha *et al*., 2005), and the evolution of oxygenic photosynthesis in an anoxic environment enables CH_4 fluxes that reach the atmosphere of 10-20 times modern (Pavlov *et al*., 2003; Kharecha *et al*., 2005). While photochemical models defined by lower boundary conditions on O_2 and CH_4 mixing ratios lack direct control over the fluxes needed to maintain them, all CH_4 fluxes predicted for our Archean and whiff atmospheres are within 30%. The CH_4:O_2 flux ratios steadily decrease, consistent with biogeochemical expectations from Chapter 3 and 5 (see also section 6.6). Given that the O_2 source is light dependent, our computational methodology utilizing diurnal averaged rate constants may overpredict both O_2 mixing ratios and lifetimes against photochemical destruction.

	pre-oxygenic photosynthesis	**Archean**	**Whiff #1**	**Whiff #2**	**Whiff #3**	**Whiff #4**	**Proterozoic**
pCH_4 [bars]	$1x10^{-3}$	$2x10^{-4}$	$4x10^{-5}$	$2x10^{-5}$	$8x10^{-6}$	$6x10^{-6}$	$2x10^{-5}$
pO_2 [bars]	$1x10^{-14}$	$1x10^{-8}$	$2x10^{-8}$	$3x10^{-8}$	$6x10^{-8}$	$1x10^{-7}$	$2x10^{-3}$
O_2 lifetime	27 min	1.2 hours	2.5 hours	4.5 hours	13.4 hours	25.2 hours	9.7 years
O_3 column [cm^{-2}]	$7x10^{11}$	$4x10^{13}$	$1x10^{14}$	$2x10^{14}$	$4x10^{14}$	$7x10^{14}$	$5x10^{18}$
H_2O_2 deposition [mol cm^{-2} s^{-1}]	$3x10^{4}$	$4x10^{10}$	$4x10^{10}$	$4.2x10^{10}$	$4.2x10^{10}$	$4.4x10^{10}$	$1.5x10^{11}$
S_8 deposition fraction	0.89	0.26	0.29	0.26	0.15	0.05	0
CH_4 : O_2 Flux ratio	Infinite	0.512	0.507	0.505	0.502	0.501	0.484
CH_4 flux [mol cm^{-2} s^{-1}]	$5.5x10^{10}$	$5.8x10^{11}$	$7.2x10^{11}$	$7.2x10^{11}$	$7.3x10^{11}$	$8.2x10^{11}$	$9.2x10^{11}$

The relatively high 10 ppb of ground-level O_2 is due to the proximal biogenic O_2 source. We refer to the model illustrated by Fig. 6-1 as our Archean atmosphere, because it is a proxy for weakly reducing atmospheres after the evolution of oxygenic photosynthesis with CH_4 mixing ratios from ~100 - 1000 ppm (see section 6.6).

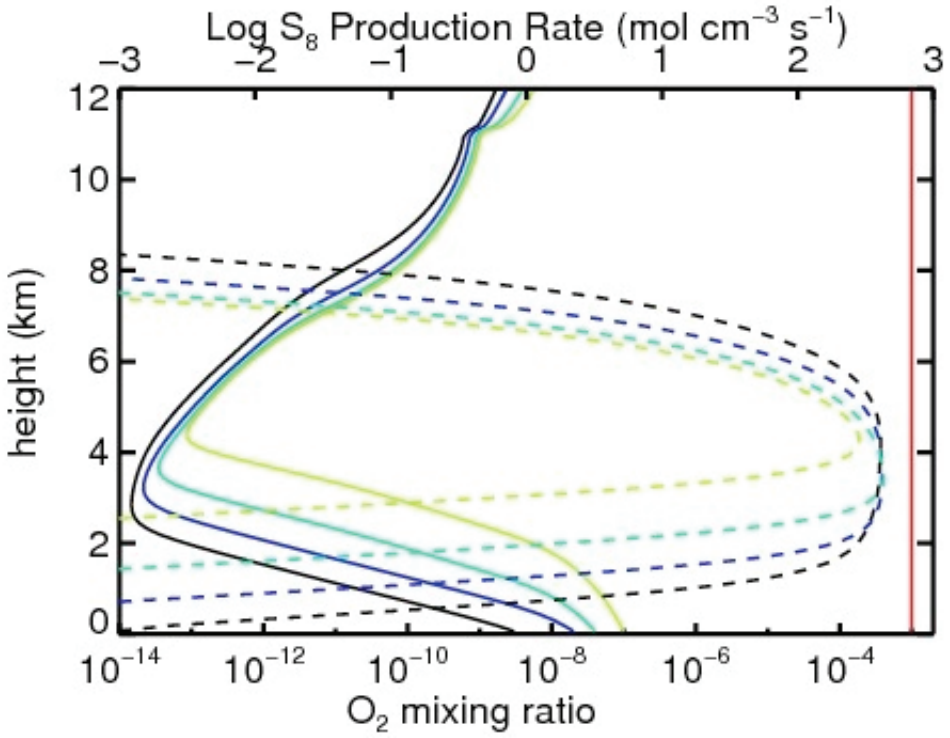

Figure 6-2 O_2 mixing ratios and S_8 production rates

O_2 vertical mixing ratios (solid lines, bottom axis) and S_8 production rates (dashed lines, top axis) as a function of height for the four whiff atmospheres described in Table 6-1. Vertical profiles for whiff atmospheres #1-#4 are shown in black, blue, green, and yellow, respectively. The computed O_2 mixing ratio for the Proterozoic reference case is shown in red – there is no S_8 production in this atmosphere. While the whiff solutions are marked by increasing ground level O_2 mixing ratios ($2x10^{-8}$, $3x10^{-8}$, $6x10^{-8}$, and $1x10^{-7}$, respectively), their O_2 vertical profiles reveal them as part of a continuum of weakly reducing atmospheres, typified by extremely anoxic tropospheres. S_8 formation occurs predominantly where O_2 mixing ratios are less than 10^{-13} and is negligible where O_2 mixing ratios are greater than 10^{-12}.

Despite increasing ground level O_2 partial pressures (pO_2), whiff atmospheres retain the primary characteristics of anoxic atmospheres, which is a sharply declining O_2 profile with height. Figure 6-2 shows the vertical profiles of pO_2 along with S_8 production rates for the whiff model atmospheres defined in Table 6-1. In each case, O_2 vertical profiles

are nearly identical to the Archean reference case (Fig. 6-1). S_8 production only occurs in the troposphere in regions where pO_2 drops below 10^{-12} bar. Prior to the oxic transition, ground level O_2 mixing ratios are not a good proxy for the overall oxidation state of the atmosphere.

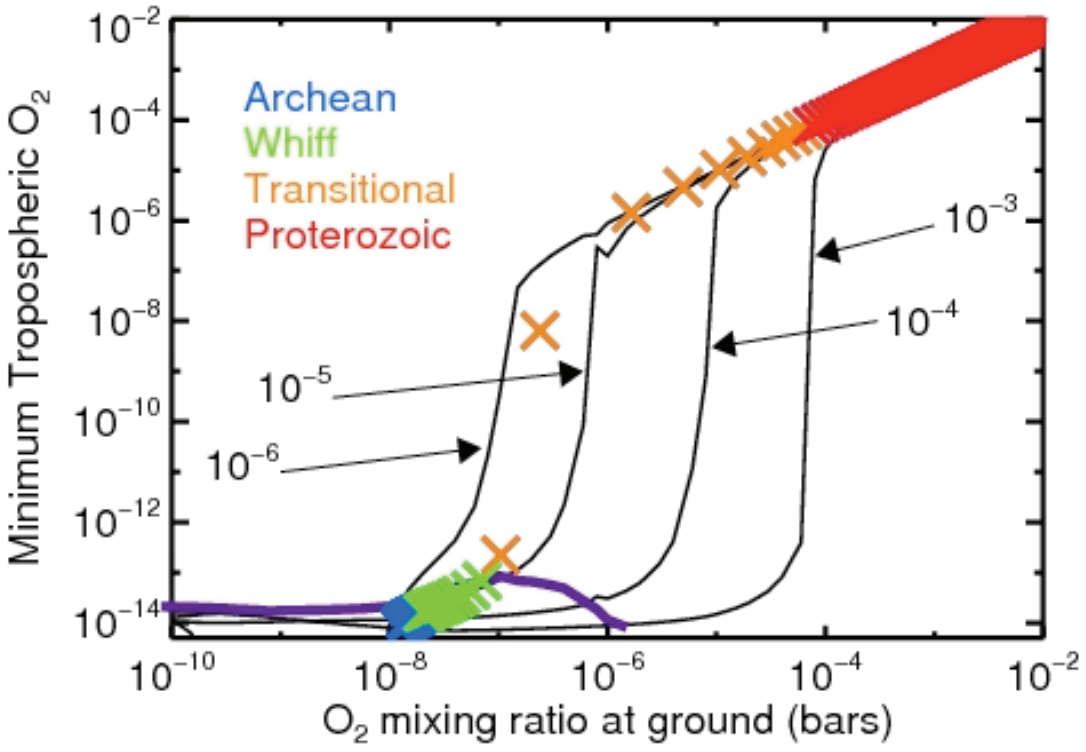

Figure 6-3 Minimum tropospheric O_2 over CH_4/O_2 phase space

A plot of the minimum tropospheric pO_2 over a large atmospheric phase space of O_2 and CH_4 mixing ratios. The minimum tropospheric pO_2 shown on the vertical axis corresponds to the ground level pO_2 on the horizontal axis and contours of the ground level CH_4 mixing ratio labeled by arrows. Regions below the purple curve indicate where more than 10% of degassed volcanic sulfur falls out as S_8. Numerical experiments indicate that once the S_8 deposition flux drops below ~10% of the total S flux, it soon drops to 0, so any atmosphere which preserves a strong MIF S signal must lie at or below the purple curve. To visualize one likely evolutionary path through this phase space, 10 Myr intervals from our biogeochemical model (Fig 6-S1) are shown as 'X' symbols, with color to indicate time: Blue = Archean ; Green = whiff ; Orange = Transitional ; Red = Proterozoic. The biogeochemical model solutions are bimodal, with attractors around variable vertical profile low O_2 solutions, and well-mixed high O_2 solutions. Complete oxidation of the troposphere (i.e. passage to the locus in the upper right of Fig. 6-3 where O_2 is well mixed) occurs quickly in the overplotted biogeochemical model results, and probably occurs even more quickly in nature.

We expand this result using photochemical modeling of 1872 atmospheres spanning mixing ratios of $2x10^{-3} < CH_4 < 1x10^{-6}$ and $1x10^{-12} < O_2 < 0.21$. Figure 6-3 shows that all atmospheres with ground level pO_2 less than ~10^{-8} bar are characterized by extremely anoxic tropospheres. S_8 deposition decreases significantly if the tropospheric minimum pO_2 exceeds 10^{-12} bar, and disappears completely at 10^{-11} bar. The initiation of tropospheric oxidation is a strong function of the CH_4 level. Figure 6-4 shows that CH_4 must drop below ~50 ppm in order for an oxic transition to occur. In a weakly reduced atmosphere with 50 ppm CH_4, Fig. 6-3 shows that the MIF-S signal disappears when the ground-level pO_2 is approximately $2x10^{-7}$ bar, one order of magnitude below a previously deduced upper limit of $2x10^{-6}$ bar for MIF-S occurrence (Pavlov and Kasting, 2002).

6.4 Discussion

The photochemical lifetimes of tropospheric gases reveal that the bulk photochemistry of Archean and whiff atmospheres are remarkably similar. The primary differences involve increases in O_2, OH, and H lifetimes at the expense of HCO and CH_3 lifetimes (Fig 6-S3.) The photochemical lifetimes for tropospheric O_2 in our whiff atmospheres range from ~1 hour to ~1 day (Table 6-1). If O_2 was lost on timescales significantly less than one day, the Archean atmosphere likely encountered diurnal cycling in the O_2 profile. Microbial mat ecosystems release reductants preferentially at night (Hoehler *et al*., 2001), which could have enhanced daily oscillations. It is intriguing that the whiff solutions which presage the oxic transition coincide with tropospheric O_2 lifetimes becoming one day or larger (Fig. 6-4). Increasing lifetimes that allow O_2 to persist over Archean nights may be a previously overlooked driver of O_2 runaway. Further development of this hypothesis would require a time-dependent photochemical model, which is beyond the scope of this study.

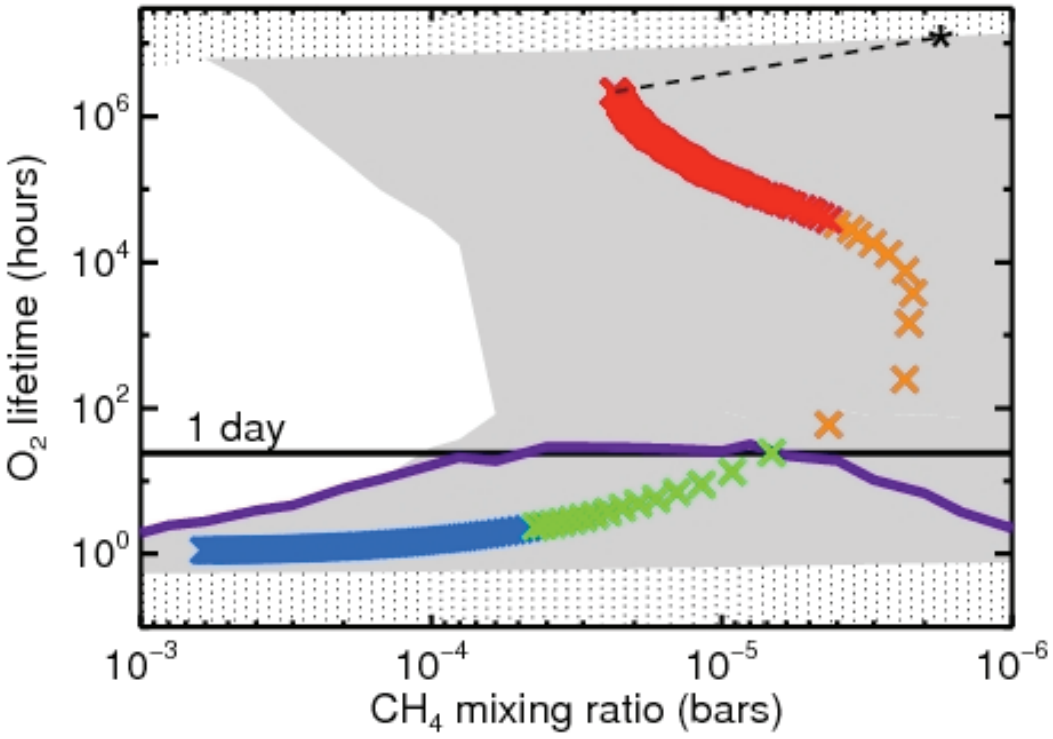

Figure 6-4 O_2 tropospheric lifetimes over CH_4/O_2 phase space.

O_2 tropospheric lifetime computed from 1872 photochemical models. The vertical dotted lines indicate regions outside of our modeled phase space. The white area has photochemical model solutions, but these are supported by CH_4 fluxes greater than $1x10^{13}$ molecules cm^{-2} s^{-1}, which are unrealistic steady-state fluxes from Earth's global biosphere (Chapter 4). The grey shaded area thus represents accessible regions of atmospheric phase space. The purple curve is defined as in Fig 6-3, so atmospheres which can preserve MIF-S need to lie near or below the purple curve. The biogeochemical model and colors are the same as in Fig. 6-3. The O_2 tropospheric lifetime computed by our photochemical model for modern conditions (fixed ground level mixing ratios of 0.21 for O_2 and $1.8x10^{-6}$ for CH_4 is $1.27x10^7$ hours (1459 years)) is marked by a * symbol. Earth's atmospheric evolution must end in the upper right of the plot, as indicated by the dashed line which connects our final computed biogeochemical model point at 1 Gyr to the modern value. The dashed path was not computed as the biogeochemical model was designed to simulate the Paleoproterozoic collapse in methane but not Neoproterozoic/Phanerozoic atmospheric evolution.

The primary distinguishing characteristic of a "whiff atmosphere" is that ground level O_2 exceeds a kinetic threshold which enables oxidative weathering of sulfides. Whiff atmospheres can support 3 - 5 fold increases in the oxidative weathering flux of sulfides, which can explain the Mt. McRae data (see section 6.6.2). The increase in oxidative weathering occurs as falling CH_4 concentrations allow for longer tropospheric O_2

lifetimes, enabling O_2 to flood the atmospheric surface layer. Horizontal transport of O_2 would remain limited (Pavlov and Kasting, 2002) given the short O_2 photochemical lifetimes and typical wind velocities of 10-30 km/hr. This would support the suggestion (Anbar *et al*., 2007) that the spike and decline of the Mt. McRae Mo and Re abundances might be explained by the onset, then saturation of, oxidative weathering processes in a restricted geographical area.

Our results show that whiff atmospheres are part of a continuum of weakly reducing atmospheres that form in the presence of large O_2 and CH_4 fluxes. As the net CH_4:O_2 flux ratio into the atmosphere decreases with time, CH_4 levels decline markedly while ground-level O_2 concentrations remain below ppm levels. While just sufficient for limited oxidative weathering, these O_2 levels are too low to trigger classical indicators of oxygenation, such as redbeds. Reducing conditions dominate whiff atmospheres with production of MIF-S containing S_8 occurring at extremely anoxic tropospheric minimums. The photochemical lifetime of O_2 only increases very steeply once CH_4 mixing ratios decline to tens of ppm (Figs. 6-3, 6-4). As the CH_4:O_2 flux ratio decreases, the chemical response of the atmosphere is a decline of methane which only subsequently allows a rise of O_2 to levels sufficient to drastically alter the world by oxidizing the continents and forming a stratospheric ozone layer. Thus, the Paleoproterozoic may be better described as a time of a great collapse of methane and its dramatic consequence, the rise of O_2.

6.5 Methods Summary

The 1D photochemical model used in this study was that described in Chapter 4, but with a factor of 8 improvement in vertical resolution to more accurately capture the tropospheric O_2 profile and resultant fluxes (for additional discussion, see section 6.6.3). The model calculates photochemical interactions of 47 atmospheric species undergoing (R1) - (R10) plus 172 other relevant reactions (see Table 6-2). In 125 m vertical steps from 0 – 80 km, and for each species (where appropriate), radiative transfer, photochemical production and loss, atmospheric transport including molecular and eddy diffusivity, diffusion-limited H escape, rainout, dry deposition, lightning, and particle

coagulation are computed self-consistently, and integrated to steady state using a reverse-Euler solver. Steady-state models are insufficient for exploring the intricate chemical details of the oxic transition, but considering the evolution of the atmosphere before and after the oxic transition as a series of quasi-steady states has strong precedent (Pavlov *et al*., 2001; Pavlov and Kasting, 2002; Chapter 4; Domagal-Goldman *et al*., 2008). CO_2 partial pressures were fixed at 1%, ensuring haze-free and non-glaciated conditions (Domagal-Goldman *et al*., 2008), although our whiff atmospheres may be near the edge of greenhouse-supported climate stability (Haqq-Misra *et al*., 2008). N_2 gas is used to set atmospheric pressure at 1 bar in each run, which makes partial pressures and mixing ratio numerically equivalent. Fluxes of volcanic gases were fixed at high-end estimates for modern outgassing discussed in Chapter 4, with fluxes of SO_2, H_2S, H_2, and CO equal to $3.5x10^9$, $3.5x10^8$, $1x10^{10}$, and $3x10^9$ molecules cm^{-2} s^{-1} respectively. O_2 and CH_4 are specified by fixed mixing ratios at the lower boundary and computed at all other heights. The model calculates the fluxes of O_2 and CH_4 necessary to maintain a steady state atmosphere subject to the above constraints. Our 1-D models represent atmospheres in direct proximity to an O_2 source region, such as a cyanobacteria-rich area, rather than global averages. The internal self-consistency of all model runs, measured by redox conservation, is better than 1 ppb. In our photochemical results, we use the S_8 deposition flux as proxy for the MIF-S signal, as in Chapter 4.

6.6 Supplementary Discussion

6.6.1 The biogeochemical model

The photochemical study was motivated by biogeochemical box model predictions in Chapters 3 and 5 in which parameterizations of redox gases (converted into O_2 and CH_4 equivalents) from the biosphere, mantle, and continental crust are input into an atmosphere “box” where they undergo photochemical destruction predicted by 1D photochemical modeling. The whiff levels of O_2 shown in Fig. 6-S1 occur during a slow, linear, and monotonic decrease in the net flux of reductants to oxidants (or CH_4:O_2 flux ratio) into the atmospheric “box”. The whiff behavior thus results from details of atmospheric photochemistry, rather than from less well constrained parameterizations of

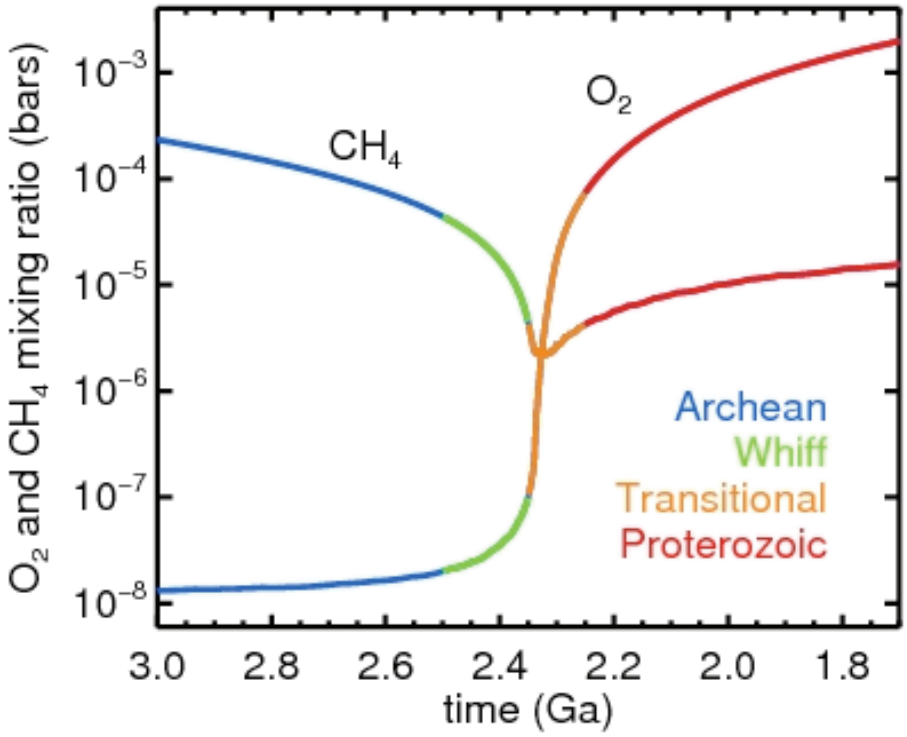

Figure 6-S1 Updated biogeochemical model results

Ground level O_2 and CH_4 mixing ratios versus time from an updated version of the biogeochemical model in Chapter 3. The model includes CH_4:O_2 fluxes in a 1:2 ratio and allows hydrogen escape to oxidize the solid Earth, which diminishes its ability to maintain a reducing atmosphere over geologic time. We use the "method 1" biosphere of Chapter 5, which self-consistently estimates sulfide->sulfate oxidative weathering fluxes, oceanic sulfate concentrations, and the anaerobic oxidation of methane. In addition, we updated our parameterization for the effective rate constant between O_2 and CH_4, k_{eff}, using the revised fluxes from the 1878 photochemical models run for this study. Changing k_{eff} has minimal effect on the dominant gas, but does affect the numerical values of the trace redox species, as shown in Chapter 3. The color scheme is used to denote time-dependent change in subsequent figures: Blue = Archean (3.0 Ga - 2.5 Ga) ; Green = whiff (2.5 Ga – 2.35 Ga) ; Orange = Transitional (2.35 Ga – 2.25 Ga) ; Red = Proterozoic (2.25 Ga – 1.5 Ga). The whiff timespan was chosen to start when CH_4 values drop enough to allow O_2 to deviate from Archean steady-state trace value, and ends when comparable photochemical models ceased S_8 deposition.

the Earth system. The most pertinent components of the biogeochemical model for this discussion are the biospheric fluxes and atmospheric chemistry. The biosphere provides the largest fluxes of oxidized and reducing gases into the Archean atmosphere, with the coupling of methanogenesis and oxygenic photosynthesis producing CH_4 and O_2 in a 1:2 stoichiometric ratio (Catling *et al*. 2001 ; Kasting *et al*. 2001), as summarized

by Eqn. (6.1). As sulfate levels rise, the anaerobic oxidation of methane can depress the net biospheric CH_4:O_2 ratio to lower than 0.5,' as shown in Chapter 5. For our atmospheric chemistry parameterization in the biogeochemical model, we define the net atmospheric annihilation of CH_4 and O_2 by an effective rate constant, k_{eff}, which describes the reverse reaction of Eqn (6.1). We define k_{eff} (with units of $Tmol^{-1}\ yr^{-1}$) as follows:

$$F_{CH4} = k_{eff}\,[O_2][CH_4] \qquad (6\text{-}S2)$$

where F_{CH4} is the CH_4 flux into the atmosphere in Tmol yr^{-1}, and $[O_2]$ and $[CH_4]$ are the global atmospheric inventories (in Tmol) computed from the photochemical model.

If the net flux ratio of CH_4:O_2 (including reducing fluxes from the solid earth) is greater than 1:2, the atmosphere will be reducing, with CH_4 dominant and O_2 present as a trace gas. The modern situation is the reverse – the CH_4:O_2 flux ratio is less than 0.5 and O_2 is dominant while CH_4 is a trace gas. CH_4 has a fairly long tropospheric lifetime in an oxic atmosphere (Kasting & Donahue, 1980 ; Chapter 4), which allows it to exist well-mixed at parts per million (ppm) levels. By contrast, O_2 has a short tropospheric lifetime in reducing atmospheres (Table 6-1, Fig. 6-S3). As a result, O_2 was not well mixed and existed as an Archean trace gas at parts per billion (ppb) levels. O_2 in reducing atmospheres and CH_4 in oxidizing atmospheres were shown analytically in Chapter 3 to be strong reciprocal functions of the dominant gas. The dominant gas defines the redox state of the atmosphere and the nature of the photochemical reactions that set the trace gases levels.

6.6.1.1 k_{eff} and the Archean and whiff atmospheres

The parameterization of atmospheric chemistry as captured by our computation of k_{eff} from 1872 photochemical models provides quantitative support to the argument that the Archean O_2 trace gas concentration is dictated by the CH_4 content. Figure 6-S1 shows that the steady-state ground level O_2 mixing ratios remains constant around 10 ppb for 10^{-4} bar < pCH_4 < 10^{-3} bar. This occurs because k_{eff} increases by an order of magnitude

while CH_4 decreases by an order of magnitude, which acts to keep O_2 levels approximately constant (Eqn. 6-S1). This behavior is seen in Fig. 6-S2, which shows k_{eff} from our photochemical models at varying O_2 and CH_4 levels, with the biogeochemical model predictions from Fig. 6-S1 overplotted. Given an analytic approximation for Archean oxygen from Chapter 3 which has $pO_2 \sim k_{eff}^{-1}[CH_4]^{-1}$, most of the rise in O_2 levels during the whiff timespan can be directly ascribed to the decrease in CH_4 concentrations, as k_{eff} remains approximately constant in the whiff atmospheres. This is broadly consistent with Fig. 6-S3 which shows atmospheric lifetimes of key trace gases remaining approximately constant in the Archean and whiff atmospheres. Geochemically, the primary distinguishing factor of a whiff atmosphere is that ground level oxygen concentrations can rise above a kinetic threshold for stimulating oxidative weathering.

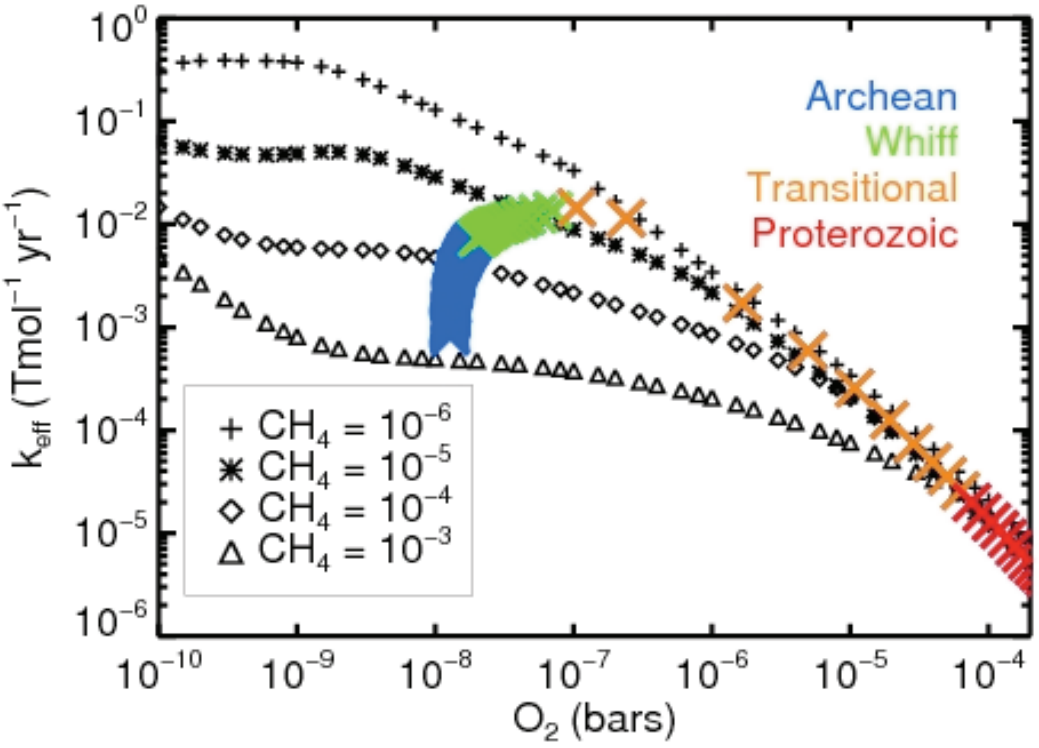

Figure 6-S2 An updated version of the effective rate constant

The effective rate constant for the net atmospheric O_2/CH_4 reaction, k_{eff}, over a phase space of O_2 and CH_4 mixing ratios. The y axis shows k_{eff} values at the O_2 mixing ratios shown on the x axis, and at CH_4 mixing ratios shown by the symbols in the legend. The biogeochemical model from Fig. 6-S1 is overplotted using large 'X' symbols, representing one possible path that Earth's atmosphere may have taken through the phase space shown. Results from 10 Myr intervals in the biogeochemical model are shown, utilizing the color scheme of Fig. 6-S1.

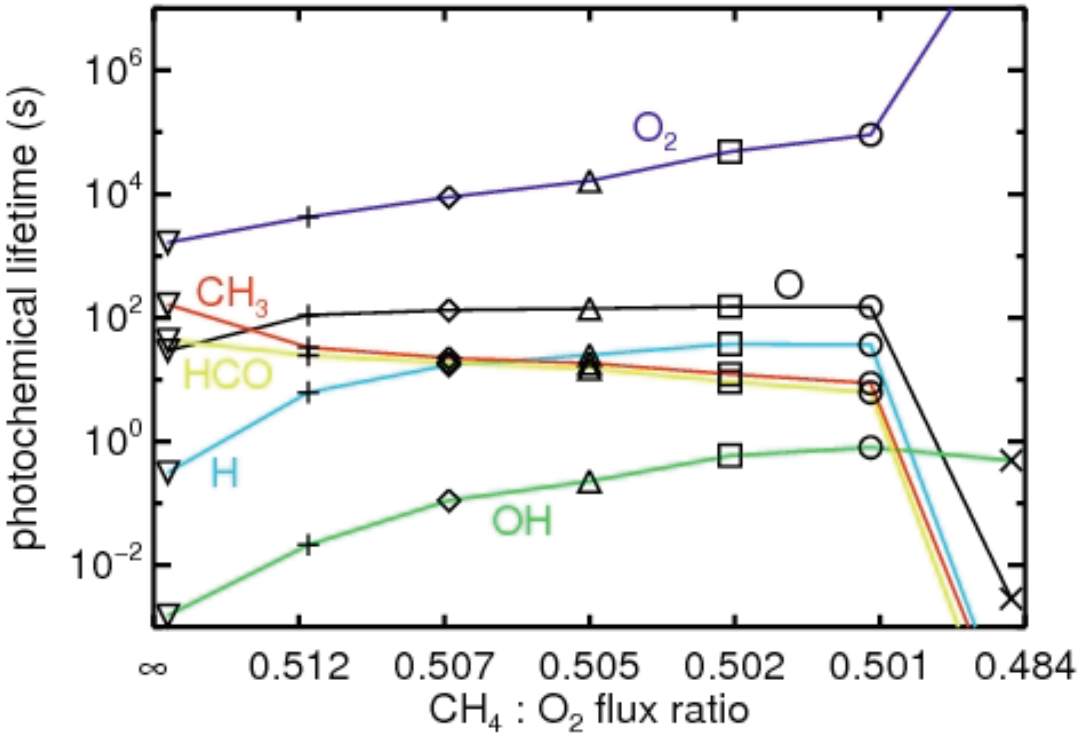

Figure 6-S3 Photochemical lifetimes in whiff atmospheres

Tropospheric photochemical lifetimes rates for O, O_2, HCO, CH_3, H, and OH for the seven atmospheres described in Table 1 and characterized by the CH_4:O_2 flux ratios shown on the horizontal axis. The O_2 lifetimes are computed by dividing the O_2 number density in the troposphere (summed from 0-11 km) by the vertical sum of all tropospheric O_2 loss processes. The results indicated by inverted triangles are from a "pre-oxygenic photosynthetic" atmosphere similar to those described by Pavlov *et al*. (2001). The "Archean" atmosphere is labeled by plus symbols. The diamonds, triangles, squares, and circles are "whiff #1 - #4", respectively, while the 'x' symbols refer to the "Proterozoic" atmosphere (see Table 6-1). The atmospheric reactions are joined between models by lines for ease in reading, but do not represent continuous results. Although representing discrete results, Fig. 6-S3 can be interpreted as a plausible evolutionary sequence from weakly reducing to weakly oxidizing atmospheres (with their defining photochemical lifetimes), driven by decreasing CH_4:O_2 flux ratios. As revealed by the lifetimes of tropospheric gases, the whiff atmospheres have nearly identical bulk photochemistry to the Archean atmosphere, and together form a category of photochemistry distinct from the oxic Proterozoic atmosphere.

6.6.2 Oxidative weathering

6.6.2.1 Mo geochemistry

In the continental crust, Mo occurs primarily as molybdenite (MoS_2). Oxidative weathering produces molybdate ions (MoO_4^{2-}) which are soluble and extremely unreactive under oxidizing oceanic conditions. Consequently, Mo is the most abundant trace metal in the modern ocean. In the presence of reduced sulfur (i.e. H_2S), Mo reforms insoluble sulfides or oxothiomolybdate ions (e.g. $MoO_{4-x}S_x^{2-}$) which are particle reactive, with the combined effect being near-quantitative removal of Mo (Barling *et al*., 2001). 40% of modern oceanic Mo is removed in the 0.3% of the seafloor which is sulfidic (Anbar & Knoll, 2002). The Mo residence time in the modern ocean is ~ 800,000 years, but would have been much shorter in anoxic or euxinic Archean/Proterozoic waters. We estimate the Mo excursion in the Mt. McRae shale occurs over 2-5 million years, using the average Mt. McRae shale sedimentation rate of 2.5 m/million years (Anbar *et al*. 2007). Given that the Mo residence time is less than the Mo excursion timescale, we interpret the Mt. McRae stratigraphy as requiring a peak then a decline in Mo input fluxes, i.e. the sequence represents a succession of steady states.

6.6.2.2 A mass balance calculation for Mo fluxes

The Mt. McRae shale records late Archean Mo concentrations of ~5 ppm, followed by a spike to 40 ppm, with a return to steady-state values of ~10 ppm (Anbar *et al*. 2007). We assume that 5 ppm represents the late Archean steady-state sedimentary Mo concentration for this locale. To form an upper limit, we further assume that no major changes in oceanic Mo solubility or depositional environment occur with slight increases in oceanic oxidation state. Under these assumptions, mass balance requires an 8 fold increase in the continental Mo flux during the excursion, with a new steady state Mo flux approximately twice the original. This 8 fold increase in the oxidative weathering flux is an upper limit because we have assumed no change in the oxidation state of the ocean. Given that oxidized Mo is insoluble, the prediction of 8 fold increase in Mo flux could be

decreased if local oxidizing conditions in the water column concentrate Mo prior to deposition.

The oxidative weathering of sulfides to sulfates should be a direct proxy for the continental Mo flux, given that molybdenite (MoS_2) is a replacement mineral for pyrite (FeS_2). In Chapter 5, we estimated the flux of sulfate to the oceans due to oxidative weathering of sulfides in low-oxygen environment. There, we showed that small increases in the sulfate flux could potentially trigger important changes in the biogeochemical cycle of marine sediments, resulting in decreasing CH_4 fluxes. Figure 5-5b shows a curve labeled 'AOM' versus time. This is the sulfate flux to the ocean due to oxidative weathering, where the 'AOM' label represents our additional assumption that the sulfate was quantitatively available to anaerobic oxidizers of methane (AOM) and sulfate reducers in the biosphere. Assuming the Mo flux is directly proportional to the sulfide to sulfate weathering flux, we predict a factor of 3.6 increase in the flux between the Archean steady state value of 2.5×10^{-3} Tmol Sulfate yr^{-1}, and the whiff values which range to about 1×10^{-2} Tmol Sulfate yr^{-1}. Oxidative weathering was parameterized as $F_W \sim [O_2]^{\beta}$, where $\beta = 0.4$ is a dimensionless constant assumed reflective of the weathering processes of average continental crust (see Chapter 3). Experimental kinetic data for pyrite oxidation reveals power-law behavior with $\beta = 0.5 \pm 0.04$ for sulfides for $1 < pO_2 < 10^{-6}$ bar (Williamson & Rimstidt, 1994). Provided we can extrapolate the $\beta = 0.5$ behavior one additional order of magnitude in pO_2, we estimate a factor of 5 increase in sulfide weathering and hence Mo flux between the late Archean and whiff solutions. Use of the stronger power law exponent for sulfides rather than bulk crust is justified by the lack of U enrichments in the Mt. McRae data (Anbar *et al*. 2007), suggesting limited oxidative weathering processes in which easy to dissolve pyrites containing Mo and Re are weathered, while U remains bound in more stable continental rocks such as feldspars and apatites. Using the data of Williamson and Rimstidt (1994), Anbar *et al*. (2007) estimate that 100 mm^3 pyrite in the presence of $pO_2 = 2 \times 10^{-6}$ bar would weather completely in 20,000 years. Extrapolating this data to $pO_2 = 10^{-7}$ bar yields a dissolution time of 80,000 years (A. Anbar, *pers. com.*), which remains significantly below the timescale of the Mo excursion in the Mt. McRae shale.

6.6.3 Supplementary Methods

A vertical resolution of 1 km has been used in previous work with this (and other related) 1-D photochemical models for Earth's ancient oxic and anoxic atmospheres (Zahnle, 1986 ; Pavlov *et al*., 2001 ; Pavlov and Kasting, 2002 ; Pavlov *et al*., 2003 ; Kharecha *et al*. 2005). In Chapter 4, we updated this well-established photochemical code, making it capable of working in both redox extremes as well as the transitional states in between. Subsequently, we have discovered that the 1 km vertical grid spacing is insufficient to provide a complete description of the O_2 vertical profile in certain anoxic atmospheres that may occur after the evolution of oxygenic photosynthesis (i.e. the atmospheres of primary interest in this chapter). Figure 6-S4 shows the vertical profile for tropospheric O_2 in our Archean model atmosphere computed on 5 vertical grids with constant step sizes of 1 km, 0.5 km, 0.25 km, 0.125 km, and 62.5m.

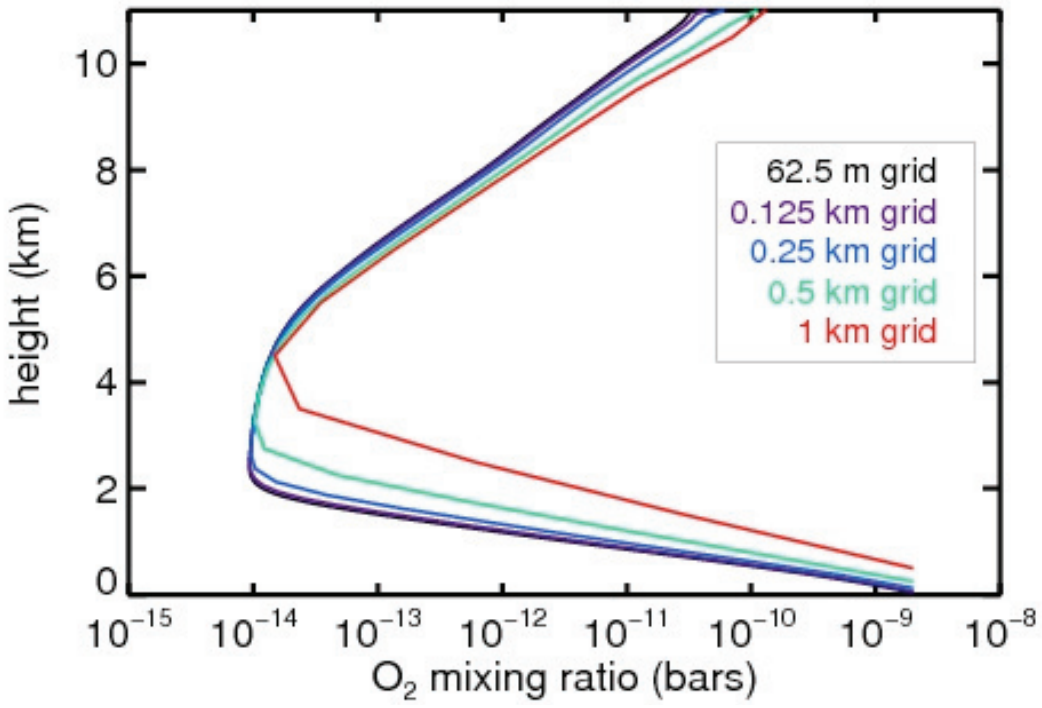

Figure 6-S4 Vertical profiles for various model grid spacings

The O_2 vertical profiles computed from 5 runs of the photochemical model with grid spacings of 1 km (red), 0.5 km (green), 0.25 km (blue), 0.125 km (purple) and 62.5 m (black). All 5 runs were computed using identical boundary conditions of the Archean reference model defined in Table 1. The O_2 profile becomes well resolved at the 0.125 km grid spacing, which we used for all other photochemical model runs in this chapter.

The fixed mixing ratio lower boundary condition on O_2 is enforced in the lowest level of the atmosphere, which is defined as halfway between the ground and the first grid point. In a reducing Archean atmosphere, significantly more O_2 is required to maintain a given O_2 mixing ratio at 0.5 km (the lowest level on the 1 km grid), than is required to maintain an given O_2 mixing ratio at 31.25 m (the lowest level on the 62.5 m grid). The total tropospheric O_2 column ranges from 5×10^{15} cm^2 in the 1km grid to 1×10^{15} cm^2 in the 62.5 m grid. Consequently, the O_2 fluxes required to support a given O_2 mixing ratio are larger when using the 1 km grid than when using the finer grids. The tropospheric O_2 profile becomes well resolved on the 0.125 m grid, which can be understood using the spatial stiffness criterion developed in Appendix 1 of Jim Kasting's Ph.D. dissertation (Kasting, 1979), where it is shown that numerical solutions to the coupled equations can become spatially stiff if

$$l_i > K/(\Delta z)^2 \qquad \text{(6-S3)}$$

where l_i is the loss frequency of O_2 (s^{-1}), K is the eddy diffusion coefficient (cm^2 s^{-1}), and Δz is the grid spacing (cm). The right hand side of Eq. (6-S3) first exceeds the left hand side throughout the entire troposphere when using the 0.125 km grid, which explains why the O_2 profile is nearly identical in the 0.125 km and 62.5 m grids.

The present work updates the fluxes needed to maintain given O_2/CH_4 mixing ratios, but does not alter the conclusions of our previous work. The most significant change occurs in our computation of k_{eff} as defined by Eq. (6-S2) and shown in Fig. 6-S2, which can be compared with Fig. 3-3. The previously computed k_{eff} allowed for errant behavior in the ground level O_2 predictions of our biogeochemical model when O_2 was a trace gas in the late Archean. The change is most noticeable in a slight 'bump' in our previous late Archean ground-level O_2 prediction seen in Fig. 3-7, which is not present in the updated Fig. 6-S1.

Table 6-2 Reaction list for the photochemical model

Photochemical reactions and rates used in the photochemical model

Sulfur Reactions

Reactants		Products	Rate[a]	Reference
$SO + O_2$	→	$O + SO_2$	$2.6 \times 10^{-13} e^{-2400/T}$	JPL-02
$SO + O + M$	→	$SO_2 + M$	$5.1 \times 10^{-31} M$ (*b*)	Singleton & Cvetanovic 1988
$SO + OH$	→	$SO_2 + H$	8.6×10^{-11}	JPL-02
$SO + NO_2$	→	$SO_2 + NO$	1.4×10^{-11}	JPL-06
$SO + O_3$	→	$SO_2 + O_2$	$4.5 \times 10^{-12} e^{-1170/T}$	Atkinson et al 2004
$SO + SO$	→	$SO_2 + S$	2.0×10^{-15} (*c*)	NIST
$SO + SO_3$	→	$SO_2 + SO_2$	2.0×10^{-15}	Chung et al 1975
$SO + HCO$	→	$HSO + CO$	5.2×10^{-12}	assumed same as $HCO+O_2$
$SO_2 + OH + M$	→	$HSO_3 + M$	1.5×10^{-12} (d)	JPL-02
			$3.0 \times 10^{-31} (300/T)^{3.3} M$ (*b*)	JPL-02
$SO_2 + O + M$	→	$M + SO_3$	1.5×10^{-11} (d)	JPL-02
			$1.3 \times 10^{-33} (300/T)^{-3.6} M$ (*b*)	JPL-02
$SO_3 + H_2O$	→	H_2SO_4	1.2×10^{-15}	JPL-02
$HSO_3 + O_2$	→	$HO_2 + SO_3$	$1.3 \times 10^{-12} e^{-330/T}$	JPL-06
$H_2S + OH$	→	$H_2O + HS$	$6.0 \times 10^{-12} e^{-70/T}$	JPL-02
$H_2S + H$	→	$H_2 + HS$	$1.5 \times 10^{-11} e^{-850/T}$	Schofield 1973
$H_2S + O$	→	$OH + HS$	$9.2 \times 10^{-12} e^{-1800/T}$	JPL-06
$HS + O$	→	$H + SO$	7.0×10^{-11}	assumed [e]
$HS + O_3$	→	$HSO + O_2$	$9.0 \times 10^{-11} e^{-280/T}$	JPL-02
$HS + NO_2$	→	$HSO + NO$	$2.9 \times 10^{-11} e^{240/T}$	JPL-02
$HS + HO_2$	→	$H_2S + O_2$	1.0×10^{-11} (*f*)	Stachnik and Molina 1987
$HS + HS$	→	$H_2S + S$	2.0×10^{-11} (*f*)	Stachnik and Molina 1987
$HS + HCO$	→	$H_2S + CO$	2.0×10^{-11} (*f*)	assumed
$HS + H$	→	$H_2 + S$	2.0×10^{-11} (*f*)	Schofield 1973
$HS + S$	→	$H + S_2$	1.0×10^{-11} (*f*)	Nicholas et al 1979
$S + O_2$	→	$SO + O$	2.3×10^{-12}	JPL-06
$S + O_3$	→	$SO + O_2$	1.2×10^{-11}	JPL-06
$S + OH$	→	$SO + H$	6.6×10^{-11}	JPL-06
$S + HCO$	→	$HS + CO$	1.0×10^{-11}	assumed
$S + HO_2$	→	$HS + O_2$	5.0×10^{-12}	assumed
$S + HO_2$	→	$SO + OH$	5.0×10^{-12}	assumed
$H + SO + M$	→	$HSO + M$		assumed same as $H+O_2+M$
$HSO + OH$	→	$H_2O + SO$	3.0×10^{-11}	assumed
$HSO + H$	→	$HS + OH$	2.0×10^{-11}	assumed
$HSO + H$	→	$H_2 + SO$	1.0×10^{-11}	assumed
$HSO + HS$	→	$H_2S + SO$	3.0×10^{-11}	assumed
$HSO + O$	→	$OH + SO$	3.0×10^{-11}	assumed
$HSO + S$	→	$HS + SO$	3.0×10^{-11}	assumed
$H + OCS$	→	$CO + HS$	$9.10 \times 10^{-12} e^{-1940/T}$	Lee et al 1977
$HS + CO$	→	$OCS + H$	$4.15 \times 10^{-14} e^{-7650/T}$	Kurbanov & Mamedov 1995
$O + OCS$	→	$CO + SO$	$2.1 \times 10^{-11} e^{-2200/T}$	JPL-06
$O + OCS$	→	$S + CO_2$	$8.33 \times 10^{-11} e^{-5530/T}$	Singleton and Cvetanovic 1988
$S + CO + M$	→	$OCS + M$	$2.2 \times 10^{-33} e^{-1780/T} M$ (*b*)	assumed same as $CO+O \rightarrow CO_2$
$OCS + S + M$	→	$OCS_2 + M$	$8.3 \times 10^{-33} M$ (*b*)	Basco and Pearson 1967

a – 2-body rates are in $cm^3 s^{-1}$; 3-body rates are in $cm^6 s^{-1}$
b – 3-body low density limit, where M is background density [cm^{-3}]
c – average of rates in NIST Chemical Kinetics Database
d – high density limit (k_∞) for 3-body reaction [$cm^3 s^{-1}$]
e – JPL-06 gives 1.6×10^{-10} but with 5× error
f – reported HS reaction rates are highly discrepant, with upper limits of specific reactions often smaller than reported rates. The rates assumed here split the difference.

Table 6-2, continued — Sulfur Reactions, continued

Reactants		Products	Rate[a]	Reference
$OCS + S$	$\rightarrow$	$CO + S_2$	$1.50 \times 10^{-10} e^{-1830/T}$	Klemm and Davis 1974
$OCS + OH$	$\rightarrow$	$CO_2 + HS$	$1.10 \times 10^{-13} e^{-1200/T}$	JPL-06
$OCS_2 + S$	$\rightarrow$	$OCS + S_2$	2.0×10^{-11}	assumed
$OCS_2 + CO$	$\rightarrow$	$OCS + OCS$	3.0×10^{-12}	assumed
$S + S + M$	$\rightarrow$	S_2+M	5.0×10^{-11} (*b*)	assumed
			$2.84 \times 10^{-33} e^{480/T} M$ (*c*)	assumed[d]
$S_2 + S_2 + M$	$\rightarrow$	$S_4 + M$	5.0×10^{-11} (*b*)	assumed
			$2.5 \times 10^{-30} M$ (*c*)	Langford and Oldershaw 1972[e]
$S + S_2 + M$	$\rightarrow$	$S_3 + M$		assumed 0.2 of $S_2 + S_2 + M$
$S + S_3 + M$	$\rightarrow$	$S_4 + M$		assumed same as $S + S_2 + M$
$S_4 + S_4 + M$	$\rightarrow$	$S_8 + M$		assumed same as S_2+S_2+M
		Photolysis Reactions[f]		
$SO + h\nu$	$\rightarrow$	$S + O$	4.9×10^{-4}	Kasting et al 1989
$SO_2 + h\nu$	$\rightarrow$	$SO + O$	1.8×10^{-4}	Kasting et al 1989
$H_2S + h\nu$	$\rightarrow$	$HS + H$	2.9×10^{-4}	Kasting et al 1989
$SO_2 + h\nu$	$\rightarrow$	$SO_2(^1B)$	1.7×10^{-3}	Kasting et al 1989
$SO_2 + h\nu$	$\rightarrow$	$SO_2(^3B)$	4.4×10^{-7}	Kasting et al 1989
$S_2 + h\nu$	$\rightarrow$	$S + S$	9.9×10^{-4}	Kasting et al 1989
$SO_3 + h\nu$	$\rightarrow$	$SO_2 + O$	4.3×10^{-5}	Burkholder & McKeen 1997
$SO_2(^1B) + M$	$\rightarrow$	$SO_2(^3B) + M$	1.0×10^{-12} (*g*)	Kasting et al 1989
$SO_2(^1B) + M$	$\rightarrow$	$SO_2 + M$	1.0×10^{-11} (*g*)	Kasting et al 1989
$SO_2(^1B)$	$\rightarrow$	$SO_2(^3B) + h\nu$	1.5×10^{3} (*h*)	Kasting et al 1989
$SO_2(^1B)$	$\rightarrow$	$SO_2 + h\nu$	2.2×10^{4} (*h*)	Kasting et al 1989
$SO_2(^1B) + O_2$	$\rightarrow$	$SO_3 + O$	1.0×10^{-16} (*g*)	Kasting et al 1989
$SO_2(^1B) + SO_2$	$\rightarrow$	$SO_3 + SO$	4.0×10^{-12} (*g*)	Kasting et al 1989
$SO_2(^3B) + M$	$\rightarrow$	$SO_2 + M$	1.5×10^{-13} (*g*)	Kasting et al 1989
$SO_2(^3B)$	$\rightarrow$	$SO_2 + h\nu$	1.13×10^{3} (*h*)	Kasting et al 1989
$SO_2(^3B) + SO_2$	$\rightarrow$	$SO_3 + SO$	7.0×10^{-14} (*g*)	Kasting et al 1989
$HSO + h\nu$	$\rightarrow$	$HS + O$	6.5×10^{-4}	assumed[i]
$S_4 + h\nu$	$\rightarrow$	$S_2 + S_2$	9.9×10^{-4}	assumed[j]
$S_3 + h\nu$	$\rightarrow$	$S_2 + S$	9.9×10^{-4}	assumed[j]
$S_8 + h\nu$	$\rightarrow$	$S_4 + S_4$	1.3×10^{-6}	Kasting et al 1989
$OCS + h\nu$	$\rightarrow$	$CO + S$	2.7×10^{-6}	JPL-02

a – 2-body rates are in $cm^3 s^{-1}$; 3-body rates are in $cm^6 s^{-1}$; photolysis rates are in s^{-1}
b – high density limit (k_∞) for 3-body reaction [$cm^3 s^{-1}$]
often smaller than reported rates. The rates assumed here are an attempt to split the difference.
c – 3-body low density limit, where M is background density [cm^{-3}]
d – this reaction has been reported in H_2S (Nicholas et al 1979) and Ar (Fair and Thrush 1969). The reported rates differ by several orders of magnitude. In Ar the reported rate is 3× faster than the analogous recombination of O. We assume that S+S is 3× faster than O+O in CO_2.
e – reported with factor 5 error; the assumed rate is 5× smaller than the reported rate
f – Photolysis rates are evaluated at the top of the Archean atmosphere (Table 1) subject to a solar flux appropriate for the 2.5 Ga Sun (Claire and Catling, 2008), for a 50° slant path, and reduced by a factor of two to account for the diurnal cycle.
g – Collisional de-excitation or reaction [$cm^3 s^{-1}$]
h – Radiative relaxation [s^{-1}]
i – assumed same as $HO_2 + h\nu$
j – assumed same as $S_2 + h\nu$

Table 6-2, continued

Hydrocarbon Reactions

Reactants		Products	Rate[a]	Reference
$CH_4 + OH$	$\rightarrow$	$CH_3 + H_2O$	$2.45 \times 10^{-12} e^{-1775/T}$	JPL-06
$CH_4 + O(^1D)$	$\rightarrow$	$CH_3 + OH$	$0.85 \times 1.5 \times 10^{-10}$	JPL-06 [b]
$CH_4 + O(^1D)$	$\rightarrow$	$H_2CO + H_2$	$0.15 \times 1.5 \times 10^{-10}$	JPL-06[b]
$^1CH_2 + CH_4$	$\rightarrow$	$CH_3 + CH_3$	3.6×10^{-11}	assumed
$^1CH_2 + O_2$	$\rightarrow$	$HCO + H$	3.0×10^{-11}	Ashfold et al 1981
$^1CH_2 + N_2$	$\rightarrow$	$^3CH_2 + N_2$	8.8×10^{-12}	assumed
$^3CH_2 + O_2$	$\rightarrow$	$HCO + OH$	$4.1 \times 10^{-11} e^{-750/T}$	Baulch et al 1994[c]
$CH_3 + O_2 + M$	$\rightarrow$	$H_2CO + OH$	$1.8 \times 10^{-12} (300/T)^{1.7}$ (d)	JPL-02
			$4.5 \times 10^{-31} (300/T)^{3.0} M$ (e)	JPL-02
$CH_3 + OH$	$\rightarrow$	$H_2CO + H_2$	1.3×10^{-11}	Baulch et al 1992[c]
$CH_3 + O$	$\rightarrow$	$H_2CO + H$	1.1×10^{-10}	JPL-06
$CH_3 + O_3$	$\rightarrow$	$H_2CO + HO_2$	$5.4 \times 10^{-12} e^{-220/T}$	JPL-06[c]
$CH_3 + CH_3 + M$	$\rightarrow$	$C_2H_6 + M$	$3.0 \times 10^{-11} (300/T)^{1.0}$ (d)	Klippenstein et al 2006
			$1.7 \times 10^{-25} (300/T)^{3.75} e^{-500/T} M$ (e)	Wang et al 2003
$CH_3 + H + M$	$\rightarrow$	$CH_4 + M$	$2.0 \times 10^{-10} (300/T)^{0.4}$ (d)	Tsang 1989
			$1.0 \times 10^{-28} (300/T)^{1.8} M$ (e)	Baulch et al 1994
$CH_3 + HCO$	$\rightarrow$	$CH_4 + CO$	5.0×10^{-11} $fg)$	NIST
$CH_3 + HNO$	$\rightarrow$	$CH_4 + NO$	$3.3 \times 10^{-12} e^{-1000/T}$	Laidler et al 1962
$CH_3 + H_2CO$	$\rightarrow$	$CH_4 + HCO$	$4.9 \times 10^{-15} (T/298)^{4.4} e^{-2450/T}$	Liu et al 2003
$CH_4 + O$	$\rightarrow$	$CH_3 + OH$	$5.8 \times 10^{-11} e^{-4450/T}$	Barassin &Combourieu 1974
$^1CH_2 + H_2$	$\rightarrow$	$CH_3 + H$	1.3×10^{-10}	Baulch et al 1994
$^1CH_2 + CO_2$	$\rightarrow$	$H_2CO + CO$	1.0×10^{-12}	assumed
$^3CH_2 + O$	$\rightarrow$	$HCO + H$	1.0×10^{-11}	Baulch et al 1992[c]
$^3CH_2 + CO_2$	$\rightarrow$	$H_2CO + O_2$	1.0×10^{-14} (f)	NIST
$C_2H_6 + OH$	$\rightarrow$	$C_2H_5 + H_2O$	$8.7 \times 10^{-12} e^{-1070/T}$	JPL-02
$C_2H_6 + O$	$\rightarrow$	$C_2H_5 + OH$	$8.54 \times 10^{-12} (T/298)^{1.5} e^{-2900/T}$	Baulch et al 1992
$C_2H_6 + O(^1D)$	$\rightarrow$	$C_2H_5 + OH$	6.2×10^{-10}	Matsumi et al 1993
$C_2H_5 + H$	$\rightarrow$	$CH_3 + CH_3$	6.0×10^{-11}	Baulch et al 1992
$C_2H_5 + O$	$\rightarrow$	$CH_3 + HCO + H$	1.1×10^{-10}	Baulch et al 1992[c]
$C_2H_5 + OH$	$\rightarrow$	$CH_3 + HCO + H_2$	4.0×10^{-11}	Tsang and Hampson 1986
$C_2H_5 + HCO$	$\rightarrow$	$C_2H_6 + CO$	1.0×10^{-10}	Tsang and Hampson 1986
$C_2H_5 + HNO$	$\rightarrow$	$C_2H_6 + NO$	$1.6 \times 10^{-12} e^{-1000/T}$	Laidler & Wojciechowski 1961
$C_2H_5 + O_2 + M$	$\rightarrow$	$CH_3 + HCO + OH$	$1.9 \times 10^{-11} (300/T)^{1.8}$ (d, f)	NIST
			$1.5 \times 10^{-28} (300/T)^{4.4} M$ (e, f)	NIST
			Photolysis Reactions[g]	
$CH_4 + h\nu$	$\rightarrow$	$^1CH_2 + H_2$	8.5×10^{-6}	Mount et al 1977
$C_2H_6 + h\nu$	$\rightarrow$	$^3CH_2 + {}^3CH_2 + H_2$	$0.8 \times 5.4 \times 10^{-6}$	Mount and Moos 1978[h]
$C_2H_6 + h\nu$	$\rightarrow$	$CH_4 + {}^1CH_2$	$0.2 \times 5.4 \times 10^{-6}$	Mount and Moos 1978
$CH_3 + h\nu$	$\rightarrow$	$^3CH_2 + H$	1×10^{-5}	assumed

a – 2-body rates [$cm^3 s^{-1}$]; 3-body rates [$cm^6 s^{-1}$]; photolysis rates [s^{-1}]
b – JPL-06 branching ratios are 75% (CH_3 +OH), 20% (CH_3O +H), 5% (H_2CO + H_2) We apportion the methanol branch equally between the other two.
c – products assumed
d – high density limit (k_∞) for 3-body reaction [$cm^3 s^{-1}$]
e – 3-body rate, where M is background density [cm^{-3}]
f – An average of uncertain rates from NIST Chemical Kinetics Database
g – Photolysis rates are evaluated at the top of the Archean atmosphere (Table 1) subject to a solar flux appropriate for the 2.5 Ga Sun (Claire and Catling, 2008), for a 50° slant path, and reduced by a factor of two to account for the diurnal cycle.
h – assumed products in place of C_2H_2 and C_2H_4

Table 6-2, continued

Basic H, C, O, N Reactions

Reactants		Products	Reaction Rate[a]	Reference
$H_2O + O(^1D)$	→	$OH + OH$	2.2×10^{-10}	JPL-02
$H_2 + O(^1D)$	→	$OH + H$	1.1×10^{-10}	JPL-06
$H_2 + O$	→	$OH + H$	$1.34 \times 10^{-15} (T/298)^{6.52} e^{-1460/T}$	Robie et al. 1990
$H_2 + OH$	→	$H_2O + H$	$5.5 \times 10^{-12} e^{-2000/T}$	JPL-02
$H + O_3$	→	$OH + O_2$	$1.4 \times 10^{-10} e^{-470/T}$	JPL-06
$H + O_2 + M$	→	$HO_2 + M$	7.5×10^{-11} (*b*)	JPL-02
			$5.7 \times 10^{-32} (300/T)^{1.6} M$ (*c*)	JPL-02
$H + HO_2$	→	$H_2 + O_2$	$0.09 \times 8.0 \times 10^{-11}$	JPL-02
$H + HO_2$	→	$H_2O + O$	$0.02 \times 8.0 \times 10^{-11}$	JPL-02
$H + HO_2$	→	$OH + OH$	$0.89 \times 8.0 \times 10^{-11}$	JPL-02
$OH + O$	→	$H + O_2$	$2.2 \times 10^{-11} e^{120/T}$	JPL-06
$OH + HO_2$	→	$H_2O + O_2$	$4.8 \times 10^{-11} e^{250/T}$	JPL-06
$OH + O_3$	→	$HO_2 + O_2$	$1.7 \times 10^{-12} e^{-940/T}$	JPL-06
$HO_2 + O$	→	$OH + O_2$	$3.0 \times 10^{-11} e^{200/T}$	JPL-06
$HO_2 + O_3$	→	$OH + 2O_2$	$1.0 \times 10^{-14} e^{-490/T}$	JPL-06
$HO_2 + HO_2$	→	$H_2O_2 + O_2$	$2.3 \times 10^{-13} e^{600/T}$	JPL-02
$HO_2 + HO_2 + M$	→	$H_2O_2 + O_2 + M$	$1.7 \times 10^{-33} e^{1000/T} M$ (*c*)	JPL-06
$H_2O_2 + OH$	→	$HO_2 + H_2O$	$2.9 \times 10^{-12} e^{-160/T}$	JPL-02
$O + O + M$	→	$O_2 + M$	$9.46 \times 10^{-34} e^{480/T} M$ (*c*)	Campbell & Gray 1973
$O + O_2 + M$	→	$O_3 + M$	3×10^{-11} (*b*)	assumed
			$6 \times 10^{-34} (300/T)^{2.4} M$ (*c*)	JPL-06
$O + O_3$	→	$O_2 + O_2$	$8.0 \times 10^{-12} e^{-2060/T}$	JPL-06
$OH + OH$	→	$H_2O + O$	$4.2 \times 10^{-12} e^{-240/T}$	JPL-02
$O(^1D) + N_2$	→	$O + N_2$	$1.8 \times 10^{-11} e^{110/T}$	JPL-02
$O(^1D) + O_2$	→	$O + O_2$	$3.2 \times 10^{-11} e^{70/T}$	JPL-02
$CO + OH$	→	$CO_2 + H$	$1.5 \times 10^{-13} (1 + 0.6p)$ (*d*)	JPL-02
$CO + O + M$	→	$CO_2 + M$	$2.2 \times 10^{-33} e^{-1780/T} M$ (*c*)	Inn 1974
$H + CO + M$	→	$HCO + M$	$1.4 \times 10^{-34} e^{-100/T} M$ (*c*)	Wagner & Bowman 1987
$H + HCO$	→	$H_2 + CO$	1.8×10^{-10}	Friedrichs et al 2002
$HCO + HCO$	→	$H_2CO + CO$	4.5×10^{-11}	Friedrichs et al 2002
$OH + HCO$	→	$H_2O + CO$	1.0×10^{-10} (*e*)	NIST
$O + HCO$	→	$H + CO_2$	5.0×10^{-11}	Baulch et al 1992
$O + HCO$	→	$OH + CO$	5.0×10^{-11}	Baulch et al 1992
$H_2CO + H$	→	$H_2 + HCO$	$2.14 \times 10^{-12} (T/298)^{1.62} e^{-1090/T}$	Baulch et al 1992
$H + H + M$	→	$H_2 + M$	$9.5 \times 10^{-33} (T/298)^{-1.33} M$ (*c*)	Walkauskas &Kaufman 1975
$HCO + O_2$	→	$HO_2 + CO$	5.2×10^{-12}	JPL-06
$H_2CO + OH$	→	$H_2O + HCO$	9.0×10^{-12}	JPL-02
$H + OH + M$	→	$H_2O + M$	$6.9 \times 10^{-31} (T/298)^{-2} M$ (*c*)	Baulch et al 1992
$OH + OH + M$	→	$H_2O_2 + M$	2.6×10^{-11} (*b*)	JPL-06
			$6.9 \times 10^{-31} (300/T)^{1.0} M$ (*c*)	JPL-06
$H_2CO + O$	→	$HCO + OH$	$3.4 \times 10^{-11} e^{-1600/T}$	JPL-06
$H_2O_2 + O$	→	$OH + HO_2$	$1.4 \times 10^{-12} e^{-2000/T}$	JPL-06
$O(^1D) + CO$	→	$CO + O$	7×10^{-11} (*f*)	Davidson et al 1978

a – 2-body rates are in $cm^3 s^{-1}$; 3-body rates are in $cm^6 s^{-1}$
b – high density limit (k_∞) for 3-body reaction [$cm^3 s^{-1}$]
c – low density limit for 3-body reaction, where M is background density[cm^{-3}]
d – *p* is atmospheric pressure in bars
e – An average of uncertain rates from NIST Chemical Kinetics Database
f – This is sometimes reported as an addition to form CO_2

Basic H, C, O, N Reactions, continued

Table 6-2, continued

Reactants		Products	Rate[a]	Reference
		Nitrogen Reactions		
$H + NO + M$	$\rightarrow$	$HNO + M$	$2.4 \times 10^{-10} (300/T)^{0.41}$ (*b*)	Tsang & Herron 1991
			$1.2 \times 10^{-31} (300/T)^{1.17} e^{-210/T} M$ (*c*)	Tsang & Herron 1991
$N + N + M$	$\rightarrow$	$N_2 + M$	$1.25 \times 10^{-32} M$ (*c*)	Knipovich 1988
$N + O_2$	$\rightarrow$	$NO + O$	$1.5 \times 10^{-12} e^{-3600/T}$	JPL-02
$N + OH$	$\rightarrow$	$NO + H$	$3.8 \times 10^{-11} e^{85/T}$	Atkinson et al 1989
$N + NO$	$\rightarrow$	$N_2 + O$	$2.1 \times 10^{-11} e^{100/T}$	JPL-06
$NO + O_3$	$\rightarrow$	$NO_2 + O_2$	$3.0 \times 10^{-12} e^{-1500/T}$	JPL-06
$NO + O + M$	$\rightarrow$	$NO_2 + M$	3.0×10^{-11} (*b*)	JPL-02
			$9.0 \times 10^{-31} (300/T)^{1.5} M$ (*c*)	JPL-02
$NO + HO_2$	$\rightarrow$	$NO_2 + OH$	$3.5 \times 10^{-12} e^{250/T}$	JPL-06
$NO + OH + M$	$\rightarrow$	$HNO_2 + M$	$3.6 \times 10^{-11} (300/T)^{0.1}$ (*b*)	JPL-06
			$7.0 \times 10^{-31} (300/T)^{2.6} M$ (*c*)	JPL-06
$NO_2 + O$	$\rightarrow$	$NO + O_2$	$5.6 \times 10^{-12} e^{180/T}$	JPL-02
$NO_2 + OH + M$	$\rightarrow$	$HNO_3 + M$	2.5×10^{-11} (*b*)	JPL-02
			$2.0 \times 10^{-30} (300/T)^{3.0} M$ (*c*)	JPL-02
$NO_2 + H$	$\rightarrow$	$NO + OH$	$4.0 \times 10^{-10} e^{-340/T}$	JPL-06
$HNO_3 + OH$	$\rightarrow$	$H_2O + NO_2 + O$	$7.2 \times 10^{-15} e^{785/T}$ (*d*)	JPL-02
$HNO_3 + OH + M$	$\rightarrow$	$H_2O + NO_2 + O + M$	$4.1 \times 10^{-16} e^{1400/T}$ (*b*, *d*)	JPL-02
			$1.9 \times 10^{-33} e^{725/T} M$ (*c*, *d*)	JPL-02
$HCO + NO$	$\rightarrow$	$HNO + CO$	1.3×10^{-11}	Nesbitt et al 1999
$H + HNO$	$\rightarrow$	$H_2 + NO$	$3.0 \times 10^{-11} e^{-500/T}$	Tsang and Herron 1991
$O + HNO$	$\rightarrow$	$OH + NO$	3.8×10^{-11}	Inomata and Washida 1999
$OH + HNO$	$\rightarrow$	$H_2O + NO$	5.0×10^{-11}	Sun et al 2001
$HNO_2 + OH$	$\rightarrow$	$H_2O + NO_2$	$1.8 \times 10^{-11} e^{-390/T}$	JPL-06
		Photolysis Reactions[e]		
$O_2 + h\nu$	$\rightarrow$	$O(^3P) + O(^1D)$	4.0×10^{-6}	JPL-02
$O_2 + h\nu$	$\rightarrow$	$O(^3P) + O(^3P)$	6.9×10^{-8}	JPL-02
$H_2O + h\nu$	$\rightarrow$	$H + OH$	1.3×10^{-5}	JPL-02
$O_3 + h\nu$	$\rightarrow$	$O_2 + O(^1D)$	5.7×10^{-3}	JPL-02
$O_3 + h\nu$	$\rightarrow$	$O_2 + O(^3P)$	1.2×10^{-3}	JPL-02
$H_2O_2 + h\nu$	$\rightarrow$	$OH + OH$	9.0×10^{-5}	JPL-02
$CO_2 + h\nu$	$\rightarrow$	$CO + O(^3P)$	1.9×10^{-9}	JPL-02
$H_2CO + h\nu$	$\rightarrow$	$H_2 + CO$	5.1×10^{-5}	JPL-02
$H_2CO + h\nu$	$\rightarrow$	$HCO + H$	6.1×10^{-5}	JPL-02
$HCO + h\nu$	$\rightarrow$	$H + CO$	1×10^{-2}	assumed
$CO_2 + h\nu$	$\rightarrow$	$CO + O(^1D)$	2.4×10^{-7}	JPL-02
$HO_2 + h\nu$	$\rightarrow$	$OH + O$	6.554×10^{-4}	JPL-02
$HNO_2 + h\nu$	$\rightarrow$	$NO + OH$	1.7×10^{-3}	assumed
$HNO_3 + h\nu$	$\rightarrow$	$NO_2 + OH$	1.6×10^{-4}	JPL-02
$NO + h\nu$	$\rightarrow$	$N + O$	1.9×10^{-6}	JPL-02
$NO_2 + h\nu$	$\rightarrow$	$NO + O$	6.3×10^{-3}	JPL-02
$HNO + h\nu$	$\rightarrow$	$NO + H$	1.7×10^{-3}	assumed

a – 2-body rates [$cm^3 s^{-1}$]; 3-body rates [$cm^6 s^{-1}$]; photolysis rates [s^{-1}]
b – high density limit (k_∞) for 3-body reaction [$cm^3 s^{-1}$]
c – low density limit for 3-body reaction, where M is background density[cm^{-3}]
d – The reaction of OH and HNO_3 has multiple channels; see JPL-02 for details
e – Photolysis rates are evaluated at the top of the Archean atmosphere (Table 1) subject to a solar flux appropriate for the 2.5 Ga Sun (Claire and Catling, 2008), for a 50° slant path, and reduced by a factor of two to account for the diurnal cycle.

Chapter 7 Time-dependent photochemical modeling of the oxic transition

In Chapters 4 and 6, we came to the conclusion that a time-dependent photochemical model of the early Earth would be a useful tool to explore the oxic transition. In this chapter, we describe how we have implemented and tested a time-dependent solver in our photochemical model. We present the first results from studies of the time evolution of the atmosphere across the oxic transition. We show that the oxic transition likely occurred over a few thousand years and provide a brief analysis of the photochemistry occurring during the transition. In addition, we show that the oxic transition is fully reversible if the flux perturbations which cause it are reversed, although it takes longer to switch back from the oxic solution to the anoxic solution. We conclude by showing mid-infrared spectra of the oxic transition, concluding with some comments on the detactability of Earth-like planets.

7.1 Steady-state versus time-dependent modeling

The oxic transition is inherently a time-dependent process because changes to the atmosphere occur on the timescale of the trace gas lifetimes (Tables 1-1 and 6-1, Figure 6-S3.) Fluxes into and out of the atmosphere were not balanced on geological timescales, as evidenced by the massive changes in atmospheric composition that took place. By contrast, the model results presented in Chapters 3 through 6 are based on steady-state solutions. This means that the numerical results are in complete balance between fluxes into and out of the system, and that the numerical solutions are converged and stable. This approximation is not limited to the work in this dissertation, as it has been made in all previous work on Archean photochemistry by Jim Kasting and his research group, as well as earlier work by James Walker and co-workers, as cited in the bibliography.

The biogeochemical model solutions in Chapters 3 and 5 evolve in time because we make small time-dependent changes to the fluxes after each time-step, starting from a steady-state solution. This manner of solution is referred to as "quasi steady-state" modeling, and is generally applied in situations where solutions evolve slowly with respect to the timesteps taken. This is an appropriate assumption during most of Earth's history, as the maximum timestep we allow the biogeochemical model to take is 1 million years. This assumption is not valid at the time of the oxic transition, as changes in the Earth system likely occurred very quickly. Our assumption that the atmosphere evolved as a series of quasi-steady states led to timescales of ~ 50 million years for the transition from the anoxic to oxic solution, which we show here is a gross overstimation. This is not necessarily a criticism of our biogeochemical model assumptions; rather, it is a criticism of our method of numerically approximating an inherently time-dependent process using steady-state solutions.

7.2 Time dependence in the photochemical model

We begin our discussion of time-dependence by describing in detail the numerical algorithm for the photochemical model.

7.2.1 The first order reverse Euler solver*

The chemistry/transport equations we are solving were defined in equations (4.1) and (4.2). Differentiating (4.2) with respect to *z* and substituting into (4.1) yields a coupled second order differential equation:

$$\frac{\partial f_i}{\partial t} = \frac{P_i}{N} - L_i f_i - \frac{1}{N}\frac{\partial}{\partial z}\left(b_{ia} f_i (H_a^{-1} - H_i^{-1})\right) + \frac{1}{N}\frac{\partial}{\partial z}\left((b_{ia} + KN)\frac{\partial f_i}{\partial z}\right) \qquad (7.1)$$

* This section is adapted from a set of hand written notes prepared by Jim Kasting, and also draws from material in Appendix B of Kasting (1979).

where the subscript *i* runs over all species at all heights, and the individual terms were defined in Chapter 4 (see also Appendix A). In describing the solver, we reduce equation (7.1) to the matrix equation

$$\frac{d\vec{x}}{dt} = \vec{F}(\vec{x}) \tag{7.2}$$

where $\vec{x}$ is a vector of mixing ratios which runs over all relevant species and all heights. $\vec{x}$ runs from 1 to M, where M is the number of chemical species for which we compute transport (NQ) multiplied by the number of model heights (NZ), so M = NQ x NZ = 35 x 640 = 22,400 in the model used in Chapter 6 and here. 11 of the 46 species in our model are solved assuming photochemical equilibrium (see Appendix A), so only 35 species are included in the system of equations represented by (7.2)

This system of equations represented by (7.2) is "stiff." Stiffness is a numerical problem which can occur when using finite-differencing to approximate the solution of a differential equation on a discrete grid. An equation is stiff if its solution contains exponentially decaying components that are not resolved by the discrete interval used for the calculation (Gear, 1971). In practice, chemical equations become stiff at large timesteps because chemical species generally have markedly different lifetimes. This limits standard forward differencing numerical approximation techniques to timesteps not much larger than the e-folding time of the fastest reacting chemical species.

To solve a stiff system without taking very small timesteps requires an "implicit" method of solution (*ibid.*). In numerical terms, this means that the terms on the right hand side of equation (7.2) must be evaluated at the future time step. This is impossible to do exactly as the right hand side of equation (7.2) is nonlinear, but can be done approximately. A number of implicit techniques exist for solving differential equations; we use the simplest method, the first-order reverse Euler method.

If we let the superscript *t* represent the timestep, we solve equation (7.2) by letting

$$\vec{x}^{t+1} = \vec{x}^{t} + \vec{F}(\vec{x}^{t+1})\Delta t \tag{7.3}$$

We define Δx as:

$$\Delta\vec{x} = \vec{x}^{t+1} - \vec{x}^{t} \tag{7.4}$$

The right hand side at the future timestep is approximated by using a first-order Taylor series expansion:

$$\vec{F}(\vec{x}^{t+1}) \simeq \vec{F}(\vec{x}^{t}) + J\Delta\vec{x} \tag{7.5}$$

where J is the Jacobian matrix:

$$J = \frac{\partial\vec{F}}{\partial\vec{x}} = \begin{pmatrix} \frac{\partial F_1}{\partial x_1} & \cdots & \frac{\partial F_1}{\partial x_M} \\ \vdots & \ddots & \vdots \\ \frac{\partial F_M}{\partial x_1} & \cdots & \frac{\partial F_M}{\partial x_M} \end{pmatrix} \tag{7.6}$$

so J is an M by M matrix with ~5 x 10^8 elements. Luckily for our computers, the Jacobian matrix that we construct for our 1D model is “banded.” This occurs because each element x_M is linked only to the other x’s on the same level of the atmosphere plus the x’s corresponding to the same species on the grid points directly above and below. Thus, J looks like:

$$J = \begin{pmatrix} \ddots & \ddots & \ddots & \ddots & & & & \\ \ddots & \ddots & \ddots & \ddots & \ddots & & 0 & \\ \ddots & \ddots & \ddots & \ddots & \ddots & \ddots & & \\ \leftarrow & 2 & N & Q & + & 1 & \rightarrow & \\ & \ddots & \ddots & \ddots & \ddots & \ddots & \ddots & \ddots \\ & & \ddots & \ddots & \ddots & \ddots & \ddots & \ddots \\ & 0 & & \ddots & \ddots & \ddots & \ddots & \ddots \\ & & & & \ddots & \ddots & \ddots & \ddots \end{pmatrix} \begin{matrix} 1 \\ \vdots \\ \vdots \\ \vdots \\ \vdots \\ \vdots \\ \vdots \\ M \end{matrix} \tag{7.7}$$

The bandwidth of the matrix is 2*NQ +1 and the length of the matrix is M, which means there are ~10^6 nonzero elements in J. By substituting equations (7.4) and (7.5), we rewrite equation (7.3) as:

$$\left[I - J\Delta t\right]\Delta\vec{x} = \vec{F}(x^t)\Delta t \tag{7.8}$$

where I is the identity matrix. Dividing through by Δt yields:

$$\left[\frac{1}{\Delta t}I - J\right]\Delta\vec{x} = \vec{F}(x^t) \tag{7.9}$$

Notice that both J and F (i.e the right hand side of (7.1)) are evaluated at time step *t*. We solve the linear system represented by (7.9) using the LINPACK linear algebra subroutines SGBFA and SGBSL which efficiently solve the banded matrices by back-substitution to find Δx. Then, the new species mixing ratios are calculated from a rearranged version of equation (7.4)

$$\vec{x}^{t+1} = \vec{x}^t + \Delta\vec{x} \tag{7.10}$$

One final point to notice about this method is that as $\Delta t \rightarrow \infty$, equation (7.9) goes to:

$$\vec{x}^{t+1} = \vec{x}^{t} - J^{-1} \vec{F}(x^{t}) \qquad (7.11)$$

which is the definition of Newton's steady-state solver. As discussed below, this is the primary mode in which we have used our code to date.

7.2.2 The time-dependent reverse Euler solver

The numerical solver that was used for the photochemical models described in Chapters 4 and 6 is already a time-dependent solver, although only steady-state solutions were analyzed. The reason is that while the first-order reverse Euler solver is guaranteed to converge to a stable solution, it can significantly diverge from the true solution while it approaches steady state. Assume for a given species at a given height, the actual time-dependent change resulting from an atmospheric perturbation is given by the solid line in Figure 7-1. We form a numerical approximation to this exact solution by estimating the derivative at the future timestep using equation (7.3). As we march through time (from left to right in Figure 7-1), the computed solution can deviate from the exact solution, but eventually converges to a stable solution somewhere near the exact solution. The entire solution is deemed to be in steady state when all species at all heights have converged, as approximated for this specific case by the circled portion of Figure 7-1. When this occurs, an implicit solver can increase the timestep without limit. Numerical experiments with the photochemical model reveal that all perturbations that we impose on the photochemical model tend to resolve within 10^6 years (consistent with the atmospheric lifetimes < 10^6 years presented in Table 1-1, given that N_2 is abundant and effectively fixed in mixing ratio), but all photochemical solutions we report as "steady-state" in Chapters 4 through 6 were integrated until timesteps greater than 10^9 years could be taken. In this manner, we are assured of a steady-state solution because we are approaching Newton's method as described in equation (7.11)

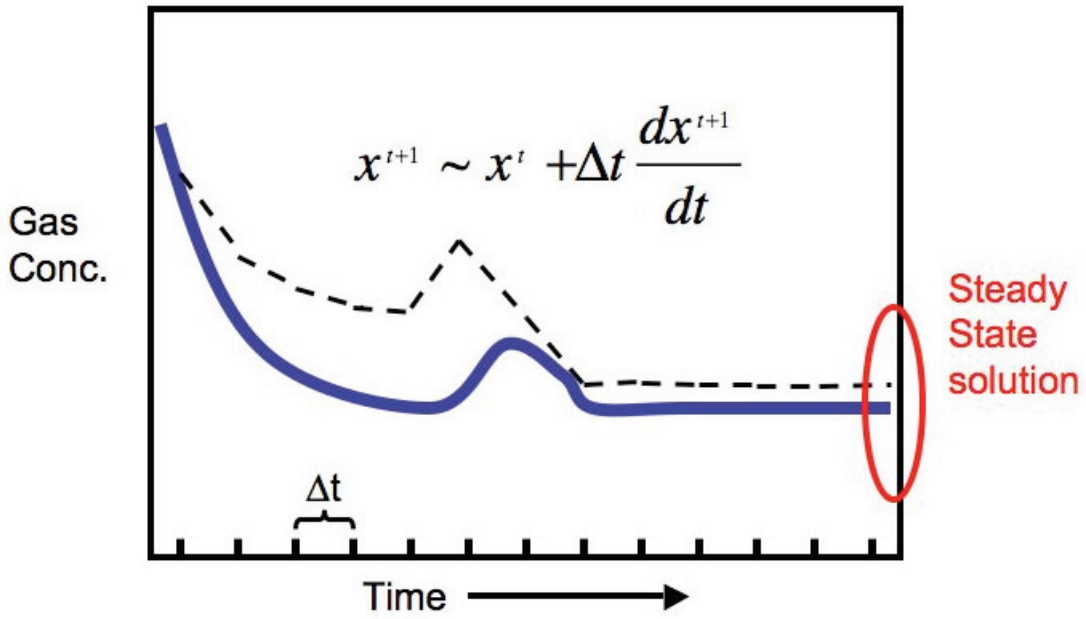

Figure 7-1 A cartoon of the time-dependent reverse Euler solver

The dashed line is a first order reverse Euler approximation to an exact solution represented by the solid (blue) line, using a fixed timestep (Δt).

The time-dependent results that we present here make use of the fundamental fact that any numerical solver provides the exact solution as the timestep approaches 0. An infinitesimal timestep is obviously only a theoretical construct, but in practice a stable convergent solver working with a small but finite timestep can provide a solution that is "close enough" within a user-specified tolerance. This is illustrated in Figure 7-2 which shows the same case as Figure 7-1 but estimated with a much smaller timestep (Δt).

Obtaining the true "exact solution" is of course impossible given finite computing time, but in practice, there will exist a maximum timestep below which the computed solution doesn't change by a significant amount. The difficult task we face is trying to decide, in advance, how to identify a solution that is "close enough" without knowing what the exact solution is. Fortunately, there exists a formalism for doing this within the literature on

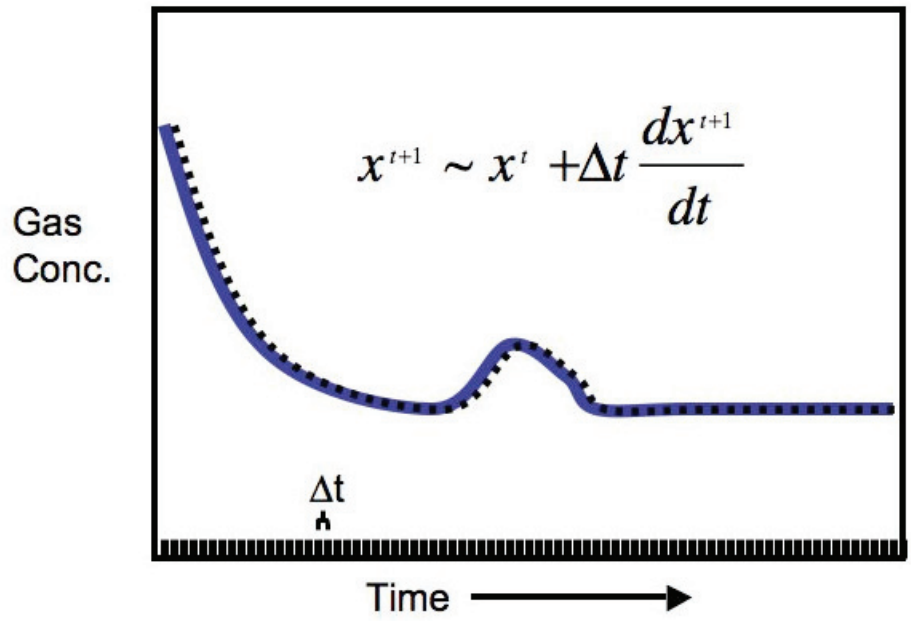

Figure 7-2 A cartoon of the time-dependent reverse Euler solver with small timestep (Δt)

The dashed line is a first order reverse Euler approximation to an exact solution represented by the solid (blue) line, using a smaller fixed timestep (Δt) than shown in Figure 7-1. Using a smaller timestep keeps the numerical approximation closer to the actual solution. It also takes forever to run.

numerical methods. We paraphrase* Mark Jacobson's textbook Fundamentals of Atmospheric Modeling, page 420:

> "A method of testing a solver's accuracy is to compare the time-dependent solution from it with an exact solution. A normalized gross error (NGE) is calculated as:

$$\text{NGE} = \frac{1}{N_{\text{tim}}} \sum_{j=1}^{N_{\text{tim}}} \left(\frac{1}{K_{s,t_j} E_{t_j}} \sum_{i=1}^{K_{s,t_j}} (N_{i,t_j} - E_{i,t_j})^2 \right) \times 100\% \qquad (7.12)$$

* The direct quote in Jacobson uses an slightly different form for the normalized error term under the second summation. We use the L^2 norm $(N_{i,j} - E_{i,j})^2$ and normalize to the entire number density E_{tj} rather than for each species individually under the summation. We thank Professor Dale Duran of the UW Atmospheric Science department for suggesting this form of the normalized error metric as more appropriate for this calculation and for general help with testing the time dependent solver in this section.

where N_{tim} is the number of time steps, $N_{i,tj}$ and $E_{i,tj}$ are predicted and exact concentrations [of species *i* and time t_j], respectively of species *i* at time t_j, and $K_{s,tj}$ is the number of exact concentrations above a minimum cutoff concentration at time t_j. Typical cutoff concentrations for atmospheric gas chemistry range from 10^{-3} to 10^{3} molecules cm^{-3}. In (7.12), concentrations may be compared at evenly spaced time intervals, such as every one-half hour, instead of every time step. Exact solutions are obtained by solving the equations with an integrator of known high accuracy or with the given scheme using an extremely small time step. Good solvers of chemical ODE's produce NGEs less than 1 percent"

A plot of normalized gross error versus timestep is expected to decrease with decreasing timestep, until a timestep is reached at which the solution doesn't improve dramatically with further decreases in timestep. We use a time-independent cutoff density $K_{s,t}$ of 1 cm^{-3} which means we ignore errors in trace gases with concentrations below approximately 10^{-19} bar in all that follows. The exact concentrations $E_{i,tj}$ are specified by using the reverse Euler scheme with an extremely small fixed timestep. For our test case, we perturb a converged steady-state solution by increasing the temperature profile by 5 degrees everywhere. This was chosen because temperature will change the reaction rate of many species in the atmosphere, but generally has a second-order effect on atmospheric photochemistry (Kasting, 1979). This perturbation changes the densities of nearly every species at every height, without fundamentally changing the chemical nature of the atmosphere. Perturbations from the temperature change resolved themselves within 10^{5} model years, which was convenient for our tests because, as we discuss below, restricting our code to very small timesteps led to long computer integration times. The code was modified to take fixed timesteps and nine models were integrated to 10^{6} model years using fixed timesteps of 160 years, 80 years,

40 years, 20 years, 10 years, 5 years, 2.5 years, 1.25 years, and 0.625 years. The 0.625 year fixed timestep model required approximately 2 weeks of computing time on a dual 2.7 Ghz MacPro to reach 10^6 model years.

Normalized gross errors were computed using equation (7.12) for each model run, adopting the densities computed by the 0.625 year fixed timestep run as the exact solutions ($E_{i,j}$). On Figure 7-3, we plot the natural logarithm of the NGE versus the natural logarithm of the timestep (Δt), a choice we will explain below. The NGE in the case of 160 years (ln 160 ~ 5) is approximately 20% (ln 20 ~ 3). This means that an average species at any given height at any given timestep deviates from the exact solution by approximately 20%. This NGE is equivalent to the rough accuracy of the overall model assumptions, estimated at 20 - 30% by Jim Kasting (Kasting, 1979). As the timestep is subsequently halved, the NGE decreases, first dropping below 1% (ln 1 = 0) in the 10 year fixed timestep model (ln 10 ~ 2.3). The NGE continues to decrease to a low of 0.1% at 1.25 years, but the overall trend below 10 years is asymptotic, as would be expected once a good approximation to the exact solution has been reached. At the smallest timesteps shown on Figure 7-12, the NGE decrease is no longer monotonic. At the very low normalized gross errors (below 0.1%) the metric is sensitive to slight changes in round-off among the most dominant species, which accounts for the apparent scatter. In the time-dependent results that follow, we fix the timestep at 10 years and take our resulting solutions to be accurate within 1%.

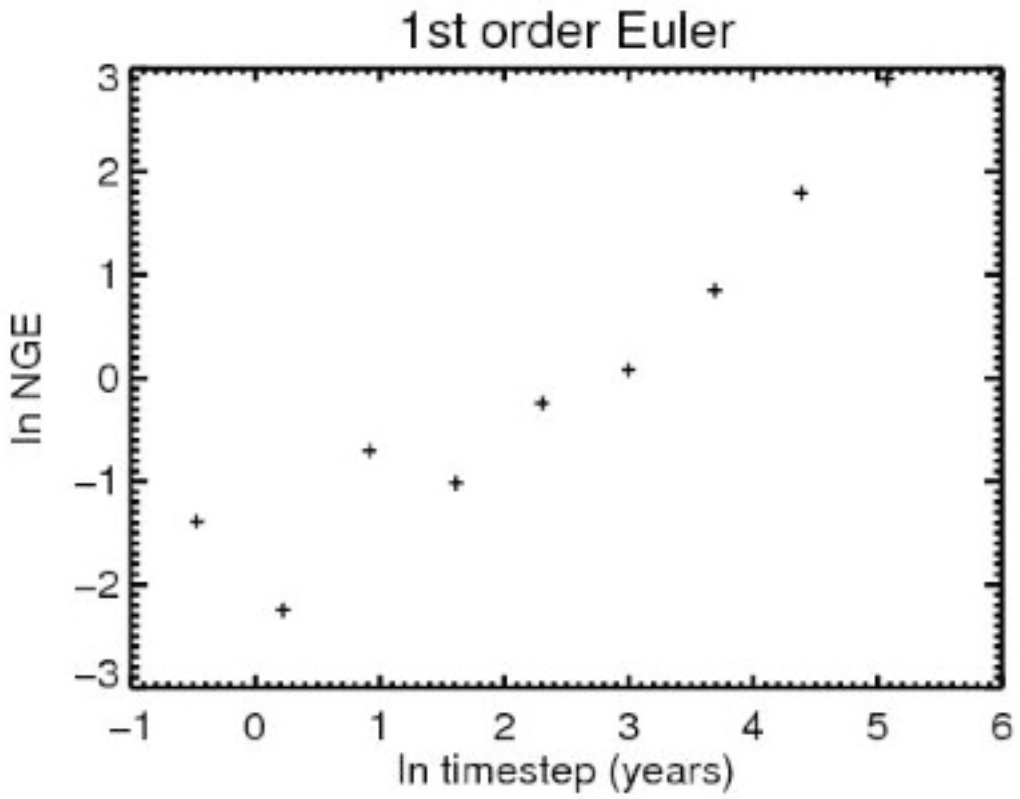

Figure 7-3 Normalized gross errors in the photochemical model

The photochemical model was run with identical perturbations 9 times, with the only change between the models being successively halved timesteps. The log of the normalized gross error given by equation (7.12) is plotted as plus symbols (+) against the log of the fixed timestep.

The "order" of a given numerical approximation to the solution of a differential equation is related to the discarded error terms in the Taylor's series expansion of the solution. For example, in:

$$x^{t+1} \sim x^t + \frac{\delta x^t}{\delta t}(\Delta t) + \frac{\delta^2 x^t}{\delta t^2}(\Delta t)^2 + \ldots \qquad (7.13)$$

the solution would be "second-order" if the Taylor series was truncated after the first two terms, so that the error was on the order of $(\Delta t)^2$. In general the order, n, of a solver is defined by:

$$\text{Error} \sim (\Delta t)^n \tag{7.14}$$

In this manner, we can use Figure 7-3 to check that our solver is working to first order accuracy, as we instructed it do via equation (7.5). The slope ln (Error) / ln (Δt) computed by the model gives an estimate of n, and we see that the solver is behaving to first order given that n ~ (3 – (-2)) / (5 - 0) = 1.

7.3 Experimental Design of time-dependent model runs

7.3.1 Code changes

In addition to the changes regarding the fixed timestep discussed above, we also change the lower boundary conditions (LBCs) on O_2 and CH_4 to be constant flux rather than constant mixing ratios which were used in Chapters 4 and 6. O_2 and CH_4 were the only fixed mixing ratio LBCs used in the previous model runs, so all species are now specified by constant deposition velocities, constant/variable flux, or both. The constant flux LBC is implemented by adding a term:

$$\frac{\phi_{LB}}{N_1\, dz} \tag{7.15}$$

to the right hand side in Equation (7.1), where ϕ_{LB} is the upward flux across the lower boundary in molecules cm^{-2} s^{-1}, N_1 is the total number density in the lowest level of the atmosphere (which is fixed via our 1 bar pressure assumption to be 2.5 x 10^{19} cm^{-3}), and dz is the height of the first layer of the atmosphere (12500 cm in the case of the models run in Chapter 6 and here). Further information on the boundary conditions is provided in Appendix A.

With a photochemical model driven by flux LBCs on O_2 and CH_4, we are free from two fundamental problems that affected the work presented in Chapter 6. Use of the fixed

mixing ratio LBCs on O_2 and CH_4 allowed us ease in computing our grid of models, but in exchange, we had no control over the absolute fluxes in the model. Given that our LBCs are an attempt to represent volcanoes and biology, constant flux more closely resembles the true independent variables than does the assumption that either process acts to maintain a fixed mixing ratio. The second problem resulting from using the fixed mixing ratio LBCs in Chapter 6 was that we had to constrain a path through CH_4/O_2 mixing ratio space via the external biogeochemical model of Chapter 5 (i.e. Figures 6-3, 6-4, 6-S2). Use of variable flux LBCs fixes both of these problems and allows us to directly investigate the photochemical response of plausible atmospheres to changes in flux across the lower boundary.

In addition, we modified the main time-stepping loop to allow for CH_4 fluxes to vary linearly with time. We allow the experimenter to specify three parameters. The first is the absolute time at which the flux perturbation begins, which we keep fixed at 100 years for all results described here. The user also specifies the magnitude of the flux change and the time period over which the change takes place. After the flux perturbation ceases, the perturbed fluxes remain at their final value and the integration continues so that the solution can relax to a steady state driven by these final boundary conditions. These final solutions are not "steady-state" as defined by our earlier criteria of running the solver to timesteps of 10^9 years. Rather, we identify them as steady-state when the solution at all levels for all species aren't changing, as in Figure 7-1.

7.3.2 Experimental design

We force our time-dependent photochemical model with linear decreases of two to five percent in the CH_4 flux relative to the O_2 flux. This forcing was based on our results in Chapters 4 through 6, which indicate that changes in the CH_4:O_2 flux ratio of a few percent enabled either a stable anoxic solution or a stable oxic solution (see Figure 5-2 and Table 6-1). Additionally, in Chapters 2 and 3, we provided arguments that reducing fluxes from volcanoes and metamorphism should decrease over time, due primarily to hydrogen escape. In Chapter 5, we postulated that anaerobic oxidation of methane

stimulated by increasing oceanic sulfate could also have played a role in decreasing the CH_4 flux relative to the O_2 flux. These biotic and abiotic arguments for a decreasing ratio of reductants to oxidants into the Archean atmosphere provide sufficient justification to investigate the response of a weakly reducing atmosphere to decreasing net flux of CH_4:O_2, while remaining agnostic as to the cause.

The results presented in this chapter start from converged steady-state solutions output from the high vertical resolution photochemical model described in section 6.6.3. The starting points for the time-dependent models presented here are either the "Archean" atmosphere described in Chapter 6 (with fixed mixing ratio LBCs of $O_2 = 2x10^{-8}$ and $CH_4 = 10^{-4}$) or a model with fixed mixing ratio LBCs of 10^{-7} on O_2 and 10^{-4} on CH_4. This second starting solution has the same amount of CH_4 at the ground, but has higher ("whiff") levels of O_2 at the ground. As a result, the model requires a higher biospheric flux than the models in Table 6-1 in order to support a higher ground-level O_2 in a higher CH_4 environment. This behavior was predicted in Figures 4-5 and 5-2, although we note that we have updated our estimates of the flux required to support a given atmosphere in section 6.6.3. Our starting solution was supported by a CH_4 flux of 2.5×10^{12} molecules cm^{-2} s^{-1} and an O_2 flux of 5×10^{12} molecules cm^{-2} s^{-1}. These fluxes are approximately 3 times larger than the cases described in Chapter 6, and hence represent a more productive biosphere. The net CH_4:O_2 ratio in this atmosphere when considering H_2, CO, and H_2S as CH_4 equivalents is 0.500. The ozone column depth is 6.7×10^{13} cm^{-2}, and the elemental sulfur deposition flux is 7.9×10^{8} molecules cm^{-2} s^{-1}, a S_8/total S deposition fraction of ~ 20%.

7.4 Results

In this section we present results from multiple runs of the time-dependent photochemical model. These model runs start from either of two initial starting models described above, and are subjected to CH_4 perturbations of various magnitudes and timescales. These models are used to investigate the timescale of the oxic transition, and for a simple examination of the dominant photochemical reactions and species at

the time of the transition. In addition, we study the reversibility of the oxic transition before concluding by an examination of mid-infrared spectra of the Earth undergoing a modeled oxic transition. In order to keep track of the various models in this section, we present Table 7-1 which lists the parameters of the various models used, and assigns model names for future reference.

Table 7-1 Time-dependent photochemical model parameters

Model names and parameters used in the time-dependent explorations in this chapter. The "starting model" column lists the negative logarithm of the O_2 and CH_4 mixing ratio LBCs. 7 / 4 thus corresponds to $pO_2 = 10^{-7}$ and $pCH_4 = 10^{-4}$. The "perturbation" column describes the percentage change in the CH_4 flux relative to the O_2 flux, which is imposed as a linear decrease over the number of years in the "years" column. The "Figure" column refers to the figures in this chapter which show data from the given model described by the label in the "model name" column.

model name	starting model	perturbation	years	Figure
A	7 / 4	-2%	instant	7-4
B	7 / 4	-2%	10^4	7-5, 7-7
C	7 / 4	-2%	10^6	7-6
D	8 / 24	-5%	10^4	7-8, 7-9, 7-10
E	7 / 4	-5%	10^4	7-11, 7-13

7.4.1 A timescale for the oxic transition

Our first experiment was a series of three model runs which drop the CH_4:O_2 flux ratio by ~ 2%. We examine the response of the atmosphere to an instantaneous drop in the CH_4:O_2 flux ratio by 2% (Model A), a drop by 2% over 10^4 years (Model B), and a drop by 2% over 10^6 years (Model C). Figure 7-4 shows the ground-level O_2 and CH_4 mixing ratios versus time for Model A. Figure 7-4 (and the subsequent figures) represent the first demonstration of a time-dependent photochemical model solution of the oxic transition.

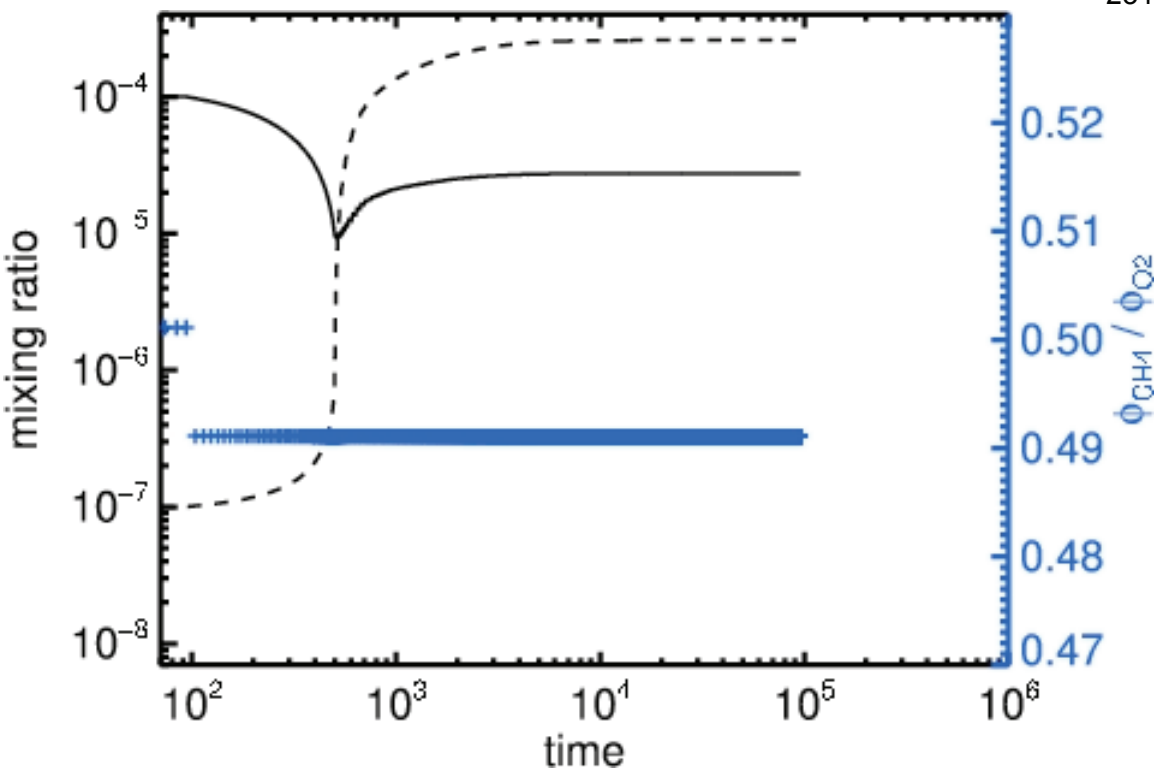

Figure 7-4 Time-dependent O_2 and CH_4 mixing ratios from Model A

Ground level CH_4 (solid line) and O_2 (dashed line) mixing ratios from the time-dependent photochemical model. Time is shown in years on the x-axis. At 100 years, an instantaneous change is made to the lower boundary condition, decreasing the CH_4 flux relative to the O_2 flux by 2%. An oxic transition occurs within 500 model years. The (blue) plus symbols (+) map to the right axis and represent the time-dependent flux ratio that is imposed on the model.

The oxic transition occurs extremely quickly in Figure 7-4, with a radically different atmosphere present less than 1000 years after the initial perturbation. CH_4 levels drop by almost an order of magnitude before O_2 levels change appreciably. A CH_4 minimum of ~10 ppm occurs at the cross over point where $pO_2 \sim pCH_4$. O_2 levels rise by over three orders of magnitude in approximately 250 models years. The flux-driven model solution regains steady state at the final flux values within 10^4 years, stabilizing at pO_2 of 2.3×10^{-4} bar and pCH_4 of 2.75×10^{-5} bar. These O_2 values are lower than required by the Paleoproterozoic paleosol constraints, and the amount of CH_4 present isn't likely to be enough to warm the Earth without significant CO_2. We will address the Proterozoic steady-state values later in this chapter, but for now continue with an examination of the transition itself and its timescale.

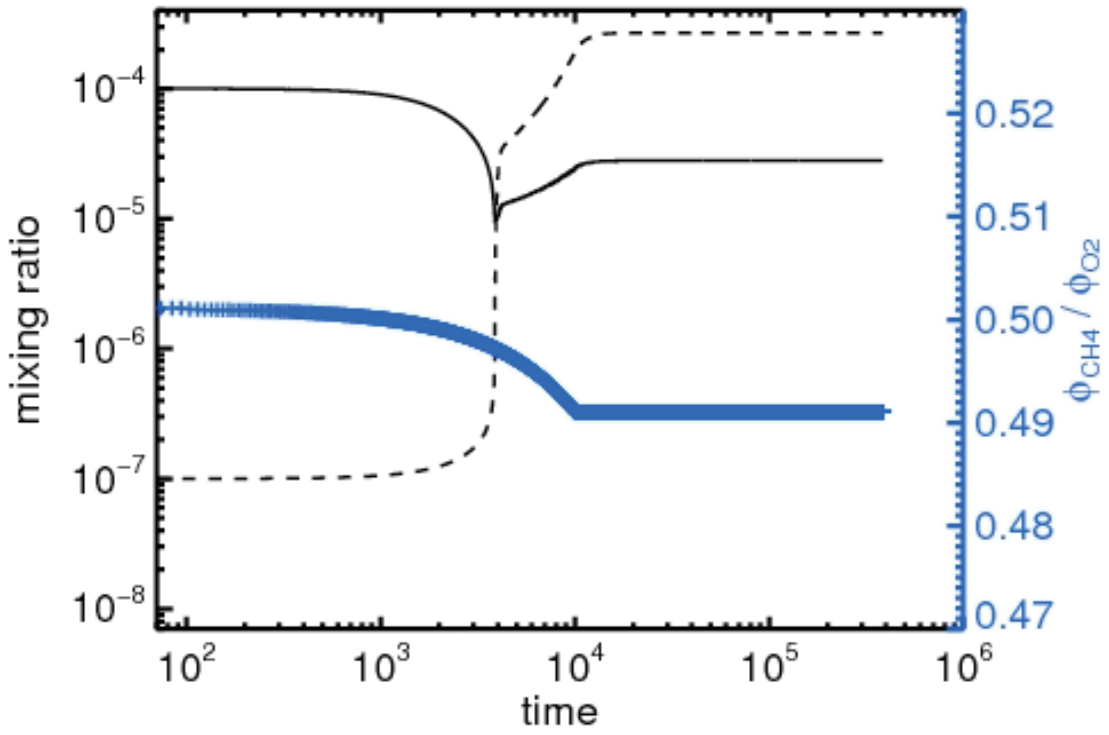

Figure 7-5 Time-dependent O_2 and CH_4 mixing ratios from Model B

Ground level CH_4 (solid line) and O_2 (dashed line) mixing ratios from the time-dependent photochemical model. Time is shown in years on the x-axis. The (blue) plus symbols (+) map to the right axis and represent the time-dependent flux ratio that is imposed on the model.

Our next two experiments with the time-dependent photochemical model involve running the same 2% flux decrease, but lengthening the time period over which it occurs. The ground level mixing ratios for O_2 and CH_4 from models driven by a 2% decreases in CH_4:O_2 occurring over 10^4 and 10^6 years are shown as Figures 7-5 and 7-6 respectively. Models A, B, and C wind up at the same pO_2 and pCH_4 well after their respective oxic transitions, which gives us confidence that our time-dependent solver is working correctly, at least when the fluxes are constant.

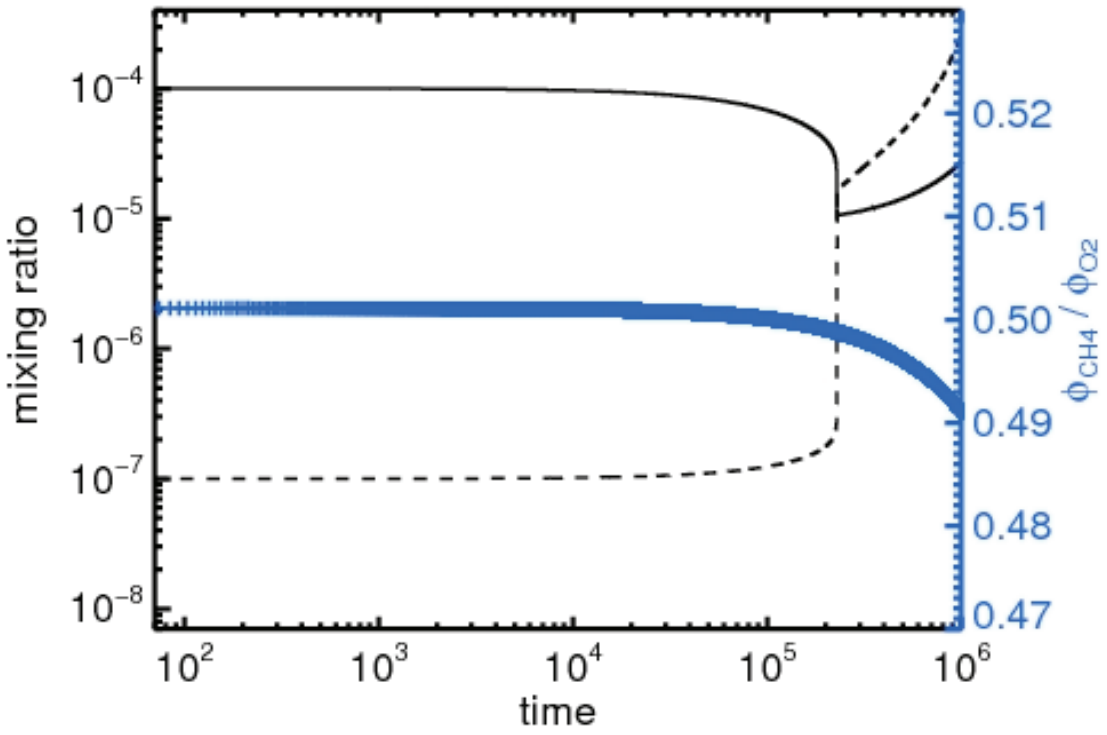

Figure 7-6 Time-dependent O_2 and CH_4 mixing ratios from Model C

Ground level CH_4 (solid line) and O_2 (dashed line) mixing ratios from the time-dependent photochemical model. Time is shown in years on the x-axis. The (blue) plus symbols (+) map to the right axis and represent the time-dependent flux ratio that is imposed on the model.

The most surprising result from the models shown in Figures 7-4 through 7-6 is that the timescale for the initial transition between the anoxic and oxic states is approximately the same. In all models, the transition from oxygen as trace gas to dominant redox gas occurs on the order of a few thousand years, when the CH_4:O_2 ratio begins to drop below 0.5. This gives credence to our earlier identification of a sharp cutoff density for CH_4 below which O_2 can compete for redox control of the atmosphere.

To further investigate the hypothesis of a short timescale for the oxic transition, we repeated the above experiments, but with 3% decreases in the CH_4:O_2 flux ratios over the same timescales. In these cases (not shown), the resulting atmosphere has a

distinct ozone layer featuring an ozone column depth of 5.5 x 10^{18} cm^2 which is close to modern levels. While the final states are different, the oxic transition occurs within a few thousand years in each model. The oxic transition occurs very quickly and appears to be independent of the timescale and magnitude of the flux perturbation. This result is further supported later in the chapter where we present models at different starting solutions also undergoing oxic transitions in ~ 10^3 years.

Given this observation, we limit ourselves to models driven by flux perturbations occurring over 10^4 years in our subsequent analysis of the photochemistry of the oxic transition. It would be ideal to drive the photochemical model with flux changes on timescales suggested by the biogeochemical model, but the computing time would be unreasonable given our brute-force method of time-dependence. While a 10^4 year timescale for flux changes of this magnitude is not likely representative of changing biology, the timescale of the initial transition between the anoxic and oxic solution does appear to be independent of the timescale, so it is reasonable to examine the details of the transition driven by such a drastic change.

7.4.2 The photochemistry of the oxic transition

Figures 7-5 and 7-6 reveal two stages of evolution of the ground level CH_4 and O_2 concentrations during the transition between the two stable atmospheric states. The first stage is a quick collapse of methane leading to an oxic transition occurring over ~ 10^3 years. This stage features a sharp rise of O_2 to approximately 35 ppm, which appears to halt the collapse in CH_4 values. From this point forward, a more stable progression occurs where both O_2 and CH_4 increase monotonically until the flux perturbation ceases and the system remains at steady state. The post transition “second-stage” behavior can be checked against the semi-analytic prediction we made in Equation (5.16) which predicts that the CH_4 concentration in an O_2 rich atmosphere is set by the O_2 concentration:

$$\frac{CH_{4,TRANS}}{CH_{4,FINAL}} = \frac{\phi_{TRANS}}{\phi_{FINAL}}\left[\frac{O_{2,TRANS}}{O_{2,FINAL}}\right]^{0.2448} = 1.01\left[\frac{259\ ppm}{35\ ppm}\right]^{0.2448} \sim 1.65 \qquad (7.16)$$

where the CH_4 flux at the end of the first stage (ϕ_{TRANS}) is 1% of the value at the end of the perturbation (ϕ_{FINAL}). The semi-analytic prediction suggests that the final CH_4 value ($CH_{4,FINAL}$) will be a factor of 1.65 larger than CH_4 value immediately after the transition ($CH_{4,TRANS}$) based on the ratio of the O_2 values at the transition ($O_{2,TRANS}$) and the final O_2 values ($O_{2,FINAL}$). In equation (5.16), the concentrations and fluxes were demanded in Tmol, but here can be in any scaleable unit given that they both appear in ratio. $CH_{4,TRANS}$ is approximately 12 ppm, which yields a prediction of $CH_{4,FINAL}$ ~ 20 ppm, which is reasonably close to the computed value of 27 ppm.

Figure 7-7 shows the tropospheric lifetimes (as defined in Chapter 6) for O_2 and CH_4 and the S_8 mixing ratio across the 10^4 year run driven by a 2% flux decrease. The lifetimes calculated from the time-dependent model strongly confirm our results from Chapter 6. Once methane begins its collapse, the S_8 signal drops off, disappearing completely by the time O_2 tropospheric lifetimes are greater than ~ 1 day.

Before analyzing the first stage of the oxic transition, we note that the overall time-dependent track taken by O_2 and CH_4 may be specific to the starting solution we have chosen. As an example, Figure 7-8 was computed starting from the "Archean" solution from Chapter 6 (see Table 6-1). This model solution was computed for $pO_2 = 10^{-8}$ bar and $pCH_4 = 2 \times 10^{-4}$ bar, and requires lower biogenic fluxes than those shown above in Figures 7-4 – 7-7. We subject this model atmosphere to a flux decrease of 5% over 10^4 years. In the results shown on Figure 7-8, CH_4 drops more precipitously than in the previous experiments, reaching a low of 1 ppm before an increasing ozone shield allows for methane to increase again. This model run may be more consistent with the geologic record of severe glaciations around the time of the oxic transition, although "whiff" levels of O_2 only occur for a geologically instantaneous amount of time. In general, we see that the magnitude of the CH_4 and O_2 fluxes are important, in addition to

their ratio. Sustained “whiff” levels of oxygen are easier to explain with larger biospheric fluxes.

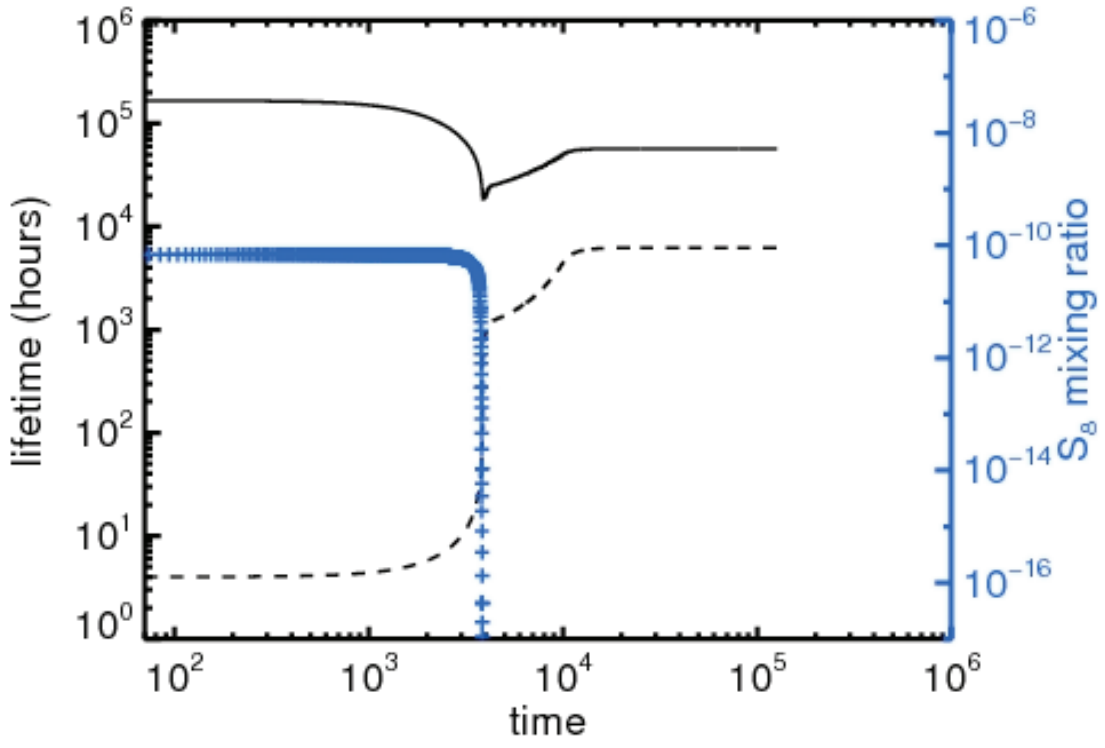

Figure 7-7 CH_4 and O_2 tropospheric lifetimes across the oxic transition

Tropospheric lifetimes (in hours) for CH_4 (solid line) and O_2 (dashed line) across the oxic transition. Time is shown in years on the x-axis. The S_8 ground level mixing ratio is shown as (blue) plus symbols (+) and are mapped to the right axis. The results were taken from Model B which was shown previously as Figure 7-5.

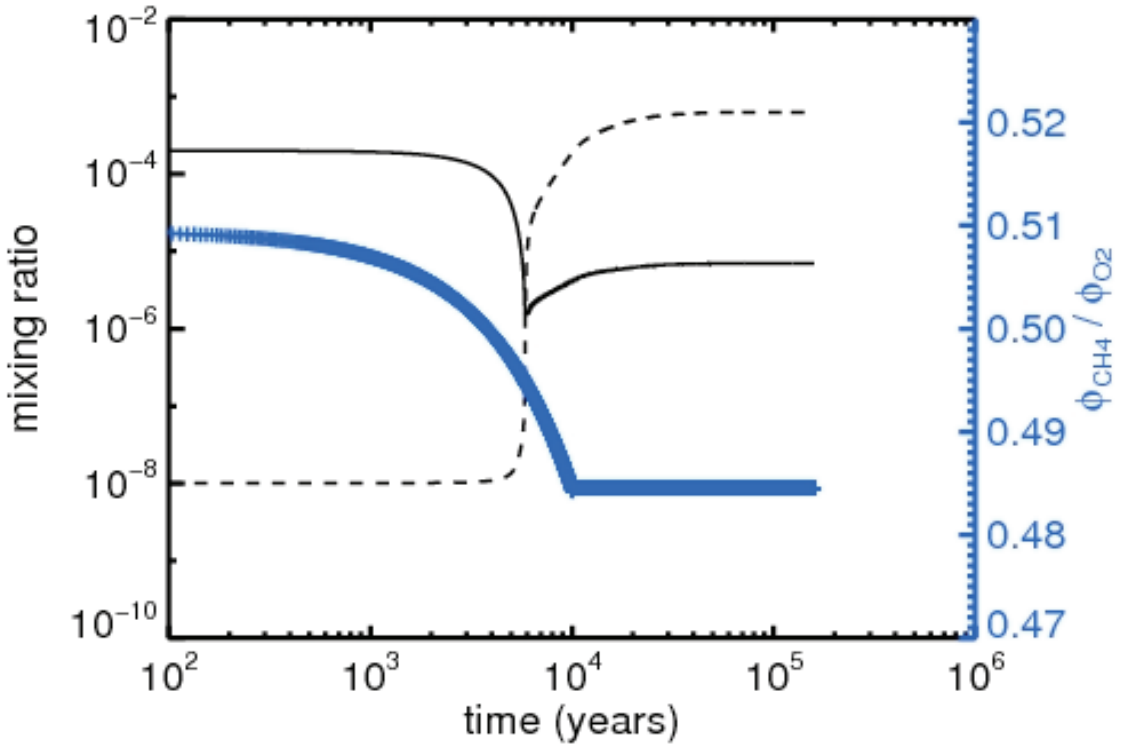

Figure 7-8 A time dependent oxic transition starting from pO_2 of 10^{-8} bar

An 5 % change in the net CH_4:O_2 flux ratio over 10^4 years was computed starting from a converged, steady-state solution at $pO_2 = 10^{-8}$ bar and $pCH_4 = 2 \times 10^{-4}$ bar.

We begin our investigation of the details of the oxic transition shown in Figure 7-8 by examining the time evolution of ground-level mixing ratios of additional interesting species. Figure 7-9 shows how H_2O_2 and H_2CO, the two largest redox species after CH_4 and O_2 both drop in magnitude at the transition, with H_2O_2 returning quickly to pre-transition values while H_2CO remains about a factor of 5 smaller. HO_2 mixing ratios remain remarkably constant across the oxic transition. O_3 rises rapidly, while CH_3, H and S_8 drop and become effectively absent from the atmosphere after the transition. The most interesting behavior is that of OH, which increases by an order of magnitude during the transition, then decreases again. OH, a vital intermediate in the catalytic destruction of CH_4 by O_2 as described in Chapter 6 and the dominant oxidant in the atmosphere, was perhaps never more important than during the oxic transition, when its mixing ratio

may have reached ~10^{-13}, compared to the modern global average mixing ratio of ~10^{-14} (IPCC, 2007).

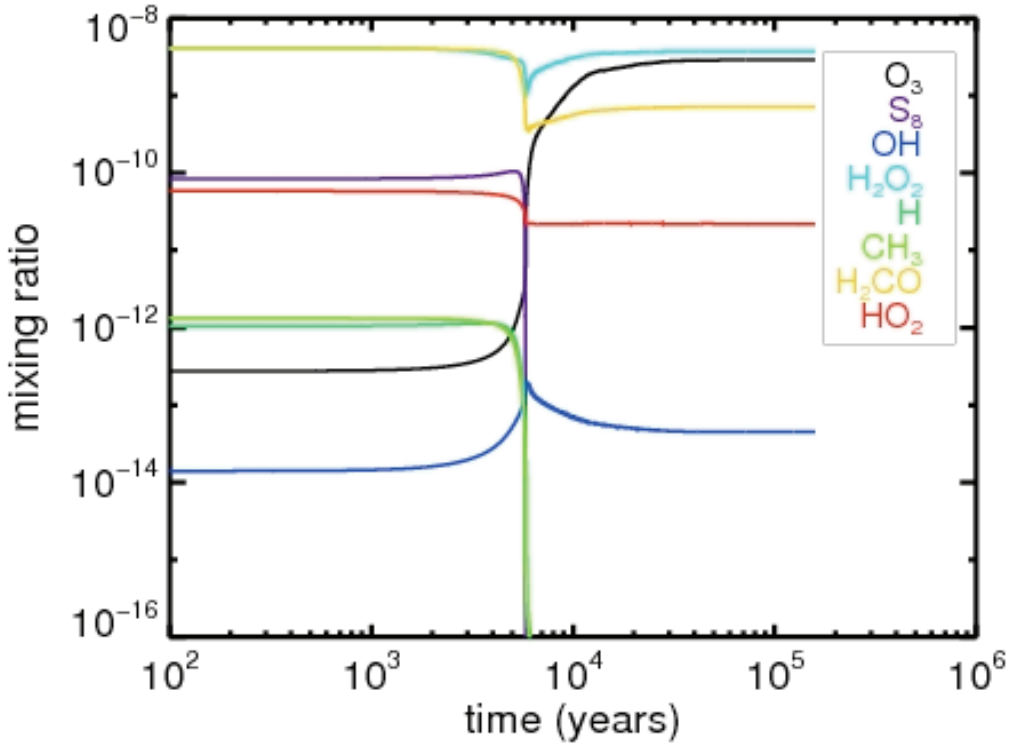

Figure 7-9 Ground-level mixing ratios from model D

Ground-level mixing ratios versus time from model D. The species are indicated by their colors in the legend.

We next look at the lifetimes of the prominent radicals involved in the destruction of CH_4, as a direct test of our results in Chapter 6. Figure 7-10 shows the lifetimes of O_2, O, CH_3, H, OH, and HCO using the same color scheme as Figure 6-S3. Figure 6-S3 was computed from 7 steady-state models chosen to represent a likely path through atmospheric phase space, while Figure 7-10 represents a continuous track through phase space.

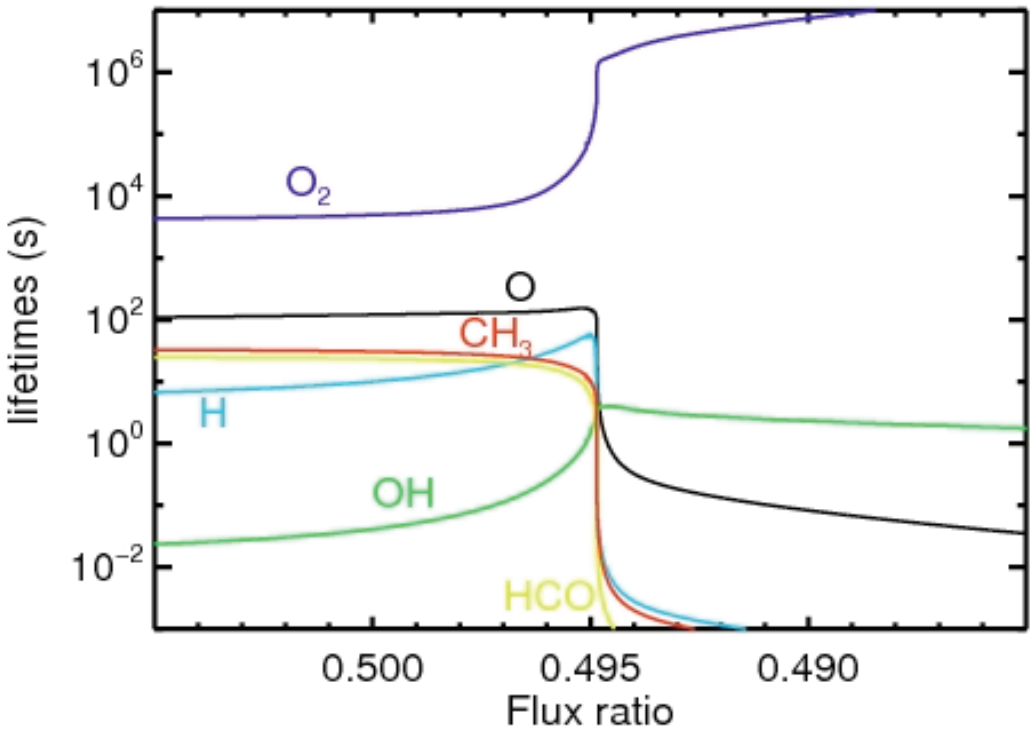

Figure 7-10 Tropospheric lifetimes across the oxic transition

The tropospheric lifetimes of O_2, O, CH_3, HCO, H, and OH across the oxic transition. The lifetimes are plotted against the net CH_4:O_2 flux ratio to enable comparison with Figure 6-S3.

Figure 7-10 reveals that the behaviors of these important radical species was well represented in our examination of the atmosphere as a succession of quasi-steady states in Figure 6-S3. In Figure 6-S3 we did not attempt to resolve the details of the oxic transition, which are seen here to be continuation of the trends described in Chapter 6. The H and OH lifetimes increase concurrently with a decrease in the CH_3 and HCO lifetimes. Both the OH and H lifetimes peak at the time of the transition (when pCH_4=pO_2), and then decrease in magnitude.

Figure 7-11 shows the vertical profiles from four timesteps computed in our time-dependent model of the oxic transition driven by a 5% decline in the CH_4:O_2 flux ratio over 10^4 years, starting from the whiff solution (Model E). The second panel strongly supports our suggestion in Chapters 4 and 6 that the MIF-S disappears while the atmosphere is still reducing, well prior to any rise in oxygen. The time difference between when S_8 deposition ceases and oxygen rises would not be detectable geologically if the atmosphere followed the path of Fig 7-11, although the general prediction that we would not expect to see MIF-S during the glacial epochs holds.

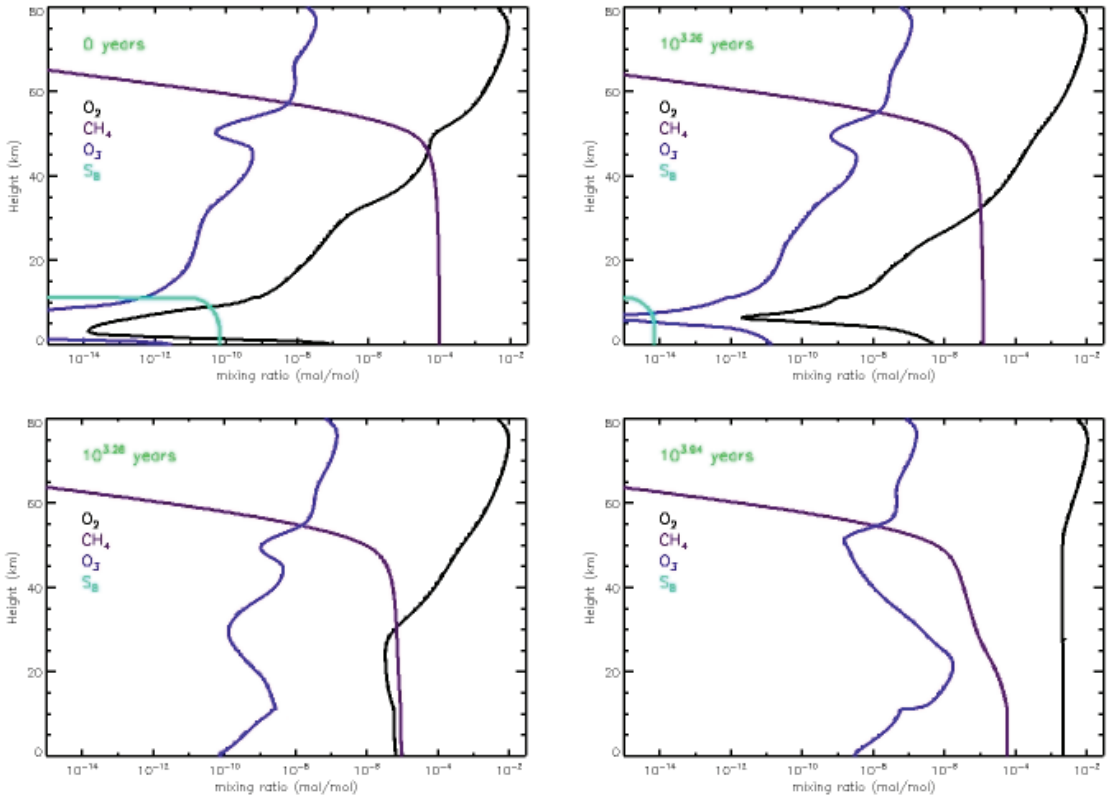

Figure 7-11 Time-dependent vertical profiles of O_2, O_3, CH_4, and S_8 from Model E

This figure shows vertical profiles from 4 timesteps (0, $10^{3.26}$, $10^{3.28}$, and $10^{3.94}$ years) in a case driven by a 5% decrease in the CH_4:O_2 flux ratio over 10^4 years. The oxic transition happens on a very short timescale over ~10^3 years . The flux evolution of the ground-level mixing ratios are very similar to that in Figure 7-5, although the post transition levels of O_2 and CH_4 are higher.

7.4.3 Reversibility

It is often assumed that once the oxic transition took place, it was permanent. The action of hydrogen escape on oxidizing the continents is irreversible (Catling *et al.*, 2001), which effectively forces this statement to be true over long timescales. Goldblatt *et al*. (2006) have also argued that the oxic transition is bistable and effectively irreversible due to ozone formation. During any given Archean day, biological fluxes into and out of the atmosphere are quantitatively larger than geologic fluxes. Given that drastic changes in the biosphere might result from a Snowball Earth event, we ran a few experiments to test if the oxic transition is reversible with respect to the flux perturbations that create them.

We find that our flux driven oxic transitions are completely reversible, at least numerically. This is not too surprising given the general principle described in Chapter 1 that atmospheric composition represent the gases that are fluxed into it on short timescales. Figure 7-12 starts with a converged steady-state solution with $pO_2 = 8 \times 10^{-3}$ bar and $pCH_4 = 9 \times 10^{-5}$ bar, a model atmosphere which contains an ozone layer comparable to the modern. This starting case was the end result of a time-dependent model run which imposed a 3% decrease in the CH_4 flux over 10^4 years on our whiff atmosphere at $pO_2 = 10^{-7}$ bar and $pCH_4 = 10^{-4}$ bar. As shown on Figure 7-12, we imposed a 3% increase in the CH_4:O_2 flux ratio over 10^4 years, and the atmosphere is seen to transition back to the anoxic state, although the time the model takes to transition from the oxic solution to the anoxic solution is approximately a factor of 5 larger than the initial timescale. This supports the claim of Goldblatt *et al*. (2007) that the reversibility of the oxic transition is path-dependent. All other model atmospheres investigated for reversibility also flipped from oxic to anoxic states when the flux perturbations were reversed. While the timescale for the sharp transition from anoxic to oxic conditions occurred over 10^3 years, the time elapsed from the initiation of the perturbation to the transition was approximately 5 times longer for each investigation of the oxic to anoxic transition than the corresponding anoxic to oxic case.

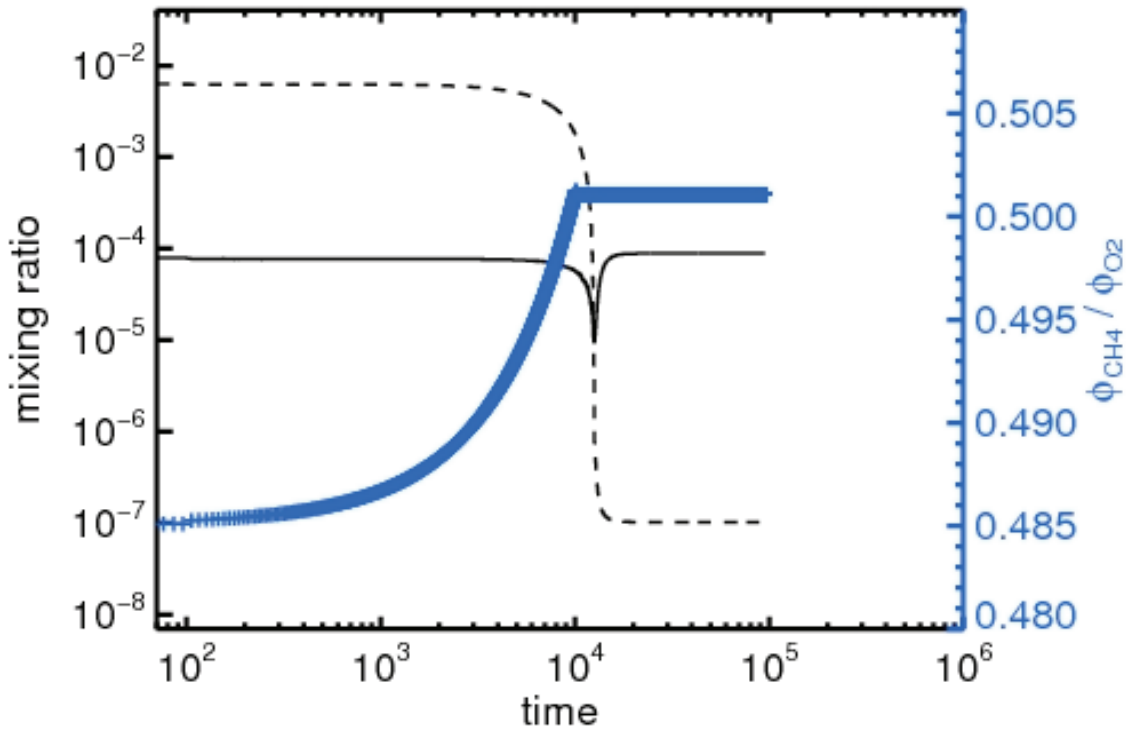

Figure 7-12 The oxic transition is reversible

Ground level CH_4 (solid line) and O_2 (dashed line) mixing ratios from the time-dependent photochemical model. Time is shown in years on the x-axis. The (blue) plus symbols (+) map to the right axis and represent the time-dependent flux ratio that is imposed on the model. This model run starts at a "Proterozoic" solution and responds to an increase in the CH_4:O_2 ratio by reverting to the anoxic state.

We hypothesized that the reversibility might have occurred due to the rapidity of the flux change, so we also ran a model with a 3% increase in CH_4:O_2 flux ratio spread over 10^6 years. This model (not shown) also transitioned back to the anoxic solution at around 10^6 model years, while the model driven by a 3 % decrease had transitioned after ~ 2 x 10^5 years. Our preliminary conclusion is that there is no fundamental constraint from the chemistry of atmospheric ozone that makes the oxic transition irreversible. If the atmosphere did transition permanently and completely to an oxic state 2.4 billion years ago, this should be taken as a constraint that the biospheric fluxes permanently remained at CH_4:O_2 ratios less than 0.5, given evidence that O_2 has been at or above 1

% present levels since approximately 2.2 billion years ago (Chapters 1-3). In this context, the only direct relevance of the reversibility arguments may be directly after the oxic transition, where the atmospheric redox state may have oscillated as modeled in section 3.7. That this may have occurred is evidenced in time-resolved data across the Paleoproterozoic glaciations which show MIF-S reappearing between the first and second glacial episode (Papineau *et al.* 2007)

7.4.4 The oxic transition and astronomical detectability

To bring this dissertation full circle, we return to one of our initial motivations – the astronomical detection of planetary atmospheres. Figure 7-13 shows mid-Infrared atmospheric spectra computed by the SMART code "smart_spectra" (Meadows and Crisp, 1996 ; Crisp, 1997) for four timesteps of a time-dependent photochemical model run driven by a 5% decrease in the CH_4:O_2 flux ratio over 10^4 years. The results support the suggestion of Segura *et al*. (2003) that the Proterozoic might have been the easiest era to detect Earth's habitability, given that both O_3 and CH_4 were present in large quantities, as shown on the lower right panel of Figure 7-13.

7.5 Summary

We have described how to use the existing reverse Euler Solver in a time-dependent mode where the concentrations at each time-step are within approximately 1 % of the exact model solution. This is not to say that the exact solution is the precise solution – merely that our method of estimating it is accurate. We examine the result of decreasing the net amount of CH_4 relative to O_2 fluxed into the lower boundary of model atmospheres. As anticipated by our quasi-steady state models, the response of the atmosphere is declining methane concentrations, while O_2 concentrations remain approximately constant at trace levels.

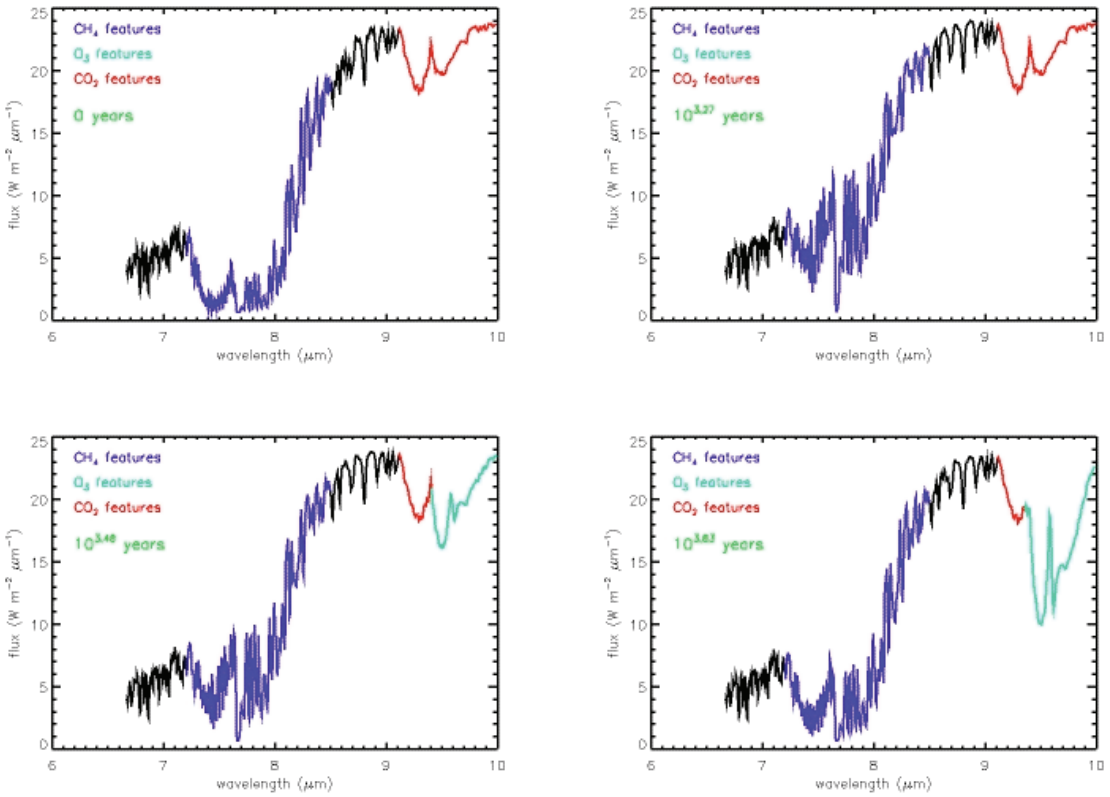

Figure 7-13 Mid-Infrared spectra of the oxic transition

Mid-IR spectra computed by SMART for four timesteps (0, $10^{3.27}$, $10^{3.48}$, and $10^{3.63}$ years) of a photochemical model run with a 5% decrease in CH_4:O_2 flux ratio over 10^4 years. This model was not shown explicitly above, but has a similar time behavior as that of Figure 7-5.

Once CH_4 drops below approximately 10 ppm, ground-level O_2 rises rapidly by orders of magnitude to approximately one order of magnitude greater than the CH_4 concentration in the first-stage of the oxic transition. Provided the net CH_4:O_2 flux ratio continues to drop, concentrations of O_2 and CH_4 evolve in a more stable fashion in a second phased described roughly by equation (7.16). In this regime, CH_4 can re-rise as UV photons which previously penetrated the troposphere are intercepted by the newly formed O_3. The oxic transition occurs over approximately 10^3 years in our model simulations, independent of the flux perturbation timescale. This supports the suggestion that there is a minimum amount of CH_4 that is stable in the presence of large CH_4 and O_2 fluxes from the biosphere. Numerically, the transition is completely reversible in the atmosphere, but given the effect of strong positive feedbacks which promote O_2 fluxes

over CH_4 fluxes, it may be difficult for the biosphere to return to a regime where it can support a weakly reducing atmosphere long after the period of the initial transition. Model mid-IR spectra of the Earth undergoing an oxic transition reveal that the Proterozoic may be the most detectable portion of Earth's evolution due to the simultaneous presence of significant CH_4 and O_3 levels approaching the modern.

Chapter 8 The evolution of solar flux from 2nm to 160 microns: quantitative estimates for planetary studies

In this Chapter[*], we break from the narrative regarding changes in atmospheric composition and turn to a fundamental constraint on the evolution of planetary atmospheres in the solar system. We examine the wavelength dependence of the solar flux, which is a necessary boundary condition for understanding both photochemistry and atmospheric escape. There are no major results presented in this Chapter – Rather, it is an announcement of a technique and computer algorithms likely to be of broad interest to planetary scientists working on the evolution of planetary atmospheres.

We describe a numerical parameterization for wavelength dependent changes to the non-attenuated solar flux appropriate for most times and places in the solar system. We combine data from the Sun and solar analogs to estimate enhanced UV and Xray fluxes for the young Sun, and use standard solar models to estimate changing visible and infrared fluxes. The parameterization, a series of multipliers relative to the modern top of the atmosphere flux at Earth, is valid from 2 nm through the infrared, and from 0.6 Gyr through 6.7 Gyr, and is extended from the solar zero age main sequence to 8.0 Gyr subject to additional uncertainties. The parameterization is applied to a representative modern day flux, providing quantitative estimates of the wavelength dependence of solar flux for a range of paleodates that are relevant to studies of the chemical evolution of planetary atmospheres. We validate the code by comparison to the solar proxies κ^1 Cet and EK Dra and through existing predictions of solar luminosity evolution.

[*] Material in this Chapter is currently under review as: Claire, M.W. and Catling, D.C. "The evolution of solar flux from 2nm to 160 microns: quantitative estimates for planetary studies." *Icarus, in review,* 2008.

8.1 Introduction

The Sun has a profound impact on planetary atmospheres. Solar radiation drives such diverse processes as the vertical temperature profile, molecular reaction rates, transport phenomena, and atmospheric escape. Understanding changes in solar radiation over the age of the solar system is therefore essential to understanding planetary atmospheric evolution (Lean, 1997). All stars evolve in time, with large bright stars dying young in spectacular explosions, while smaller and cooler stars effectively live forever. Our Sun's path lies between these two extremes; it is currently half way through an approximately 10 billion year "middle age" during which, astronomically speaking, nothing dramatic happens. However, as the Sun has aged on the main sequence, the flux in the X-ray and ultraviolet (UV) associated with the magnetically heated upper atmosphere has diminished, while the visible and infrared flux associated with the photosphere has increased by ~30%. A realistic numerical combination of these two trends forms the subject of this chapter.

The goal of this work is to provide quantitative estimates of the top of the atmosphere solar flux at wavelengths longward of 2 nm, at any given time and place in the solar system. Previous work on this topic (Skumanich, 1972; Zahnle and Walker, 1982; Ayres, 1997; Ribas *et al*., 2005) has illuminated many complicated aspects of the observational and theoretical problem, which we will only briefly describe here while motivating our approach. Numerical parameterizations of solar flux evolution have been applied in recent studies of the atmospheric evolution of Mars, Venus, Titan, and Earth (Lammer *et al*., 2003; Penz *et al*., 2005; Lammer *et al*., 2006; Rybicki, 2006), but these applications primarily focus on extreme UV and X-ray fluxes, and examine changes in total integrated solar energy over large (10-100 nm) wavelength regions. Photochemical models of planetary atmospheres demand knowledge of the solar flux at finer (nm scale but not angstroms) resolution through the UV and visible, while climate models are sensitive to changes in visible and infrared fluxes. State of the art photochemical models of early planetary atmospheres have generally either ignored the faint Sun,

introduced unphysical step functions to account for enhanced early UV emission (e.g., Kasting *et al*., 1979; Pavlov *et al*., 2001; Chapter 4), or used flux calibrated spectra from solar proxies to approximate the Sun at a specific age (Segura *et al*., 2007). Our goal is to broaden the applicability of recent astronomical data by providing computationally efficient paleoflux estimates applicable at any planet over a broad range of the electromagnetic spectrum and solar ages.

We construct a series of time and wavelength dependent "flux multipliers," relative to the modern day flux at the top of Earth's atmosphere. The end result is a combination of three distinct parameterizations that capture the effects of different physics in different solar regimes. First, we develop broadband flux multipliers for the UV and shorter wavelengths. Stellar magnetic activity, which drives emission from the upper solar atmosphere, declines with age (Pace and Pasquini, 2004), so our shortwave relative flux multipliers start larger than 1 and decrease with stellar age. Second, we create a parameterization based on photospheric continuum fluxes, with flux multipliers increasing (towards 1) with age as a result of hydrogen burning in the solar core (Gough, 1981). Finally, we add in the effects of strong line emission where data is available. These parameterizations are described in sections 8.2 and 8.3, along with their limitations due to uncertainties about the earliest and future solar rotation rates. The parameterizations are combined via linear weights and applied to high-resolution observations of the flux at the top of Earth's atmosphere in section 8.4. section 8.5 checks the results against existing spectral data and predictions of solar luminosity evolution, while section 8.6 discusses ways to extend the parameterizations to varying solar conditions and to the pre-main sequence.

8.2 Magnetic Processes and shortwave fluxes.

Solar shortwave (X-ray and UV) emissions are fundamentally linked to the Sun's evolving magnetic field. The causal relation was first discussed by Skumanich (1972), and is generally referred to as the age-activity-rotation effect. Increasing opacity at shorter wavelengths coupled with a variable atmospheric temperature profile conspire to

change the character of solar radiation from continuum absorption to that of emission between (and shortward) of wavelengths of 200 and 150 nm (Vernazza *et al*., 1981). UV emission lines arise predominantly from the region of the stellar atmosphere known as the chromosphere, where temperatures increase with height from a minimum of 4500 K near 300 km to around 2200 km (above a surface at 0 km defined as unity optical depth at 550 nm – the "photosphere"). An abrupt temperature rise occurs through the "transition region" to the corona, which is the region above 2500 km with kinetic temperatures near 1 million Kelvin that is responsible for most of the remaining solar shortwave emission. Physical processes in the chromosphere, transition region, and corona are dictated by the solar magnetic field, via complex pathways whose details are still under active debate (Aschwanden *et al*., 2007).

Regardless of the precise mechanism by which the magnetic field dissipates energy in the solar atmosphere, the global picture is relatively well established. The magnetic field, generated deep in the sun by a rotational dynamo (Parker, 1970), couples to the solar wind out to the solar Alfvén radius, approximately 20 Solar radii. This coupling of internal rotational energy to the outer reaches of the stellar atmosphere enables the stellar wind to shed angular momentum over the solar lifetime. The fundamental physics of rotation, which promotes strong magnetic activity and enhanced chromospheric fluxes in young stars, forces stars to spin slower as they age, decreasing their magnetic activity and subsequent shortwave emissivity (Pace and Pasquini, 2004).

The evolution of shortwave solar radiation has been the subject of a number of previous investigations, generally motivated by advances in UV and X-ray telescope technology (Skumanich, 1972; Zahnle and Walker, 1982; Ayres, 1997). The most comprehensive study is the `Sun in Time' program, which recently published multi-wavelength results from 20 years of telescopic observation of solar analogs - nearby G stars that are compositionally similar to the Sun but vary in age (Ribas *et al*., 2005), subsequently referred to as "R05." Observed fluxes from 6 solar analogs ranging from 100 Myr through 6.7 Gyr in age were normalized to a distance of 1AU from a star of 1 solar mass and radius, allowing direct inter-comparison. UV and X-ray fluxes were shown to

increase for younger Sun-like stars in each wavelength bin studied, with monotonically increasing relative fluxes at shorter wavelengths. Stellar fluxes within integrated wavelength bins were fit for stars of various ages via power laws (i.e. as Flux = $\alpha\tau^{\beta}$, with α and β constants and τ time in Gyr after formation.) Coefficients for wavelength bins between 0.1-2, 2-10, 10-36, 36-92, and 92-118 nm were presented in Table 5 of R05 and plotted as flux ratios versus time in Fig. 8 of R05, recreated here as our Fig. 8-1. It is acceptable to consider these integrated broadband regions in the far UV and X-ray, given that high energy lines transitions are effectively saturated, forming a sort of "shortwave continuum." This label is imperfect as the physical conditions do not reflect

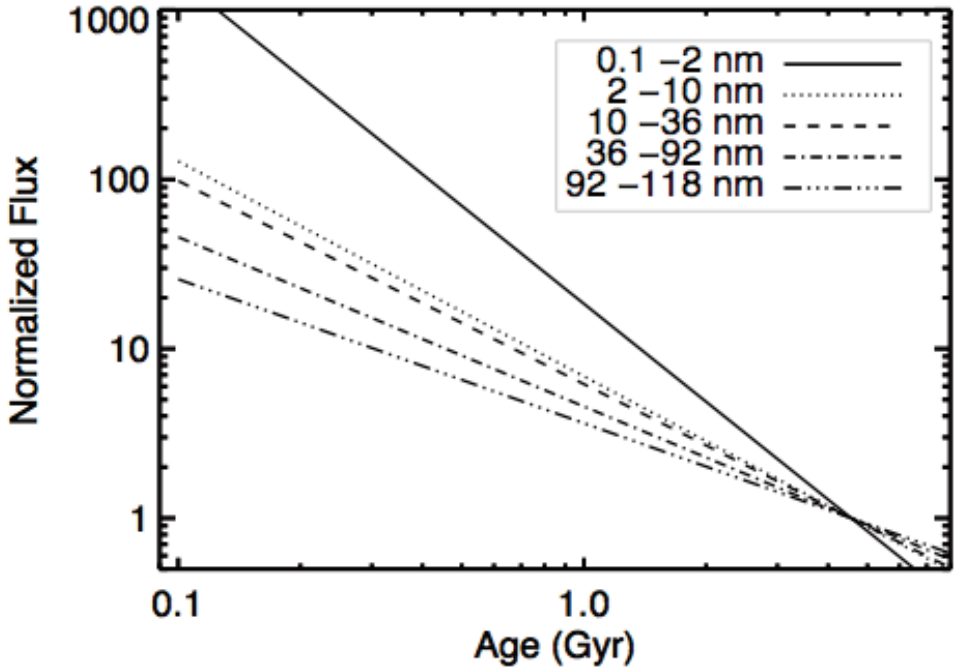

Figure 8-1 Reproduction of Fig. 8 of Ribas *et al.* (2005)

Plots of logarithmic normalized flux versus logarithmic stellar ages are presented as $F \propto (\tau/4.56\ \mathrm{Gyr})^{\beta}$, with the coefficients determined by fitting astronomical data. The normalized flux decreases monotonically with increasing wavelengths and with increasing age. This behavior is captured by a monotonic increase of β towards zero at increasing wavelengths.

local thermodynamic equilibrium, but merely reflects the underlying reality that multiple minor line transitions form a backdrop upon which the strongest lines appear in emission. R05 also provide fluxes of and power law fits to strong emission lines

between 28.4 and 165.7nm. Of these, the strong hydrogen Lyman alpha emission line (centered at 121.6 nm), which carries up to 50% of the entire modern solar UV flux shortward of 170 nm (Ribas *et al*., 2005; Krivova *et al*., 2006), is the most important for photochemical modeling of planetary atmospheres (e.g. Yung and DeMore, 1999).

Unfortunately for our purpose, R05 do not provide integrated fluxes longward of 120 nm, nor line fluxes longward of 170 nm, due to stated difficulties in accounting for the continuum. In absence of integrated data from 120-200 nm, the results of R05 are extrapolated in the following manner. As seen in Fig. 8-1, shorter wavelengths have corresponding higher relative fluxes at earlier times. This behavior corresponds to a monotonic increase in β, the power law exponent, towards zero with increasing wavelength. The physical basis for this lies in the age-activity-rotation behavior discussed above; As the magnetic heating of the outer atmopshere drops, the high energy coronal plasma cools faster than the relatively cool plasma responsible for longer wavelength radiation (Ayres, 1999). On Fig. 8-2, we plot values of β versus wavelength with R05's integrated wavelength bins shown as solid lines. The exponent measured from flux ratios of the Lyman alpha line (β= -0.72) is shown as an extra-large 'x' symbol. We performed a linear least-squares fit to the midpoints of the integrated broadband data together with the Lyman alpha point, with relative error specified as the width of the wavelength interval, ensuring that the fit falls though the very important Lyman alpha data point.

Within our broad error criteria, the linear fit of the power law exponent β to wavelength λ with the lowest χ^2 is given by:

$$\beta(\lambda) = -1.3 + 4.8 \times 10^{-3} \lambda \qquad (8.1)$$

where λ runs from 2 - 200 nm, which we take as a maximum wavelength limit for any contribution from the "shortwave continuum," given the changing character of solar radiation from emission to absorption. This fit is plotted as a dashed line on Fig. 8-2.

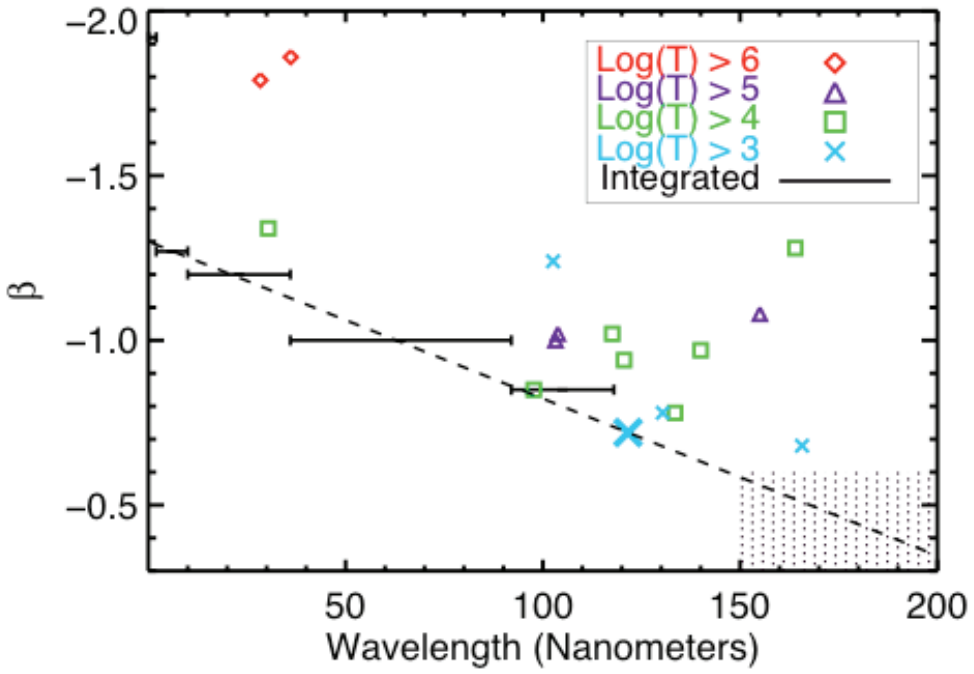

Figure 8-2 Power law exponents β versus wavelength

Values of β measured from individual lines are shown as symbols, labeled in the legend by the logarithm of the line formation temperature, T. Line formation temperatures are a proxy for height in the solar atmosphere, with Log(T) ≥ 5 implying line formation in the solar corona. Values of β measured from integrated wavelength bins (which include contributions of all line and continuum flux in the bin) are shown as solid black lines, with the width corresponding to the size of the wavelength bin. A fit of β against wavelength is shown as a dashed line. This fit, given by Eq. (8.1) was made to pass through the measured value of Lyman alpha line flux, the thick (blue) x symbol at [121.6 , -0.72]. The vertical hashes between 150 and 200 nm mark the region where we will further enhance the parameterization.

Equation (8.1) does not pass through R05's data for integrated fluxes from 0.1-2nm (β=-1.97), so extrapolations shortward of 2 nm using this fit will underestimate the hard X-ray flux. As in R05, fitting the power laws to integrated data will slightly underestimate the fluxes at a given line center, in exchange for energy conservation across the wavelength interval in question. This is justifiable in photochemical models which integrate photons in wavelength bins with resolution of nanometers, but can introduce errors in the unusual case where a species cross section changes drastically over a region of strong line flux, such as occurs with O_2 and the Lyman alpha line (Chabrillat and Kockarts, 1997). R05 estimate their errors in each β to be ± 0.1, and state that their approach is sufficient to

match observations within 20%. A similar error estimate is applicable to our Eq. (8.1), with perhaps larger uncertainties in the extrapolated near UV regime, but we take the estimates, as do R05, as sufficient for a first order approximation of solar flux evolution. Exponents that fit measured flux ratios for specific strong spectral lines are also shown on Fig. 8-2, labeled by the approximate temperature of the solar atmosphere at which the line was generated.

We apply the fit given by Eq. (8.1) in the region from 2 nm to 200 nm, and compute relative flux ratios as a function of time and wavelength via:

$$\text{Flux ratio}(\tau,\lambda) = \frac{\alpha\tau^{\beta(\lambda)}}{\alpha 4.56^{\beta(\lambda)}} = \left(\frac{\tau}{4.56}\right)^{\beta(\lambda)} \tag{8.2}$$

where the scaling parameters α are given in R05, but are not used here, due to the normalization to the modern Sun. It is important to note that this extrapolation is only one part of a competing set of physical process (including strong lines and photospheric models) that will be combined for our final set of flux multipliers between 150 and 200nm. The vertical dashed lines on Fig. 8-2 and subsequent figures indicate the regions we will enhance further before final combination in section 8.4.1. This parameterization for the “shortwave continuum” can be easily tested/modified when additional near-UV data become available from the Sun in Time project. Figure 8-3a is analogous to Fig. 8-1 and displays our extrapolated normalized UV flux ratios versus age for various wavelengths. Figure 8-3b displays a portion of our ultimate goal, the ultraviolet “continuum” flux ratios versus wavelength for various solar ages.

We would be remiss without discussing one final caveat regarding the applicability of this parameterization to the earliest Sun. Observations of young star clusters such as the Pleiades (~100 Myr (Meynet *et al*., 1993)) reveal that approximately 20% of young stars don’t follow the standard age-activity curves, and instead are rotating extremely quickly (Soderblom *et al*., 1993a). The presence of these “ultra-fast rotators” diminishes as star

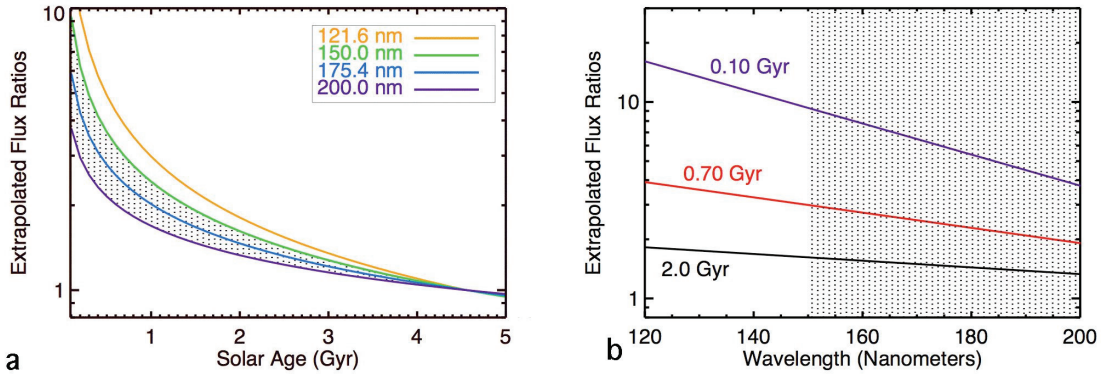

Figure 8-3 Flux ratios versus age and wavelength

Logarithmic normalized flux ratios versus solar age, labeled by wavelength. This figure is analogous to Fig. 8-1 except that it it log-linear, and also uses the extrapolated $\beta(\lambda)$ relation of Eq. (8.1) to calculate flux ratios at longer wavelengths. b) UV flux ratios versus wavelength at various paleodates. The vertical hashes between 150 and 200nm mark the region where we will further enhance the parameterization.

clusters age, and are absent (Soderblom *et al.*, 1993b) in clusters the age of the Hyades (~625 Myr (Perryman *et al.*, 1998).) Given that G-type stars are born with a wide range of rotational velocities which appear to be funneled down to a rotational period of approximately 10 days by 600 Myr, it is not feasible to predict the exact rotational history of the Sun prior to 600 Myr. The Sun in Time solar analogs have been chosen as representative of the likely rotational evolution for the young Sun, but users of this parameterization for the earliest Sun must be aware of the cautions described above.

8.3 Photospheric Processes and the Faint Young Sun

We now explore solar photospheric radiation which has an opposite behavior to the shortwave processes modeled above. The photospheric continuum flux arises from the surface layers and lower solar atmosphere where the atoms and radiation are in thermodynamic equilibrium. As hydrogen is fused to form helium in the solar core, the mean molar mass increases, leading to core contraction and increased central temperatures, which increases the rate at which hydrogen is converted to helium. This positive feedback on mass/energy conversion is expressed at the solar surface as an

increasing total energy flux over the Sun's hydrogen-burning lifetime. This has been modeled in an integrated sense as:

$$\frac{L(\tau)}{L_{\odot}} = \frac{1}{1+0.4(1-\tau/\tau_0)} \tag{8.3}$$

where τ_0 and $L_{\odot}$ are the modern age and luminosity of the Sun, and $L(\tau)$ describes the time evolution of bolometric luminosity (Gough, 1981), an equation we update in section 8.5. Equation (8.3) implies that the bolometric luminosity of the Sun has increased by approximately 30% from the time when the Sun first reached hydrostatic equilibrium on the main sequence (i.e. zero age main sequence (ZAMS)), to the present. This increasing luminosity leads to the "faint young sun" problem of atmospheric evolution on the terrestrial planets (Sagan and Mullen, 1972; Kasting and Catling, 2003).

In order to specify the wavelength dependence of solar continuum flux changes, we first turn to the detailed solar evolution models of Bahcall *et al*. (2001). Figure 8-4 displays their photospheric effective temperatures, T_{eff}, (using 5777 K for the present day (Cox, 2000)) versus stellar age along with our fit (R^2=0.9936) valid for $0<\tau<8$ Gyr where "τ=0" is the ZAMS.

$$T_{eff}(\tau) = 0.074\tau^5 - 1.679\tau^4 + 13.553\tau^3 - 49.543\tau^2 + 104.217\tau + 5619.105 \tag{8.4}$$

Next, we use the stellar atmospheric code ATLAS9 (Kurucz, 1979; Sbordone *et al*., 2004) with the updated opacities of Castelli and Kurucz (2003) to model solar continuum flux versus wavelength for various stellar age/photospheric temperature values using Eq. (8.4). We compute a grid of 37 Kurucz model atmospheres in 5K increments between 5610K and 5790K, fixing solar metallicity (Grevesse and Sauval, 1998), gravity (log g = 4.437), microturbulence velocity (2 km/s), and pure mixing-length convection without overshooting (L/H = 1.25, where L/H is the ratio of mixing length to scale height). Stellar

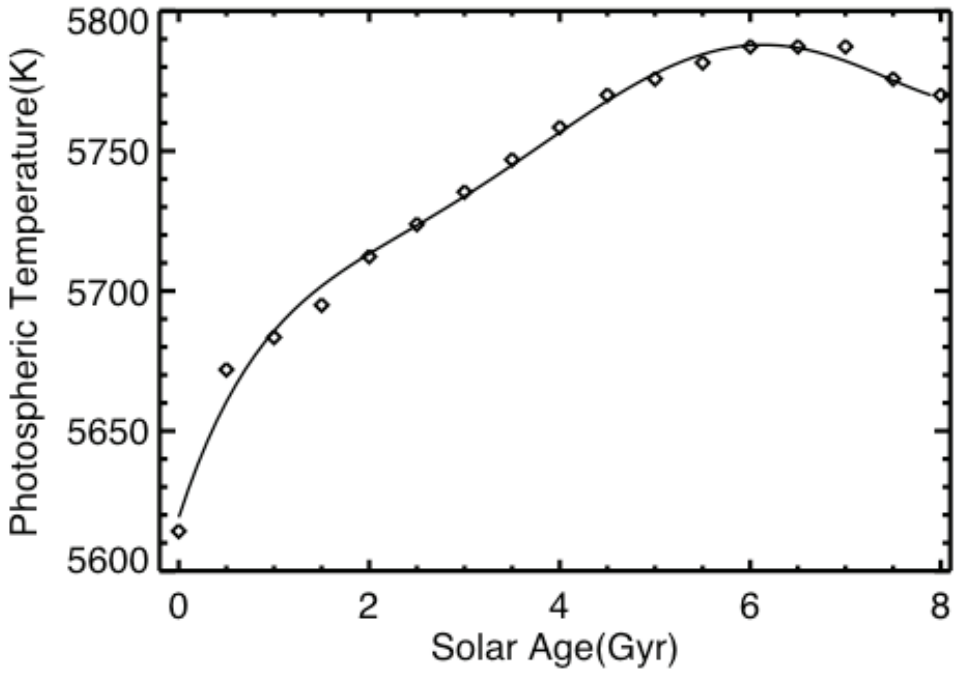

Figure 8-4 Photospheric temperature versus age

Photospheric temperature versus age from the standard solar model of Bahcall *et al*. (2001), whose model predictions are presented as diamonds. The solid line is a polynomial fit to the model results given by Eq. (8.4). The effective temperature decreases after 6 Gyr because the (square root of the) solar radius increases more quickly than the luminosity after this time, as discussed by Bahcall *et al*. (2001).

surface fluxes were extracted from the model atmospheres, and converted from frequency to wavelength units in the standard manner.

To compute the flux at Earth, we must account for changes in the solar radius. Standard solar models predict that the radius of the Sun has increased with time. We fit (R^2=0.9998) the results of Bahcall *et al*. (2001) by:

$$\frac{R(\tau)}{R_{\odot}} = 0.0003\tau^3 - 0.0009\tau^2 + 0.0255\tau + 0.8752 \qquad (8.5)$$

where $R(\tau)$ is the solar radius at time τ , $R_{\odot}$ is the present day solar radius, and τ is age in Gyr, ranging from 0 to 8Gyr. The flux at Earth, $F_{EARTH}(\tau)$, is therefore computed as:

$$F_{EARTH}(\tau) = F_{STAR}(\tau)\frac{4\pi R(\tau)^2}{4\pi(1\,AU + R_{\odot} - R(\tau))^2} \cong F_{STAR}(\tau)\left(\frac{R(\tau)}{1\,AU}\right)^2 \qquad (8.6)$$

where $F_{STAR}(\tau)$ is the stellar surface flux from the Kurucz model and 1 AU is the average distance from the Earth to the Sun, assumed constant over the age of the solar system.

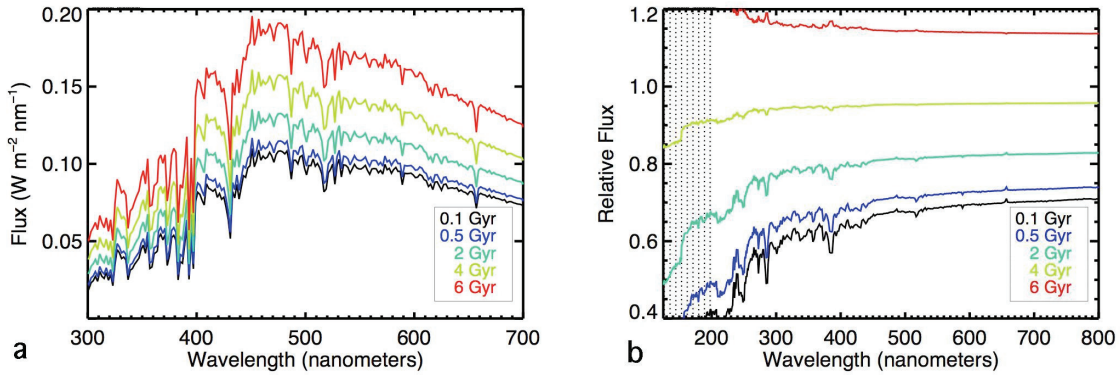

Figure 8-5 Photospheric and relative fluxes

a) Plots of the Kurucz model fluxes at 1AU for the photospheric temperature/age relations described by Eq. (8.4) and shown in Fig. 8-4. b) Kurucz model flux ratios at 1 AU versus age and wavelength in the visible and near IR. The vertical hashes between 150 and 200nm mark the region where we will further enhance the parameterization.

Figure 8-5a shows our predictions of solar photospheric flux at Earth for various paleodates. We see the expected classical behavior that the peak wavelength moves to shorter wavelength at higher temperatures (Wien's law), and that the flux at every wavelength is higher for higher temperature photospheres. We can also see how the luminosity (which is proportional to the integrated flux) increases, and that this increase is driven by enhanced visible radiation near the peak of the curve. We arrive at Fig. 8-5b, the relative flux multipliers for the visible and infrared, by dividing the flux curves at a given age by the present day flux. A common zeroth-order correction for the faint young sun is to multiply the current solar flux (for the example of 0.7 Gyr) by 75% to account for the decrease in bolometric luminosity predicted by Eq. (8.3). Figure 8-5b represents a

first-order improvement on this correction by factors ranging up to 2 in the near UV. Although only displayed on Fig. 8-5 through the visible/near UV, the Kurucz wavelength grid extends through the far infrared to 160000 nm, so this portion of the parameterization is valid in the IR to the extent that the Kurucz models capture the relevant physics.

8.4 The evolution of solar flux

8.4.1 Combining the parameterizations

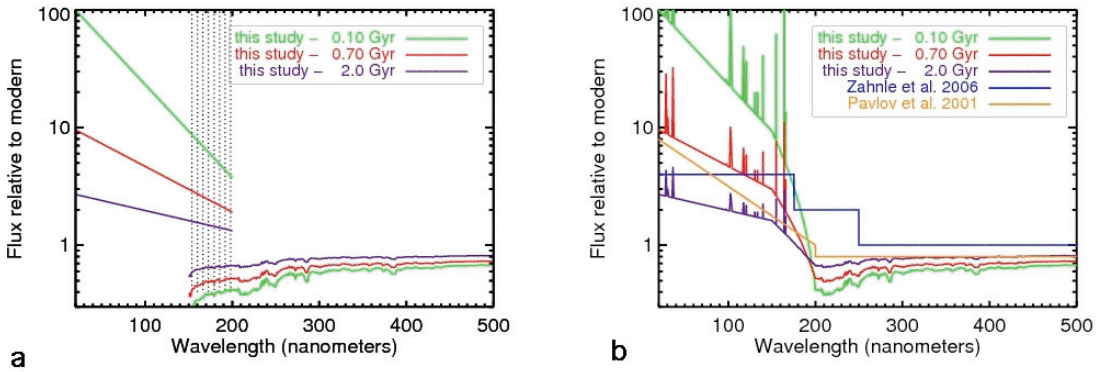

Figure 8-6 Flux ratios at 1AU by wavelength for the 0.1, 0.7, and 2.0 Gyr Sun

a) Flux ratios at 1AU by wavelength for the 0.1, 0.7, and 2.0 Gyr Sun – for X-ray/UV and photospheric processes separately. The vertical hashes between 150 and 200nm mark the region where we will further enhance the parameterization. b) Flux ratios at 1 AU from 6a) combined via a linear weighting of the two parameterizations between 150 nm and 200 nm. Strong line flux ratios from R05 (shown in Fig. 8-2) are added in 0.2nm bins. Our parameterizations are nominally valid from 2-16000 nm and for main sequence evolution from 0.6 Gyr to 6.7 Gyr, with extensions from 0.1 Gyr – 8 Gyr subject to additional caveats discussed in the text. Previous parameterizations from Pavlov *et al*. (2001) and Zahnle *et al*. (2006) (aka. Chapter 4) are shown for comparison.

We now explain how we combine the three parameterizations of UV/X-ray “continuum”, strong line emission, and photospheric fluxes. The R05 integrated results formally extend to 120 nm, which we extrapolated to 200 nm in Fig. 8-2 and Eq. (8.1). R05 mention that the reason for the cut-off of their strong-line data at 170 nm was difficulty in accounting for the continuum contribution. This is fully consistent with detailed physical models that show the last major chromospheric absorbtion edge at 168.1 nm (Vernazza

et al., 1981). Figure 8-6 combines Figs. 8-3b and 8-5b, and shows our relative flux multipliers, first as separate shortwave and photospheric components (Fig. 8-6a), and then combined together (Fig. 8-6b) by a linear weighting of the two components between 150 nm and 200 nm. Also included in the combined parameterization are the strong line fluxes from Fig. 8-2, added in 0.2 nm bins. Figure 8-6b is a graphical representation of our goal, a parametric representation of relative flux multipliers for a given wavelength at a given paleodate, along with previous efforts shown for comparison.

8.4.2 The modern solar flux

A parameterization of relative flux multipliers allows freedom of choice for the specification of the modern-day flux. For the general purposes considered here, we choose to use the Solar Irradiance Reference Spectra normalized to the multi-wavelength ATLAS 1 observations, which were obtained near the peak of a sunspot cycle and hence represents an average behavior of the active Sun (Thuillier *et al*., 2003; Thuillier *et al*., 2004). We chose a solar maximum spectrum for our reference as many lines which provide significant paleoflux are negligible at solar minimum (Ribas *et al*., 2005). Utilizing the R05 fits ensure that we capture total integrated flux in our shortest wavelengths bins, even if specific lines pertinent to the early Sun are not present in the modern spectrum.

Thuillier *et al*. (2004) present solar spectra from 0.5-2400 nm in units of mW m^{-2} nm^{-1} (i.e. spectral irradiance). For photochemical modeling, it is common to use units of photons cm^{-2} s^{-1} nm^{-1} (i.e. actinic flux). The conversion from the energy units of irradiance to the quantized units of actinic flux is made via:

$$\text{Actinic Flux} = \frac{10^{-7} \times \text{Irradiance}}{E_\lambda} = 5.039 \times 10^{8}\ \text{Irradiance} \times \lambda \qquad (8.7)$$

where the 10^{-7} converts mW m^{-2} to W cm^{-2}, E_λ is the energy per photon in Joules (E_l = $1.98468 \times 10^{-16} / \lambda$) and λ is wavelength measured in nanometers.

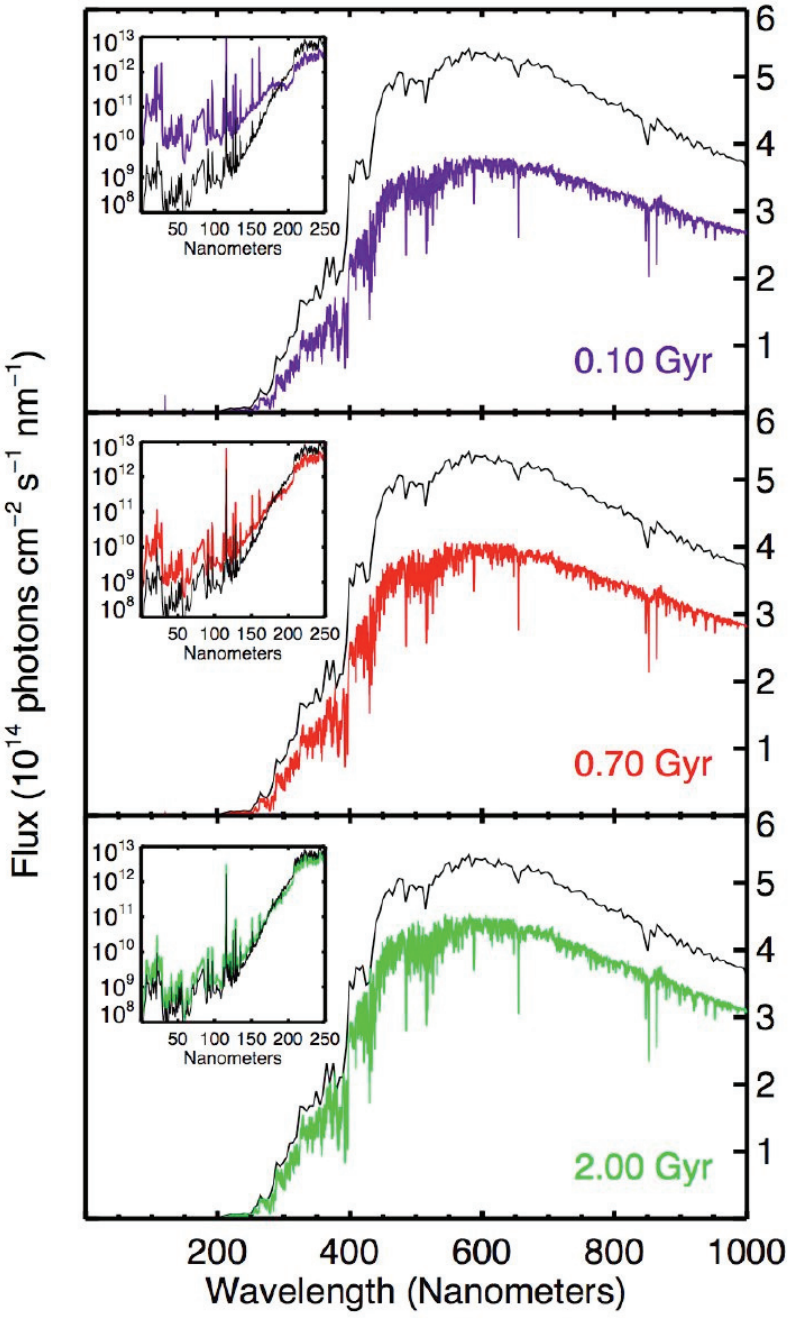

Figure 8-7 Predicted flux at Earth versus wavelength for the 0.1, 0.7, and 2.0 Gyr Sun

Each panel displays a high-resolution thick-lined trace of flux for the given paleodate, along with a thin-lined modern flux trace binned at 2 nm resolution for comparison. In each panel, the visible portion of the flux is displayed linearly in units of 10^{13} photons cm^{-2} s^{-1} nm^{-1}, and is mapped to the right side axes. The inset of each subplot shows the UV region of the spectrum, displaying logarithmic flux (from 10^{7}-10^{12} photons cm^{-2} s^{-1} nm^{-1}) versus wavelength from 10-250 nm.

8.4.3 The Evolution of Solar Flux

Figure 8-7 shows our relative flux multipliers applied to a representative modern-day solar flux in energy units, and subsequently converted to quantized units. The solar actinic flux at 0.1, 0.7, and 2.0 Gyr are shown as they compare to the modern day (4.56 Gyr) flux, with insets showing the emission-line behavior in the UV.

8.5 Verification

In order to validate the parameterization, we compared its predictions to astronomical measurements from two young solar analogs, κ^1 Cet and EK Dra.

8.5.1 κ^1 Cet

κ^1 Cet is young solar analog from the Sun in Time dataset, but its precise age is unknown. While R05 estimate κ^1 Cet at 0.6 Gyr, Lachaume *et al*. (1999) estimate its age at 0.3 Gyr using an equally robust methodology. In order to test our predictions for the young Sun, we compile multiple wavelength spectral data for Kappa Cet from the Extereme Ultraviolet Explorer (via MAST Archive - http://archive.stsci.edu/), FUSE (Scott Engle, personal communication) , and the Hubble Space Telescope Imaging Spectrograph (via CoolCAT - http://casa.colorado.edu/~ayres/CoolCAT). The FUSE data are uncorrected for solar contamination and hence contain added geocoronal emission in the Lyman series (92-97.3 nm) and O IV lines (103.2-103.7 nm) (Ed Guinan, personal communication.) These data are compiled on Fig 8-8a, along with our predictions for the Sun at 0.3 Gyr, which overlies the Kappa Cet data very well. The largest deviation of our predictions from the data is a factor of ~2 between 195 and 210 nm. While Kappa Cet is a solar analog, it is not necessarily a solar twin. The effective temperature of Kappa Cet is 5750 K while the Bahcall *et al*. (2001) prediction (Eq. (8.4)) for the Sun at 0.3 Gyr is 5646 K. This temperature differential can explain the discrepancy in the near UV. For comparative purposes, Fig 8-8a also shows a recently modeled low-resolution spectrum

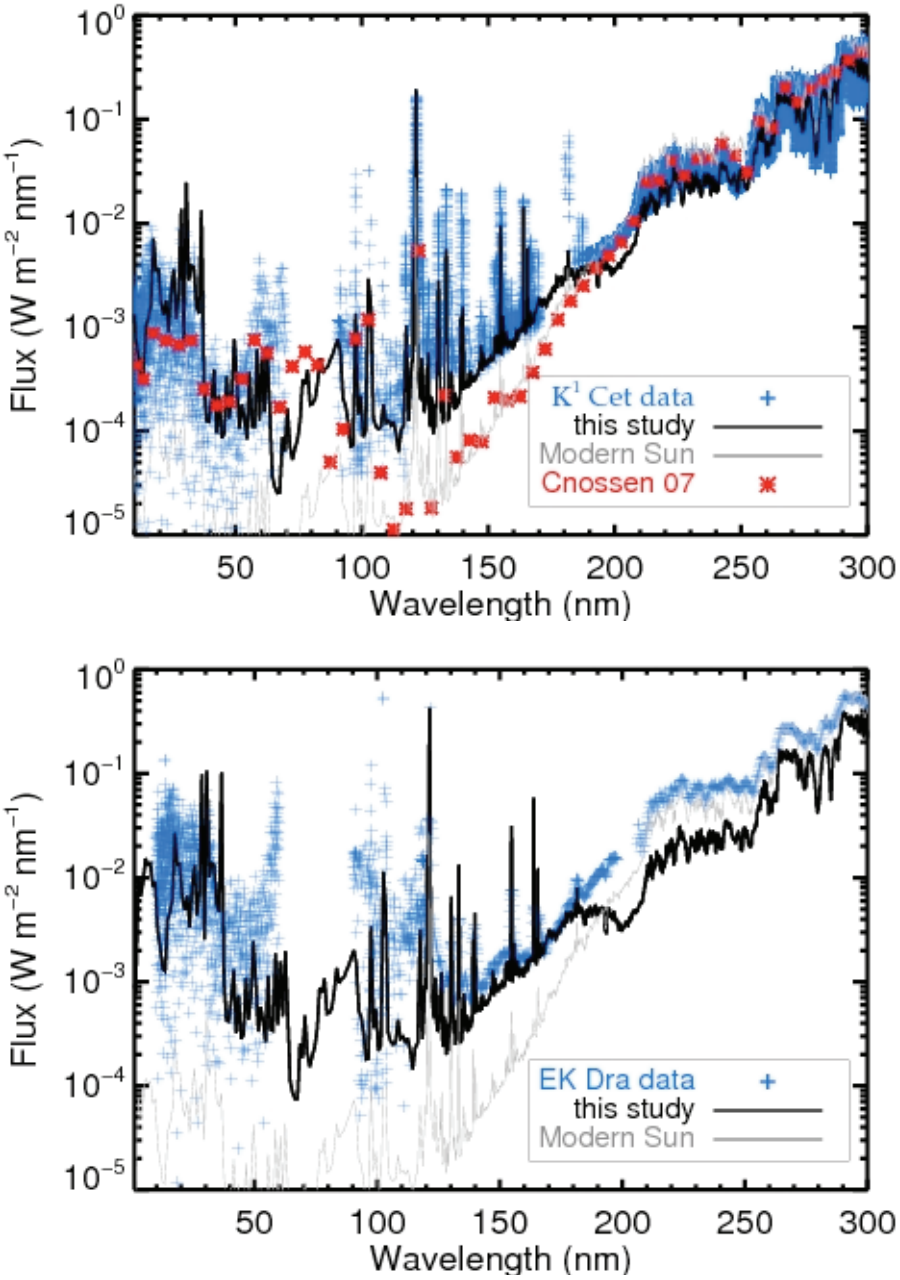

Figure 8-8 Comparison with κ1 Cet and EK Dra

a) Comparison of model predictions to available data for κ1 Cet. Data (+ symbols) are from EUVE (10-70 nm), FUSE (90-119 nm), and HST-STIS (120-300 nm). The high resolution spectral flux (at top of Earth's atmosphere) for the Sun at 0.3 Gyr from this study is shown as a thick solid line, with the modern solar flux shown for comparison as a thin solid line. The Cnossen *et al*. 2007 modeled flux at 1AU from κ1 Cet is shown as * symbols (Cnossen *et al*., 2007). b) EK Dra data are shown as + symbols, and are taken from EUVE (10-70 nm), FUSE (90 119 nm), and Segura *et al*. (2007) (115 - 300 nm). The Sun at 0.1 Gyr as predicted by this study is shown as a thick solid line, with the modern Sun shown for comparison as a thin solid line.

for κ^1 Cet by Cnossen *et al*. (2007). This spectrum, created via spectral synthesis of emission measure estimations, matches the data well in the near UV and X-ray, but is consistently lower than the data throughout most of the far UV and Lyman continuum, a region which is difficult to model given lack of observational constraints. Also overplotted on Fig 8-8a is the modern solar spectrum, which appears to fit the Cnossen *et al*. (2007) model well in this region, although this is likely coincidental. Overall, our predictions are surprisingly accurate given the simplicity of the methodology.

EK Dra

Our parameterization has increased uncertainty for stars younger than 0.6 Gyr given the previously discussed rotational funneling effect which effectively homogenizes the spin down rate of G stars. EK Dra is a member of the Pleiades moving group and hence ~100 Myr old (Meynet *et al*., 1993). Like Kappa Cet, it was a member of the Sun in Time program, so we would expect our parameterization to fit it fairly well, at least at the strong lines. Figure 8-8b shows available data for EK Dra from EUVE, FUSE, and the UV spectrum of Segura *et al*. (2007), which was taken from existing IUE data and models of observational data in the visible. No empirical measurement exists for this star's Lyman alpha flux and the existing low-resolution IUE data are compromised by geocoronal emission. We have followed Segura *et al*. (2007) in adopting the R05 estimate for the EK Dra Lyman alpha flux. Unavailable strong-line data (also noticeable in Fig 8-8a.) becomes more evident in the EK Dra comparison, and motivates additional temporal studies of lines such as He I (58.4, 108.5 nm), Mg X (61, 62.5 nm), the He II series (92.7 – 97.2 nm), S VI (93.3, 94.4 nm), and NIII (99.1 nm). The effective temperature of EK Dra is 5765 K (Segura *et al*. 2007), which is directly comparable to the modern Sun. Similar to Kappa Cet, EK Dra is a solar analog but not a solar twin, with noticeable differences appearing again between the near UV spectral characteristics of EK Dra and our predictions for the young Sun. Near UV observations of young G stars with cooler effective temperatures would help illuminate this problem (Dorren and Guinan, 1994).

8.5.2 The Faint Young Sun

As a check on the photospheric portion of our parameterization, we test against known results for the time evolution of solar luminosity. First, we numerically integrate our predicted fluxes over wavelength, obtaining estimates of the bolometric flux (here, we use energy rather than quantized flux units) at a variety of solar ages. We then normalize each estimate by our predicted modern bolometric flux (1331 W cm^{-2} when integrated from 2-2400 nm, consistent with previous estimates (Thuillier *et al*., 2003)) to obtain the relative bolometric flux at each solar age. The dashed line on Fig. 8-9 shows that our computed luminosity evolution matches the classic parameterization of Eq. (8.3) quite well, except during the first 0.5 Gyr. As a check on both our results and the fit of Gough (1981), we examine an independent luminosity evolution curve from the Padova stellar astrophysics group (Girardi *et al*., 2000). We fit the normalized luminosity from their version of the "standard solar model" over the interval from $0 < t < 8$ Gyr (R^2=0.9996) as:

$$\frac{L(\tau)}{L_{\odot}} = -5.773\times10^{-5}\tau^4 + 1.591\times10^{-3}\tau^3 - 6.953\times10^{-3}\tau^2 + 6.988\times10^{-2}\tau + 0.6957 \quad (8.8)$$

which is plotted as a solid line on Fig. 8-9. The normalized luminosity evolution of Girardi *et al*. (2000) is very similar to that of Bahcall *et al*. (2001) despite the fact that these models predict different effective temperature and solar radius evolution. Eq. (8.8) deviates from Eq. (8.3) by more than 1% prior to 0.5Gyr and after 6Gyr, and therefore represents an updated parameterization for solar luminosity evolution with increased precision during the extremes of solar hydrogen-burning evolution.

We performed additional tests of integrated flux in various wavelength regions. Using energy units for the flux, we find that the integrated contribution from wavelengths less than 400 nm to the total flux was approximately constant at ~ 8% throughout stellar evolution, while the integrated contribution from wavelengths shorter than 200 nm

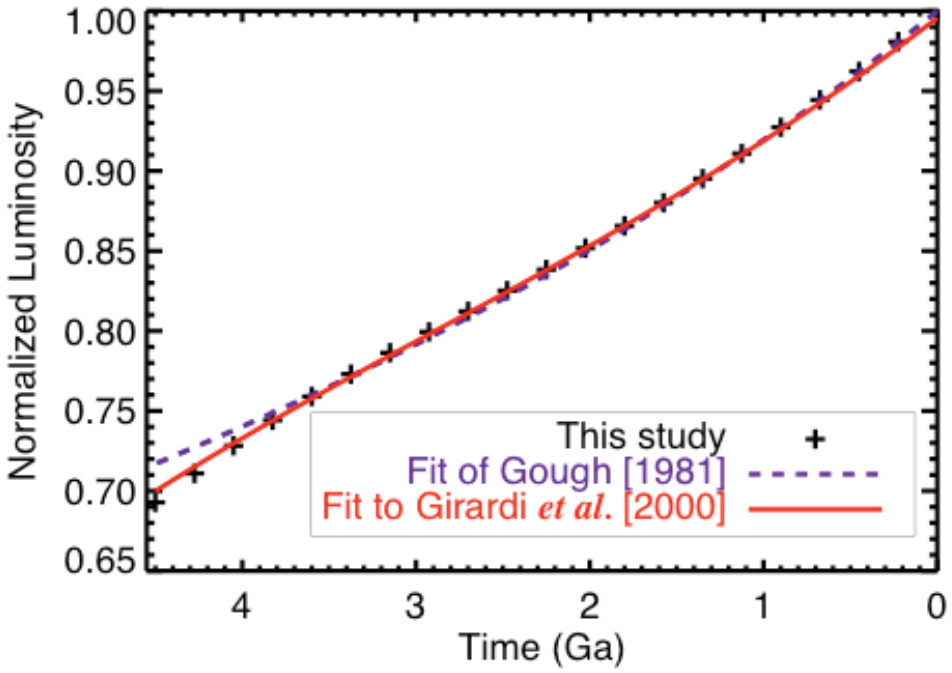

Figure 8-9 Normalized Luminosity versus time

Normalized luminosity versus time computed from our parameterization is shown as plus symbols (+). Equation (8.3), the prediction of Gough *et al*. (1981), is shown as a dashed (purple) line. Equation (8.8), a fit to the standard solar model `ms100z019.dat' of Girardi *et al*. (2000) is shown as a solid (red) line.

decreases by a factor of 10 (0.1% to 0.01%) from the ZAMS to the present, consistent with declining chromospheric activity. The fractional contribution of the Lyman alpha line to the entire flux shortward of 170nm increases from ~20% for the early sun to approximately 36.5% in the ATLAS 1 normalized spectrum of Thuillier *et al*. (2004). When using quantized units (i.e actinic flux) we find that the relative fraction of H Lyman Alpha photons with respect to all photons less than 170 nm remains approximately 40% from the ZAMS to the present. These fractions are consistent with previous estimates in R05, but are not entirely independent.

8.6 Discussion

We have constructed a numerical parameterization for modifications to solar flux as a function of solar age and wavelength. Specifically, we have considered enhancements

in UV and X ray flux due to enhanced magnetic activity and decreases in visible and infrared flux due to lower energy generation rates. The relative flux at other solar system planets can be easily estimated by including an additional wavelength-independent flux multiplier relative to Earth's distance from the Sun (i.e. Flux $\propto 1/a_p^2$ where a_p is the average planetary semimajor axis in astronomical units.) Although not discussed explicitly here, the methodology of relative flux multipliers could also be extended to account for other physical processes. Examples include seasonal changes in Sun-planet distance (Spencer, 1971), or evolution of solar activity over a sunspot cycle (Lean *et al*., 2001).

The fluxes displayed in Fig. 8-7 were chosen as representative of the "average" sun. The method presented above is applicable to any absolute measurement of top-of-atmosphere flux, and so could be applied to measured fluxes at varying solar conditions and/or flare events, as a means of estimating flux variations of these events at various paleodates. In addition, the parameterizations provided are valid for studies of the future evolution of the Sun, at least to approximately 6.7 Gyr. Extensions of these parameterizations to encompass the full main sequence evolution of the Sun should be feasible with suitable changes made to Eqs. (8.4) and (8.5). Indeed, if the flux ratios calculated by R05 can be extrapolated in time an extra Gyr, the presented parameterization is nominally valid until 8Gyr.

Extensions of these results to pre-main sequence evolution would be desirable, as this would describe the radiation environment of planetary formation and early evolution. Young stars are extremely active, and are embedded in disks for ~3-10 Myrs. (e.g. Silverstone *et al*., 2006). The very dust and gas from which planets form obscures detailed flux observations at the quality of the R05 data set. Even if young stellar surface fluxes could be estimated, the dust and gas in the disk would require radiative transfer calculations if there is significant opacity between the star and planets. In our calculations, we have implicitly assumed constant optical path between the Sun and the Earth, which we assume remains fixed at 1AU during main sequence evolution. Nevertheless, with additional care, the parameterizations in this chapter could potentially be extended to include pre-main sequence evolution of the Sun.

These parameterizations provide a reasonable first-order approximation to the solar flux at various paleodates, but they are far from perfect. Nonetheless, approximate corrections for the faint sun and magnetic activity are a necessary improvement bearing in mind the crude schemes implemented by published models of evolving planetary atmospheres. The quantitative flux predictions should be integrated over nanometer-sized bins rather than being considered detailed predictions of flux at the angstrom scale. Future enhancements include the addition of additional strong lines in the far UV (e.g. He I, He II, N III), strong lines in the near UV (e.g. Mg II, Fe II, Ca II), better understanding of the Lyman continuum, and better treatment of the region between 150 and 200 nm, where we have both extrapolated data and linearly combined parameterizations. This final region is of particular interest to photochemical modelers of Earth's early atmosphere, as light of this wavelength reached the lower atmosphere in absence of substantial atmospheric ozone on the early Earth (Kasting and Donahue, 1980; Cnossen *et al*., 2007). In particular, mass-independent fractionation in sulfur isotopes has been attributed to changes in photon optical depth in this wavelength region (Farquhar *et al*., 2000; Farquhar *et al*., 2007; Lyons, 2007; Domagal-Goldman *et al*., 2008) and so there are observable geochemical consequences. Observations of young (cooler) G stars, coupled with NLTE modeling of line-blanketing in stars with varying effective temperatures and metallicities would illuminate this problem.

8.7 Conclusions

We have described how to compute wavelength-dependent scaling factors for solar flux anywhere in the solar system from 0.6 Gyr to 6.7 Gyr. With additional care, the parameterization is valid from 0 to 8 Gyr. These first-order parameterizations are valid from 2 nm through the infrared. Interactive Data Language (IDL) and FORTRAN codes that calculate relative flux modifiers, as well as estimated solar spectra are available upon request to the first author.

Chapter 9 Conclusions

Earth's oxygen rich atmosphere was not always here. Evidence of ancient atmospheric sulfur reactions, stored cryptically in the minor isotopes of sulfur, reveal that conditions on Earth prior to 2.4 billion years ago were significantly different than the present. Molecular oxygen, the gas that makes up 21% of our current atmosphere and dominates reactions in the atmosphere, ocean, and biosphere was simply not present in significant quantities. The burden of proof for this concept, which had been debated for many years, was only obtained in the early 2000s with the identification of MIF-S and its subsequent constraints on atmospheric O_2 levels. The geologic record has provided us with a strange puzzle lacking easy explanation - an abrupt rise in oxygen concentrations from trace levels to a few percent of present levels in a geologic instant.

This dissertation provides a quantitative examination of this rise of atmospheric oxygen approximately 2.4 Ga, and represents an advance given that most previous discussions of the topic were qualitative. We describe three distinct numerical models constrained by data from the geologic record whenever possible. In this section, we summarize the various results from these models, and recount how these results have forced us to reconsider late Archean events as being better described by declining methane levels rather than rising oxygen levels.

In Chapter 8, we describe a parameterization of the evolution of the wavelength dependence of the solar flux. Solar photons drive the disequilibrium in planetary atmospheres and time-dependent change in solar energy is vital in understanding the chemical and climatic evolution of terrestrial planets. The solar flux at Earth contains two primary evolving components. The first are the UV photons which drive photochemical reactions, a phenomenon which decreases as the Sun ages. The second component are the visible photons which are vital for planetary climate, and increase in quantity as the Sun evolves. During the late Archean, UV fluxes were a few times higher than present, but the more important effect was the decreased visible light – the well

known “Faint Young Sun” problem of atmospheric evolution (e.g. Sagan and Mullen, 1972). The pertinent results of this is that additional greenhouse gases were needed to keep the late Archean Earth warm.

In examining the nature and timing of Earth’s oxic transition, we have arrived at the following overall conclusions. There are two stable steady states for the atmosphere after the evolution of oxygenic photosynthesis. One of these states is a weakly reducing atmosphere with climatically significant CH_4 which helps resolve the Faint Young Sun problem. This atmosphere has trace amounts of O_2 at the ground due to the strong biological flux, but the O_2 is rapidly consumed by photochemical reactions, depleting in relative abundance by multiple orders of magnitude in the first few kilometers of altitude. This results in extremely low oxygen concentrations in the middle troposphere, which has enough reducing power to stimulate gas phase polymerization of sulfur. In these low oxygen atmospheres, sulfur can fall out of the atmosphere as elemental sulfur particles, the primary vector by which mass independent fractionation of sulfur isotopes (MIF-S) are stored in the geologic record. In contrast, the second stable atmospheric solution is similar to the modern environment. This solution has significant and well-mixed quantities of both O_2 and CH_4, with O_2 being the dominant gas. No elemental sulfur is polymerized in this atmosphere, so MIF-S preservation in the geologic record is inhibited.

Both of these two stable atmospheres are supported by fluxes that are reasonable to expect from ancient and modern planetary outgassing and biospheres. A surprising discovery developed in Chapters 3 through 7 is that flux changes of only a few percent separate these two stable states. In response to large fluxes of CH_4 and O_2 into the atmosphere, atmospheric chemistry will proceed until one or the other of the species is the victor, with the redox state of the atmosphere being defined by the gas that remains after the bulk of the destruction occurs. When the net flux of reductants to oxidants is greater than 0.5, the atmosphere exists in the state where CH_4 is dominant and O_2 is a trace constituient.

Given the existence of two separate atmospheric states, we set out to explore how an atmosphere could evolve from the reducing state to the oxic state using a biogeochemical box model (Chapter 3). This is most easily explained by decreasing the net flux of reductants relative to the oxidants into the atmosphere over geologic timescales. In Chapter 3, we argued that hydrogen escape can drive the irreversible oxidation of the continental crust, leading to a decreasing flux of reductants over geologic time, showing that this scenario is quantitatively self-consistent with available data from Earth's crustal materials. On geologic timescales, we believe the solid planet evolved in a manner such that reducing gases were able to overwhelm biological fluxes of oxygen until approximately 2.4 billion years ago. On a different planet with more or less reduced materials in the mantle or crust, or with more or less nutrients to stimulate biological activity, the oxic transition could occur much earlier or later in planetary history.

The primary response of the atmosphere to declining inputs of reductants is a slow decline in atmospheric methane concentrations, eventually leading to sharp collapse in methane levels. Given that methane was likely a strong component of the Archean greenhouse warming, and that this timescale for temperature change is much quicker than can be counteracted by negative-feedbacks within the carbonate-silicate cycle, the sharp decline in methane could have triggered the massive glaciations seen in the geologic record at this time. We also argue that a collapse in methane is the best explanation for why the MIF-S signal disappeared when it did. We showed in Chapter 4 that the MIF-S signal can only be preserved in the geologic record if there is sufficient reducing power to polymerize sulfur, an absence of ozone shielding the 190-220 nm window, and sufficient sulfur flux from volcanoes. We showed that all 3 of these must simultaneously occur, expanding the results of Pavlov and Kasting (2002) who focused solely on the ozone component.

Evidently, something happened ~2.4 billion years ago which began a decrease in the net amount of reductants fluxed in the atmosphere with respect to the oxidants. Narrowing our viewpoint from global planetary forces which affect the evolution of redox

fluxes over geologic timescales, we focus on the time period immediately before and after the transition. On short timescales, the atmosphere can respond strongly to biological fluxes, and we showed in Chapter 3 that the biospheric response to temperature swings from declining methane could have strong effect on atmospheric evolution.

Our motivation in Chapter 5 was examining the role of methanotrophs in the oxic transition, given evidence from mass-dependent sulfur isotopes indicating that oceanic sulfate concentrations began increasing approximately 2.7 billion years ago (e.g. Canfield, 2000). We hypothesized that increasing sulfate concentrations would stimulate the anaerobic oxidation of methane, which would help lower the flux of methane with respect to the oxygen flux from the biosphere. We showed that this would indeed affect the biosphere, but most significantly as a positive feedback on the oxic transition itself. We showed using a simple parameterization of biological activity that the primary effect of this metabolism would be to allow both oxygen and methane to rise to higher values immediately after the oxic transition.

The results in Chapter 6 were motivated by the results of Anbar *et al.* (2007) and Kaufman *et al*. (2007). The results shown contained simultaneous evidence for both MIF-S and oxidative weathering of sulfides in one geologic unit, which was presented as a paradox. We addressed this paradox via photochemical models demonstrating that oxygen concentrations at the ground could rise as high at 10^{-6} PAL while overall conditions remaining reducing enough in the lower troposphere to polymerize sulfur and hence preserve MIF-S. We showed that a typical track taken by our biogeochemical model during the collapse of methane naturally passes through a region of atmospheric phases space which can describe the data.

In Chapter 7, we present the first time-dependent photochemical description of the rise of oxygen. We show that the oxic transition likely occurred within a few thousand years, a timescale which is independent of the time over which the relevant fluxes decrease. This result gives credence to our hypothesis in Chapter 4 that atmospheric CH_4 must

drop below 50 ppm before the oxic transition could take place. In the time-dependent models, this cutoff density varies depending on the CH_4 flux, occurring at 30 ppm and 10 ppm in the two cases investigated. In the face of large fluxes of oxygen and methane, the atmosphere can stably maintain high concentrations of methane and trace amounts of oxygen, but once the methane is depleted, the system can rapidly switch to the other stable solution with high O_2. As the O_2 rises, O_3 formation begins to shield the troposphere from photons between 200 and 300 nm. This reduces the amount of OH formed from tropospheric H_2O photolysis, slowing the methane loss rate and allowing climatically significant quantities of methane to persist after the oxic transition.

While we haven't solved the problem of the great oxidation event completely, we have made significant progress as a result of thinking about the problem quantitatively. The scientific community has been asking "what caused the rise of oxygen" for many years without any obvious solution emerging. We conclude this dissertation by suggesting a new research question that might prove more tractable for future researchers than "what caused the rise of oxygen?", namely, "*What caused the great collapse of methane?*" We have shown that an transition from oxygen poor to oxygen rich conditions is a natural response to declining methane concentrations in the atmosphere. A collapse in methane levels can explain the glacial evidence for snowball Earth, the disappearance of MIF-S, as well as increasing lifetimes for oxygen which could stimulate limited oxidative weathering. In answer to our new question, we have shown that declining methane concentrations are a long-term consequence of hydrogen escape acting on the continents, and that a declining CH_4:O_2 flux ratio is also expected from changes in biological ecosystems. To the extent that these factors are general, the work of this dissertation helps constrain processes that may operate on Earth-like planets elsewhere that affect the redox evolution atmospheres and ultimately the development of complex life that depends on oxygen as we do ourselves.

BIBLIOGRAPHY

Aharon P and Fu BS (2000) Microbial sulfate reduction rates and sulfur and oxygen isotope fractionations at oil and gas seeps in deepwater Gulf of Mexico. Geochimica Et Cosmochimica Acta 64, 233-246.

Aharon P (2005) Redox stratification and anoxia of the early Precambrian oceans: Implications for carbon isotope excursions and oxidation events. Precambrian Research, 137, 207-222.

Ahrens TJ (1993) Impact Erosion Of Terrestrial Planetary-Atmospheres. Annual Review Of Earth And Planetary Sciences, 21, 525-555.

Aiuppa A *et al.* (2005) H_2S fluxes from Mt. Etna, Stromboli, and Vulcano (Italy) and implications for the sulfur budget at volcanoes. *Geochimica et Cosmochimica Acta* **69**(7): 1861-1871.

Allen M and Frederick JE (1982) Effective photo-dissociation cross-sections for molecular-oxygen and nitric-oxide in the schumann-runge bands. *Journal of the Atmospheric Sciences* **39**(9): 2066-2075.

Anbar AD *et al.* (1993) Photodissociation in the atmosphere of mars - impact of high-resolution, temperature-dependent CO_2 cross-section measurements. *Journal Of Geophysical Research-Planets* **98**(E6): 10925-10931.

Anbar AD, Knoll AH (2002) Proterozoic ocean chemistry and evolution: a bioinorganic bridge? *Science*, **297**, 1137-1142.

Anbar AD *et al.* (2007) A whiff of oxygen before the Great Oxidation Event? *Science* **317**(5846): 1903-1906.

Anders E, Grevesse N (1989) Abundances of the elements - Meteoritic and solar. *Geochimica et Cosmochimica Acta*, **53**, 197-214.

Andres RJ, Kasgnoc AD (1998) A time-averaged inventory of subaerial volcanic sulfur emissions. *Journal of Geophysical Research-Atmospheres* **103**, 25251–25261.

Armstrong, JC *et al.* (2002) Rummaging through Earth's attic for remains of ancient life. *Icarus* **160**(1): 183-196.

Arnold GL, Anbar AD, Barling J, Lyons TW (2004) Molybdenum isotope evidence for widespread anoxia in mid-Proterozoic oceans. *Science* **304**: 87-90.

Arthur MA, Dean WE, Neff ED, Hay BJ, King J, Jones G (1994) Varve-calibrated records of carbonate and organic carbon accumulation over the last 2000 years in the Black Sea. *Global Biogeochemical Cycles*, **8**, 195-217.

Arthur MA (2000) Volcanic contributions to the carbon and sulfur geochemical cycles and global change. In *Encyclopedia of Volcanoes* (ed. Sigurdsson H). Academic Press, pp. 1045–1056.

Aschwanden MJ, Winebarger A, Tsiklauri D, Peter H (2007) The coronal heating paradox. *Astrophysical Journal* **659**, 1673-1681.

Ashfold MNR *et al.* (1981) Singlet Methylene Kinetics - Direct Measurements Of Removal Rates Of A1A1 And B1B1 CH2 And CD2. *Chemical Physics* **55**(2): 245-257.

Atkinson R *et al.* (1989) Evaluated Kinetic And Photochemical Data For Atmospheric Chemistry - Supplement-III. *International Journal of Chemical Kinetics* **21**(2): 115-150.

Atkinson R *et al.* (2004) Evaluated kinetic and photochemical data for atmospheric chemistry: Volume I - gas phase reactions of O-x, HOx, NOx and SOx species. *Atmospheric Chemistry and Physics* **4**: 1461-1738.

Ayres TR (1997) Evolution of the solar ionizing flux. *Journal of Geophysical Research, [Planets]* **102**, 1641-1651.

Ayres TR (1999) Sleuthing the dynamo. II - Hubble Space Telescope Goddard High Resolution Spectrograph observations of solar-type dwarfs in young galactic clusters. *Astrophysical Journal* **525**, 240-246.

Bahcall JN, Pinsonneault MH, Basu S (2001) Solar models: Current epoch and time dependences, neutrinos, and helioseismological properties. *Astrophysical Journal* **555**, 990-1012.

Banks, PMKG (1973) *Aeronomy*. New York, Academic Press.

Barassin J and Combouri J (1974) Kinetic Study Of Reactions Between Atomic Oxygen And Chloromethanes .2. Reactions CH3CL+O, CHCL3 + O, CCL4 + O And CH4 + O - Experimental Results. *Bulletin De La Societe Chimique De France Partie I-Physicochimie Des Systemes Liquides Electrochimie Catalyse Genie Chimique*(1-2): 1-5.

Barley ME, Bekker A, Krapez B (2005) Late Archean to Early Paleoproterozoic global tectonics, environmental change and the rise of atmospheric oxygen. *Earth And Planetary Science Letters*, **238**, 156-171.

Barling J *et al.* (2001) Natural mass-dependent variations in the isotopic composition of molybdenum. *Earth and Planetary Science Letters.* **193**: 447-457.

Barnes RO and Goldberg ED (1976) Methane production and consumption in anoxic marine-sediments. *Geology* **4**, 297-300.

Basco N and Pearson AE (1967) Reactions Of Sulphur Atoms In Presence Of Carbon Disulphide Carbonyl Sulphide And Nitric Oxide. *Transactions of the Faraday Society* **63**(539P): 2684-&.

Bau, M, Hohndorf, A, Dulski P, Beukes NJ (1997) "Sources of rare-earth elements and iron in Paleoproterozoic iron-formations from the Transvaal Supergroup, South Africa: Evidence from neodymium isotopes." *Journal Of Geology* **105**: 121-129.

Baulch DL *et al.* (1992) Evaluated Kinetic Data For Combustion Modeling. *Journal of Physical and Chemical Reference Data* **21**(3): 411-734.

Baulch DL *et al.* (1994) Evaluated Kinetic Data For Combustion Modeling Supplement-I. *Journal of Physical and Chemical Reference Data* **23**(6): 847-1033.

Beaumont V and Robert F (1999) Nitrogen isotope ratios of kerogens in Precambrian cherts: a record of the evolution of atmosphere chemistry? *Precambrian Research* **96**, 63-82.

Bebout BM, *et al.* (2002) Long-term manipulations of intact microbial mat communities in a greenhouse collaboratory: Simulating Earth's present and past field environments. *Astrobiology*, **2**, 383-402.

Beichman, CA *et al.* (1999) *The Terrestrial Planet Finder (TPF): A NASA Origins Program to Search for Habitable Planets.* **JPL Publication 99-3**. Pasadena, CA.

Bekker A, Karhu JA, Eriksson KA, Kaufman AJ (2003) Chemostratigraphy of Paleoproterozoic carbonate successions of the Wyoming Craton: Tectonic forcing of biogeochemical change? *Precambrian Research* **120**: 279-325.

Bekker A, *et al.* (2004) Dating the rise of atmospheric oxygen. *Nature*, **427**, 117-120.

Bergquist, BA and Blum JD (2007) Mass-dependent and -independent fractionation of Hg isotopes by photoreduction in aquatic systems. *Science* **318**(5849): 417-420.

Berman-Frank I, Lundgren P, Falkowski P (2003) Nitrogen fixation and photosynthetic oxygen evolution in cyanobacteria. *Research In Microbiology*, **154**, 157-164.

Berner RA (1980) *Early Diagenesis: A Theoretical Approach*. Princeton University Press, Princeton, N.J.

Berner, RA (1982) Burial of organic-carbon and pyrite sulfur in the modern ocean - Its geochemical and environmental significance. *American Journal of Science* **282**: 451-473.

Berner, RA *et al.* (2000) Isotope fractionation and atmospheric oxygen: Implications for Phanerozoic O_2 evolution. *Science* **287**(5458): 1630-1633.

Berner RA and Kothavala Z (2001) GEOCARB III: A revised model of atmospheric CO2 over phanerozoic time. *American Journal Of Science*, **301**, 182-204.

Berner RA, Beerling DJ, Dudley R, Robinson JM, Wildman RA (2003) Phanerozoic atmospheric oxygen. *Annual Review Of Earth And Planetary Sciences*, **31**, 105-134.

Berner RA (2004) *The Phanerozoic Carbon Cycle*. Oxford University Press, New York, pp.150.

Betts JN, Holland HD (1991) The oxygen-content of ocean bottom waters, the burial efficiency of organic-carbon, and the regulation of atmospheric oxygen. *Global And Planetary Change*, **97**, 5-18.

Beukes NJ, Dorland H, Gutzmer J, Nedachi M, Ohmoto H (2002) Tropical laterites, life on land, and the history of atmospheric oxygen in the Paleoproterozoic. *Geology*, **30**, 491-494.

Bezos A and Humler E (2005) The Fe3+/Sigma Fe ratios of MORB glasses and their implications for mantle melting. *Geochimica Et Cosmochimica Acta*, **69**, 711-725.

Bjerrum, CJ and Canfield, DE (2002) Ocean productivity before about 1.9 Gyr ago limited by phosphorus adsorption onto iron oxides. *Nature* **417**: 159-162.

Bjerrum CJ and Canfield DE (2004) New insights into the burial history of organic carbon on the early Earth. *Geochemistry Geophysics Geosystems*, **5**, Art. No. Q08001 (online).

Blankenship RE and Hartman H (1998) The origin and evolution of oxygenic photosynthesis. *Trends Biochem. Sci.* **23**: 94-97.

Boetius A, *et al.* (2000) A marine microbial consortium apparently mediating anaerobic oxidation of methane. *Nature* **407**, 623-626.

Borowski WS, Paull CK, and Ussler W (1996) Marine pore-water sulfate profiles indicate in situ methane flux from underlying gas hydrate. *Geology* **24**, 655-658.

Borowski WS, Paull CK, and Ussler W (1999) Global and local variations of interstitial sulfate gradients in deep-water, continental margin sediments: Sensitivity to underlying methane and gas hydrates. *Marine Geology* **159**, 131-154.

Boss, AP (2002) Formation of gas and ice giant planets. *Earth and Planetary Science Letters* **202**(3-4): 513-523.

Brochier C and Philippe H (2002) Phylogeny - A non-hyperthermophilic ancestor for bacteria. *Nature* **417**(6886): 244-244.

Brocks JJ, Logan GA, Buick R, Summons RE (1999) Archean molecular fossils and the early rise of eukaryotes. *Science*, **285**, 1033-1036.

Brocks JJ, Buick R, Summons RE, Logan GA (2003) A reconstruction of Archean biological diversity based on molecular fossils from the 2.78 To 2.45 billion-year-dld Mount Bruce Supergroup, Hamersley Basin, Western Australia. *Geochimica et Cosmochimica Acta*, **67**, 4321-4335.

Brocks JJ, Love GD, Summons RE, Knoll AH, Logan GA, Bowden SA (2005) Biomarker evidence for green and purple sulphur bacteria in a stratified Palaeoproterozoic sea. *Nature*, **437**, 866-870.

Buick R, Dunlop JSR, Groves DS (1981) Stromatolite recognition in ancient rocks: An appraisal of irregularly laminated structures in an early Archean chert-barite unit from North Pole, Western Australia. *Alcheringa* **5**: 161-181.

Buick R (1992) The antiquity of oxygenic photosynthesis: Evidence from stromatolites in sulphate-deficient Archaean lakes. *Science* **255**: 74-77.

Buick R, Marais DJD, Knoll AH (1995) Stable isotopic compositions of carbonates from the Mesoproterozoic Bangemall Group, Northwestern Australia. *Chemical Geology* **123**: 153-171.

Burkholder, JB and McKeen S (1997) UV absorption cross sections for SO_3. *Geophysical Research Letters* **24**(24): 3201-3204.

Caldeira K, Kasting JF (1992a) The life span of the biosphere revisited. *Nature*, **360**, 721-723.

Caldeira K, Kasting JF (1992b) Susceptibility of the early Earth to irreversible glaciation caused by carbon dioxide clouds. *Nature*, **359**, 226-228.

Campbell, IM and Gray, CN (1973) Rate Constants For O(^{3}P) Recombination And Association With N(4S). *Chemical Physics Letters* **18**(4): 607-609.

Canfield DE (1991) Sulfate reduction in deep-sea sediments. *American Journal of Science* **291**, 177-188.

Canfield DE, Teske A (1996) Late-Proterozoic rise in atmospheric oxygen concentration inferred from phylogenetic and sulfur isotope studies. *Nature*, **382**, 127-132.

Canfield DE (1998) A new model for Proterozoic ocean chemistry. *Nature*, **396**, 450-453.

Canfield DE, Habicht KS, Thamdrup B (2000) The Archean sulfur cycle and the early history of atmospheric oxygen. *Science*, **288**, 658-661.

Canfield, DE (2004) The evolution of the Earth surface sulfur reservoir. *American Journal of Science* **304**(10): 839-861.

Canfield DE (2005) The early history of atmospheric oxygen: Homage to Robert A. Garrels. *Annual Review Of Earth And Planetary Sciences*, **33**, 1-36.

Canfield DE, Rosing MT, Bjerrum C, (2006) Early anaerobic metabolisms. *Philosophical Transactions of the Royal Society B-Biological Sciences*. 361**,** 1819-1834.

Canfield DE, Poulton SW, Narbonne GM (2007) Late-Neoproterozoic deep-ocean oxygenation and the rise of animal life. *Science* **315**, 92-95.

Canil D (1999) Vanadium partitioning between orthopyroxene, spinel and silicate melt and the redox states of mantle sources regions for primary magmas. *Geochimica et Cosmochimica Acta*, **63**, 557-572.

Canil, D (2002) Vanadium in peridotites, mantle redox and tectonic environments: Archean to present. *Earth and Planetary Science Letters* **195**: 75-90.

Castelli, F and Kurucz, RL (2003) New Grids of ATLAS9 Model Atmospheres*. Modeling of Stellar Atmospheres*, Vol. 210, Uppsala, Sweden.

Catling DC, Zahnle KJ, McKay CP (2001) Biogenic methane, hydrogen escape, and the irreversible oxidation of early Earth. *Science*, **293**, 839-843.

Catling DC, Claire MW, and Zahnle KJ (2004) Understanding the evolution of atmospheric redox state from the Archean to the Proterozoic. in *Field Forum on Processes on the Early Earth*, University of Witwatersrand, Kaapvaal Craton, S. Africa, pp. 17-19.

Catling DC, Claire MW (2005) How Earth's atmosphere evolved to an oxic state: A status report. *Earth And Planetary Science Letters*, **237**, 1-20. (Chapter 2)

Catling DC, Glein CR, Zahnle KJ, McKay CP (2005) Why O_2 is required by complex life on habitable planets and the concept of planetary "oxygenation time". *Astrobiology*, **5**, 415-438.

Catling DC (2006) Comment on "A Hydrogen-Rich Early Earth Atmosphere". *Science*, **311**, 38a-.

Catling DC, Claire MW, Zahnle KJ, (2007) Anaerobic methanotrophy and the rise of atmospheric oxygen. *Philosophical Transactions of the Royal Society A-Mathematical Physical And Engineering Sciences*. 365**,** 1867-1888. (Chapter 5)

Chabrillat S, Kockarts G, (1997) Simple parameterization of the absorption of the solar Lyman-alpha line. *Geophysical Research Letters*. 24, 2659-2662.

Chaloner WG (1989) Fossil charcoal as an indicator of paleoatmospheric oxygen level. *Journal of the Geological Society*, **146**, 171-174.

Chambers, JE (2004) Planetary accretion in the inner Solar System. *Earth and Planetary Science Letters* **223**(3-4): 241-252.

Chameides, WL and Walker, JCG (1981) Rates of fixation by lightning of carbon and nitrogen in possible primitive terrestrial atmospheres. *Origins of Life and Evolution of the Biosphere* **11**: 291-302.

Charlson RJ, Lovelock JE, Andreae MO, Warren SG (1987) Oceanic phytoplankton, atmospheric sulphur, cloud albedo and climate. *Nature* **326**, 655–661.

Chigira M and Oyama T (1999) Mechanism and effect of chemical weathering of sedimentary rocks. *Eng. Geol.* **55**: 3-14.

Christensen UR (1985) Thermal Evolution Models For The Earth. *Journal Of Geophysical Research-Solid Earth And Planets*, **90**, 2995-3007.

Chung K *et al.* (1975) Photochemistry Of SO_2 Excited Within Its First Allowed Band (3130 A) And Forbidden Band (3700-4000 A). *International Journal of Chemical Kinetics* **7**(2): 161-182.

Claire MW, Catling DC, Zahnle KJ (2006) Biogeochemical modeling of the rise in atmospheric oxygen. *Geobiology*, **4**, 239-269. (Chapter 3)

Claire, MW and Catling DC (2008) The evolution of solar flux from 2 nm to 160 microns: quantitative estimates for planetary studies. *in review*. (Chapter 8)

Clayton RN *et al.* (1973) Component of primitive nuclear composition in carbonaceous meteorites. *Science* **182**(4111): 485-488.

Cloud PE (1968) Atmospheric and hydrospheric evolution on the primitive Earth. *Science* **160**, 729–736.

Cloud PE (1972) A working model of the primitive Earth. *American Journal of Science* **272**: 537-548.

Cloud PE (1988) *Oasis in Space*. Norton, New York, pp. 509.

Cnossen I *et al.* (2007) Habitat of early life: Solar X-ray and UV radiation at Earth's surface 4-3.5 billion years ago. *Journal of Geophysical Research, [Planets]* **112**.

Cockell CS (2000) The ultraviolet history of the terrestrial planets - implications for biological evolution. *Planetary and Space Science* **48**(2-3): 203-214.

Colman AS *et al.* (2000) The global diagenetic flux of phosphorus from marine sediments to the oceans: Redox sensitivity and the control of atmospheric oxygen levels. *Marine Authigenesis: From Global to Microbial*, **SEPM Special Pub. No. 66**.

Connolly JAD (1990) Multivariable Phase-Diagrams - An Algorithm Based On Generalized Thermodynamics. *American Journal Of Science*, **290**, 666-718.

Connolly JAD and Cesare B (1993) C-O-H-S Fluid Composition And Oxygen Fugacity In Graphitic Metapelites. *Journal Of Metamorphic Geology*, **11**, 379-388.

Coplen TB (1994) Reporting Of Stable Hydrogen, Carbon, And Oxygen Isotopic Abundances. *Pure And Applied Chemistry*, **66**, 273-276.

Cox AN (Ed.) (2000) *Allen's Astrophysical Quantities* Springer/Verlag, New York.

Crisp D (1997) Absorption of sunlight by water vapor in cloudy conditions: A partial explanation for the cloud absorption anomaly. *Geophysical Research Letters* **24**(5): 571-574.

Criss RE (1999) *Principles of Stable Isotope Distribution*. New York, Oxford University Press. Pp 264.

D'Hondt S, Rutherford S, Spivack AJ (2002) Metabolic activity of subsurface life in deep-sea sediments. *Science*, **295**, 2067-2070.

Davidson JA *et al.* (1978) Temperature-Dependence Of Deactivation Of $O(^1D)$ by CO From 113 K to 333 K. Journal of Chemical Physics **69(3)** 1216-1217.

de Pater I and Lissauer JJ (2001) *Planetary Sciences*. Cambridge University Press, New York, pp.528.

Delano JW (2001) Redox history of the Earth's interior: implications for the origin of life. *Origins of Life and Evolution of the Biosphere*, **31**, 311-341.

Des Marais DJ, Strauss H, Summons RE, Hayes JM (1992) Carbon isotope evidence for the stepwise oxidation of the Proterozoic environment. *Nature*, **359**, 605-609.

Des Marais DJ (2000) Evolution - When did photosynthesis emerge on Earth? *Science*, **289**, 1703-1705.

Des Marais DJ *et al.* (2002) Remote sensing of planetary properties and biosignatures on extrasolar terrestrial planets. *Astrobiology*, **2**, 153-181.

Devol AH (1983) Methane oxidation rates in the anaerobic sediments of Saanich Inlet. *Limnology and Oceanography* **28**, 738-742.

Di Giulio, M (2003) The ancestor of the Bacteria domain was a hyperthermophile. *Journal of Theoretical Biology* **224**(3): 277-283.

Dickens AF, Gelinas Y, Masiello CA, Wakeham S, Hedges JI (2004) Reburial of fossil organic carbon in marine sediments. *Nature* **427**: 336-339.

Domagal-Goldman S, Johnston D, Farquhar J, Kasting J (2008) Organic haze, glaciations, and multiple sulfur isotopes in the mid-Archean era. *Earth and Planetary Science Letters* **269,** 29-40.

Donohue CL, Essene EJ (2000) An oxygen barometer with the assemblage garnet-epidote. *Earth And Planetary Science Letters*, **181**, 459-472.

Dorren JD and Guinan EF (1994) HD-129333 - The Sun in its infancy. *Astrophysical Journal* **428**, 805-818.

DuRand MD, Olson RJ, Chisholm SW (2001) Phytoplankton population dynamics at the Bermuda Atlantic Time-series station in the Sargasso Sea. *Deep-Sea Research Part Ii-Topical Studies In Oceanography*, **48**, 1983-2003.

Dutkiewicz A, Volk H, George SC, Ridley J, Buick R (2006) Biomarkers from Huronian oil-bearing fluid inclusions: An uncontaminated record of life before the Great Oxidation Event. *Geology*, **34**, 437-440.

Eriksson PG and Cheney ES (1992) Evidence for the transition to an oxygen-rich atmosphere during the evolution of red beds in the lower Proterozoic sequences of southern Africa. *Precambrian Research* **54**: 257-269.

Eyles N (1993) Earths Glacial Record and Its Tectonic Setting. *Earth-Science Reviews* **35**, 1-248.

Falkowski PG (1997) Evolution of the nitrogen cycle and its influence on the biological CO2 pump in the oceans. *Nature* **387**: 272-275.

Falkowski PG and Raven JA (1997) *Aquatic Photosynthesis*. Oxford, Blackwell.

Fanale FP (1971) A case for catastrophic early degassing of the Earth. *Chemical Geology* **8**: 79-105.

Farquhar J, Bao H, Thiemans M (2000) Atmospheric influence of Earth's earliest sulfur cycle. *Science*, **289**, 756-758.

Farquhar J *et al.* (2001) Observation of wavelength-sensitive mass-independent sulfur isotope effects during SO_2 photolysis: application to the early atmosphere. *Journal of Geophysical Research* **106**: 1-11.

Farquhar J and Wing BA (2003) Multiple sulfur isotopes and the evolution of the atmosphere. *Earth and Planetary Science Letters*, **213**, 1-13.

Farquhar J and Wing BA (2005) The terrestrial record of stable sulphur isotopes: a review of the implications for evolution of Earth's sulphur cycle. In *Mineral Deposits and Earth Evolution.* Geological Society, Special Publications, London, 248, 167–177.

Farquhar J *et al.* (2007) Isotopic evidence for Mesoarchaean anoxia and changing atmospheric sulphur chemistry. *Nature* **449**, 706-709.

Fenchel TK, King GM, Blackburn TH (1998) *Bacterial Biogeochemistry: The Ecophysiology of Mineral Cycling*. New York, Academic Press.

Field CB, Behrenfeld MJ, Randerson JT, Falkowski P (1998) Primary production of the biosphere: Integrating terrestrial and oceanic components. *Science*, **281**, 237-240.

Fike DA, Grotzinger JP, Pratt LM, and Summons RE (2006) Oxidation of the Ediacaran Ocean. *Nature* **444**, 744-747.

Finlayson-Pitts J, Barbara J, Pitts JN (2000) *Chemistry of the Upper and Lower Atmosphere: Theory, Experiments, and Applications*. Academic Press, San Diego, pp.969.

Franchi IA (2008) Oxygen isotopes in asteroidal materials. *Oxygen in the Solar System*. **68:** 345-397.

Francois LM and Gerard JC (1988) Ozone, climate and biospheric environment in the ancient oxygen-poor atmosphere. *Planetary and Space Science* **36**(12): 1391-1414.

Friedrichs G *et al*. (2002) Quantitative detection of HCO behind shock waves: The thermal decomposition of HCO. *Physical Chemistry Chemical Physics* **4**(23): 5778-5788.

Frost BR (1991) Introduction To Oxygen Fugacity And Its Petrologic Importance. In: *Reviews In Mineralogy* (ed. Lindsley DH). Mineralogical Society of America, Washington, D.C., pp. 1-9.

Gaillardet J, Dupre B, Louvat P, Allegre CJ (1999) Global silicate weathering and CO_2 consumption rates deduced from the chemistry of large rivers. *Chemical Geology* **159**: 3-30.

Gao, YQ and Marcus RA (2001) Strange and unconventional isotope effects in ozone formation. *Science* **293**(5528): 259-263.

Garrels RM, Mackenzie FT (1971) *Evolution of sedimentary rocks*. Norton, New York, pp.397.

Garrels RM and Perry EA (1974) Cycling of carbon, sulfur and oxygen through geological time. In: Goldberg, E. D. (Eds.), *The Sea*, Wiley Interscience, New York, pp. 303-316.

Gear CW (1971) *Numerical Initial Value Problems in Ordinary Differential Equations*. Englewood Cliffs, Prentice-Hall, Inc.

George SC *et al.* (2008) Preservation of hydrocarbons and biomarkers in oil trapped inside fluid inclusions for > 2 billion years. *Geochimica et Cosmochimica Acta* **72**(3): 844-870.

Giorgi, F. and W. L. Chameides (1985) The rainout parameterization in a photochemical model. *Journal of Geophysical Research* **90**: 7872-7880.

Girardi L, Bressan A, Bertelli G, Chiosi C (2000) Evolutionary tracks and isochrones for low- and intermediate-mass stars: From 0.1 to 7 $M_{\odot}$ and from Z=0.0004 to 0.03. *Astronomy and Astrophysics* **141**, 371-383.

Godderis Y, Veizer J (2000) Tectonic control of chemical and isotopic composition of ancient oceans: The impact of continental growth. *American Journal Of Science*, **300**, 434-461.

Goldblatt C, Lenton TM, and Watson AJ (2006) Bistability of atmospheric oxygen and the Great Oxidation. *Nature* **443**, 683-686.

Gough DO (1981) Solar interior structure and luminosity variations. *Solar Physics* **74**, 21-34.

Grevesse N and Sauval AJ (1998) Standard solar composition. *Space Science Reviews* **85**, 161-174.

Habicht KS, Gade M, Thamdrup B, Berg P, Canfield DE (2002) Calibration of sulfate levels in the Archean ocean. *Science*, **298**, 2372-2374.

Haese RR, Meile C, Van Cappellen P, De Lange GJ (2003) Carbon geochemistry of cold seeps: Methane fluxes and transformation in sediments from Kazan mud volcano, eastern Mediterranean Sea. *Earth and Planetary Science Letters* **212**, 361-375.

Harries J, Ruth S, Russell JM (1996) On the distribution of mesospheric H_2 inferred from HALOE measurements of H_2O and CH_4. *Geophysical Research Letters*, **23**, 297-300.

Haqq-Misra JD *et al.* (2008) A Revised, Hazy Methane Greenhouse for the Archean Earth. *Astrobiology* **in press.**

Hayes JM (1994) Global methanotrophy at the Archean-Preoterozoic transition. In: *Early Life on Earth* (ed. Bengtson S). Columbia University Press, New York, pp. 220-236.

Hayes, JM, Strauss H, Kaufman AJ (1999) The abundance of ^{13}C in marine organic matter and isotopic fractionation in the global biogeochemical cycle of carbon during the past 800 Ma. *Chemical Geology* **161**: 103-125.

Hayes JM and Waldbauer JR (2006) The carbon cycle and associated redox processes through time. *Philosophical Transactions Of The Royal Society B-Biological Sciences*, **361**, 931-950.

Hinrichs KU (2002) Microbial fixation of methane carbon at 2.7 Ga: was an anaerobic mechanism responsible? *Geology Geochemistry Geophysics*, Article #1042 (online).

Hinrichs KU and Boetius A (2002) The anaerobic oxidation of methane: New insights in microbial ecology and biogeochemistry. In *Ocean Margin Systems,* Springer-Verlag, Berlin, pp. 457-477.

Hinrichs KU, Hmelo LR, Sylva SP (2003) Molecular fossil record of elevated methane levels in Late Pleistocene coastal waters. *Science* **299**: 1214-1217.

Hoehler TM, Bebout BM, DesMarais DJ (2001) The role of microbial mats in the production of reduced gases on the early Earth. *Nature*, **412**, 324-327.

Hofmann, HJ *et al.* (1999) Origin of 3.45 Ga Coniform Stromatolites in Warrawoona Group, Western Australia. *Geological Society Of America Bulletin* **111**(8): 1256-1262.

Hoffman, PF, Kaufman AJ, Halverson GP, Schrag DP (1998) A Neoproterozoic Snowball Earth. *Science* **281**: 1342-1346.

Hoffman PF and Schrag DP (2002) The Snowball Earth hypothesis: Testing the limits of global change. *Terra Nova*, **14**, 129-155.

Holland HD (1978) *The Chemistry of the Atmosphere and Oceans*. Wiley, New York, pp.351.

Holland HD (1984) *The Chemical Evolution of the Atmosphere and Oceans*. Princeton University Press, Princeton, pp.582.

Holland HD and Beukes NJ (1990) A paleoweathering profile from Griqualand West, South Africa: Evidence for a dramatic rise in atmospheric oxygen between 2.2 and 1.9 B.Y.B.P. *American Journal of Science* **290-A**: 1-34.

Holland HD (1994) Early Proterozoic atmospheric change. In *Early Life on Earth*. New York, Columbia University Press, Bengtson, S. (ed.) 237-244.

Holland HD (1999) When did the Earth's atmosphere become oxic?: A Reply. *Geochemical News* **100**: 20-22.

Holland HD (2002) Volcanic gases, black smokers, and the Great Oxidation Event. *Geochimica et Cosmochimica Acta*, **66**, 3811-3826.

Holland HD (2003) Discussion of the article by A. C. Lasaga and H. Ohmoto on "The oxygen geochemical cycle: dynamics and stability", Geochim. Cosmochim. Acta 66,361-381, 2002. *Geochimica et Cosmochimica Acta*, **67**, 787-789.

Holland HD (2006) The oxygenation of the atmosphere and oceans. *Philosophical Transactions Of The Royal Society B-Biological Sciences*, **361**, 903-915.

Holser WT, Schidlowski M, Mackenzie FT, Maynard JB (1988) Geochemical cycles of carbon and sulfur. In: *Chemical Cycles in the Evolution of the Earth* (eds. Gregor CB, Garrels RM, Mackenzie FT, Maynard JB). Wiley, New York, pp. 105-173.

Hornafius JS, Quigley D, Luyendyk BP (1999) The world's most spectacular marine hydrocarbon seeps (Coal Oil Point, Santa Barbara Channel, California): Quantification of emissions. *Journal Of Geophysical Research-Oceans*, **104**, 20703-20711.

Houghton JT, Eds. (1994) *Climate Change, 1994: Radiative Forcing of Climate Change and an Evaluation of the IPCC IS92 Emission Scenarios*. Cambridge, Cambridge University Press.

House CH *et al.* (2003) Geobiological analysis using whole genome-based tree building applied to the Bacteria, Archea, and Eukarya. *Geobiology* **1**: 15-26.

Huizenga JM (2001) Thermodynamic modelling of C-O-H fluids. *Lithos*, **55**, 101-114.

Hunten DM (1990) Kuiper-Prize Lecture - Escape Of Atmospheres, Ancient And Modern. *Icarus*, **85**, 1-20.

Hunten DM (1993) Atmospheric evolution on the terrestrial planets. *Science*, **259**, 915-920.

Hunten DM and Donahue TM (1976) Hydrogen loss from the terrestrial planets. *Annual Review Of Earth And Planetary Sciences*, **4**, 265-292.

Hurtgen MT, Arthur MA, Suits NS, Kaufman AJ (2002) The sulfur isotopic composition of Neoproterozoic seawater sulfate: implications for a snowball Earth? *Earth and Planetary Science Letters* **203**: 413-429.

Hurtgen MT, Arthur MA, Halverson GP (2005) Neoproterozoic sulfur isotopes, the evolution of microbial sulfur species, and the burial efficiency of sulfide as sedimentary pyrite. *Geology* **33**(1): 41-44.

Huston DL and Logan GA (2004) Barite, BIFs and bugs: evidence for the evolution of the Earth's early hydrosphere. *Earth And Planetary Science Letters*, **220**, 41-55.

Ingvorsen K and Brock TD (1982) Electron flow via sulfate reduction and methanogenesis in the anaerobic hypolimnion of Lake Mendota. *Limnology and Oceanography* **27**, 559-564.

Inomata S and Washida N (1999) Rate constants for the reactions of NH_2 and HNO with atomic oxygen at temperatures between 242 and 473 K. *Journal of Physical Chemistry A* **103**(26): 5023-5031.

IPCC (2007) *Climate Change 2007: The Physical Science Basis.* Solomon S *et al.* (eds.). Cambridge, United Kingdom, Cambridge University Press. 996p.

Inn ECY (1974) Rate Of Recombination Of Oxygen-Atoms And CO At Temperatures Below Ambient. *Journal of Chemical Physics* **61**(4): 1589-1590.

Iversen N and Jorgensen BB (1985) Anaerobic Methane Oxidation Rates at the Sulfate Methane Transition in Marine-Sediments from Kattegat and Skagerrak (Denmark). *Limnology and Oceanography* **30**, 944-955.

Iversen N and Jorgensen BB (1993) Diffusion coefficients of sulfate and methane in marine sediments: Influence of porosity. *Geochimica Et Cosmochimica Acta* **57**, 571-578.

Jacobson MZ *Fundamentals of Atmospheric Modeling*. Cambridge University Press, New York (2005) 813p.

Jorgensen BB, Bottcher ME, Luschen H, Neretin LN, and Volkov II (2004) Anaerobic methane oxidation and a deep H_2S sink generate isotopically heavy sulfides in Black Sea sediments. *Geochimica Et Cosmochimica Acta* **68**, 2095-2118.

Junge CE, Schidlowski M, Eichmann R, Pietrek H (1975) Model calculations for the terrestrial carbon cycle: carbon isotope geochemistry and evolution of photosynthetic oxygen. *Journal of Geophysical Research*, **80**, 4542-4552.

Kah LC, Lyons TW, Frank TD (2004) Low marine sulphate and protracted oxygenation of the Proterozoic biosphere. *Nature* **431**: 834-838.

Kaltenegger L *et al.* (2007) Spectral evolution of an Earth-like planet. *Astrophysical Journal* **658**(1): 598-616.

Kargel JS and Lewis JS (1993) The Composition And Early Evolution Of Earth. *Icarus*, **105**, 1-25.

Karhu JA and Holland HD (1996) Carbon isotopes and the rise of atmospheric oxygen. *Geology*, **24**, 867-870.

Kasting JF (1979) Evolution of oxygen and ozone in the Earth's atmosphere. *Ph.D. thesis*, University of Michigan, pp.259.

Kasting JF, Liu SC, Donahue TM (1979) Oxygen levels in the prebiological atmosphere. *Journal of Geophysical Research* **84**, 3097-3107.

Kasting JF, Donahue TM (1980) The evolution of atmospheric ozone. *Journal of Geophysical Research*, **85**, 3255-3263.

Kasting JF, Pollack JB, Crisp D (1984) Effects of high CO_2 levels on surface temperature and atmospheric oxidation state of the early earth. *Journal of Atmospheric Chemistry*, **1**, 403-428.

Kasting JF and Ackerman TP (1986) Climatic consequences of very high CO_2 levels in the earth's early atmosphere. *Science*, **234**, 1383-1385.

Kasting JF (1988) Runaway and moist greenhouse atmospheres and the evolution of Earth and Venus. *Icarus*, **74**, 472-494.

Kasting JF *et al.* (1989) Sulfur, ultraviolet radiation, and the early evolution of life. *Origins of Life and Evolution of the Biosphere* **19**: 95-108.

Kasting JF (1990) Bolide impacts and the oxidation state of carbon in the Earth's early atmosphere. *Origins of Life and Evolution of the Biosphere* **20**, 199–231.

Kasting JF (1992) Models relating to Proterozoic atmospheric and oceanic chemistry. In: *The Proterozoic Biosphere: A Multidisciplinary Study* (ed. Schopf JW, Klein C). Cambridge University Press, Cambridge, pp. 1185-1187.

Kasting JF (1993). "Earth's early atmosphere." *Science* **259**: 920-926.

Kasting JF *et al.* (1993) Habitable zones around main sequence stars. *Icarus* **101**: 108-128.

Kasting JF, Eggler DH, Raeburn SP (1993) Mantle redox evolution and the oxidation state of the Archean atmosphere. *Journal Of Geology*, **101**, 245-257.

Kasting JF (1997) Habitable zones around low mass stars and the search for extraterrestrial life. *Origins of Life*, **27**, 291-307.

Kasting JF and Brown LL (1998) Setting the stage: the early atmosphere as a source of biogenic compounds. In: *The Molecular Origins of Life: Assembling the Pieces of the Puzzle* (ed. Brack A). Cambridge University Press, New York, pp. 35-56.

Kasting, J. F. (2001) The rise of atmospheric oxygen (Perspective). *Science* **293**: 819-820.

Kasting JF, Pavlov AA, Siefert JL (2001) A coupled ecosystem-climate model for predicting the methane concentration in the Archean atmosphere. *Origins of Life and Evolution of the Biosphere*, **31**, 271-285.

Kasting JF and Catling DC (2003) Evolution of a habitable planet. *Annual Review of Astronomy and Astrophysics*, **41**, 429-463.

Kasting JF (2005) Methane and climate during the Precambrian era. *Precambrian Research*, **137**, 119-129.

Kasting JF and Howard MT (2006) Atmospheric composition and climate on the early Earth. *Philosophical Transactions of the Royal Society B-Biological Sciences* **361**, 1733-1741.

Kaufman AJ (1997) Palaeoclimatology - An ice age in the tropics. *Nature* **386**, 227-228.

Kaufman AJ, Hayes JM, Klein C (1990) Primary and diagenetic controls of isotopic compositions of iron-formation carbonates. *Geochimica et Cosmochimica Acta* **54**: 3461-3473.

Kaufman AJ *et al.* (2007) Late Archean biospheric oxygenation and atmospheric evolution. *Science*. **317,** 1900-1903.

Kemp AIS and Hawkesworth CJ (2004) Granitic Perspectives on the Generation and Secular Evolution of the Continental Crust. In: *Treatise on Geochemistry - Volume 3: The Crust* (ed. Rudnick RL). Elsevier, Amsterdam, pp. 349-410.

Kenrick P, Crane PR (1997) The origin and early evolution of plants on land. *Nature*, **389**, 33-39.

Kharecha P, Kasting JF, Siefert J (2005) A coupled atmosphere-ecosystem model of the early Archean Earth. *Geobiology*, **3**, 53-76.

Kirschvink JL (1992) Late Proterozoic low-latitude global glaciation: the snowball earth. In: *The Proterozoic Biosphere* (ed. Klein JWSaC). Cambridge University Press, Cambridge, pp. 51-52.

Klein C (2005) Some Precambrian banded iron-formations (BIFs) from around the world: Their age, geologic setting, mineralogy, metamorphism, geochemistry, and origin. *American Mineralogist* **90**(10): 1473-1499.

Kleine T, Munker C, Mezger K, Palme H (2002) Rapid accretion and early core formation on asteroids and the terrestrial planets from Hf-W chronometry. *Nature* **418**: 952-955.

Klemm RB and Davis DD (1974) Flash Photolysis-Resonance Fluorescence Kinetics Study Of Reaction S(3P) + OCS. *Journal of Physical Chemistry* **78**(12): 1137-1140.

Klippenstein SJ *et al.* (2006) Predictive theory for the combination kinetics of two alkyl radicals. *Physical Chemistry Chemical Physics* **8**(10): 1133-1147.

Knipovich OM *et al.* (1988) Volume Recombination Of Nitrogen-Atoms In Afterglow Of Condensed Discharges. *Zhurnal Fizicheskoi Khimii* **62**(6): 1694-1699.

Knoll AH and Barghoorn ES (1977) Archean microfossils showing cell division from the Swaziland System of South Africa. *Science* **198**: 396-398.

Knoll AH (1979) Archean photoautotrophy: some alternatives and limits. *Origins of Life and Evolution of the Biosphere* **9**: 313-327.

Knoll AH and Carroll SB (1999) Early animal evolution: Emerging views from comparative biology and geology. *Science* **284**: 2129-2137.

Knutson HA *et al.* (2007) A map of the day-night contrast of the extrasolar planet HD 189733b. *Nature* **447**(7141): 183-186.

Kopp RE, Kirschvink JL, Hilburn IA, Nash CZ (2005) The paleoproterozoic snowball Earth: A climate disaster triggered by the evolution of oxygenic photosynthesis. *Proceedings Of The National Academy Of Sciences Of The United States Of America*, **102**, 11131-11136.

Kral TA, Brink KM, Miller SL, McKay CP (1998) Hydrogen consumption by methanogens on the early Earth. *Origins of Life and Evolution of the Biosphere*, **28**, 311-319.

Krivova NA, Solanki SK, Floyd L (2006) Reconstruction of solar UV irradiance in cycle 23. *Astronomy and Astrophysics* **452**, 631-639.

Kruger M, Treude T, Wolters H, Nauhaus K, Boetius A (2005) Microbial methane turnover in different marine habitats. *Palaeogeography Palaeoclimatology Palaeoecology* **227**, 6-17.

Kulikov YN, Lammer H, Lichtenegger HIM, Penz T, Breuer D, Spohn T, Lundin R, Biernat HK (2006) A comparative study of the influence of the active young sun on the early atmospheres of Earth, Venus, and Mars. *Space Science Reviews*, **in review**.

Kump LR, Kasting JF, Barley ME (2001) The rise of atmospheric oxygen and the "upside-down" Archean mantle. *Geology Geochemistry Geophysics*, **2**, (online).

Kump LR and Seyfried WE (2005) Hydrothermal Fe fluxes during the Precambrian: Effect of low oceanic sulfate concentrations and low hydrostatic pressure on the composition of black smokers. *Earth And Planetary Science Letters*, **235**, 654-662.

Kump LR and Barley ME (2007) Increased subaerial volcanism and the rise of atmospheric oxygen 2.5 billion years ago. *Nature*. **448,** 1033-1036.

Kump LR (2008) The rise of atmospheric oxygen. *Nature*. **451,** 277-278.

Kurbanov MA and Mamedov KF (1995) The role of the reaction CO+SH->COS+H in hydrogen formation in the course of interaction between CO And H_2S. *Kinetics and Catalysis* **36**(4): 455-457.

Kurucz RL (1979) Model atmospheres for G, F, A, B, and O stars. *Astrophysical Journal Supplement Series* **40**, 1-340.

Lachaume R, Dominik C, Lanz T, Habing HJ (1999) Age determinations of main-sequence stars: combining different methods. *Astronomy And Astrophysics* **348**, 897-909.

Laidler KJ and Wojciechowski BW (1961) Kinetics And Mechanisms Of Thermal Decomposition Of Ethane .2. Reaction Inhibited By Nitric Oxide. *Proceedings of the Royal Society of London Series a-Mathematical and Physical Sciences* **260**(130): 103-&.

Laidler KJ *et al.* (1962) Kinetics And Mechanisms Of Thermal Decomposition Of Propane .2. Reaction Inhibited By Nitric Oxide. *Proceedings of the Royal Society of London Series a-Mathematical and Physical Sciences* **270**(1341): 254-&.

Lammer H, Kulikov YN, Lichtenegger HIM (2006) Thermospheric X-ray and EUV heating by the young Sun on early Venus and Mars. *Space Science Reviews* **122**, 189-196.

Lammer H *et al.* (2003) Loss of water from Mars: Implications for the oxidation of the soil. *Icarus* **165**, 9-25.

Langford RB and Oldersha.Ga (1972). Flash-Photolysis Of H_2S. *Journal of the Chemical Society-Faraday Transactions I* **68**(8): 1550-&.

Lean J (1997) The sun's variable radiation and its relevance for earth. *Annual Review Of Astronomy And Astrophysics* **35**, 33-67.

Lean JL, White OR, Livingston WC, Picone JM (2001) Variability of a composite chromospheric irradiance index during the 11-year activity cycle and over longer time periods. *Journal Of Geophysical Research, [Space Physics]* **106**, 10645-10658.

Lecuyer C and Ricard Y (1999) Long-term fluxes and budget of ferric iron: implication for the redox states of the Earth's mantle and atmosphere. *Earth and Planetary Science Letters*, **165**, 197-211.

Lee JH *et al.* (1977) Absolute Rate Parameters For Reaction Of Atomic-Hydrogen With Carbonyl Sulfide And Ethylene Episulfide. *Journal of Chemical Physics* **67**(4): 1705-1709.

Lee YN and Schwartz SE (1981) Evaluation of the rate of uptake of nitrogen dioxide by atmospheric and surface liquid water. *Journal of Geophysical Research* **86**: 11971-11983.

Lenton TM and Watson AJ (2000). "Redfield revisited: II. What regulates the oxygen content of the atmosphere?" *Global Biogeochemical Cycles* **14**: 249-268.

Li ZXA and Lee CTA (2004) The constancy of upper mantle fO_2 through time inferred from V/Sc ratios in basalts. *Earth And Planetary Science Letters*, **228**, 483-493.

Lindsay JF and Brasier MD (2002) Did global tectonics drive early biosphere evolution? Carbon isotope record from 2.6 To 1.9 Ga carbonates of Western Australian basins. *Precambrian Research*, **114**, 1-34.

Liu JY *et al.* (2003) Theoretical study and rate constant calculation of the CH_2O+CH_3 reaction. *Journal of Chemical Physics* **119**(14): 7214-7221.

Logan GA, Hayes JM, Hieshima GB, Summons RE (1995) Terminal Proterozoic reorganization of biogeochemical cycles. *Nature* **376**: 53-56.

Lovelock JE and Kump LR (1994) Failure Of Climate Regulation In A Geophysiological Model. *Nature*, **369**, 732-734.

Lovelock JE (2000) *The Ages of Gaia* London, Oxford University Press pp 227.

Luff R and Wallmann K (2003) Fluid flow, methane fluxes, carbonate precipitation and biogeochemical turnover in gas hydrate-bearing sediments at Hydrate Ridge, Cascadia Margin: Numerical modeling and mass balances. *Geochimica Et Cosmochimica Acta* **67**, 3403-3421.

Lyons JR (2007) Mass-independent fractionation of sulfur isotopes by isotope-selective photodissociation of SO_2. *Geophysical Research Letters* **34**, 5.

Macgregor AM (1927) The problem of the Precambrian Atmosphere. *South African Journal of Science* **24**: 155-172.

Manabe S and Wetherald RT (1967) Thermal equilibrium of the atmosphere with a given distribution of relative humidity. *Journal of Atmospheric Sciences* **24**, 241–259.

Manning CE and Ingebritsen SE (1999) Permeability of the continental crust: Implications of geothermal data and metamorphic systems. *Reviews Of Geophysics*, **37**, 127-150.

Marrero TR and Mason EA (1972) Gaseous Diffusion Coefficients. *Journal of Physical and Chemical Reference Data* **1**: 3-118.

Martens CS and Berner RA (1977) Interstitial water chemistry of anoxic Long Island Sound sediments .1. Dissolved-gases. *Limnology and Oceanography* **22**, 10-25.

Martin MW *et al.* (2000). "Age of Neoproterozoic bilatarian body and trace fossils, White Sea, Russia: Implications for metazoan evolution." *Science* **288**(5467): 841-845.

Marty B and Tolstikhin IN (1998) CO_2 fluxes from mid-ocean ridges, arcs and plumes. *Chemical Geology* **145**, 233–248.

Mason R (1990) *Petrology of the Metamorphic Rocks*. Boston, Unwin Hyman.

Massie ST and Hunten DM (1981) Stratospheric eddy diffusion coefficients from tracer data. *Journal of Geophysical Research* **86**: 9859-9868.

Masterson AL, Wing BA, Farquhar JA, Franz H, Lyons JR (2006) Poster 226 – Anomalous isotopic fractionation during broadband SO_2 photochemistry: contributions from direct and indirect photodissociation. *Astrobiology* **6**, p. 192.

Matsumi Y *et al.* (1993) Isotopic branching ratios and translational energy-release of H-atoms and D-atoms in reaction of $O(^1D)$ atoms with alkanes and alkyl chlorides. *Journal of Physical Chemistry* **97**(26): 6816-6821.

Mauersberger K (1987) Ozone isotope measurements in the stratosphere. *Geophysical Research Letters* **14**(1): 80-83.

McDonough WF and Sun SS (1995) Composition of the Earth. *Chemical Geology*, **120**, 223-253.

Meadows VS and Crisp D (1996) Ground-based near-infrared observations of the Venus nightside: The thermal structure and water abundance near the surface. *Journal Of Geophysical Research-Planets* **101**(E2): 4595-4622.

Melezhik VA, Fallick AE, Medvedev PV, Makarikhin VV (1999) Extreme $\delta^{13}C_{carb}$ enrichment in ~2.0 Ga magnesite-stromatolite-dolomite- 'red beds' association in a global context: a case for the world-wide signal enhanced by a local environment. *Earth-Science Reviews*, **48**, 71-120.

Melezhik VA, Fallick AE, Rychanchik DV, Kuznetsov AB (2005) Palaeoproterozoic evaporites in Fennoscandia: implications for seawater sulphate, the rise of atmospheric oxygen and local amplification of the $\delta^{13}C$ excursion. *Terra Nova*, **17**, 141-148.

Melnik YP (1982) *Precambrian banded iron-formations: Physicochemical conditions of formation*. Elsevier, Amsterdam, pp.310.

Meynet G, Mermilliod JC, Maeder A (1993) New Dating of Galactic Open Clusters. *Astronomy & Astrophysics Supplement Series* **98**, 477-504.

Middelburg JJ, Soetaert K, and Herman PMJ (1997) Empirical relationships for use in global diagenetic models. *Deep-Sea Research Part I-Oceanographic Research Papers* **44**, 327-344.

Milkov AV, Etiope G (2005) Global methane emission through mud volcanoes and its past and present impact on the Earth's climate-a comment. *International Journal Of Earth Sciences*, **94**, 490-492.

Milkov AV, Sassen R, Apanasovich TV, Dadashev FG (2003) Global gas flux from mud volcanoes: A significant source of fossil methane in the atmosphere and the ocean. *Geophysical Research Letters*, **30**, 9- (1-4).

Miller SL and Urey HC (1959) Organic compound synthesis on the primitive Earth. *Science* **130**: 245-251.

Mix LJ *et al.* (2006) The astrobiology primer: An outline of general knowledge - Version 1, 2006. *Astrobiology* **6**(5): 735-813.

Moisan JR, Moisan TA, Abbott MR (2002) Modelling the effect of temperature on the maximum growth rates of phytoplankton populations. *Ecological Modelling*, **153**, 197-215.

Moore LR, Goericke R, Chisholm SW (1995) Comparative Physiology Of Synechococcus And Prochlorococcus - Influence Of Light And Temperature On Growth, Pigments, Fluorescence And Absorptive Properties. *Marine Ecology-Progress Series*, **116**, 259-275.

Morner NA, Etiope G (2002) Carbon degassing from the lithosphere. *Global And Planetary Change*, **33**, 185-203.

Mount GH and Moos HW (1978) Photoabsorption cross-sections of methane and ethane, 1380-1600 A, at T=295 K and T=200 K. *Astrophysical Journal* **224**(1): L35-L38.

Mount GH *et al.* (1977) Photoabsorption cross-sections of methane from 1400 to 1850 A. *Astrophysical Journal* **214**(1): L47-L49.

Murakami T, Utsunomiya S, Imazu Y, Prasad N (2001) Direct evidence of Late Archean to Early Proterozoic anoxic atmosphere from a product of 2.5 Ga old weathering. *Earth and Planetary Science Letters* **184**: 523.

Nair H *et al.* (1994) A photochemical model of the Martian atmosphere. *Icarus* **111**: 124-150.

Nakamura K and Kato Y (2004) Carbonatization of oceanic crust by the seafloor hydrothermal activity and its significance as a CO_2 sink in the Early Archean. *Geochimica et Cosmochimica Acta*, **68**, 4595-4618.

NIST *NIST Chemical Kinetics Database*, Standard Reference Database 17, Version 7.0 (Web Version), Release 1.4.

Nesbitt FL *et al.* (1999) Temperature dependence of the rate constant for the reaction $HCO+O_2$ -> HO_2 + CO at T = 200-398 K. *Journal of Physical Chemistry A* **103**(16): 3038-3043.

Nicholas JE *et al.* (1979) Kinetics and mechanism of the decomposition of H_2S, CH_3SH And $(CH_3)2S$ In A Radio-Frequency Pulse Discharge. *Journal of the Chemical Society-Faraday Transactions I* **75**: 1868-1875.

Nisbet EG and Sleep NH (2001) The habitat and nature of early life. *Nature* **409**: 1083-1091.

Nisbet EG *et al.* (2007) The age of Rubisco: the evolution of oxygenic photosynthesis. *Geobiology* **5**(4): 311-335.

Ohmoto H and Kerrick D (1977) Devolatilization Equilibria In Graphitic Systems. *American Journal Of Science*, **277**, 1013-1044.

Ohmoto H (1996) Evidence in pre-2.2 Ga paleosols for the early evolution of atmospheric oxygen and terrestrial biota. *Geology*, **24**, 1135-1138.

Ohmoto H (1997) When did the Earth's atmosphere become oxic? *Geochemical News* **93**: p. 13.

Ohmoto H *et al.* (2006) Sulphur isotope evidence for an oxic Archaean atmosphere. *Nature* **442**(7105): 908-911.

Ono S *et al.* (2003) New insights into Archean sulfur cycle from mass-independent sulfur isotope records from the Hamersley Basin, Australia. *Earth and Planetary Science Letters*, **213**, 15-30.

Ono S, Wing B, Johnston D, Farquhar J, Rumble D (2006) Mass-dependent fractionation of quadruple stable sulfur isotope system as a new tracer of sulfur biogeochemical cycles. *Geochimica Et Cosmochimica Acta*. **70,** 2238-2252.

Onstott TC *et al.* (2006) Martian CH_4: Sources, Flux, and Detection. *Astrobiology*, **6**, 377-395.

Pace G and Pasquini L (2004) The age-activity-rotation relationship in solar-type stars. *Astronomy and Astrophysics* **426**, 1021-1034.

Papineau D, Mojzsis SJ, Coath CD, Karhu JA, McKeegan KD (2005) Multiple sulfur isotopes of sulfides from sediments in the aftermath of Paleoproterozoic glaciations. *Geochimica et Cosmochimica Acta* **69**, 5033–5060.

Papineau D *et al.* (2007) Multiple sulfur isotopes from Paleoproterozoic Huronian interglacial sediments and the rise of atmospheric oxygen. *Earth and Planetary Science Letters* **255**(1-2): 188-212.

Parker EN (1970) Generation Of Magnetic Fields In Astrophysical Bodies .1. Dynamo Equations. *Astrophysical Journal* **162**, 665-673.

Partensky F, Hess WR, Vaulot D (1999) Prochlorococcus, a marine photosynthetic prokaryote of global significance. *Microbiology and Molecular Biology Reviews* **63**: 106-127.

Partzsch GM, Lattard D, McCammon C (2004) Mossbauer spectroscopic determination of Fe^{3+}/Fe^{2+} in synthetic basaltic glass: a test of empirical fO_2 equations under superliquidus and subliquidus conditions. *Contributions To Mineralogy And Petrology*, **147**, 565-580.

Patchett PJ and Arndt NT (1986) Nd Isotopes And Tectonics Of 1.9-1.7 Ga Crustal Genesis. *Earth And Planetary Science Letters*, **78**, 329-338.

Pavlov AA, Kasting JF, Brown LL, Rages KA, Freedman R (2000) Greenhouse warming by CH_4 in the atmosphere of early Earth. *Journal of Geophysical Research*, **105**, 11,981-11,990.

Pavlov AA, Kasting JF, Brown LL (2001) UV-shielding of NH_3 and O_2 by organic hazes in the Archean atmosphere. *Journal of Geophysical Research*, **106**, 23,267-23,287.

Pavlov AA, Kasting JF (2002) Mass-independent fractionation of sulfur isotopes in Archean sediments: strong evidence for an anoxic Archean atmosphere. *Astrobiology*, **2**, 27-41.

Pavlov AA, Hurtgen MT, Kasting JF, Arthur MA (2003) Methane-rich Proterozoic atmosphere? *Geology*, **31**, 87-90.

Pearson DG, Canil D, Shirey SS (2004) Mantle Samples Included in Volcanic Rocks: Xenoliths and Diamonds. In: *Treatise on Geochemistry - Volume 2: The Mantle and Core* (ed. Carlson RW). Elsevier, Amsterdam, pp. 171-275.

Penz T, Lammer H, Kulikov YN, Biernat HK (2005) The influence of the solar particle and radiation environment on Titan's atmosphere evolution. *Advances in Space Research* **36**, 241-250.

Perryman MAC *et al*. (1998) The Hyades: distance, structure, dynamics, and age. *Astronomy & Astrophysics* **331**, 81-120.

Petsch ST (2004) The Global Oxygen Cycle. In: *Treatise on Geochemistry - Volume 8: Biogeochemistry* (ed. Schlesinger WH). Elsevier, Amsterdam, pp. 515-555.

Pinti DL and Hashizume K (2001) ^{15}N depleted nitrogen in early Archean kerogens: Clues on ancient marine chemosynthetic-based ecosystems? A comment to Beaumont,V., Robert,F., 1999. Precambrian Res. 96, 62-82. *Precambrian Research* **105**: 85-88.

Pinti DL, Hashizume K, Matsuda J (2001) Nitrogen and argon signatures in 3.8 To 2.8 Ga metasediments: Clues on the chemical state of the Archean ocean and the deep biosphere. *Geochimica et Cosmochimica Acta* **65**: 2301-2315.

Poulton SW, Fralick PW, Canfield DE (2004) The transition to a sulphidic ocean ~1.84 billion years ago. *Nature*, **431**, 173-177.

Prasad N and Roscoe SM (1996) Evidence of anoxic to oxic atmosphere change during 2.45-2.22 Ga from lower and upper sub-Huronian paleosols, Canada. *Catena* **27**: 105-121.

Prather M, *et al.* Atmospheric chemistry and greenhouse gases. in *Climate Change 2001, The Scientific Basis*, Cambridge University Press, Cambridge, U.K., pp. 239-287.

Raghoebarsing AA *et al.* (2006) A microbial consortium couples anaerobic methane oxidation to denitrification. *Nature*, **440**, 918-921.

Rashby SE *et al.* (2007) Biosynthesis of 2-methylbacteriohopanepolyols by an anoxygenic phototroph. *Proceedings of the National Academy of Sciences of the United States of America* **104**(38): 15099-15104.

Rasmussen B and Buick R (1999) Redox state of the Archean atmosphere: Evidence from detrital heavy minerals in ca. 3250-2750 Ma sandstones from the Pilbara Craton, Australia. *Geology*, **27**, 115-118.

Rasmussen B (2000) Filamentous microfossils in a 3,235-million-year-old volcanogenic massive sulphide deposit. *Nature* **405**: 676-679.

Raymond SN, Quinn T, Lunine JI (2005a) The formation and habitability of terrestrial planets in the presence of close-in giant planets. *Icarus*, **177**, 256-263.

Raymond SN, Quinn T, Lunine JI (2005b) Terrestrial Planet Formation in Disks with Varying Surface Density Profiles. *Astrophysical Journal*, **632**, 670-676.

Raymond SN, Quinn T, Lunine JI (2006a) High-resolution simulations of the final assembly of Earth-like planets 2: water delivery and planetary habitability. *Astrobiology*, **in press**.

Raymond SN, Quinn T, Lunine JI (2006b) High-resolution simulations of the final assembly of Earth-like planets I: Terrestrial accretion and dynamics. *Icarus*, **183**, 265-282.

Reeburgh WS and Heggie DT (1977) Microbial methane consumption reactions and their effect on methane distributions in freshwater and marine environments. *Limnology and Oceanography* **22**, 1-9.

Reeburgh WS *et al.* (1991) Black-Sea Methane Geochemistry. *Deep-Sea Research Part A-Oceanographic Research Papers*, **38**, S1189-S1210.

Reeburgh WS (1996) "Soft Spots" in the global methane budget. *in Microbial growth on C1 compounds*, Kluwer, Dorecht, pp. 334-342.

Ribas I, Guinan EF, Gudel M, Audard M (2005) Evolution of the solar activity over time and effects on planetary atmospheres. I. High-energy irradiances (1–1700 angstrom). *Astrophysical Journal* **622**, 680–694.

Robie DC *et al.* (1990) The intramolecular kinetic isotope effect for the reaction $O(^3P)$+HD. *Journal of Chemical Physics* **92**(12): 7382-7393.

Rogers JJW and Santosh M (2004) *Continents and Supercontinents*. Oxford University Press, New York, pp.289.

Ronov AB (1983) The earth's sedimentary shell: quantitative patterns of its structure, composition, and evolution. *AGI reprint series - originally published in International Geology Review v.24, 1982*, **5**, 1-80.

Rosing MT (1999) 13C-depleted carbon microparticles in >3700-Ma sea-floor sedimentary rocks from West Greenland. *Science* **283**: 674-676.

Rosing MT and Frei R (2004) U-Rich Archaean Sea-Floor Sediments From Greenland - Indications of > 3700 Ma Oxygenic Photosynthesis. *Earth and Planetary Science Letters* **217**(3-4): 237-244.

Rothman DH, Hayes JM, Summons RE (2003) Dynamics of the Neoproterozoic carbon cycle. *Proceedings Of The National Academy Of Sciences Of The United States Of America*, **100**, 8124-8129.

Rouxel OJ, Bekker A and Edwards KJ (2005) Iron isotope constraints on the Archean and Paleoproterozoic ocean redox state. *Science* **307**(5712): 1088-1091.

Rudnick RL and Gao S (2004) The composition of the continental crust. In: *Treatise on Geochemistry - Volume 3: The Crust* (ed. Rudnick RL). Oxford University Press, pp. 1-64.

Rudnick RL, McDonough WF, O'Connell RJ (1998) Thermal structure, thickness and composition of continental lithosphere. *Chemical Geology*, **145**, 395-411.

Runnegar B (1991) Precambrian oxygen levels estimated from the biochemistry and physiology of early eukaryotes. *Global And Planetary Change*, **97**, 97-111.

Ruttenberg KC (2004) The Global Phosphorus Cycle. In: *Treatise on Geochemistry - Volume 8: Biogeochemistry* (ed. Schlesinger WH). Elsevier, Amsterdam, pp. 585-643.

Rybicki KR (2006) On the energy flux reaching planets during the parent star's evolutionary track: The Earth-Sun system. *Publications Of The Astronomical Society Of The Pacific* **118**, 1124-1135.

Rye R, Kuo PH, Holland HD (1995) Atmospheric carbon dioxide concentrations before 2.2 billion years ago. *Nature* **378**, 603–605.

Rye R, Holland HD (1998) Paleosols and the evolution of atmospheric oxygen: A critical review. *American Journal Of Science*, **298**, 621-672.

Sack RO, Carmichael ISE, Rivers M, Ghiorso MS (1980) Ferric-Ferrous Equilibria In Natural Silicate Liquids At 1bar. *Contributions To Mineralogy And Petrology*, **75**, 369-376.

Sagan C and Mullen G (1972) Earth and Mars: Evolution of atmospheres and surface temperatures. *Science* **177**: 52-56.

Sander SP *et al.* (2002) Chemical Kinetics and Photochemical Data for Use in Atmospheric Studies, Evaluation Number 14, Jet Propulsion Laboratory, Pasadena. **JPL Publication 02-25**.

Sander SP *et al.* (2006) Chemical Kinetics and Photochemical Data for Use in Atmospheric Studies, Evaluation Number 15, Jet Propulsion Laboratory, Pasadena. **JPL Publication 06-2**.

Savarino J, Romero A, Cole-Dai J, Bekki S, Thiemens M (2003) UV induced mass-independent sulfur isotope fractionation in stratospheric volcanic sulfate. *Geophysical Research Letters* **30**

Sbordone L, Bonifacio P, Castelli F, Kurucz RL (2004) ATLAS and SYNTHE under Linux. *Memorie della Societa Astronomica Italiana Supplement* **5**, 93.

Schidlowski M (1988) A 3,800-million-year isotopic record of life from carbon in sedimentary rocks. *Nature*, **333**, 313-318.

Schidlowski M (2001) Carbon isotopes as biogeochemical recorders of life over 3.8 Ga of Earth history: evolution of a concept. *Precambrian Research*, **106**, 117-134.

Schofield K (1973) Evaluated chemical kinetic rate constants for various gas phase reactions. *Journal of Physical and Chemical Reference Data* **2**: 25-84.

Schubert G, Turcotte DL, Olsen P (2001) *Mantle Convection in the Earth and Planets*. Cambridge, Cambridge University Press.

Schwartzman D (1999) *Life, Temperature, and the Earth: The Self-Organizing Biosphere*. New York, Columbia University Press.

Seinfeld JH and Pandis SN (1998) *Atmospheric Chemistry and Physics: From Air Pollution to Climate Change* New York, John Wiley & Sons, pp 1326.

Segura A *et al.* (2003) Ozone concentrations and ultraviolet fluxes on Earth-like planets around other stars. *Astrobiology* **3**(4): 689-708.

Segura A *et al.* (2005) Biosignatures from earth-like planets around M dwarfs. *Astrobiology* **5**(6): 706-725.

Segura A, Meadows VS, Kasting JF, Crisp D, Cohen M, (2007) Abiotic formation of O_2 and O_3 in high-CO_2 terrestrial atmospheres. *Astronomy & Astrophysics* **472**, 665-679.

Shen Y, Knoll AH and Walter MR (2003) Evidence for low sulphate and anoxia in a mid-Proterozoic marine basin. *Nature* **423**: 632-635.

Shields G and Veizer J (2002) Precambrian marine carbonate isotope database: Version 1.1. *Geochemistry Geophysics Geosystems* **3**.

Silver LT and Chappell BW (1988) The Penisular Ranges Batholiths: an insight into the evolution of the Cordilleran batholiths of southwestern North America. *Transactions of the Royal Society of Edinburgh: Earth Science*, **79**, 105-121.

Silverstone MD *et al*. (2006) Formation and evolution of planetary systems (FEPS): Primordial warm dust evolution from 3 to 30 Myr around sun-like stars*. Astrophysical Journal* **639**, 1138-1146.

Singleton DL and Cvetanovic RJ (1988) Evaluated chemical kinetic data for the reactions of atomic oxygen O(^{3}P) with sulfur-containing compounds. *Journal of Physical and Chemical Reference Data* **17**(4): 1377-1437.

Skumanich A (1972) Time Scales For Ca Ii Emission Decay, Rotational Braking, And Lithium Depletion. *Astrophysical Journal* **171**, 565-567.

Sleep NH and Windley BF (1982) Archean Plate-Tectonics - Constraints And Inferences. *Journal Of Geology*, **90**, 363-379.

Sleep NH and Zahnle K (1998) Refugia from asteroid impacts on early Mars and the early Earth. *Journal Of Geophysical Research-Planets* **103**(E12): 28529-28544.

Sleep NH and Zahnle KJ (2001) Carbon dioxide cycling and implications for climate on ancient Earth. *Journal of Geophysical Research*, **106**, 1373-1399.

Sleep NH (2005a) Dioxygen over Geologic Time. In: *Metal Ions in Biological Systems, Volume 43 - Biogeochemical Cycles of Elements* (ed. Sigel A, Sigel H, Sigel R). Taylor & Francis, Boca Raton, FL, pp. 49-73.

Sleep NH (2005b) Evolution of the continental lithosphere. *Annual Review Of Earth And Planetary Sciences*, **33**, 369-393.

Sleep NH and Hessler AM (2006) Weathering of quartz as an Archean climatic indicator. *Earth And Planetary Science Letters*, **241**, 594-602.

Sleep NH and Bird DK (2007) Niches of the Pre-photosynthetic Biosphere and Geologic Preservation of Earth's Earliest Ecology. *Geobiology*, **5** (2) 101-117.

Slinn WGN *et al.* (1978) Some aspects of the transfer of atmospheric trace constituents past the air-sea interface. *Atmospheric Environment* **12**: 2055-2087.

Soderblom DR, Stauffer JR, Hudon JD, Jones BF (1993a) Rotation and Chromospheric Emission amoung F-dwarfs, G-dwarfs, and K-dwarfs of the Pleiades. *Astrophysical Journal Supplement Series* **85**, 315-346.

Soderblom DR, Stauffer JR, Hudon JD, Jones BF (1993b) Angular-Momentum Among Zero-Age Main-Sequence Solar-Type Stars. *Astrophysical Journal* **409**, 624-634.

Spencer JW (1971) Fourier series representation of the position of the Sun. *Search* **2**, 172.

Stachnik RA and Molina MJ (1987) Kinetics of the reactions of SH radicals with NO_2 And O_2. *Journal of Physical Chemistry* **91**(17): 4603-4606.

Summons JR, Jahnke LL, Hope JM, Logan GA (1999) 2-Methylhopanoids as biomarkers for cyanobacterial oxygenic photosynthesis *Nature* **400**: 554-557.

Summons RE and Brocks JJ (2004) Sedimentary Hydrocarbons, Biomarkers for Early Life. In: *Treatise on Geochemistry - Volume 8: Biogeochemistry* (ed. Schlesinger WH). Elsevier, Amsterdam, pp. 63-115.

Summons RE, Bradley AS, Jahnke LL, Waldbauer JR (2006) Steroids, triterpenoids and molecular oxygen. *Philosophical Transactions Of The Royal Society B-Biological Sciences*, **361**, 951-968.

Sun F *et al.* (2001) Reactions of NH_2 with NO_2 and of OH with NH_2O. *Journal of Physical Chemistry A* **105**(25): 6121-6128.

Swain MR *et al.* (2008) The presence of methane in the atmosphere of an extrasolar planet. *Nature* **452**(7185): 329-331.

Tang EPY, Tremblay R, Vincent WF (1997) Cyanobacterial dominance of polar freshwater ecosystems: Are high-latitude mat-formers adapted to low temperature? *Journal Of Phycology*, **33**, 171-181.

Taylor SR and McLennan SM (1995) The geochemical evolution of continental crust. *Reviews in Geophysics*, **33**, 241-265.

Teske A, Dhillon A, Sogin ML (2003) Genomic markers of ancient anaerobic microbial pathways: Sulfate reduction, methanogenesis, and methane oxidation. *Biological Bulletin*, **204**, 186-191.

Thiemens MH and Heidenreich JE (1983) The mass-independent fractionation of oxygen - a novel isotope effect and its possible cosmochemical implications. *Science* **219**(4588): 1073-1075.

Thiemens MH (2006) History and applications of mass-independent isotope effects. *Annual Review of Earth and Planetary Sciences* **34**: 217-262.

Thuillier G *et al.* (2003) The solar spectral irradiance from 200 to 2400 nm as measured by the SOLSPEC spectrometer from the ATLAS and EURECA missions. *Solar Physics* **214**, 1-22.

Thuillier G *et al.* Solar irradiance reference spectra for two solar active levels. *in Solar variability and its effects on climate*. American Geophysical Union, Washington, D.C., 2004, pp. 256-261.

Tian F, Toon OB, Pavlov AA, De Sterck H (2005) A Hydrogen-Rich Early Earth Atmosphere. *Science*, **308**, 1014-1017.

Tinetti G *et al.* (2007) Water vapour in the atmosphere of a transiting extrasolar planet. *Nature* **448**(7150): 169-171.

Toon OB and Farlow NH (1981) Particles above the tropopause - measurements and models of stratospheric aerosols, meteoric debris, nacreous clouds, and noctilucent clouds. *Annual Review of Earth and Planetary Sciences* **9**: 19-58.

Toon OB, Kasting JF, Turco RP, Liu MS (1987) The sulfur cycle in the marine atmosphere. *Journal of Geophysical Research* **92**, 943– 963.

Toon OB *et al.* (1989) Rapid calculation of radiative heating rates and photodissociation rates in inhomogeneous multiple scattering atmospheres. *Journal of Geophysical Research* **94**: 16,287-16,301.

Troen I and Mahrt L (1986). A simple-model of the atmospheric boundary-layer - sensitivity to surface evaporation. *Boundary-Layer Meteorology* **37**(1-2): 129-148.

Tsang W and Hampson RF (1986) Chemical kinetic database for combustion chemistry .1. Methane and related compounds. *Journal of Physical and Chemical Reference Data* **15**(3): 1087-1279.

Tsang W (1989) Rate constants for the decomposition and formation of simple alkanes over extended temperature and pressure ranges. *Combustion and Flame* **78**(1): 71-86.

Tsang W and Herron JT (1991) Chemical kinetic data-base for propellant combustion .1. Reactions involving NO, NO_2, HNO, HNO_2, HCN and N_2O. *Journal of Physical and Chemical Reference Data* **20**(4): 609-663.

Turnbull MC *et al.* (2006) Spectrum of a habitable world: Earthshine in the near-infrared. *Astrophysical Journal* **644**(1): 551-559.

Tyrell T (1999) The relative influences of nitrogen and phosphorus on oceanic primary production. *Nature*, **400**, 525-531.

Ueno Y *et al.* (2006) Evidence from fluid inclusions for microbial methanogenesis in the early Archaean era. *Nature* **440**(7083): 516-519.

Valentine DL (2002) Biogeochemistry and microbial ecology of methane oxidation in anoxic environments: a review. *Antonie Van Leeuwenhoek*, **81**, 271-282.

Van Cappellen P and Ingall ED (1996) Redox stabilization of the atmosphere and oceans by phosphorus-limited marine production. *Science* **271**: 493-496.

Van Cappellen P and Wang YF (1996) Cycling of iron and manganese in surface sediments: A general theory for the coupled transport and reaction of carbon, oxygen, nitrogen, sulfur, iron, and manganese. *American Journal of Science* **296**, 197-243.

Vernazza JE, Avrett EH, Loeser R (1981) Structure of the solar chromosphere .3. Models of the EUV brightness components of the quiet Sun. *Astrophysical Journal* **45**, 635-725.

Wagner AF and Bowman JM (1987) The addition and dissociation reaction H + CO reversible HCO .1. Theoretical RRKM studies. *Journal of Physical Chemistry* **91**(20): 5314-5324.

Wakeham SG *et al.* (2004) Archaeal lipids and anaerobic oxidation of methane in euxinic water columns: A comparative study of the Black Sea and Cariaco Basin. *Chemical Geology* **205**: 427-442.

Walkauskas LP and Kaufman F (1975) Gas phase hydrogen atom recombination. *Symp. Int. Combust. Proc.* **15**: 691.

Walker JCG (1977) *Evolution of the Atmosphere*. Macmillan, New York, pp.318.

Walker JCG (1980) The oxygen cycle. *The Natural Environment and the Biogeochemical Cycles*. O. Hutzinger. Berlin, Springer-Verlag**:** 87-104.

Walker JCG, Hays PB, Kasting JF (1981) A negative feedback mechanism for the long-term stabilization of Earth's surface temperature. *Journal of Geophysical Research*, **86**, 9776-9782.

Walker JCG, Klein C, Schidlowski M, Schopf JW, Stevenson DJ, Walter MR (1983) Environmental evolution of the Archean-Early Proterozoic Earth. In: *Earth's Earliest Biosphere* (ed. Schopf JW). Princeton University Press, Princeton, New Jersey, pp. 260-290

Walker JCG and Brimblecombe P (1985) Iron and sulfur in the pre-biologic ocean. *Precambrian Research* **28**, 205–222.

Walker JCG (1987) Was the Archaean biosphere upside-down? *Nature* **329**, 710–712.

Walker JCG (1990a) *Numerical Adventures with Geochemical Cycles*. Oxford University Press, pp.210.

Walker JCG (1990b) Origin of an Inhabited Planet. In: *Origin of the Earth* (ed. Newsom HE, Jones JH). Oxford University Press, New York, pp. 371-375.

Wallmann K, Drews M, Aloisi G, Bohrmann G (2006) Methane discharge into the Black Sea and the global ocean via fluid flow through submarine mud volcanoes. *Earth and Planetary Science Letters* **248**, 545-560.

Walter FM and Barry DC (1991) Pre- and main-sequence evolution of solar activity. In: *The Sun in Time* (ed. Sonett CP, Giampapa MS, Matthews MS). University of Arizona Press, Tucson, AZ, pp. 633-657.

Walter M (1995) Biogeochemistry - Fecal pellets in world events. *Nature* **376**: 16-17.

Wang BS *et al.* (2003) Experimental and theoretical investigations on the methyl-methyl recombination reaction. *Journal of Physical Chemistry A* **107**(51): 11414-11426.

Warneck P (2000) *Chemistry of the natural atmosphere* Academic Press, New York.

Warren SG, Brandt RE, Grenfell TC, McKay CP (2002) Snowball Earth: Ice thickness on the tropical ocean. *Journal Of Geophysical Research-Oceans*, **107**.

Watson A, Lovelock JE, Margulis L (1978) Methanogenesis, fires and the regulation of atmospheric oxygen. *Biosystems*, **10**, 293-298.

Watson AJ, Donahue TM, Walker JCG (1981) The dynamics of a rapidly escaping atmosphere: applications to the evolution of Earth and Venus. *Icarus*, **48**, 150-166.

Watson RT, Rodhe H, Oeschger H, Siegenthaler U (1990) Greenhouse gases and aerosols. In: *Climate Change: The IPCC Scientific Assessment* (ed. Houghton JT, Jenkins GJ, Ephraums JJ). Cambridge University Press, Cambridge, pp. 1-40.

Wedepohl KH (1995) The Composition Of The Continental-Crust. *Geochimica et Cosmochimica Acta*, **59**, 1217-1232.

Whiticar MJ (2002) Diagenetic relationships of methanogenesis, nutrients, acoustic turbidity, pockmarks and freshwater seepages in Eckernforde Bay. *Marine Geology* **182**, 29-53.

Wilde P, Lyons TW and Quinby-Hunt MS (2004) Organic carbon proxies in black shales: Molybdenum. *Chemical Geology* **206**: 167-176.

Wildman RA *et al.* (2004) Burning of forest materials under late Paleozoic high atmospheric oxygen levels. *Geology*, 457-460.

Williamson MA and Rimstidt JD (1994) The kinetics and electrochemical rate-determining step of aqueous pyrite oxidation. *Geochimica et Cosmochimica Acta* **58**, 5443-5454.

Wille M *et al.* (2007) Evidence for a gradual rise of oxygen between 2.6 and 2.5 Ga from Mo isotopes and Re-PGE signatures in shales. *Geochimica et Cosmochimica Acta* **71**(10): 2417-2435.

Wilson JF *et al.* (1978) Granite-greenstone terrains of Rhodesian Archaean craton. *Nature* **271**(5640): 23-27.

Wood BE *et al.* (2002) Measured mass loss rates of solar-like stars as a function of age and activity. *Astrophysical Journal* **574**: 412-425.

Wuebbles DJ and Hayhoe K (2002) Atmospheric methane and global change. *Earth Science Reviews* **57**: 177-210.

Yang WB and Holland HD (2003) The Hekpoort paleosol profile in Strata 1 at Gaborone, Botswana: Soil formation during the great oxidation event. *American Journal Of Science*, **303**, 187-220.

Young GM, Long DGF, Fedo CM, Nesbitt HW (2001) Paleoproterozoic Huronian basin: product of a Wilson cycle punctuated by glaciations and a meteorite impact. *Sedimentary Geology*, **141**, 233-254.

Young ED *et al.* (2008) Mass-independent oxygen isotope variation in the solar nebula. *Oxygen in the Solar System*. **68:** 187-218.

Yung YL (1976) A numerical method for calculating the mean intensity in an inhomogeneous Rayleigh scattering atmosphere. *Journal of Quantitative Spectroscopy & Radiative Transfer* **16**: 755-761.

Yung YL and DeMore WB (1999) *Photochemistry of Planetary Atmospheres* Oxford University Press, New York.

Zahnle KJ and Walker JCG (1982) The evolution of solar ultraviolet luminosity. *Reviews of Geophysics and Space Physics* **20**, 280-292.

Zahnle KJ (1986) Photochemistry of methane and the formation of hydrocyanic acid (HCN) in the Earth's early atmosphere. *Journal of Geophysical Research*, **91**, 2819-2834.

Zahnle KJ and Sleep NH (2002) Carbon dioxide cycling through the mantle and implications for the climate of ancient Earth. In *The Early Earth: Physical Chemical and Biological Development* (eds Fowler CM, Ebinger CJ, Hawkesworth CJ). Geological Society of London Special Publication, 199. Geological Society of London, London, UK, pp. 231–257.

Zahnle KJ, Claire MW, Catling DC (2006) The loss of mass-independent fractionation in sulfur due to a Paleoproterozoic collapse of atmospheric methane. *Geobiology* **4** 271-283. (Chapter 4)

Zahnle KJ (2008) Atmospheric chemistry - Her dark materials. *Nature* **454**(7200): 41-42.

Appendix A The photochemical code

The details of the photochemical model used in Chapters 4, 6, and 7 have been described in the literature in a piecemeal fashion over the last 30 years (e.g. Kasting, 1979; Kasting *et al.*, 1980; Kasting, 1988; Kasting *et al.,* 1989; Kasting, 1990; Pavlov *et al.,* 2001; Zahnle *et al.,* 2006). While it would be theoretically possible for a motivated individual to piece together a reasonably complete understanding of the various modules in the code, it would be effectively impossible to recreate the exact code that was used in any one effort. In this Appendix, we will not completely solve this problem, but will compile brief explanations and literature citations for all components of the code in one place. We will elaborate where we have made improvements in the course of this dissertation, and highlight regions which are uncertain or could be improved.

This appendix starts with an expanded explanation of the coupled chemistry/transport equations used in the model. We discuss how these equations are cast onto the vertical grid and how we implement the upper and lower boundary conditions. We continue by addressing general model parameters and describe a model timestep, discussing the photolysis, rainout, and particle routines. We describe changes made in the lightning subroutine which enabled greater model stability, and conclude with a list of high-priority areas for improvement.

A.1 Finite differencing the model equations

As described in Chapter 4 and 7, we solve the time-dependent coupled transport/chemistry equation:

$$\frac{\partial f_i}{\partial t} = \frac{P_i}{N} - L_i f_i - \frac{1}{N}\frac{\partial}{\partial z}\left(b_{ia} f_i (H_a^{-1} - H_i^{-1})\right) + \frac{1}{N}\frac{\partial}{\partial z}\left((b_{ia} + KN)\frac{\partial f_i}{\partial z}\right) + \frac{1}{N}\frac{\partial}{\partial z}(v_{FALL} N_i) \qquad (A.1)$$

where f_i is the mixing ratio of the species *i*, P is the chemical production (molecules cm^3 s^{-1}), L is the chemical loss (molecules s^{-1}), N is atmospheric density (molecules cm^{-3}), b_{ia} is the binary diffusion coefficient(Banks, 1973) between *i* and the background atmosphere *a*; H_a and H_i are the scale heights of the background atmosphere and of species *i*; and *K* is the eddy diffusion coefficient. v_{FALL} is a (positive downwards) fall velocity which applies to particulate species only, as discussed further below. Molecular diffusion (the terms involving b_{ia}) is only implemented for H and H_2 and v_{FALL} = 0 for non-particle species, so for most species in our code the vertical transport is by eddy diffusion only and Equation (A.1) reduces to:

$$\frac{\partial f_i}{\partial t} = \frac{P_i}{N} - L_i f_i + \frac{1}{N}\frac{\partial}{\partial z}\left((KN)\frac{\partial f_i}{\partial z} \right) \qquad \text{(A.2)}$$

Eddy diffusion (and the eddy diffusion coefficient) is an attempt to reduce the complicated effects of atmospheric turbulence and mixing into a single parameter. Its use in atmospheric modeling is widespread, and is the primary method of approximating the effect of turbulent flows (inherently a three-dimensional phenomenon) on a one-dimensional grids. Eddy diffusion coefficients are primarily determined from empirical observation, and have been measured for the present atmosphere via observation of ^{14}C tracers created from the atomic bomb explosions in the 1950's and 60's (Massie & Hunten, 1981). Varying the eddy diffusion profile does effect the vertical structure of the atmosphere (Kasting, 1979; Kasting, 1990), but it has a negligible effect on the redox state of the atmosphere (Kasting, 1979), so we keep it fixed as described in section 4.2.1 in all our investigations. Jim Kasting's dissertation discusses the effect of uncertainty in the eddy diffusion profile has on the photochemistry, but a more complete exploration of the uncertainties in atmospheres of varying composition would be worthwhile. Estimated profiles could be tested against theoretical parameterizations of eddy diffusion such as those of Troen & Mahrt (1986). With the further advance of a coupled climate calculation, the tropopause could be self-consistently defined and first-order changes to eddy diffusion could be calculated for our various atmospheres.

For simplicity in our following presentation*, we ignore the molecular diffusion and advection terms which are a portion of equation (A.1), focusing on equation (A.2) which is the primary equation solved for all species other than H or H_2 and particles. The photochemical model uses a fixed step-size vertical grid illustrated as Figure A-1.

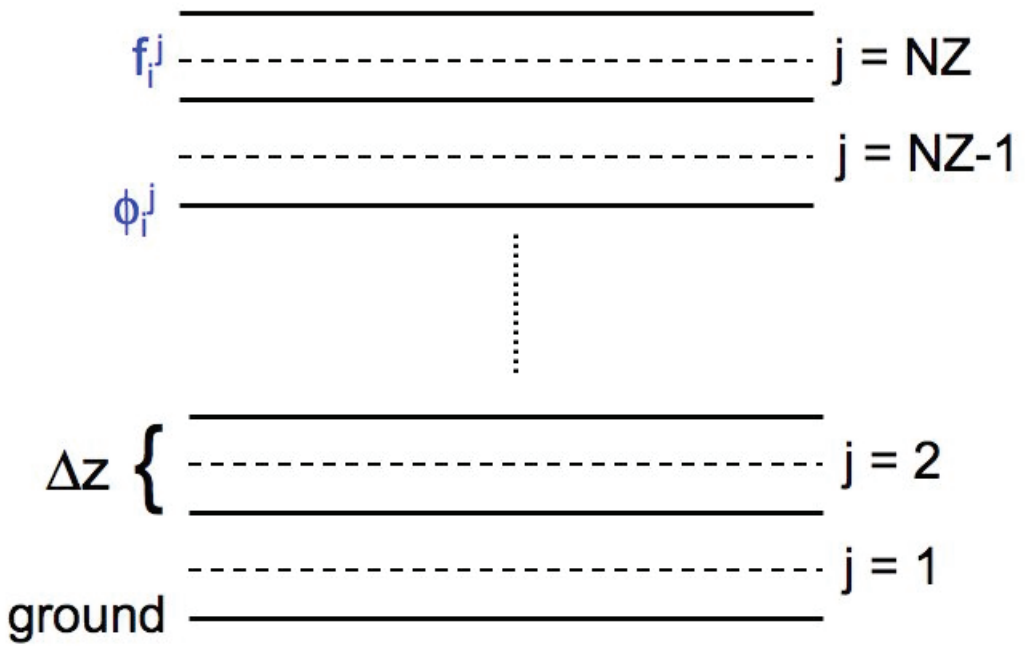

Figure A-1 The vertical grid of the photochemical model

Atmospheric layers are labeled with the index j which runs from 1 to NZ, where NZ is the number of model heights (80 in Chapter 4, 640 in Chapter 6 and 7). Mixing ratios f_i^j for a species i are defined at the midpoints of the layers, while the fluxes ϕ_i^j are defined on the layer boundaries. The layer size is Δz and was 1km in the models of Chapter 4, and 0.125 km in Chapters 6 and 7.

The spatial derivatives $\partial f_i/\partial z$ are approximated using second-order centered finite differences:

$$\frac{\partial f_i^{j+1/2}}{\partial z} = \frac{f_i^{j+1} - f_i^j}{\Delta z} \qquad \text{(A.3)}$$

* This description of the casting of the model equations onto the vertical grid is adapted from a set of handwritten notes kindly provided to me by Jim Kasting.

Equation (A.2) is cast onto our grid in finite difference form as:

$$\frac{\partial f_i^j}{\partial t} = \frac{1}{N^j(\Delta z)^2}\left[(KN)^{j+1/2}(f_i^{j+1} - f_i^j) - (KN)^{j-1/2}(f_i^j - f_i^{j-1})\right] + \frac{P_i^j}{N^j} - L_i^j f_i^j \qquad \text{(A.4)}$$

K and N have subscripts of j ±1/2 to indicate that the quantities are computed at the layer boundaries. Equation (A.4) is valid only at the interior points j=2,…,NZ-1 because f_i^0 and f_i^{NZ+1} are not defined. Using the definition of flux (Equation (4.2) without the molecular diffusion terms)

$$\phi = -KN\frac{\partial f}{\partial z} \qquad \text{(A.5)}$$

we can rewrite equation (A.4) as:

$$\frac{\partial f_i^j}{\partial t} = \frac{-1}{N^j \Delta z}\left[\phi_i^{j+1/2} - \phi_i^{j-1/2}\right] + \frac{P_i^j}{N^j} - L_i^j f_i^j \qquad \text{(A.6)}$$

Equation (A.6) is defined everywhere on the vertical grid provided that fluxes across the upper and lower boundaries are specified.

A.1.1 Lower Boundary Conditions

We simplify equation (A.6) by replacing j with 1, and dropping the subscript i for each species to obtain:

$$\frac{\partial f^1}{\partial t} = \frac{1}{N^1 \Delta z}\left[(KN)^{1+1/2}\left(\frac{f^2 - f^1}{\Delta z}\right) + \phi^{GROUND}\right] + \frac{P^1}{N^1} - L^1 f^1 \qquad \text{(A.7)}$$

where ϕ_{GROUND} is the (positive upward) flux across the lower boundary. There are three different lower boundary conditions (LBCs) that are implemented in the photochemical model: constant mixing ratio, constant deposition velocity, and constant flux.

Constant mixing ratio LBCs are the least physical, and are used primarily for experimenter convenience. They are implemented by setting the right hand side of equation (A.7) to 0. Constant mixing ratio LBCs were used for O_2 and CH_4 in Chapters 4 and 6, and were not used in Chapter 7. N_2 and CO_2 are treated as special cases and are effectively "inert" in our model – they are both held fixed at constant mixing ratios at all altitudes. This simplification corresponds to the physical assumption that any photochemical destruction or gain of CO_2 or N_2 is balanced instantaneously by fluxes across the lower boundary to maintain the fixed mixing ratios at all heights. Both of these gases feature large fluxes into and out of the modern atmosphere, but are effectively well mixed. If the N_2 reservoir has remained as large as it currently is through Earth history, this is a fine assumption. It is harder to justify for CO_2, as CO_2 concentrations have varied through Earth history in response to temperature changes (i.e. the carbonate silicate cycle discussed in Chapter 2). In addition, CO_2 is strongly photolyzed in the upper atmosphere. In this context, it would be worthwhile to attempt computing CO_2 concentrations in the main matrix in order to examine the effect of the fixed mixing ratio assumption.

Dry deposition velocities are used to represent the net effect of all possible interactions of gas with the planetary surface in the absence of precipitation. Complex microphysical processes such as atmospheric turbulence, diffusion across the air/water interface, and surface uptake are combined into one parameter. Deposition velocities are typically estimated for individual processes and added together as "resistances in series," in which one component (often the diffusion across the ocean/air interface) typically dominates the overall surface sink for the molecule. The deposition velocities used in this dissertation are given in Table A-1 below. The choices of deposition velocities are attributed to Slinn *et al.* (1978) and Lee & Schwartz (1981), except for H_2 and CO which were taken from Kharecha *et al.* (2005). The model is not very sensitive to changes in the deposition velocities of minor species. In computing the models in Chapter 4, we

examined the effect of changing the LBCs for CO and H_2, and found the model to be sensitive to the deposition velocities of these more abundant gases only in conditions of very low biospheric flux (see section 4.2.5.)

Deposition velocities are implemented by using

$$\phi^{GROUND} = -N_j^1 \times v_{DEP} \quad \text{(A.8)}$$

in equation (A.7) where N_j^1 is the species number density in the lowest layer, and v_{DEP} for the given species are given in Table A-1. The negative sign in equation (A.8) accounts for the fact that the flux is downward from the lowest layer of the atmosphere to the ground.

Table A-1 Deposition Velocities

All deposition velocities are in cm s^{-1}

Deposition Velocity	Species
1	O, H, OH, HO_2, HCO, CH_3, HNO, SO_2, H_2SO_4, HSO
0.2	H_2O_2, H_2CO, SO_4aer, S_8aer, HNO_3
0	H_2O, C_2H_6, HS, S, SO, S_2, S_3, S_4, S_8, SO_3, OCS, N
2.4×10^{-4}	H_2
1.2×10^{-4}	CO
3×10^{-4}	NO
3×10^{-3}	NO_2
0.02	H_2S
0.07	O_3

Constant flux LBCs are implemented by specifying a positive value of ϕ^{GROUND} in equation (A.7). All of the models described in this dissertation use constant flux

boundary conditions for H_2, CO, and H_2S, as quantified in Chapter 4. O_2 and CH_4 were specified by constant flux in Chapter 7. SO_2 has strong fluxes into and out of the atmosphere, so both constant flux and constant deposition velocity LBCs are implemented. Deposition velocities are specified in the lowest layer using equations (A.7) and (A.8), so our constant fluxes are distributed equally over 0 - 20 km which approximates the effects of volcanic plumes. For experiments described in section 4.2.5, H_2 and CO fluxes were distributed in the same manner using the deposition velocities cited in Table A-1.

A.1.2 Upper Boundary Conditions

Replacing j with NZ in equation (A.6) yields:

$$\frac{\partial f^{NZ}}{\partial t} = \frac{-1}{N^{NZ}\Delta z}\left[\phi^{TOP} + (KN)^{NZ-1/2}\left(\frac{f^{NZ} - f^{NZ-1}}{\Delta z}\right)\right] + \frac{P^{NZ}}{N^{NZ}} - L^{NZ} f^{NZ} \qquad \text{(A.9)}$$

where ϕ^{TOP} is the upward flux at the top of the atmosphere. In all cases except for N, H, H_2, ϕ^{TOP} is assumed equal to 0, which enforces conditions of diffusive equilibrium (i.e. anything that goes up must come down). The other options for the upper boundary conditions are a constant downward flux or a constant upward effusion velocity. A constant downward flux of -10^8 molecules cm^{-2} s^{-1} is implemented for atomic N, in order to account for N_2 photolysis occurring above the upper boundary. In practice the atomic N concentrations in the upper atmosphere do not have much bearing on photochemistry, but it would be more correct to approximate the downward flux of N from the computed N_2 photolysis rate in the upper layer of the atmosphere than assume this constant flux. Another worthwhile addition would be to compute the photolysis of CO_2 above the upper boundary, with return fluxes of CO and O, as discussed by Pavlov *et al.* (2001).

Effusion velocities (v_{EFF}) are defined in a similar numerical fashion to the deposition velocities of equation (A.8), so that ϕ^{TOP} = N v_{EFF} represents an upward flux. We compute effusion velocities for H and H_2 from the molecular diffusion terms used in (A.1):

$$v_{EFF} = \frac{b_{ia}}{N^{NZ}}\left(\frac{1}{H_a} - \frac{1}{H_i}\right) \tag{A.10}$$

where the binary diffusion coefficients for H and H_2 diffusing through N_2 are computed from fits to laboratory data (Marrero & Mason, 1972).

$$\begin{aligned} b_{H,N_2} &= 2.7x10^{19}(T / 200)^{0.75} \\ b_{H_2,N_2} &= 1.4x10^{19}(T / 200)^{0.75} \end{aligned} \tag{A.11}$$

In formulating the effusion velocities in this manner, we are assuming that diffusion of hydrogen to the upper atmosphere is the rate-limiting step in the escape of hydrogen, as discussed in section 3.3.3.

A.2 General model parameters

The model computes the interactions of 46 atoms and molecules undergoing the 182 photochemical reactions listed in Table 6-2. Transport and chemistry (i.e. equation (A.1)) are solved for the following 35 “long-lived” species: O, O_2, H_2O, H, OH, HO_2, H_2O_2, H_2, CO, HCO, H_2CO, CH_4, CH_3, C_2H_6, NO, NO_2, HNO, H_2S, HS, S, SO, SO_2, H_2SO_4, HSO, S_2, SO_4AER, S_4, S_8, SO_3, OCS, S_8AER, S_3, O_3, HNO_3, and N.

For the models in this dissertation, nine species (HNO_2, $O(^1D)$, $^1CH_2$, $^3CH_2$, C_2H_5, $SO_2(^1B)$, $SO_2(^3B)$, HSO_3, and OCS_2) are solved in “photochemical equilibrium” at each height, ignoring the effects of transport. In this approximation, the left hand side and the third term on the right hand side of equation (A.2) are set to 0, which allows for specification of the mixing ratios as:

$$f_i = \frac{1}{N}\frac{P_i}{L_i} \tag{A.12}$$

This method of solution only works for species with no non-linearities (i.e. S_4 reacting with itself to form S_8), and care must be taken to compute them in the proper order (i.e. if species A reacts to form species B, then A must be computed first). The photochemical equilibrium approximation (equation (A.12)) is used only for "short-lived" species with linear chemistry, and is invoked primarily to speed up the computation by removing these species from the large matrix inversions described in section 7.2.1. The inclusion of short-lived and long-lived species in the model is somewhat of a historic artifact from the days of slower computers. Previous versions of the code had approximately half the species identified as "long-lived" and half as "short-lived," and the short-lived species were solved with multiple iterations of a Newton-Raphson solver. The Newton-Raphson method could handle non-linear reactions, and was used to speed up the code by inverting multiple small matrices rather than one huge matrix, but it is no longer used in the present model. Returning to such a scheme would undoubtedly speed up the modern version of the code, but would require verification in each experiment that the model perturbations haven't made any species long-lived or more abundant. Given the increase in speed and memory of modern computers, we went the other way and put most species in the long-lived category, reserving the short-lived loop for linear photochemical equilibrium species that can be computed without iteration.

A.3 A photochemical model run walkthrough

In this section, we describe the general progression of our photochemical model.

A.3.1 Initial setup

Our vertical grid is illustrated in Figure A-1. On this grid, we specify a fixed temperature profile $T(z) = 290 – 6.5z – 0.25\ z^2$ in the troposphere and fixed at 191.25 K above. The fixed stratospheric temperature profile is reasonable for an ozone-free atmosphere, but is not correct for our oxic models, which should feature a stratospheric temperature inversion due to the presence of ozone. The tropopause is fixed at 11 km, which marks the boundary between the well-mixed troposphere and the stratosphere via a kink in the eddy diffusion profile, and also marks the point above which H_2O acts as a non-condensable gas. Photochemistry isn't overly sensitive to temperature for small perturbations around modern conditions, but the code could be enhanced here without too much work. A temperature structure could be computed for the initial conditions from a radiative-convective climate code. In a time-dependent model, the climate could be periodically recomputed during a computation. The tropopause height could be computed self-consistently from the temperature structure and water vapor profile, rather than being fixed at 11km independent of conditions.

The saturation vapor pressure of water is computed from Magnus' equation, as described in Appendix A of Kasting (1988). The tropospheric H_2O concentrations are then set by following a Manabe-Wetherald relative humidity profile (Manabe & Wetherald, 1967). The complete cycle of condensation and evaporation of H_2O is not computed directly. Instead, we keep the H_2O mixing ratio fixed to the relative humidity profile. This numerical simplification translates into the physical assumption of an "infinite ocean," from which water evaporates to balance the effect of precipitation. Another way of stating this is that while our model explicitly conserves the H to O ratio, it does not attempt to conserve H_2O.

The model computes the total atmospheric number density assuming hydrostatic equilibrium and a 1 bar atmosphere. The N_2 pressure is set as 1 bar minus the pressure of CO_2 and O_2. Our Archean atmospheres therefore have N_2 densities of approximately 0.99 bar, where a uniformitarian argument would lead to the prediction of 0.72 bar of N_2 in the Archean. While most of the pressure dependent reaction rates won't change dramatically as a result of this drop from 1 bar to 0.72 bar, changing the code to have a

more flexible definition of pressure would be a worthwhile improvement to make. An updated code could be used to investigate possible pressure variations through Earth history, and also to investigate more and less dense atmospheres of extrasolar terrestrial planets.

A.3.1.1 Lightning

Lightning production of NO and CO are included as described in Appendix A of Kasting (1979), and elaborated on in Kasting (1990). We describe this parameterization in some detail because before embarking on the work described in Chapter 4, we fixed a significant error in the lightning parameterization which dramatically enhanced the numerical stability of our model. Nitrogen oxides are very important in understanding the behavior of ozone in the modern stratosphere (IPCC, 2007). The primary source of (non-anthropogenic) nitrogen oxides is lightning. NO is created from N_2 and O_2 in the high temperature electrical discharge of lightning, where temperatures quickly reach approximately 30000 K before the compression shocks expand and incorporate cold surrounding air. This process occurs in seconds, but this is fast enough for equilibrium thermodynamics to occur at these temperatures which allows equilibration in the following reactions among major species:

$$\begin{aligned} 1/2\ N_2 + 1/2\ O_2 &\rightleftharpoons NO \\ CO + 1/2\ O_2 &\rightleftharpoons CO_2 \\ H_2 + 1/2\ O_2 &\rightleftharpoons H_2O \\ 1/2\ O_2 &\rightleftharpoons O \end{aligned} \qquad \text{(A.13)}$$

Kasting (1979) shows that a simple thermodynamic calculation assuming a single freeze-out temperature provides very similar results to the more complicated physical models of Chameides (e.g. Chameides & Walker, 1981; Giorgi & Chameides, 1985). Both models predict that the relative NO production rates are a function of changing oxygen levels, dropping as the square root of the O_2 concentration until a pO_2 of 10^{-3} PAL, where they stabilizes at 5% due to the production of O_2 from CO_2 equilibrating with

N_2 to form NO. NO production rates are scaled in this manner against the modern production rates of NO (10^9 molecules cm^{-2} s^{-1}).

Prior versions of this code only accounted for the production of NO and O_2 without accounting for the production of CO, H_2 and O. More importantly, the corresponding losses were not accounted for in the model. For example, while the production of NO was computed in the first reaction of equation (A.13), the corresponding loss of O_2 was not. We updated the chemical accounting in the model such that production of NO was balanced by loss of ½ O_2, and so on for each equilibrium reaction in (A.13). Neglecting both sides of the equations in (A.13) led directly to problems conserving redox in model. Prior to making the changes described above, we isolated the redox problem in the lightning subroutine by running 5 photochemical models changing only the production rate of NO. For each of these models, we observed the effect on the total redox conservation by summing up the total fluxes of oxidants and reductants across both model boundaries. Table A-2 shows how problems with redox conservation were directly proportional to the (user-specified) NO production rate. In effect, NO was being created from nothing in the troposphere.

Table A-2 Redox conservation properties of the original lightning subroutine

NO production rate and redox conservation are given in units of molecules cm^{-2} s^{-1}. Redox conservation was directly proportional to the NO production rate before we updated the chemistry to account for the chemical losses during lightning chemistry

NO production	Redox conservation
1×10^9	2.70×10^8
1×10^6	2.91×10^5
1×10^5	2.90×10^4
1×10^4	2.85×10^3
0	6.09×10^1

Once complete accounting for chemical production and loss is accounted for in the lightning subroutine, redox conservation in the model remains steady at less than ± 1 x 10^2 molecules cm^{-2} s^{-1} in nearly all models run. When compared to typical oxygen fluxes on the order of 10^{11}-10^{12} molecules cm^{-2} s^{-1}, the model conserves redox to approximately one part per billion. Given all the complicated fluxes within the earth system (e.g. see Chapter 3), it is perhaps unreasonable to expect that the real atmosphere conserves redox to this level of accuracy. In the context of our model atmosphere, however, "redox conservation" is better seen as a measure of internal numerical self-consistency. This numerical metric is formed by adding up the total amount of oxidants and reductants entering and exiting the atmosphere, with the balance being whatever is created or destroyed within the model grid. The chemistry solver conserves mass explicitly, so the problems with redox conservation are seen to be entirely the result of creating mass in the form of NO from lightning bolts.

A.3.2 A model timestep

A.3.2.1 Photolysis, radiative transfer, and rainout

Photolysis and rainout rates are computed on the first timestep, after 100 seconds, and then every subsequent three timesteps. We updated the photolysis routine between the work described in Chapters 4 and 6, but the updates were only to implement more modern coding standards, and to allow flexibility in future changes. The numerical output of the code before and after these changes are identical. We therefore describe the current implementation of the photolysis routine.

The primary changes made to the photolysis routine allow for all species cross sections to be temperature and pressure (and therefore height) dependent in both the raditative transfer and photolysis schemes, across all wavelengths. Species cross sections of any resolution are read in and interpolated to a user specified wavelength grid. For consistency with prior results, we retain the wavelength grid and species cross section that the model has used for many years (from the 1983 JPL recommendation), but have

made it trivial to include a new species in the photolysis routine. Multiple improvements to cross section measurements have been made over the years which have not been implemented in this model, including the temperature-dependent CO_2 cross section, which is known to be very important for Martian photochemistry (Anbar *et al.*, 1993; Nair *et al.*, 1994). This is a high priority area for improvement in the model.

The code loops over each wavelength while computing photolysis rates. For each wavelength the pure absorption optical depth is compared to the Rayleigh scattering optical depth at 20 km. If the absorption optical depth is five times greater than the scattering optical depth, the optical path is computed analytically from the absorbing species. Otherwise (and for most wavelengths longward of the near UV), radiative transfer is computed using the multiple scattering technique of Yung (1976), including the effects of absorption and Rayleigh scattering. Pavlov *et al.* (2001) updated the radiative transfer scheme to use a δ 2-stream of Toon *et al.* (1989) which is more flexible in allowing for particle absorption in specific atmospheric layers.

Photolysis rates are then computed using equation (1.5). The solar zenith angle is held fixed at 50 degrees and the surface albedo is 0.25. The solar flux is computed as described in Chapter 8 for 2.5 Ga, and is interpolated to the wavelength grid. The photolysis rates computed in this manner are multiplied by a factor of 0.5 to account for diurnal cycling. It would be interesting to compute the effect of the diurnal cycling approximation against a time-dependent model with variable solar zenith angle approximating the course of an entire Archean day. It is possible that some of the O_2 dependent photolysis rates maybe be significantly different from one half of the noon rates, given that the O_2 flux is light dependent and O_2's apparent short lifetime (Chapter 6).

Some species have additional complexities in their cross sections and photolysis rates, and are computed independently of equation (1.5). NO predissociation is computed using the method of Allen & Frederick (1982). The O_2 cross section is computed by an exponential sum parameterization that has not been described in the literature, but has

been incorporated into these photochemical models since approximately 1989. This is a high-priority item for improvement, given that a primary use of these models is to investigate the photochemistry of oxygen. The S_8 cross sections and photolysis scheme are computed as described in Kasting *et al.* (1989), and remain very uncertain.

Chemical production and loss are computed for each species based on the reaction rates given in Table 6-2 and the time-dependent diurnally averaged photolysis rates computed as described above. For each species, chemical loss rates are computed in molecules s^{-1} by multiplying the relevant rates by the species number density. Chemical production is computed for each species in molecules cm^{-3} s^{-1} by multiplying the relevant reaction rates by the densities of both species involved in the reaction. Photolysis and three body reactions are treated as special cases of the above, with photons being assigned an effective "density" of 1 cm^{-3}, and three body reactions containing the effect of background pressure included in the reaction rate.

Aqueous chemistry and rainout are also estimated in our model. Henry's law coefficients for gas dissolution are computed, and then modified to account for aqueous phase reactions within the carbonate and sulfate equilibria. The vapor pressure of H_2SO_4 and S_8 are computed relative to the temperature and H_2O concentration at each height, and rainout rates are computed using the methodology of Giorgi & Chameides (1985).

A.3.2.2 Particles

We have two species H_2SO_4 and S_8 for which we compute both gas and particle phases. At each timestep, evaporation, condensation, the resulting particle size distributions, and fall velocities are computed in a rough fashion. Lifetimes of the particle against sedimentation, diffusion, and rainout are computed, to determine which is the most important. The minimum of these three loss lifetimes is then compared against the particle coagulation lifetime computed from Toon & Farlow (1981). Particle growth is then scaled by the ratio of the smallest loss lifetime to the coagulation lifetime to the 0.25

power. Particles are not allowed to decrease in size at low altitudes, a somewhat questionable assumption. Particle fall velocities are computed using the Stokes-Cunningham equation.

Once particles form, they are subject to additional transport forces. They fall under the influence of gravity at a fall velocity which depends on the particle size. The advection term in equation (A.1) is only computed for the two particle species:

$$\frac{1}{\mathrm{N}}\frac{\partial}{\partial z}(v_{FALL}N_i) \qquad \text{(A.14)}$$

where v_{FALL} is the fall velocity which is positive downwards (unlike our definition of fluxes which are positive upwards). The numerical approximation of second-order centered differences is employed (see e.g. equation (A.3)). As before, this approaches works in the middle of the vertical grid, but requires care to avoid undefined terms at the upper and lower boundary. In this case, the advection terms computed for the 2nd layer are used for the 1st layer and the advection term for the upper layer is taken to the be that of the NZ-1 layer.

The lower boundary condition for the aerosol particles are computed at each timestep as the combination of the dry deposition velocity (Table A-1) and the particle fall velocity computed in the lowest layer. The “zero flux” upper boundary condition is defined by setting the effusion velocity equal to the fall velocity in the upper layer. This is a reasonable way to proceed, but practically it can lead to numerical problems in the upper stratosphere where the aerosols completely evaporate due to low temperatures and pressures. Computing a fall velocity requires a non-zero value for the aerosol density, so after each timestep, aerosol mixing ratios are reset to the largest of their computed value or 10^{-30}. Pavlov *et al.* (2001) use a separate tridiagonal matrix to solve particle species up to a height of 60 km, and use an analytic parameterization in the uppermost layers, which is a mild improvement. The code could benefit from a complete re-examination of the way particles are handled.

For completeness, we note that a parallel branch of development in this code has added a third particulate species – hydrocarbon aerosols. Pavlov *et al.*, (2001) consider the hydrocarbon haze that can form when CH_4/CO_2 ratios approach unity. In all models run for this dissertation, we have kept CO_2 fixed at 0.01 bar, and CH_4 never exceeded 0.001 bar, so our model with gas-phase hydrocarbon chemistry truncated at C_2H_6 is sufficient. Domagal-Goldman *et al.*, (2008) have argued that a Gaian feedback might stabilize the Earth system in a weak haze regime in the mid Archean, which could explain that evidence for glaciations at 2.9 Ga, although alternate Gaian explanations which buffer the Earth in a haze-free fashion are also possible (Zahnle, 2008). Regardless, the Earth was likely not hazy in the late Archean once methane started to drop, so our decision to not included hydrocarbon chemistry shouldn't have a major effect on any of the results regarding the nature and timing of the oxic transtion.

A.3.2.3 Error checking and Time-stepping

We have described how we have computed the various terms of equation (A.1) for all species at all heights. In section 7.2, we discussed the numerical algorithm by which this system of equations is solved simultaneously for a given timestep. Before returning to the start of the time-stepping loop, the stepsize for the next timestep is adjusted depending on how drastically the solution changed during the present timestep.

While computing the new concentrations using equation (7.10) in section 7.2.1, a numerical tally is kept of the largest (absolute) relative change of the new concentrations for each timestep. Species with mixing ratios below 10^{-20} are ignored while compiling the relative errors. The value of the next timestep (Δt) is chosen based on the largest relative error (E_{MAX}) in the previous timestep (Δt_{PREV}). If E_{MAX} is small, the model uses a larger Δt for the next timestep. If E_{MAX} is too large, the new concentrations are not saved, and the timestep is tried again with smaller Δt. The conditions that are used to advance the timesteps in the the steady-state photochemical models in Chapters 4 and 6 are

shown in Table A-3. For these models, we did not analyze the time-dependent path that the solution took to reach steady state.

Table A-3 Relative error and future timesteps

The model chooses the size of the future timestep based on the maximum relative change that occurs to any new species concentration

Error condition	Next time step
$E_{MAX} > 0.25$	$\Delta t = 0.7\ \Delta t_{PREV}$
$0.15 < E_{MAX} < 0.25$	$\Delta t = 1.0\ \Delta t_{PREV}$
$E_{MAX} < 0.07$	$\Delta t = 1.2\ \Delta t_{PREV}$
$E_{MAX} < 0.01$	$\Delta t = 1.4\ \Delta t_{PREV}$
$E_{MAX} < 0.008$	$\Delta t = 2.0\ \Delta t_{PREV}$
$E_{MAX} < 0.004$	$\Delta t = 3.0\ \Delta t_{PREV}$
$E_{MAX} < 0.001$	$\Delta t = 4.0\ \Delta t_{PREV}$
$E_{MAX} < 0.0005$	$\Delta t = 5.0\ \Delta t_{PREV}$

For the models where we analyzed the time-dependent path of the model towards reaching steady state (i.e. in Chapter 7), we set the error conditions one order of magnitude stricter than those in Table A-3. For example, the next timestep was taken to be 1.4 times the previous timestep only if E_{MAX} was less than 0.1%, rather than 1%, which was used in Chapters 4, and 6. In general, this method of selecting the next timestep is ad-hoc, but works well in practice. More clever schemes exist for computing appropriate values of the future timesteps based on the behavior of the solution on the previous few timesteps. The most well known of these are the multi-step predictor-corrector solvers, such as those described by Gear (1971). Gear's method of solution also uses the concept of relative errors over the past few timesteps to choose the numerical order of the solver at future timestep, selecting anywhere between 1^{st}-order reverse-Euler to 5^{th}-order reverse Euler depending on the nature of the time-dependent

change occurring in the solution. Adding a Gear-type time-dependent solver should be a high priority for future efforts, as it will enable time-dependent calculations of the sort presented in Chapter 7 to be performed in a computationally efficient manner.

A.4 Recommended changes to the photochemical model

In the course of this dissertation we have made some changes to the photochemical model which have dramatically improved model stability (lightning) and allowed us to work in new regimes of photochemical phase space. We have also fixed portions of the code that have second-order effects on photochemistry, but were worth fixing in the spirit of reducing uncertainty in the model results. An example of this second category is the solar flux changes described in Chapter 8. Here, we compile a list of additional changes that could be made to the model that at a minimum would go towards removing user doubt, and may possibly allow unanticipated avenues for new exploration.

- Coupling of a radiative-convective climate model into the photochemical model
- Introducing a Gear-type solver for time-dependent explorations
- Implementing the two-stream radiative transfer scheme of Toon *et al.* (1989)
- Refining the wavelength grid, and adding modern cross section measurements
- Verification of the O_2 cross section exponential sum calculation
- Verification of the sulfur polymerization rates, species cross sections, and photolysis rate schemes
- Investigation of self-consistent eddy-diffusion and tropopause heights
- Inclusion of CO_2 in the main matrix with inclusion of temperature-dependent lower boundary conditions
- A re-evaluation of the CO_2 and N_2 upper boundary conditions
- A re-evaluation of how particles are handled
- A self-consistent description of atmospheric pressure

VITA

Mark Claire was born in Washington, D.C in 1974 and graduated from Bethesda–Chevy Chase high school in 1992. He obtained a Bachelor of Science from The Evergreen State College in Olympia, WA in 1997, with a focus on Physics and Mathematics. He worked for the US National Science Foundation from 1998-2002 as a Science Education Analyst for the Division of Undergraduate Education and as a Computer Specialist for the Division of Information Systems. He entered graduate school at the University of Washington in 2002 and was awarded a Masters in Astronomy in 2005 and a Doctorate in Astronomy and certificate in Astrobiology in 2008.